Multiscale and multiaxial mechanics of multi-layered soft composites : application to the human annulus fibrosus

Abderrahman Tamoud

UNIVERSITE DE LILLE
LABORATOIRE DE GENIE CIVIL ET GEO-ENVIRONNEMENT
ÉCOLE DOCTORALE SCIENCE DE L'INGENIERIE ET DES SYSTEMES (ENGSYS)

UNIVERSITE DES SCIENCES ET TECHNOLOGIE HOUARI-BOUMEDIENE
LABORATOIRE DE MECANIQUE AVANCEE
FACULTE DE GENIE MECANIQUE, DEPARTEMENT CONSTRUCTION MECANIQUE ET PRODUCTIQUE

Thèse en cotutelle

Pour obtenir le grade de

Docteur de l'Université des Sciences et Technologie Houari-Boumediène
Spécialité : Construction, Fabrication et Fiabilité mécanique

et

Docteur de l'Université de Lille
Spécialité : Mécanique, Energétique, Matériaux

Présentée par

Abderrahman TAMOUD

Soutenue le 1 décembre 2021

Intitulée

Mécanique multi-échelle et multiaxiale des composites souples multicouches : Application à l'annulus fibrosus humain

Multiscale and multiaxial mechanics of multi-layered soft composites: Application to the human annulus fibrosus

Jury

Jean-François GANGHOFFER	Professeur	Université de Lorraine	Président
Grégory CHAGNON	Professeur	Université Grenoble Alpes	Rapporteur
Saïd RECHAK	Professeur	Ecole Nationale Polytechnique d'Alger	Rapporteur
Faiza BOUMEDIENE	Professeur	Université des Sciences et de la Technologie Houari Boumediene	Examinateur
Fahed ZAÏRI	Neurochirurgien	Ramsay Générale de Santé	Invité
Amar MESBAH	Professeur	Université des Sciences et de la Technologie Houari Boumediene	Directeur de thèse
Fahmi ZAÏRI	Professeur	Université de Lille	Directeur de thèse

Acknowledgement

Cette thèse s'inscrit dans le cadre d'une collaboration entre le Laboratoire Génie Civil et géo-Environnement (LGCgE) de l'Université de Lille et le Laboratoire de Mécanique Avancée de l'Université des Sciences et de la Technologie Houari Boumediene.
Elle a été soutenue financièrement par le programme de bourses PROFAS B+ et le programme de bourses de mobilité internationale de l'Université de Lille (MOBILEX). Je profite de l'occasion pour remercier les deux programmes pour le support financier.

Je souhaite, en premier lieu, exprimer toute ma gratitude et mes remerciements à mes directeurs, le Professeur ***Fahmi ZAÏRI*** *et le Professeur* ***Amar MESBAH*** *pour m'avoir encadré, guidé et encouragé tout au long de mes travaux. J'ai beaucoup appris à leurs côtés, que ce soit au niveau scientifique qu'au niveau humain.*
** Merci* ***Fahmi****, d'avoir toujours montré un grand intérêt pour mes travaux. Merci de m'avoir transmis votre passion pour la recherche et votre rigueur de travail qui m'ont permis de mener à bien ce projet.*
** Merci* ***Amar*** *pour votre disponibilité et votre grande réactivité face à tous mes problèmes.*

Un remerciement tout particulier à l'ensemble des membres de mon jury pour avoir accepté de contribuer à l'évaluation de mes travaux de recherche et de participer à ma soutenance de thèse.
Je remercie Monsieur le Professeur ***Jean-François GANGHOFFER*** *pour l'honneur qu'il me fait d'accepter la présidence de ce jury.*
Mes vifs remerciements sont adressés à Monsieur le Professeur ***Grégory CHAGNON*** *et Monsieur le Professeur* ***Saïd RECHAK*** *pour avoir accepté de juger ce travail en tant que rapporteurs et pour leurs rapports pertinents.*
Je remercie également Madame le Professeur ***Faiza BOUMEDIENE*** *et Monsieur le Professeur* ***Jean-François GANGHOFFER*** *pour avoir accepté d'examiner mes travaux de recherches.*

Je tiens à remercier mes parents pour leur soutien permanent, constant et surtout sans aucune faille ; avec la patience et la confiance que vous avez toujours placées en moi ; vous m'avez permis d'avancer en toute quiétude. J'espère qu'ils trouveront en ce modeste travail une récompense de ce qu'ils ont fait pour moi.

Je tiens à remercier chaleureusement mon épouse ***Neddou*** *pour sa présence constante à mes côtés.*

Je souhaite remercier les personnes sans qui je ne serais pas là aujourd'hui et qui me supportent au quotidien, je pense bien évidemment à ma famille. Votre amour et votre confiance en moi me permettent de me surpasser chaque jour un peu plus. Mention spéciale à mes ***sœurs*** *et leurs familles.*

Pour finir, je remercie aussi tous mes amis et toutes les personnes qui m'ont aidé et qui ont contribué de près ou de loin à mener à bien ce travail de recherche.

Multiscale and multiaxial mechanics of multi-layered soft composites: Application to the human annulus fibrosus

Summary

General introduction

Back pain is a common health problem affecting about 50 to 80% of humans at least one time during their life. The pain is sometimes related to muscles and ligaments, but when it is intense and chronic it is often linked to the intervertebral disc injuries and dysfunctions. This soft tissue located in the vertebral column gives to the body the mobility needed to achieve the different movements while resisting in parallel to the loads coming from the body weight and the daily activities. Any small issue in the intervertebral discs may cause many troubles in the human back varying from a simple back pain to disc hernia and sometimes could lead to paralysis. For this reason, the importance of studying the intervertebral disc conduct and predicting its response under the different physiological movements is mandatory in order to understand the chemo-mechano-biological mechanisms taking place inside the disc soft tissues which could help avoiding damage and producing better treatment procedures if damage is already present. Great progresses in this field were achieved over the recent years. Although important differences could be witnessed between the discs of different individuals, many experimental contributions succeeded to identify the mechanical response of the disc at different scales: complete spine scale, functional spine unit scale and material volume element scale. However, accessing the core of the disc in-vivo while maintaining unchanged its natural response is very hard to achieve which represents an obstructing point in the intervertebral disc research. That is why multi-physics simulations relating the microstructure of the chemo-biological tissue to its multiaxial response become mandatory for understanding the disc behavior under normal activity. However, the multi-subject problematic translated by the complex interactions between the different microstructural elements of the disc makes the task very complex. Also, due to the high heterogeneity of the biological tissues intervening in the intervertebral disc and the varying response between different individuals, a huge amount of experimental works of hardly available human cadavers should be established in order to construct and validate a reliable model of the disc.

Objective and thesis plan

The damage in annulus fibrosus soft tissues is a complex multiscale phenomenon due to a complex structural arrangement of collagen network at different scales of hierarchical organization. A fully three-dimensional constitutive representation that considers the regional variation of the structural complexity to estimate annulus multiaxial mechanics till failure has not yet been developed. In the present PhD dissertation, a model, formulated within the framework of nonlinear continuum mechanics, is developed to predict deformation-induced damage and failure of annulus under multiaxial loading histories considering as time-dependent physical process both chemical-induced volumetric effects and damage accumulation. In order to realize our objective, the actual thesis was planned following several well-constructed steps that will be described in details through the following chapters:

In **Chapter I**, a microstructure-based model is proposed to connect structural features, intrinsic mechanics and electro-chemical properties of annulus soft tissues. The multi-layered lamellar/inter-lamellar annulus model is constructed by considering the effective interactions between adjacent layers and the chemical-induced volumetric strain. The model/experiments comparison demonstrates that the evaluation of the overall time-dependent response involves considering stress, volumetric change and auxetic feature simultaneously in relation to structural features.

In **Chapter II**, the model is enriched by considering the hierarchical structure of the soft tissue from the nano-sized collagen fibrils to the micro-sized oriented collagen fibers. The stochastic process of progressive damage events operating at different scales of the solid phase is introduced for the extracellular matrix and the network of nano-sized fibrils/micro-sized fibers. The directional effects on annulus mechanics and failure are highlighted in relation to external loading mode, structure features, damage events and hydration.

In **Chapter III**, the model is further developed by considering the regional variation of the complex structural organization of collagen network at different scales to predict the regional anisotropic

multiaxial damage of the intervertebral disc. After model identification using single lamellae extracted from different disc regions, the model predictability is verified for various multiaxial elementary loading modes representative of the spine movement. The stretching along the circumferential and radial directions till failure serves to check the predictive capacities of the annulus model for the different regions. Model results under simple shear, biaxial stretching and plane-strain compression are further presented and discussed.

In **Chapter IV**, a full human disc model is constructed using the regional annulus model to examine the heterogeneous mechanics in the disc core. Damage fields in the disc are analyzed under axial compression, axial twist and combined loadings to assess the areas where the risk of failure is the highest.

Chapter I

A microstructure-based model for time-dependent mechanics of multi-layered soft tissues and its application to intervertebral disc annulus

A microstructure-based model for time-dependent mechanics of multi-layered soft tissues and its application to intervertebral disc annulus[1]

Abstract

In recent experimental studies an unusual time-dependent transversal behavior of the annulus fibrosus of the intervertebral disc mainly caused by the coupling between mechanics and electro-chemical activity was disclosed. In this contribution, a microstructure-based model is proposed to connect structural features, intrinsic mechanics and electro-chemical properties of multi-layered soft tissues with a special attention to disc annulus. A hybrid experimental/modeling decoupling strategy is proposed to obtain the constitutive representation of each layer of the disc annulus thanks to full-field strain data. The layers are then reconnected to each other to get the overall time-dependent response considering inter-layer ionic diffusion as well as stress/strain continuity along the interfaces. The final constitutive model is shown to describe the experimentally observed behavior of bovine tissues under free swelling immediately followed by quasi-static stretching, deviating from chemical equilibrium and provoking auxeticity, and then relaxation, allowing equilibrium return. The model/experiments comparison demonstrates that the evaluation of the overall time-dependent response involves considering stress, volumetric change and auxetic feature simultaneously in relation to diffusion-mechanics and structural features in terms of collagen orientation/content, interlamellar matrix inter-spacing fiber-reinforced layers and gradual thickness of layers. The effective contribution of fiber-reinforced and unreinforced interlamellar layers on the coupling is discussed with respect to the model. Using the model, microstructure and coupling effects are independently investigated in order to highlight their role on the damage-related annulus shearing.

Keywords: Multi-layered soft tissues; Microstructure; Volumetric strain; Constitutive model; Time-dependent response.

[1] This chapter is based on the following paper: Tamoud, A., Zaïri, F., Mesbah, A., Zaïri, F., 2021. A microstructure-based model for time-dependent mechanics of multi-layered soft tissues and its application to intervertebral disc annulus. Meccanica 56, 585-606.

Nomenclature

$\mathbf{F}$: Deformation gradient tensor
$\mathbf{E}$: Green-Lagrange strain tensor
$\mathbf{C}$: Right Cauchy-green strain tensor
$\mathbf{B}$: Left Cauchy-green strain tensor
$\boldsymbol{\sigma}$: Cauchy stress tensor
$\mathbf{R}$: Rotational basis-change tensor
$\mathbf{I}$: Identity tensor
$\mathbf{D}$: Ions diffusivity tensor
$\mathbf{k}$: Permeability tensor
$\boldsymbol{x}$, $\boldsymbol{y}$, $\boldsymbol{z}$: Cartesian coordinate vectors
$\boldsymbol{a}$: Unit vector of collagen fiber
$\boldsymbol{n}$: Unit vector at the inter-layer interfaces
+/-: cationic/anionic
c : Ions concentration
t : time
θ : Fiber angle with respect to the $\boldsymbol{xy}$-plane
z : Layer thickness
m : Number of layers
ϕ : Volume fraction
W : Free energy function
p : Pressure
I : Chemical invariant
$\bar{I}$: Isochoric invariant
J : Volumetric change
λ : Stretch
ν : Poisson's ratio

Operators

$\nabla(\bullet)$ Gradient
$\otimes$ Direct (outer) product
$(\bullet)^T$ Transpose
$\cdot$ Simple contraction

Abbreviations

LM: Lamellar
ILM: Inter-lamellar
ECM: Extracellular matrix
OCF: Oriented collagen fibers
PG: Proteoglycan

I.1. Introduction

The biological soft tissues are electro-chemically active media and many of them are fiber-reinforced laminates. Their constitutive modeling including structure-property relationship is of prime importance for a better understanding of the tissue biomechanics. It may also help in a broader way to better understand injury mechanisms, to detect and monitor pathologies and to design new bio-substitutes.

The formulation of a constitutive model has to consider three main key points in order to physically describe the underlying chemo-mechanical mechanisms and the macro-response: (i) firstly, a microstructure representation has to be proposed, (ii) secondly, free energy functions have to be defined for each constituent of the microstructure, (iii) thirdly, the electro-chemical activity resulting in the fluid flow inside the tissue has to be taken into account. In existing constitutive models, the structural features of the soft tissue are basically related to the intrinsic properties of extracellular matrix (ECM) and collagen fibers (Holzapfel et al., 2000; Peng et al., 2005; Balzani et al., 2006;

Guo et al., 2006; Kroon and Holzapfel, 2007; Li and Robertson, 2009; Chen et al., 2011). The presence of the fluid phase is implicitly modeled by considering a volumetric contribution into the free energy function (Rodriguez et al., 2006; Pierce et al., 2013; Swedberg et al., 2014; McEvoy et al., 2018; Derrouiche et al., 2019b; Kandil et al., 2019). In other constitutive models based on bi- or tri-phasic theory, the osmotic swelling effects due to the electro-chemical activity in the soft tissue are more explicitly taken into account by considering the interactions between charged ECM and fluid phase (Mow et al., 1980; Holmes and Mow, 1990; Lai et al., 1991; Iatridis et al., 2003; Yao and Gu, 2007; Ehlers et al., 2009; Stalhand et al., 2011; Stracuzzi et al., 2018).

This work is focused on a highly complex multi-layered soft tissue, that is, the annulus fibrosus of the intervertebral disc. The annulus fibrosus is a fiber-reinforced tissue in which the ECM is reinforced by oriented type-I collagen fibers (OCF) providing tensile strength and mechanical stiffness (Holzapfel et al., 2005; Roberts et al., 2006). To these "solid" components, the soft tissue contains also a fluid phase (composed of water, mobile charges and small proteins) that interacts with the fixed charges of the ECM providing the chemo-mechanical coupling (Derrouiche et al., 2019a, 2020b). The successive fiber-reinforced lamellar (LM) layers, exhibiting alternate fiber angles, are inter-separated by an interlamellar (ILM) matrix, i.e. intermediate ground substance devoid of OCF (Pezowicz et al., 2006). The organization is such that the thickness of layers is graded and increases from the outer annulus towards the inner annulus (Cassidy et al., 1989; Marchand and Ahmed, 1990; Hsu and Setton, 1999; Holzapfel et al., 2005). It is only in very recent experimental studies that the ILM zone has been appreciated from structural/mechanical viewpoint (Michalek et al., 2009; Vergari et al., 2016; Tavakoli et al., 2016, 2017, 2018). It is considered as the main factor ensuring disc structural integrity and disc shearing resistance. To date, the modeling studies including the ILM zone are rare (Nerurkar et al., 2011; Labus et al., 2014; Adam et al., 2015; Mengoni et al., 2015; Derrouiche et al., 2019b; Kandil et al., 2019). This ground substance is introduced solely into numerical models of the disc and its role is generally limited to a sliding zone

with either cohesive or non-cohesive features. Recently, Derrouiche et al. (2019b) and Kandil et al. (2019) proposed a numerical model of the annulus considering the LM/ILM interaction effects on the intrinsic properties and the fluid transfer through the multi-layered soft tissue in the aim to consider the shrinkage and swelling mechanisms. The latter may be considered as indicators of the chemo-mechanical coupling in annulus during the annulus stretching[2]. This coupling in annulus is believed to be the main responsible of an unusual time-dependent transversal behavior with out-of-bounds Poisson's ratios (higher than 0.5 and smaller than 0 for isotropic media) during short-term stretching followed by equilibrium return during long-term interrupted stretching (relaxation) towards more usual values (Baldit et al., 2014; Derrouiche et al., 2019b, 2020a; Kandil et al., 2019). To date, no analytical constitutive modeling is proposed to describe these effects in annulus.

The purpose of this chapter is to formulate a constitutive model for the annulus time-dependent response as the result of the coupling between mechanics and electro-chemical activity. We propose a two-stage strategy consisting in a decoupling stage of each layer of the multi-layered soft tissue using full-field strain data and a re-coupling stage reconnecting the layers by inter-layer ionic diffusion as well as stress/strain continuity along the interfaces. The final model is then utilized to examine the effective role of the relevant structural features (ILM zone and LM/ILM dimensions) and the diffusion-mechanics on the time-dependent response of the multi-layered soft tissue. The response is examined under three successive steps: free swelling, quasi-static stretching and relaxation.

The outline of the present chapter is as follows. Section I.2 is devoted to the microstructure-based model formulation. The hybrid experimental/modeling decoupling strategy is described in Section

[2] This loading path is representative of the compression mechanics of disc. Indeed, the vertebral column is permanently subjected to an axial compression (due to muscular tension and body weight) prior to further 3D loadings that expose the annulus to a tensile stretching in the disc circumferential direction due to the swelling of the "gelatinous" nucleus pulposus retained by the adjoining concentric annulus lamellae (Nachemson and Morris, 1964).

I.3. The effective contribution of the LM and ILM layers on the coupling is discussed in Section I.4. Concluding remarks are given in Section I.5.

The following notation is used throughout the text. Tensors and vectors are denoted by normal boldfaced letters and italicized boldfaced letters, respectively, while scalars and individual components of vectors and tensors are denoted by normal italicized letters. Simple contraction of two vectors or two tensors is denoted by a dot ‘‘$\cdot$’’, and a direct (outer) product by the symbol $\otimes$. Superscript $(\bullet)^T$ indicates the transpose quantity.

I.2. Model formulation

I.2.1. Kinematics of the soft tissue

Let us first introduce the kinematics for which an illustration is provided in Figure I.1. In the context of finite-strain continuum mechanics, the deformation gradient $\mathbf{F}$ describes the transformation of a material point of the continuum medium. It is defined as $\mathbf{F} = \partial \boldsymbol{x}_{\Omega} / \partial \boldsymbol{X}_{\Omega_0}$ for a transformation from the initial position $\boldsymbol{X}_{\Omega_0}$, in the configuration Ω_0 at time $t = 0$, to the current position $\boldsymbol{x}_{\Omega}$, in the configuration Ω at time $t \neq 0$.

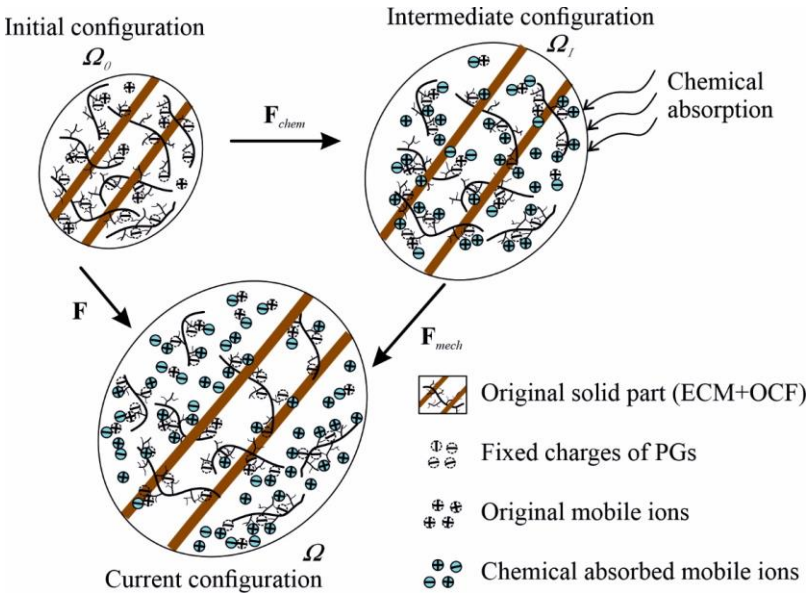

Figure I.1. Decomposition of the deformation gradient $\mathbf{F}$ into chemically-induced fluid transfer part $\mathbf{F}_{chem}$ and purely mechanical part $\mathbf{F}_{mech}$.

The Jacobian of the transformation, equivalent to the volumetric change of the continuum body, is noted $J = \det(\mathbf{F}) > 0$.

As schematically represented in Figure I.2a, each LM layer of the soft tissue is connected with its neighborhood via an ILM layer.

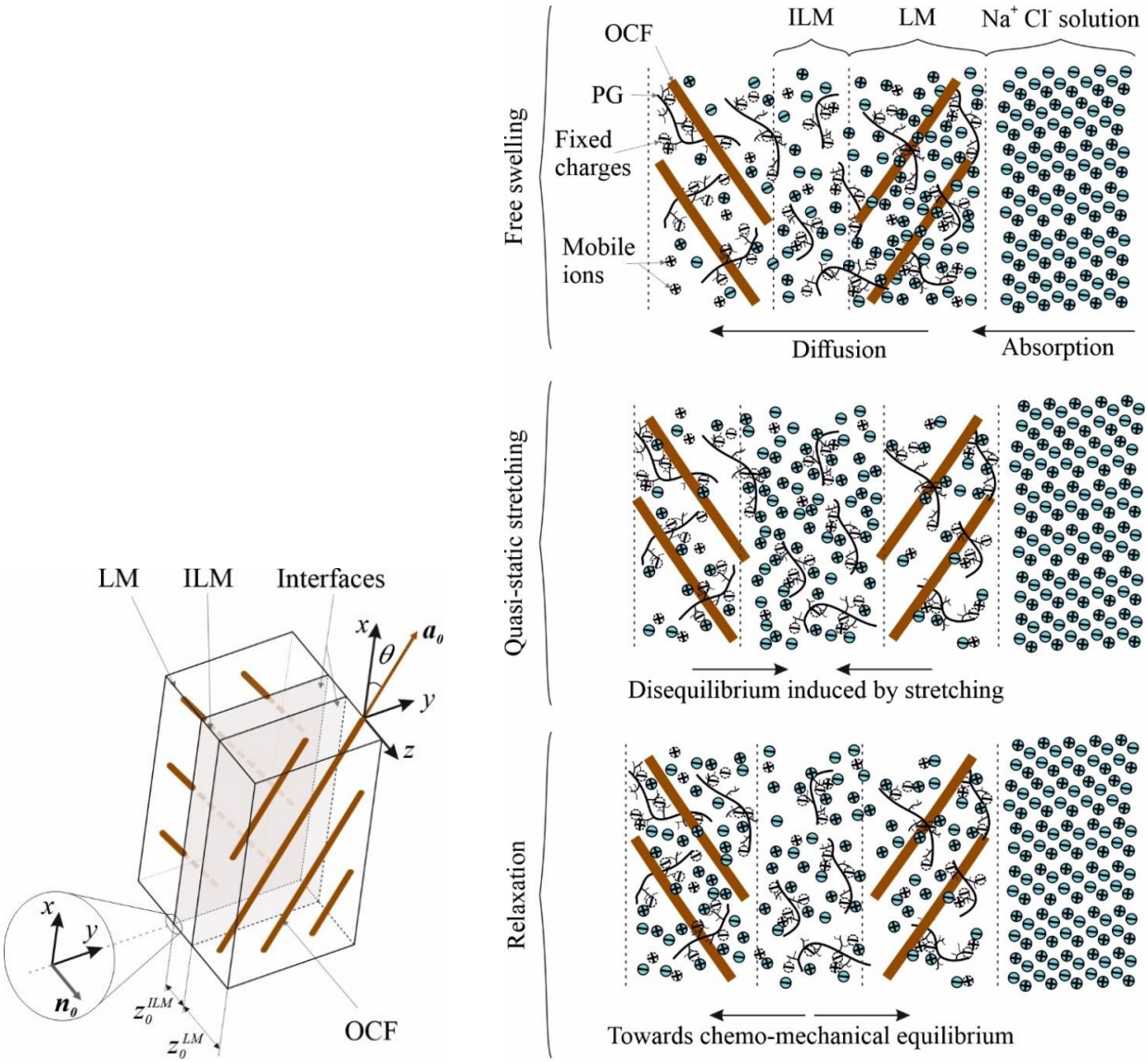

(a) (b)

Figure I.2. Chemo-mechanical interactions: (a) Mechanical interactions between layers due to the stress/strain continuity along the interfaces (The main $\boldsymbol{a}_0$-axis of OCF in LM forms an angle θ with

the ***x***-axis), (b) Electro-chemical interactions due to transfer mechanisms through the thickness of the multi-layered soft tissue upon different successive loading steps (free swelling/quasi-static stretching/relaxation).

The LM layer is regarded as a three-phase medium consisting in ECM, OCF and fluid phase whereas the ILM layer is a two-phase medium consisting in ECM and fluid phase[3]. The deformation gradient $\mathbf{F}$ of the multi-layered soft tissue is given by:

$$\mathbf{F} = \sum_{i=1,3...}^{m} \phi_{layer\_0}^{i} \mathbf{F}^{LM\_i} + \sum_{i=2,4...}^{m-1} \phi_{layer\_0}^{i} \mathbf{F}^{ILM\_i} \tag{I.1}$$

where $\mathbf{F}^{LM\_i}$ and $\mathbf{F}^{ILM\_i}$ are the deformation gradients of layers i (LM or ILM) and $\phi_{layer\_0}^{i}$ is the volume fraction of the layer *i* in the initial configuration Ω_0:

$$\phi_{layer\_0}^{i} = \frac{z_{layer\_0}^{i}}{\sum_{i=1}^{m} z_{layer\_0}^{i}} \tag{I.2}$$

in which *m* is the total number of layers and $z_{layer\_0}^{i}$ is the initial thickness of the layer *i*.

The condition of continuity of the deformation along the interfaces writes:

$$\mathbf{F}^{i}.\boldsymbol{n}_0^{i} = \mathbf{F}^{i+1}.\boldsymbol{n}_0^{i} \tag{I.3}$$

where $\boldsymbol{n}_0^{i}$ (i=1, …m-1) is the arbitrary unit vector between two adjacent layers as illustrated in Figure I.2a.

To combine chemical deformation and mechanical deformation in each layer, the conceptual sequence of configurations is used by the introduction of an intermediate chemical configuration Ω_1 at time $t \neq 0$ as illustrated in Figure I.1. The total deformation gradient $\mathbf{F}$ takes the following multiplicative form:

$$\mathbf{F} = \mathbf{F}_{chem}.\mathbf{F}_{mech} \tag{I.4}$$

[3] ECM represents all non-fibrillar "solid" components and is mainly constituted by a network of randomly oriented and negatively charged proteoglycan (PG) macromolecules, conferring hydrophilic properties to the disc soft tissues (Urban and Maroudas, 1981), randomly oriented type-II collagen and other types of collagen. In the special case of the disc, the proportions of the latter constituents vary from a disc region to another (Roberts et al., 1989).

Two successive arrangements are thus considered. The first one, related to the chemical dilatation of the continuum body, is characterized by the chemically-induced volumetric deformation gradient:

$$\mathbf{F}_{chem} = \frac{\partial \boldsymbol{X}_{\Omega_1}}{\partial \boldsymbol{X}_{\Omega_0}} \tag{I.5}$$

where $\boldsymbol{X}_{\Omega_1}$ is the position of the material point in the chemical configuration. The second one, related to the mechanical behavior of the continuum body, is characterized by the mechanical deformation gradient:

$$\mathbf{F}_{mech} = \frac{\partial \boldsymbol{x}_{\Omega}}{\partial \boldsymbol{X}_{\Omega_1}} \tag{I.6}$$

In view of these transformations, the volumetric change J is defined as:

$$J = J_{chem} J_{mech} \tag{I.7}$$

The mechanical deformation is assumed incompressible, i.e. $J_{mech} = 1$, and the volumetric change writes:

$$J = J_{chem} = \det\left(\mathbf{F}_{chem}\right) \tag{I.8}$$

where J_{chem} is the chemically-induced volumetric change that only depends on the internal fluid variation:

$$J_{chem} = \sum_{i=1,3...}^{m} \phi^{i}_{layer\_0} J_{chem}^{LM\_i} + \sum_{i=2,4...}^{m-1} \phi^{i}_{layer\_0} J_{chem}^{ILM\_i} \tag{I.9}$$

in which J^{i}_{chem} is the volumetric change of the layer i.

The right Cauchy-Green deformation is $\mathbf{C} = \mathbf{F}^{T}.\mathbf{F}$ and the invariants of its mechanical part $\mathbf{C}_{mech} = \mathbf{F}^{T}_{mech}.\mathbf{F}_{mech}$ are (Spencer, 1984):

$$\begin{aligned}
\bar{I}_1 &= \mathrm{trace}\left(\mathbf{C}_{mech}\right) \\
\bar{I}_2 &= \left(\mathrm{trace}\left(\mathbf{C}_{mech}\right)^2 - \mathrm{trace}\left(\mathbf{C}_{mech}^2\right)\right)\Big/2 \\
\bar{I}_3 &= \det\left(\mathbf{C}_{mech}\right) = 1 \\
\bar{I}_4 &= \boldsymbol{a}_0 . \mathbf{C}_{mech} . \boldsymbol{a}_0 \\
\bar{I}_5 &= \boldsymbol{a}_0 . \left(\mathbf{C}_{mech}\right)^2 . \boldsymbol{a}_0
\end{aligned} \tag{I.10}$$

The unit vector $\boldsymbol{a}_0$ of the fibers direction in the initial configuration is expressed in the Cartesian coordinates by $\boldsymbol{a}_0 = \cos\theta\, \boldsymbol{x} + \left|\sin\theta\right| \boldsymbol{y}$ in which θ is the angle between the loading direction and the fibers main axis, see Figure I.2a.

Similarly, the invariants of the chemical part $\mathbf{C}_{chem} = \mathbf{F}_{chem}^T . \mathbf{F}_{chem}$ can be defined as follows:

$$\begin{aligned}
I_1 &= \mathrm{trace}\left(\mathbf{C}_{chem}\right) \\
I_2 &= \left(\mathrm{trace}\left(\mathbf{C}_{chem}\right)^2 - \mathrm{trace}\left(\mathbf{C}_{chem}^2\right)\right)\Big/2 \\
I_3 &= \det\left(\mathbf{C}_{chem}\right) = J^2 \\
I_4 &= \boldsymbol{a}_0 . \mathbf{C}_{chem} . \boldsymbol{a}_0 \\
I_5 &= \boldsymbol{a}_0 . \mathbf{C}_{chem}^2 . \boldsymbol{a}_0 \\
I_6 &= \boldsymbol{a}_0 . \mathbf{C}_{chem}^3 . \boldsymbol{a}_0
\end{aligned} \tag{I.11}$$

where $\boldsymbol{a}_0$ is again the unit vector of the fibers direction. Note that a sixth invariant is introduced in Eq. (I.11) according to the derivations in Appendix I.A for the volumetric change in a fiber-reinforced material system.

I.2.2. Free energy: microstructure and chemo-mechanics decomposition

According to the chemo-mechanics decomposition, the free energy W is decomposed into two parts:

$$W = W_{mech} + W_{chem} \tag{I.12}$$

The interaction between solid and fluid phases is considered via the concept of volume fraction. For each layer, the respective (time-dependent) volume fraction of the main constituents is expressed as a function of its chemically-induced volumetric change J_{chem}^i:

$$\phi_{ECM}^{i} = \frac{\phi_{ECM\_0}^{i}}{J_{chem}^{i}}$$
$$\phi_{OCF}^{i} = \frac{\phi_{OCF\_0}^{i}}{J_{chem}^{i}} \tag{I.13}$$
$$\phi_{fluid}^{i} = 1 - \frac{1-\phi_{fluid\_0}^{i}}{J_{chem}^{i}}$$

where $\phi_{ECM\_0}^{i}$, $\phi_{OCF\_0}^{i}$ and $\phi_{fluid\_0}^{i}$ are the initial volume fractions in each layer *i*, and

$$\begin{aligned} &\phi_{ECM}^{i} + \phi_{OCF}^{i} + \phi_{fluid}^{i} = 1 \quad && i = 1,3,\ldots m \quad && \text{in} \quad \text{LM} \\ &\phi_{ECM}^{i} + \phi_{fluid}^{i} = 1 \quad && i = 2,4,\ldots m-1 \quad && \text{in} \quad \text{ILM} \end{aligned} \tag{I.14}$$

in which *m* is the total number of layers.

The mechanical part W_{mech}^{i} is written as follows for the LM and ILM layers, respectively:

$$\begin{aligned} &W_{mech}^{LM\_i} = \phi_{ECM}^{i} W_{ECM}^{i}\left(\mathbf{F}_{mech}^{LM\_i}\right) + \phi_{OCF}^{i} W_{OCF}^{i}\left(\mathbf{F}_{mech}^{LM\_i}\right) \quad && i = 1,3,\ldots m \\ &W_{mech}^{ILM\_i} = \phi_{ECM}^{i} W_{ECM}^{i}\left(\mathbf{F}_{mech}^{ILM\_i}\right) && i = 2,4,\ldots m-1 \end{aligned} \tag{I.15}$$

where W_{ECM}^{i} and W_{OCF}^{i} are the ECM and OCF free energies, respectively.

The intrinsic response of the ECM tangled PG macromolecules is supposed incompressible and fully defined by their stiffness. The ECM free energy W_{ECM}^{i} takes a simple Neo-Hookean form which depends only on the first-invariant:

$$W_{ECM}^{i} = \frac{1}{2} G_{ECM}\left(\bar{I}_{1}^{i} - 3\right) \tag{I.16}$$

in which G_{ECM} is the ECM shear modulus.

In addition to fibers direction, the transition from initially undulated to fully stretched states of the OCF (Pezowicz et al., 2006) affects their intrinsic nonlinear response. Thus, the OCF free energy W_{OCF}^{i} takes the following exponential form which depends only on the fourth-invariant (Holzapfel et al., 2000):

$$W_{OCF}^{i} = \frac{1}{2}\frac{C_1}{C_2}\left(\exp\left(C_2\left(\bar{I}_{4}^{i} - 1\right)^2\right) - 1\right) \tag{I.17}$$

in which C_1 and C_2 are material constants and, their ratio C_1/C_2 represents the OCF stiffness.

The chemically-induced volumetric part W^i_{chem} is a function of the fluid free energy W^i_{fluid} and is written in the same form for the LM and ILM layers:

$$W^i_{chem} = \phi^i_{fluid} W^i_{fluid}\left(\mathbf{F}^i_{chem}\right) \tag{I.18}$$

The derivation details of the fluid free energy W^i_{fluid} are provided in Appendix I.A. The final expression is given by:

$$W^i_{fluid} = \frac{1}{2}\frac{K_1}{K_2}\left(\exp\left(K_2\left(J^i_{chem}-1\right)^2\right)-1\right) \tag{I.19}$$

where K_1 and K_2 are material constants and, their ratio K_1/K_2 represents the volumetric stiffness. The volumetric change J^i_{chem} takes different forms for the LM and ILM layers:

$$\begin{aligned} J^{LM\_i}_{chem} &= \sqrt{I^i_6 - I^i_1 I^i_5 + I^i_2 I^i_4} \qquad i = 1,3,...m \\ J^{ILM\_i}_{chem} &= \sqrt{I^i_3} \qquad\qquad\qquad\quad i = 2,4,...m-1 \end{aligned} \tag{I.20}$$

Further details are provided in Appendix I.A.

The free energy W of the multi-layered soft tissue is the sum of free energies of the LM layers $W^{LM\_i} = W^i_{mech} + W^i_{chem}$ and free energies of the ILM layers $W^{ILM\_i} = W^i_{mech} + W^i_{chem}$:

$$W = \sum_{i=1,3,..}^{m}\left(\phi^i_{layer} W^{LM\_i}\right) + \sum_{i=2,4,..}^{m-1}\left(\phi^i_{layer} W^{ILM\_i}\right) \tag{I.21}$$

where ϕ^i_{layer} is the (time-dependent) volume fraction of each layer in the current configuration Ω:

$$\phi^i_{layer} = \frac{J^i_{chem} z^i_{layer\_0}}{\sum_{j=1}^{m} J^j_{chem} z^j_{layer\_0}} \tag{I.22}$$

Note that, in the intervertebral disc, the proportions of individual layers vary from the outer annulus towards the inner annulus (Cassidy et al., 1989; Marchand and Ahmed, 1990; Hsu and Setton, 1999; Holzapfel et al., 2005). In our approach, the thickness of layers varies continuously following a

special function in the aim to describe a gradual variation of fractions through the multi-layered soft tissue (see Appendix I.B for more details).

I.2.3. Constitutive stress-strain response

According to Eq. (I.21), the Cauchy stress $\boldsymbol{\sigma}$ in the multi-layered soft tissue is expressed as:

$$\boldsymbol{\sigma} = \sum_{i=1,3,..}^{m} \left(\phi_{layer}^{i} \boldsymbol{\sigma}^{LM\_i} \right) + \sum_{i=2,4,..}^{m-1} \left(\phi_{layer}^{i} \boldsymbol{\sigma}^{ILM\_i} \right) \tag{I.23}$$

in which $\boldsymbol{\sigma}^{LM\_i}$ and $\boldsymbol{\sigma}^{ILM\_i}$ are the Cauchy stresses in the LM and ILM layers.

In order to respect the compatibility along the interfaces, the conditions of continuity of the stresses is:

$$\boldsymbol{\sigma}^{i}.\boldsymbol{n}^{i} = \boldsymbol{\sigma}^{i+1}.\boldsymbol{n}^{i} \tag{I.24}$$

where $\boldsymbol{n}^{i}$ (i=1, …m-1) is the arbitrary unit vector between two adjacent layers in the current configuration Ω.

The mechanical and chemical contributions in the stress may be additively split in reason of the chemo-mechanical coupling:

$$\boldsymbol{\sigma} = \sum_{i=1,3,..}^{m} \phi_{layer}^{i} \left(\boldsymbol{\sigma}_{mech}^{LM\_i} + \boldsymbol{\sigma}_{chem}^{LM\_i} \right) + \sum_{i=2,4,..}^{m-1} \phi_{layer}^{i} \left(\boldsymbol{\sigma}_{mech}^{ILM\_i} + \boldsymbol{\sigma}_{chem}^{ILM\_i} \right) \tag{I.25}$$

Each part of the Cauchy stress is obtained from the differentiation of the free energy functions with respect to the corresponding deformations:

$$\boldsymbol{\sigma}_{mech}^{i} = 2\mathbf{F}_{mech}^{i} \cdot \frac{\partial W_{mech}^{i}}{\partial \mathbf{C}_{mech}^{i}} . \mathbf{F}_{mech}^{i^{T}} - p^{i}\mathbf{I} \tag{I.26}$$

$$\boldsymbol{\sigma}_{chem}^{i} = \frac{\partial W_{chem}^{i}}{\partial J_{chem}^{i}} \mathbf{I} \tag{I.27}$$

where p^{i} represents a hydrostatic pressure in each layer introduced in reason of the mechanical incompressibility and determined from boundary conditions. The term $\mathbf{I}$ represents the identity tensor.

In Eq. (I.26), the derivation may be expressed as follows:

$$\frac{\partial W_{mech}^{i}}{\partial \mathbf{C}_{mech}^{i}} = \sum_{\delta=1}^{5} \left(\frac{\partial W_{mech}^{i}}{\partial \bar{I}_{\delta}^{i}} \frac{\partial \bar{I}_{\delta}^{i}}{\partial \mathbf{C}_{mech}^{i}} \right) \tag{I.28}$$

with

$$\begin{aligned}
&\frac{\partial \bar{I}_{1}^{i}}{\partial \mathbf{C}_{mech}^{i}} = \mathbf{I} \\
&\frac{\partial \bar{I}_{2}^{i}}{\partial \mathbf{C}_{mech}^{i}} = \bar{I}_{1}^{i}\mathbf{I} - \mathbf{C}_{mech}^{i} \\
&\frac{\partial \bar{I}_{3}^{i}}{\partial \mathbf{C}_{mech}^{i}} = \bar{I}_{3}^{i} \left(\mathbf{C}_{mech}^{i} \right)^{-1} \\
&\frac{\partial \bar{I}_{4}^{i}}{\partial \mathbf{C}_{mech}^{i}} = \boldsymbol{a}_{0} \otimes \boldsymbol{a}_{0} \\
&\frac{\partial \bar{I}_{5}^{i}}{\partial \mathbf{C}_{mech}^{i}} = \boldsymbol{a}_{0} \otimes \mathbf{C}_{mech}^{i}.\boldsymbol{a}_{0} + \boldsymbol{a}_{0}.\mathbf{C}_{mech}^{i} \otimes \boldsymbol{a}_{0}
\end{aligned} \tag{I.29}$$

After a series of straightforward derivations, the different parts of the Cauchy stress are given by:

$$\begin{aligned}
\boldsymbol{\sigma}_{mech}^{LM_i} = {} & \phi_{ECM}^{i} G_{ECM} \mathbf{B}_{mech}^{LM_i} - p^{i}\mathbf{I} \\
& + \left(2\phi_{OCF}^{i} C_{1} \left(\bar{I}_{4}^{LM_i} - 1 \right) \exp\left(C_{2} \left(\bar{I}_{4}^{LM_i} - 1 \right)^{2} \right) \right) \mathbf{F}_{mech}^{LM_i}.\left(\boldsymbol{a}_{0} \otimes \boldsymbol{a}_{0} \right).\mathbf{F}_{mech}^{LM_i^{T}}
\end{aligned} \tag{I.30}$$

$$\boldsymbol{\sigma}_{mech}^{ILM\_i} = \phi_{ECM}^{i} G_{ECM} \mathbf{B}_{mech}^{ILM\_i} - p^{i}\mathbf{I} \tag{I.31}$$

$$\boldsymbol{\sigma}_{chem}^{i} = \phi_{fluid}^{i} K_{1} \left(J_{chem}^{i} - 1 \right) \exp\left(K_{2} \left(J_{chem}^{i} - 1 \right)^{2} \right) \mathbf{I} \tag{I.32}$$

where $\mathbf{B}_{mech}^{i} = \mathbf{F}_{mech}^{i}.\mathbf{F}_{mech}^{i^{T}}$ is the mechanical part of the left Cauchy-Green deformation.

I.2.4. Electro-chemical diffusivity kinetics

Due to the physiological environment and the intrinsic ionic strength of the ionized ECM, the biological soft tissues are able to retain water up to several times their dehydrated volumetric state. As the fixed charges density of the charged hydrated ECM is large, a significant electro-chemical flux occurs through the multi-layered soft tissues leading to their swelling (Frijns et al., 1997). Because of swelling, an osmotic pressure is generated (Urban et al., 1978). According to the

classical Donnan theory, the osmotic pressure p_{osm} equals the difference between internal and external pressures:

$$p_{osm} = p_{int} - p_{ext} \tag{I.33}$$

In the case of a homogeneous swelling, the internal pressure p_{int} is a function of the concentration of the cationic $^{+}$ and anionic $^{-}$ electronic charges, c^{+} and c^{-}, and the external pressure p_{ext} depends on the concentration of the external solution c_{ext}^{*} (Huyghe and Janssen, 1997):

$$\begin{aligned} p_{int} &= \varphi_{int} RT\left(c^{+} + c^{-}\right) \\ p_{ext} &= \varphi_{ext} RT\left(c_{ext}^{*} + c_{ext}^{*}\right) \end{aligned} \tag{I.34}$$

in which R is the gas constant, T is the absolute temperature and, φ_{int} and φ_{ext} are the internal and external osmotic coefficients, respectively.

The phenomenon of ionic migration of the solute in the charged hydrated soft tissue is related to absorption and diffusion process as illustrated in Figure I.2b. The motion process of the ions may be classically expressed using the second Fick law depending on time and space (Ferguson et al., 2004; Soukane et al., 2009):

$$\frac{\partial c^{\pm}\left(x,y,z,t\right)}{\partial t} = \nabla\left(\mathbf{D}^{\pm}\left(\nabla c^{\pm}\left(x,y,z,t\right)\right)\right) \tag{I.35}$$

where $\mathbf{D}^{\pm}$ is the diffusivity of the ions.

Diffusivity in biological soft tissues is anisotropic due to material heterogeneity (Hsu and Setton, 1999; Antoniou et al., 2004) and depends on the strain and the principal direction of diffusion (Jackson et al., 2006, 2008, 2009; Travascio and Gu, 2007). The tensor of the diffusivity takes the following form:

$$\mathbf{D}^{\pm}\left(J_{chem}\right) = \mathrm{diag}\left(D_{xx}^{\pm}, D_{yy}^{\pm}, D_{zz}^{\pm}\right) \tag{I.36}$$

the terms $D_{xx}^{\pm}$, $D_{yy}^{\pm}$ and $D_{zz}^{\pm}$ being the diffusivity in the ***x***, ***y*** and ***z*** directions, respectively.

The diffusivity of the ions is expressed as follows (Gu et al., 2004):

$$\mathbf{D}^{\pm} = D_{free}^{\pm} \exp\left(-\alpha\left(r_s^{\pm}\mathbf{k}^{-1/2}\right)^{\beta}\right) \tag{I.37}$$

where α and β are two coefficients, $D_{free}^{\pm}$ is the free diffusivity of the spherical solutes in the external solution, $r_s^{\pm}$ is the solute size and $\mathbf{k}$ is the permeability tensor given by (Gu et al., 2004; Perie et al., 2006):

$$\mathbf{k}\left(J_{chem}\right) = \left(\frac{J_{chem} - \phi_{fluid\_0}}{1 - \phi_{fluid\_0}}\right)^{-M} \mathbf{k}_0 \tag{I.38}$$

in which M is a coefficient and $\mathbf{k}_0$ is the zero-strain permeability tensor in the ***x***, ***y*** and ***z*** directions, and:

$$\mathbf{k}_0 = \mathrm{diag}\left(k_{xx\_0}, k_{yy\_0}, k_{zz\_0}\right) \tag{I.39}$$

the term k_{xx_0}, k_{yy_0} and k_{zz_0} being the permeability in the ***x***, ***y*** and ***z*** directions, respectively.

It worth noticing that the chemically-induced volumetric stress $\boldsymbol{\sigma}_{chem}$ of the multi-layered annulus and the swelling pressure given by the classical Donnan theory may be equalized: $\boldsymbol{\sigma}_{chem} = p_{osm}\mathbf{I}$. What may seem like a reconciliation of the two theories is especially valid when the ionic equilibrium is achieved (chemical potential of the fluid is null). Indeed, the chemical disequilibrium generated by a stretching and the equilibrium return when the stretching is interrupted induce differentiations between layers swelling as illustrated in Figure I.2b.

I.3. Hybrid experimental/modeling decoupling strategy

I.3.1. Database

The model is applied on annulus specimens extracted from bovine cervical spine discs using two useful macro-quantities to design the material kinetics and to identify the model parameters: the volumetric change and the macro-stress. The experimental protocol is detailed elsewhere (Derrouiche et al., 2020a) but some important information is provided succinctly here.

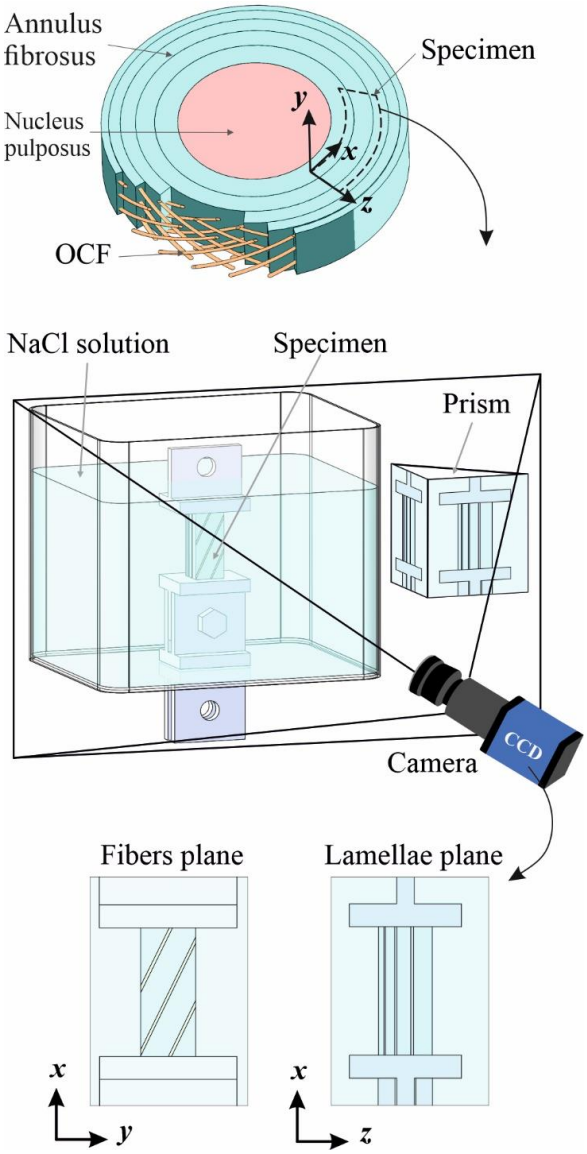

Figure I.3 Annulus specimen extracted from intervertebral disc and stretched in the circumferential direction ***x*** with simultaneous local displacement measurements in fibers plane ***xy*** and in lamellae plane ***xz*** using a right-angle prism.

Specimens of square cross-section (25 × 10 × 10 mm^3) were cut from the inner region of the annulus ring in the circumferential direction as illustrated in Figure I.3. The specimen, fixed by a rapidly polymerizing cyanoacrylate glue to metallic plates and mounted on the testing machine, was constantly immersed in a physiological solution with a NaCl concentration c_{ext}^{*} = 0.154 mEq.ml-1 during room temperature (22°C) experiments. The digital image correlation technique was used to measure the full-field displacement on the two main planes of the specimen: fibers plane ***xy*** and

lamellae plane ***xz***. After spraying speckles on the sample surfaces, the images were recorded using a CCD camera with a resolution of 290 pixels/mm, a recording frequency of 3 Hz and a size of 1628×1236 pixels.

The correlation calculation was performed using the Davis correlation software to obtain the contour of the Green-Lagrange deformation $\mathbf{E} = \left(\mathbf{F}^T\mathbf{F} - \mathbf{I}\right)/2$ and the average deformations (axial: E_{xx} and transversal: E_{yy} and E_{zz}) as a function of time. The lens axis of the CCD camera was kept perpendicular to fibers plane ***xy*** while lamellae plane ***xz*** was simultaneously recorded using a right-angle prism as proposed by Roux et al. (2003) and Parsons et al. (2004) for other materials. As illustrated in Figure I.4, the time-dependent response of the tissue was studied under three different successive loading steps[4]:

- The first step is a free swelling: The local strains were measured until the balance of swelling.
- The second step is a quasi-static stretching: The sample was strained up to a strain of 4% at a strain-rate of 0.001 s^{-1} in order to study the mechanical behavior coupled with chemistry. Before starting the second step, the sample was preconditioned by a series of ten loading-unloading cycles at low amplitude of 1% at a strain-rate of 0.001 s^{-1} in order to stimulate fluid exchanges inside the tissue.
- The third step is a relaxation: At the end of a stretching step, the strain is kept constant until the equilibrium of the response.

[4] The experimental results have been analyzed statistically taking into account: (i) the errors related to the inter-specimen variability using fifteen samples tested under the same physiological and mechanical conditions by the analysis of variance (ANOVA) method with a variability factor of $p < 0.05$, and (ii) the errors related to the correlation procedure with an average error of 9.7%.

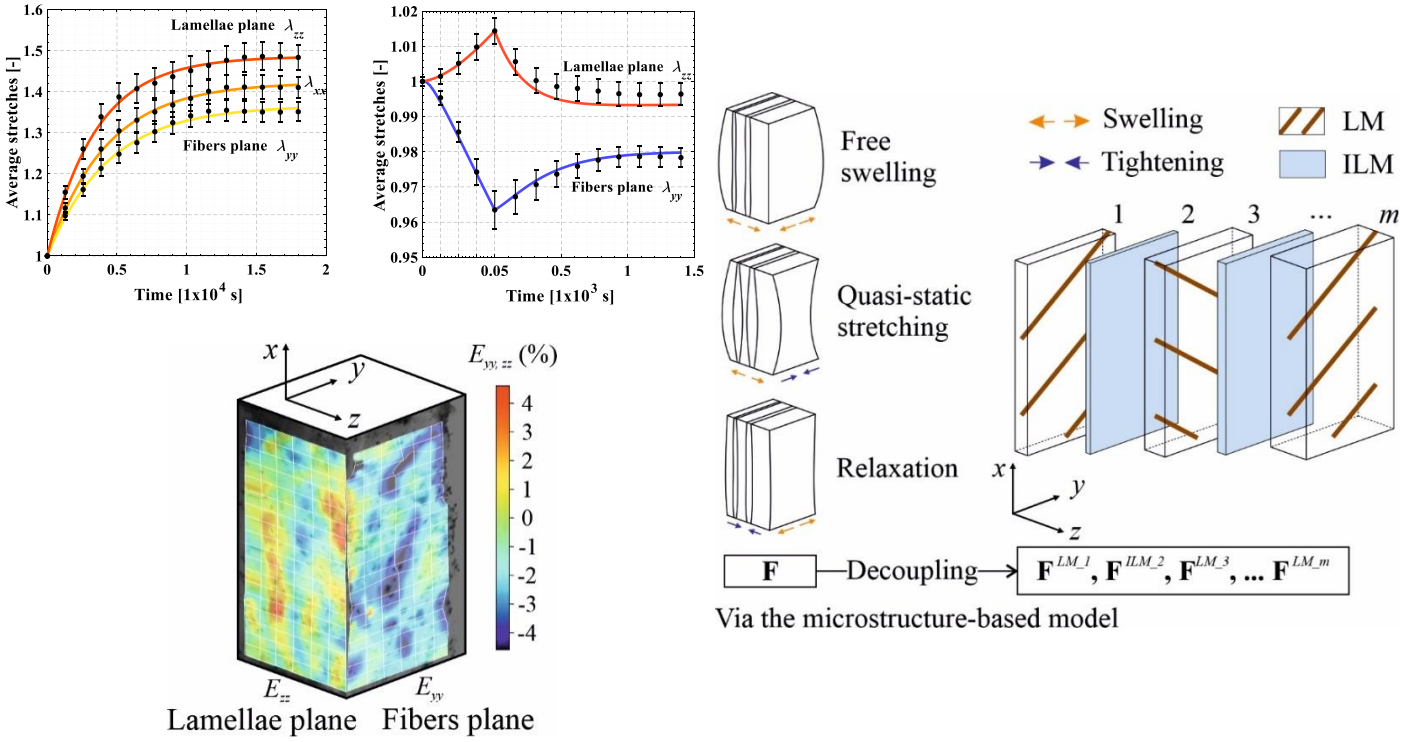

(a) (b)

Figure I.4. Hybrid experimental/modeling decoupling strategy: (a) from real-time strain field captured in fibers plane ***xy*** and in lamellae plane ***xz*** using digital image correlation method, the average deformation gradient **F** is determined in each plane and (b) the deformation of individual (homogenized) layer is extracted using the microstructure-based model. Especially, our strategy allows identifying the volumetric deformation of an individual layer from the specimen volumetric deformation upon different successive loading steps (free swelling/quasi-static stretching/relaxation). The chemo-mechanical response of an individual layer is then deduced. The reconstruction of the multi-layered tissue is finally achieved by considering the chemo-mechanical interactions described in Figure I.2.

During the three successive loading steps, the volumetric change J was obtained using the average axial stretch λ_{xx} and the average transversal stretches λ_{yy} and λ_{zz}:

$$J = \lambda_{xx}\lambda_{yy}\lambda_{zz} \tag{I.40}$$

Figure I.5a presents the volumetric response of the annulus specimen in the form of symbols with standard deviation error bars. During the free swelling, from dehydrated state to chemically-induced hydrated state, the soft tissue absorbs a large amount of fluid, the volume at the equilibrium state being approximately 2.8 times the initial volume V_0. The quasi-static stretching and relaxation steps

lead to small volume changes compared to the free swelling. Nonetheless, the chemically-induced volumetric response influences considerably the mechanical features. During the second and third steps, the applied force F was simultaneously recorded and was converted into true axial stress σ_{xx} :

$$\sigma_{xx} = \frac{F}{A} = \frac{F}{A_0 \lambda_{yy} \lambda_{zz}} \tag{I.41}$$

where A and A_0 are the instantaneous and initial sections, respectively.

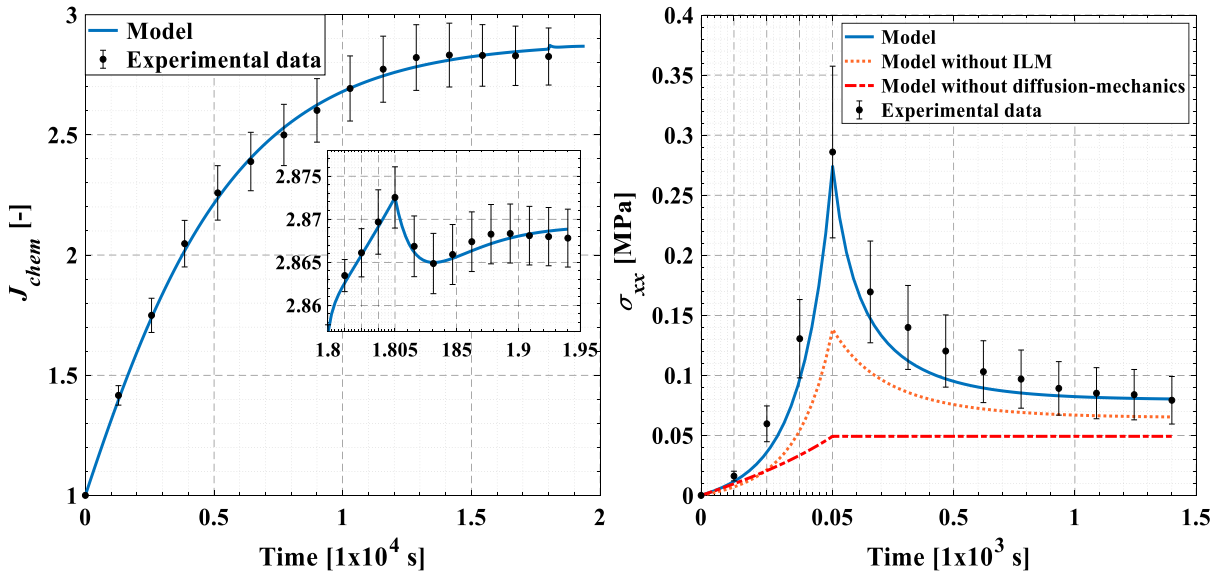

(a) (b)

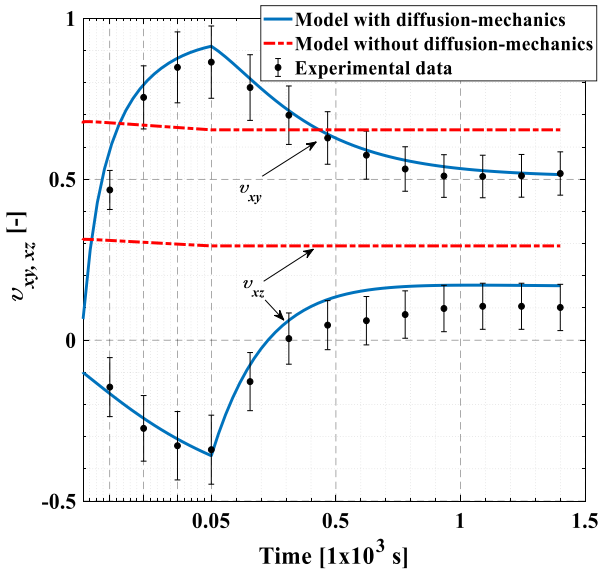

(c)

Figure I.5. Model vs. experiments: (a) Volumetric change, (b) Stress, (c) Apparent Poisson's ratio.

The stress evolution is presented in Figure I.5b in the form of symbols with standard deviation error bars. After a nonlinear increase during the stretching step, a substantial stress decrease occurs during the first few times of the relaxation period which is then followed by a more gradual decrease tending towards a stabilized state. As another basic mechanical quantity, the apparent Poisson's ratio[5] can be estimated from strains. It describes the transversal behavior of axially stretched specimens and is defined as the ratio between the transversal strain and the axial strain. The two-dimensional material is different according to the two main specimen planes:

$$\begin{aligned} \nu_{xz} &= -\frac{E_{zz}}{E_{xx}} \quad \text{in lamellae plane} \\ \nu_{xy} &= -\frac{E_{yy}}{E_{xx}} \quad \text{in fibers plane} \end{aligned} \tag{I.42}$$

The apparent Poisson's ratio is depicted in Figure I.5c during the two successive mechanical steps in the form of symbols with standard deviation error bars. Shrinkage and swelling mechanisms induce the unusual transversal behavior of the axially stretched specimen in its two main planes: $\nu_{xz} > 0.5$ (fibers plane) and $\nu_{xz} < 0$ (lamellae plane). The auxetic behavior of the lamellae plane is followed during the relaxation by positive values tending towards equilibrium. In the fibers plane, the Poisson's ratio presents values higher than 0.5 and reaches approximately 1.0 at the end of the stretching step. Subsequently, it decreases during the relaxation period to 0.5 at equilibrium.

I.3.2. Deformation of a layer

Under a free swelling, the deformation gradients of a layer *i* are:

$$\begin{aligned} \mathbf{F}^i_{mech} &= \mathbf{I} \\ \mathbf{F}^i_{chem} &= \mathrm{diag}\left(\lambda^i_{chem\_x}, \lambda^i_{chem\_y}, \lambda^i_{chem\_z}\right) \quad i = 1, 2, \ldots m \end{aligned} \tag{I.43}$$

in which $\lambda^i_{chem\_x}$, $\lambda^i_{chem\_y}$ and $\lambda^i_{chem\_z}$ are the chemical stretches in the ***x***, ***y*** and ***z*** directions, respectively.

[5] It is termed apparent Poisson's ratio since it is dependent on the fluid amount and it is not intrinsic to the tissue.

Assuming mechanical incompressibility, the mechanical deformation gradients under an axial stretching may be expressed as:

$$\begin{aligned} \mathbf{F}_{mech}^{LM\_i} &= \mathbf{R}_z^{\theta^i}.\mathrm{diag}\left(\lambda_f, \lambda_f^{-1/2}, \lambda_f^{-1/2}\right).\mathbf{R}_z^{\theta^{iT}} && i = 1,3,...m \\ \mathbf{F}_{mech}^{ILM\_i} &= \mathrm{diag}\left(\frac{\lambda}{\lambda_{chem\_x}^i}, \left(\frac{\lambda}{\lambda_{chem\_x}^i}\right)^{-1/2}, \left(\frac{\lambda}{\lambda_{chem\_x}^i}\right)^{-1/2}\right) && i = 2,4,...m-1 \end{aligned} \tag{I.44}$$

where λ is the applied stretch and, λ_f is the stretch in the fiber direction.

The quantity $\mathbf{R}_z^{\theta^i}$ is the basis-change tensor in each layer, with a rotation θ^i around the ***z***-axis:

$$\mathbf{R}_z^{\theta^i} = \begin{bmatrix} \cos\theta^i & \sin\theta^i & 0 \\ -\sin\theta^i & \cos\theta^i & 0 \\ 0 & 0 & 1 \end{bmatrix} \tag{I.45}$$

After a series of lengthy but straightforward derivations, we get the mechanical deformation gradient of the LM layers:

$$\mathbf{F}_{mech}^{LM\_i} = \begin{bmatrix} \dfrac{\lambda}{\lambda_{chem\_x}^i} & S_3^i & 0 \\ S_3^i & \dfrac{\lambda_{chem\_x}^i}{\lambda}\left(\left(S_3^i\right)^2 + \left(S_2^i\right)^{1/2}\right) & 0 \\ 0 & 0 & \left(S_2^i\right)^{-1/2} \end{bmatrix} \tag{I.46}$$

where

$$\begin{aligned} S_1^i &= \left(\sqrt{\frac{\tan^4\theta^i}{4} - \left(\frac{\lambda}{3\lambda_{chem\_x}^i\cos^2\theta^i}\right)^3} - \frac{\tan^2\theta^i}{2}\right)^{1/3} \\ S_2^i &= \left(S_1^i + \frac{\lambda}{3\lambda_{chem\_x}^i\cos^2\theta^i}\frac{1}{S_1^i}\right)^2 \\ S_3^i &= \cos\theta^i\sin\theta^i\left(S_2^i - \frac{1}{\sqrt{S_2^i}}\right) \end{aligned} \tag{I.47}$$

The chemical stretches are empirically expressed as follows:

$$\lambda^{i}_{chem\_j}(t) = \xi^{i}_{j}\left(1-\exp\left(-\frac{t}{\tau^{i}_{j}}\right)\right) \quad i=1,2,...m \quad j=x,y,z \tag{I.48}$$

in which ξ^{i}_{j} is the chemical expansion at the equilibrium state and τ^{i}_{j} is the chemical expansion rate. The term *t* corresponds to the swelling time in Eq. (I.43) and to the stretching and relaxation times in Eq. (I.48). The identification exercise of fitting parameters of Eq. (I.48) can be formulated as an optimization problem and solved numerically using Matlab software (Pyrz and Zaïri, 2007). Using the experimental transversal stretches, λ_{exp_y} and λ_{exp_z}, and the experimental volumetric change, J_{exp}, the objective function $F^{obj}_{swelling}$ to be minimized for the three loading steps is:

$$F^{obj}_{swelling} = \frac{1}{\eta}\sum_{h=1}^{\eta}\left(\left(\frac{\lambda^{h}_{mod\_y}-\lambda^{h}_{exp\_y}}{\lambda^{h}_{exp\_y}}\right)^2+\left(\frac{\lambda^{h}_{mod\_z}-\lambda^{h}_{exp\_z}}{\lambda^{h}_{exp\_z}}\right)^2+\left(\frac{J^{h}_{mod\_chem}-J^{h}_{exp}}{J^{h}_{exp}}\right)^2\right) \tag{I.49}$$

where η is the number of considered data points. The identification result is presented in the top of Figure I.4a for the three successive loading steps. It is worth noticing that the free swelling is anisotropic. The transversal free swelling stretch is higher in the lamellae plane than in the fibers plane. The axial free swelling stretch is found between the two transversal free swelling stretches.

I.3.3. Electro-chemical flux through the multi-layered soft tissue

The electro-chemical flux operates as an inter-layer transfer process of the ions as illustrated in Figure I.2b. Only ions exchange along the lamellae ***z*** direction may be thus considered with the satisfaction of the continuity conditions between layers, and Eq. (I.35) is rewritten as follows in each layer:

$$\frac{\partial c^{i^{\pm}}(z,t)}{\partial t} = D^{i^{\pm}}_{zz}\left(J^{i}_{chem}\right)\frac{\partial^2 c^{i^{\pm}}(z,t)}{\partial z^2} \tag{I.50}$$

The solution of the Fickian law can be analytically obtained (Oldham and Spanier, 1970; Crank, 1979; Tixier and Mobasher, 2003) and it may be expressed for a layer as follows:

$$\frac{c^{i^{\pm}}\left(z,t\right)-c^{i^{\pm}}\left(\sum_{j=2}^{i} z_{layer}^{j-1},t\right)}{c^{i^{\pm}}\left(z,t_0\right)-c^{i^{\pm}}\left(\sum_{j=1}^{i} z_{layer}^{j},t\right)}=\frac{4}{\pi}\sum_{n=0}^{\infty}\left(\frac{\sin\left(\left(2n+1\right)\pi\frac{z}{z_{layer}^{i}}\right)}{2n+1}\exp\left(-\left(\frac{\left(2n+1\right)\pi}{z_{layer}^{i}}\right)^{2}D_{zz}^{i^{\pm}}t\right)\right) \quad \text{(I.51)}$$

in which

$$\begin{aligned} &c^{i^{\pm}}\left(\sum_{j=2}^{i} z_{layer}^{j-1},t\right) \quad \text{at} \quad z=\sum_{j=2}^{i} z_{layer}^{j-1} \\ &c^{i^{\pm}}\left(\sum_{j=1}^{i} z_{layer}^{j},t\right) \quad \text{at} \quad z=\sum_{j=1}^{i} z_{layer}^{j} \end{aligned} \quad \text{(I.52)}$$

The terms in Eq. (I.52) are the concentrations of the electronic charges in the left and right border sides of the layer *i*, respectively, ensuring the continuity conditions of the ions diffusivity between the adjacent layers. The concentrations of the electronic charges in both ends of the multi-layered annulus, i.e. the left border side of the layer 1 and the right border side of the layer *m*, are equal to the concentration of the external solution c_{ext}^{*}:

$$c^{1^{\pm}}\left(0,t\right)=c^{m^{\pm}}\left(z_{tissue},t\right)=c_{ext}^{*} \quad \text{(I.53)}$$

At t=0, the concentration of the electronic charges inside each layer of the tissue is given by the Donnan equation (Maroudas, 1975):

$$c^{i^{\pm}}\left(z,0\right)=\frac{\pm c_0^F+\sqrt{\left(c_0^F\right)^2+\left(2c_{ext}^{*}\right)^2}}{2} \quad \text{(I.54)}$$

where c_0^F is the fixed charge density at the initial configuration.

Table I.1 provides the diffusivity and permeability parameters taken from the literature (Gu et al., 2004; Perie et al., 2006; Jackson et al., 2009) and involved in Eqs. (I.37) and (I.38). They are used as direct input data along with the volumetric change (Figure I.5a) to evaluate the spatio-temporal distribution of the anionic concentration through the multi-layered annulus.

Parameters	Values	References

D^{-}_{free}	$1\times10^{-9}\left[\mathrm{m^2 s^{-1}}\right]$	1.61	Gu et al. (2004)
D^{+}_{free}	$1\times10^{-9}\left[\mathrm{m^2 s^{-1}}\right]$	1.16	Gu et al. (2004)
r_s^{-}	$\left[\mathrm{nm}\right]$	0.142	Gu et al. (2004)
r_s^{+}	$\left[\mathrm{nm}\right]$	0.197	Gu et al. (2004)
α	$\left[-\right]$	1.25	Gu et al. (2004)
β	$\left[-\right]$	0.681	Gu et al. (2004)
k_{zz_0}	$1\times10^{-15}\left[\mathrm{m^4 N^{-1} s^{-1}}\right]$	0.42	Perie et al. (2006)
M	$\left[-\right]$	4.81	Perie et al. (2006)
c_0^F	$\left[\mathrm{mEq\,ml^{-1}}\right]$	0.125	Jackson et al. (2009)

Table I.1. Parameters of Eqs. (I.37) and (I.38).

It is provided in Figure I.6 upon the three successive loading steps. During the free swelling (Figure I.6a), the anionic charges are non-uniformly distributed through the tissue and the balance of swelling tends with time towards a uniform anionic distribution and a chemical equilibrium. The application of a quasi-static tensile loading (Figure I.6b) provokes a disequilibrium and the anionic concentration exhibits a strong contrast between LM and ILM layers with decrease and increase with time, respectively. The thinner ILM zones appear to exhibit uniform ionic diffusion. When the applied stretch is kept constant (Figure I.6c), the electro-chemical response tends towards chemical equilibrium and uniform anionic distribution is obtained.

Relaxation

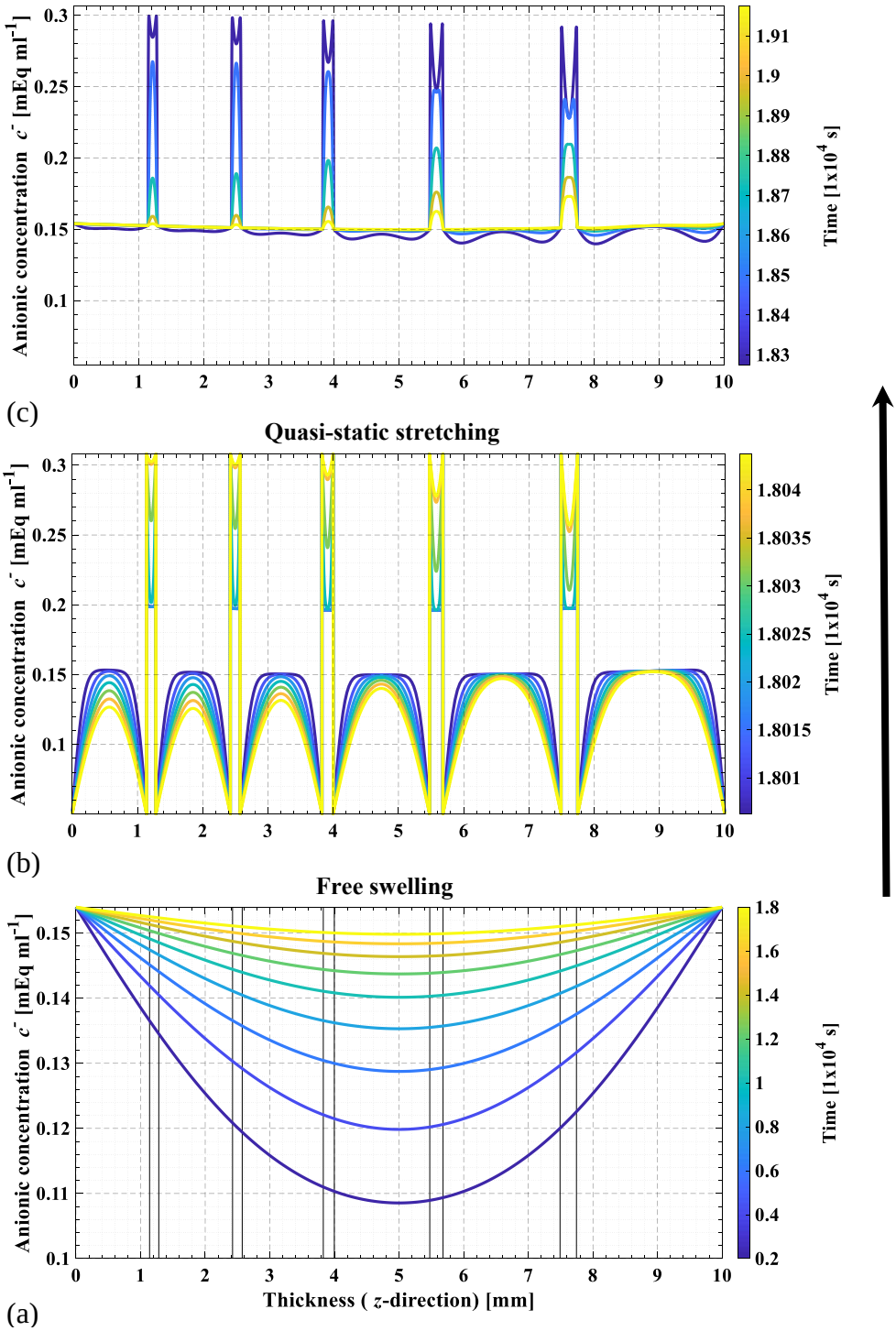

Figure I.6. Anionic concentration through the thickness of the multi-layered soft tissue upon different successive loading steps along with temporal changes: (a) free swelling, (b) quasi-static and (c) relaxation.

I.3.4. Stress of the multi-layered annulus

The stresses in each layer, $\boldsymbol{\sigma}_{mech}^{LM\_i}$, $\boldsymbol{\sigma}_{mech}^{ILM\_i}$ and $\boldsymbol{\sigma}_{chem}^{i}$, see Eqs. (I.30)-(I.32), reduced to the uniaxial form, are determined using the deformation gradients, issued from the hybrid experimental/modeling decoupling strategy. The stress components are expressed as follows:

$$\sigma_{mech\_xx}^{i} \neq 0 \text{ and } \sigma_{mech\_kl}^{i} = 0 \text{ for all other components} \tag{I.55}$$

$$\sigma_{chem\_xx}^{i} = \sigma_{chem\_yy}^{i} = \sigma_{chem\_zz}^{i} \text{ and } \sigma_{chem\_kl}^{i} = 0 \text{ for all other components} \tag{I.56}$$

The stress-stretch relationships take the following forms:

$$\begin{aligned}\sigma_{mech\_xx}^{LM\_i} = {} & \phi_{ECM}^{i} G_{ECM} \left(\left(\frac{\lambda}{\lambda_{chem\_x}^{i}} \right)^2 + S_3{}^2 - \frac{1}{S_2} \right) \\ & + 2\phi_{OCF}^{i} \left(C_1 \left(\bar{I}_4^{i} - 1 \right) \exp\left(C_2 \left(\bar{I}_4^{i} - 1 \right)^2 \right) \right) \left(\lambda \cos\theta^{i} \right)^2\end{aligned} \tag{I.57}$$

$$\sigma_{mech\_xx}^{ILM\_i} = \phi_{ECM}^{i} G_{ECM} \left(\left(\frac{\lambda}{\lambda_{chem\_x}^{i}} \right)^2 - \frac{\lambda_{chem\_x}^{i}}{\lambda} \right) \tag{I.58}$$

$$\sigma_{chem\_xx}^{i} = \phi_{fluid}^{i} K_1 \left(J_{chem}^{i} - 1 \right) \exp\left(K_2 \left(J_{chem}^{i} - 1 \right)^2 \right) \tag{I.59}$$

The total stress of the multi-layered annulus $\boldsymbol{\sigma}$ is simply given by Eq. (I.25). The re-coupling is obtained by considering the electro-chemical flux through the multi-layered soft tissue, as constitutively presented in Section I.3.3, while considering stress/strain continuity along the interfaces to account for mechanical interactions between adjacent layers, see Eqs (I.3) and (I.24). The latter compatibility was also considered by van Dommelen et al. (2003) for semi-crystalline polymer systems regarded as two-phase (crystalline/amorphous) layered composite inclusions.

Several inputs related to structural features are required by the modeling. The initial volume fraction of fluid is 74% by wet weight (Demers et al., 2004; Perie et al., 2006). The initial volume fraction of OCF is 7% (Oshima et al., 1993; Demers et al., 2004) and the angle with respect the loading axis is 26° for the inner zone (Holzapfel et al., 2005). The thickness of the ILM zone is one eighth that

of the LM layer (Tavakoli et al., 2017) while a gradual variation of thickness is adopted through annulus.

The parameters involved in the stress expression have been identified using the experimental stress σ_{exp} for the stretching and relaxation steps by means of the following objective function F_{stress}^{obj}:

$$F_{stress}^{obj} = \frac{1}{\eta}\sum_{h=1}^{\eta}\left(\frac{\sigma_{mod}^{h} - \sigma_{exp}^{h}}{\sigma_{exp}^{h}}\right)^2 \tag{I.60}$$

where η is again the number of considered data points and σ_{mod} is the stress provided by the model. Table I.2 gives the identified values with a goodness of fit $R^2 = 0.986$.

Parameters		Values
G_{ECM}	$[\text{KPa}]$	4 (0.37) *
C_1	$[\text{MPa}]$	3.21 (0.02) *
C_2	$[-]$	11.40 (2) *
K_1	$[\text{KPa}]$	61.40 (0.24) *
K_2	$[-]$	0.12 (0.02) *

Table I.2. Parameters of Eqs. (I.30)-(I.32).
* Between brackets is the standard deviation.

I.3.5. Model vs. experimental data

The model is compared to experimental observations of the time-dependent mechanical behavior of the multi-layered annulus in terms of volumetric change, stress and Poisson's ratio in Figure I.5. A global view at this figure shows the ability of the model to capture the macro-response upon the different successive loading steps.

I.4. Model results and discussion

The model/experiments comparison in Figure I.5 demonstrates that the evaluation of the overall time-dependent response involves considering volumetric change, Poisson's ratios and stress simultaneously in relation to structural features and diffusion-mechanics. The model can be now used to analyze structural features and diffusion-mechanics effects independently.

I.4.1. Axial (circumferential) stress and volumetric stress/strain responses

Although the ILM zone is devoid of OCF and represents a small fraction of the whole tissue, Figure I.5b shows that it contributes significantly to the apparent stiffness and the stabilized relaxed due to the ILM swelling inducing a significant chemically-induced volumetric stress in the ILM zone. Physically, perpendicular fibrils bridging two adjacent LM layers are observed in the ILM zone (Tavakoli et al., 2017). These perpendicular fibrils could play the role of "elastic springs" in order to retain the significant ILM swelling. In the absence of diffusion, the apparent stiffness decreases and the stress no longer relax upon interrupted stretching. The absence of the electro-chemical activity (loss of fixed charges) simulates the dysfunction of whole PG macromolecules, their loss being the main indication of disc degeneration[6]. As a consequence of the inter-layer fluid transfer mechanism, the unusual time-dependent transversal behavior is vanished without diffusion and the two Poisson's ratios become time-independent.

The effective contribution of the LM and ILM layers on the coupling can be also discussed with respect to the model. Figure I.7 presents the chemical response in terms of volumetric change and corresponding stress. As a consequence of the electrolytic properties of PG macromolecules, the ionic diffusion between layers presented in Figure I.6 comes with internal fluid transfer resulting in tissue volumetric deformation. The incompressible fluid is diffused under electrolytic conditions and the diffusion occurs with the same flow rate along the thickness of the multi-layered tissue during its hydration. In the meantime, a decrease in diffusivity rate with swelling time occurs until the saturation state that leads to identical ionic concentration (Figure I.6a) and volumetric change (Figure I.7a) between two adjacent layers. The application of a stretching leads to very distinct ionic concentration between two adjacent layers as result of chemical disequilibrium provoked by fluid transfer along the thickness of the multi-layered soft tissue (Figure I.6b). The chemical imbalance

[6] Age-related changes include decreased PG macromolecules content and a corresponding reduction in chemically-induced volumetric stress leading to a decrease in annulus stiffness (Eyre, 1979; Buckwalter, 1995; Roberts et al., 2006).

during the stretching process leads to fluid flow from the LM layers to the ILM layers with a significant difference in fluid amount between the two zones (Figure I.7a). A shrinkage in the LM layers and a significant swelling in the ILM layers. At the end of the stretching step, the volumetric change in the ILM zone is approximately two times that at the equilibrium state.

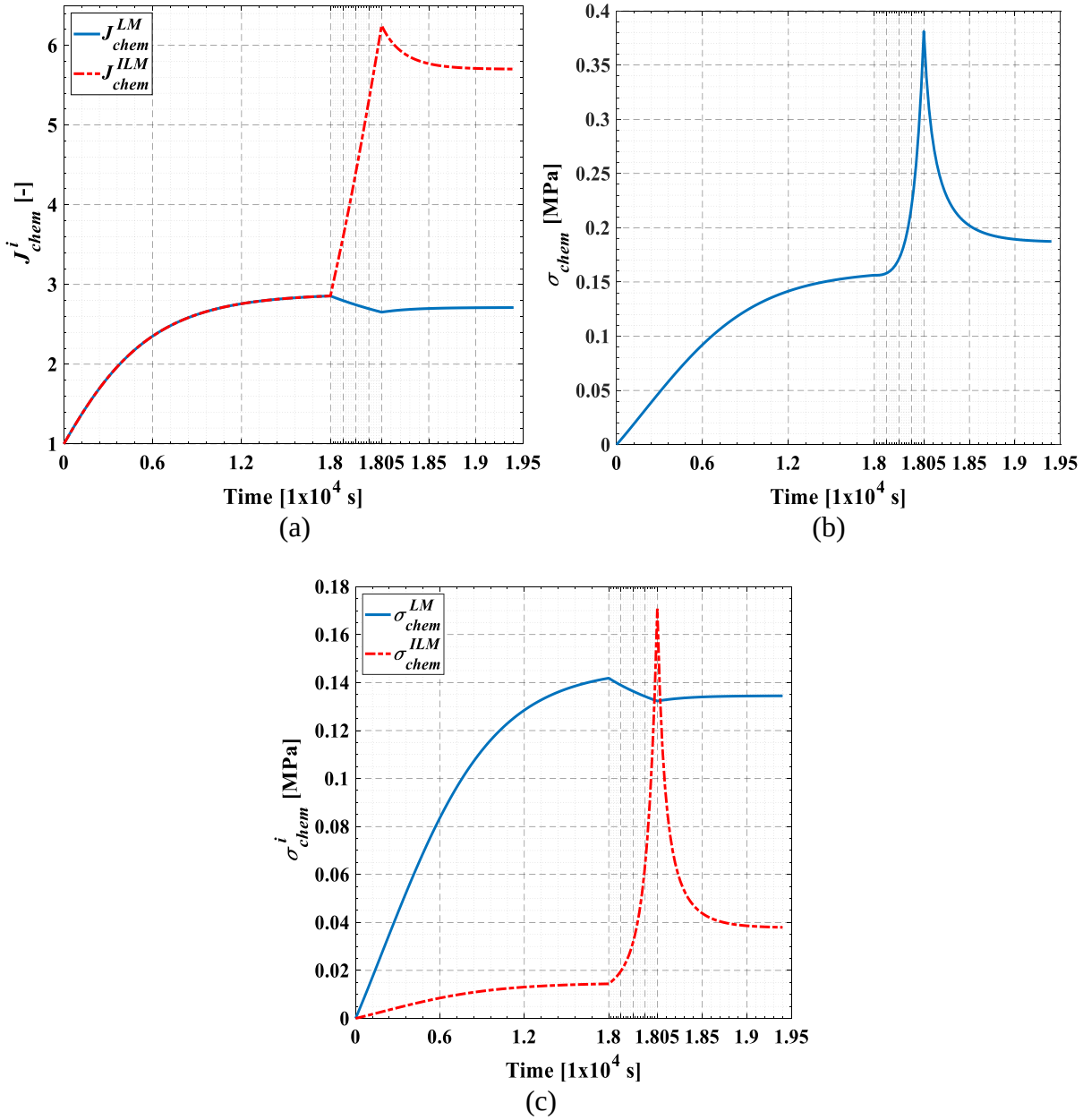

Figure I.7. Model results: (a) Volumetric change of the LM and ILM layers, (b) Chemical stress of the layered soft tissue, (c) Chemical stress of the LM and ILM layers.

It worth noticing this large difference results in a significant change in the volume fraction of the constituents. In addition, the structural features play a fundamental role in the electro-chemical

behavior of layers. A small decrease in the LM ionic concentration leads to a strong increase in the ILM ionic concentration, resulting in significant volumetric deformation compared to that of the LM layers (Figure I.7a). This model result is in accordance with the literature (Huyghe and Jongeneelen, 2012; Vergari et al., 2016) in which a localized strain of about two to three times higher in the ILM zone was reported on bovine annulus specimens. After the imbalance of the ionic concentration, the electrolytes return, during the relaxation process (Figure I.6c), to the less concentrated zones to ensure ionic stability in all the soft tissue. This electro-chemical effect progressively restores uniform ionic concentration until the return to the chemical equilibrium state of the stretched sample, giving more usual Poisson's ratio values between 0 and 0.5 in both planes (Figure I.5c). The large difference in the volumetric change, upon the three successive loading steps (Figure I.5a), results in significant difference in the corresponding chemical stress as illustrated in Figure I.7b. This feature at the specimen scale is connected to the chemical response at the scale of a layer through the concentration and diffusion of ions. As illustrated in Figure I.7c, the chemical stress in the LM and ILM layers is profoundly affected by the distribution of ions within each layer from the dehydrated state to the chemically-induced hydrated state coupled to mechanics. In particular, at the end of the free swelling, the chemical stress in the LM layers is eight times that in the ILM layers.

I.4.2. Shearing

Figure I.8a shows the annulus shearing predicted by the model in response to changes in structural features and diffusion-mechanics. It is well-known that the misalignment of fibers with respect to the loading axis provokes a shearing in the fiber-reinforced layer (Pipes and Pagano,1970; Nerurkar et al., 2009) but an equilibrated stratification with uniform thickness leads to cancel the shearing. This feature is obviously taken into account by the model as shown in Figure I.8a. In spite of alternate fiber angles between successive LM layers, the model shows that the tissue presents a

shearing when thickness variation of layers is considered as a consequence of non-equilibration of the stratified system.

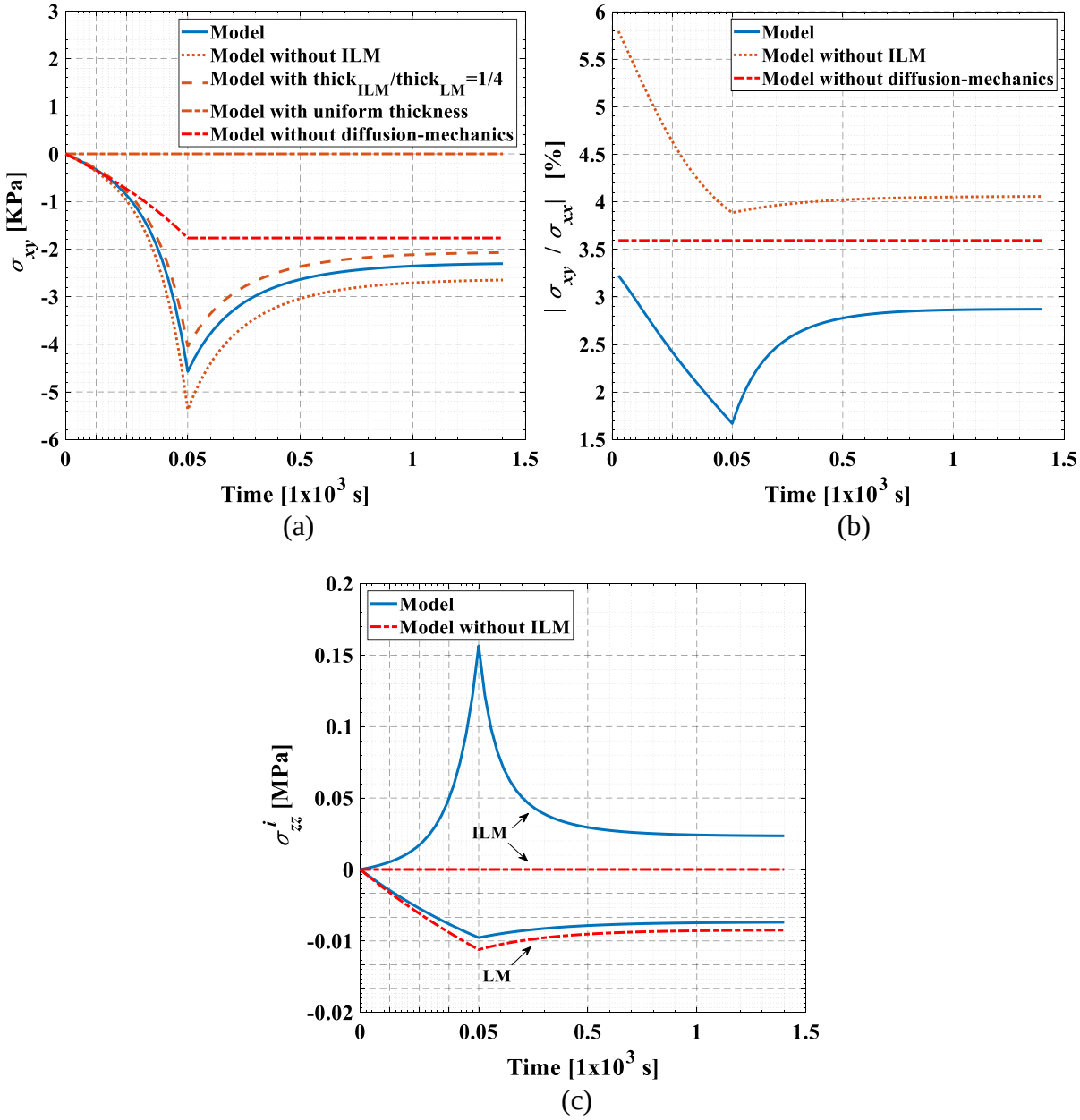

Figure I.8. Model results: (a) Shear stress, (b) Ratio between shear stress and axial stress, (c) Transversal stress.

Another important structural feature is the ILM zone. The highest shearing occurs in the absence of ILM zone but the increase of relative dimensions between ILM and LM layers diminish the shearing extent. In accordance with experimental observations of Michalek et al. (2009), and latter of Vergari et al. (2016), on bovine annulus specimens, the shearing does not result from a sliding mechanism

between layers due to strong LM-ILM cohesion. The model shows that annulus shearing results from an antagonist combination of ILM thickness and dimensional graduation. The loss of diffusion-mechanics provokes a diminution of axial and shear stresses but their relative extent increases as demonstrated in Figure I.8b. In the absence of ILM zone, this ratio is even higher. The transversal stress in LM is also increased when ILM zone is neglected (Figure I.8c). The coupled effect of aged-related deterioration of ILM zone and PG loss has for consequence to enhance shearing which is considered as the main factor of disc damage mechanisms such as disc herniation (Iatridis and Gwynn, 2004). More work is clearly needed to propose a more proper description of the aging and degeneration evolution using physically realistic kinetics.

I.4.3. Limitations

Some limitations ought to be mentioned. One limitation of this study is the use of data obtained at room temperature (22°C) which does not replicate the real physiological environment in-vivo. The latter could influence osmotic effects, since osmotic pressure is related to temperature (Emanuel et al., 2018). The biological reactions have not been considered in the current study which could influence the predicted plots of the electro-chemical activity in the soft tissue. Also, the current theory requires a more accurate description of the collagen network at different scales (Tavakoli et al., 2017, 2018). Another limitation of this study concerns the mechanical conditions used to illustrate the model. Although it is representative of the disc compression mechanics, the model application should not be limited to the uniaxial circumferential data. The application on multiaxial loading paths is indeed mandatory to further verify the model (Kandil et al., 2020). Finally, because the annulus mechanics is different between species, it would have been more clinically relevant to conduct the model application on human data by including directional and regional effects.

I.5. Conclusion

In this work, we have presented a physically-based model including realistic structural features (collagen orientation/content, interlamellar thickness and dimensional graduation) in the material representation of the disc annulus along with the electro-chemical activity of the soft tissue. The model successfully reproduced a series of experimental data on bovine tissues under free swelling, quasi-static stretching and relaxation. It was demonstrated that for the evaluation of the overall time-dependent response, it is fundamental to consider simultaneously the structural features and diffusion-mechanics effects on volumetric change, Poisson's ratios and stress. The final model is a powerful tool to better understand the annulus mechanics in relation to loading conditions, electro-chemical environment, intrinsic properties / proportion / orientation (if any) of constituents (extracellular matrix, fibers, fluid) and structural features.

The mathematical structure of the constitutive model is general enough to be applicable to the time-dependent response of all electro-chemically active multi-layered soft tissues, whatever biological or synthetic (such as hydrogels). In particular, the model could be employed to design prostheses including regional variation (Jiang et al., 2019) and interaction with electro-chemical environment to better mimic the healthy disc function. Moreover, the model could be used to better understand the tissue response changes during aging and degeneration in response to changes in the tissue composition. These aspects will be the subject of future works.

Appendix I.A. Volumetric free energy function

The Cayley-Hamilton theorem applied to the chemical part $\mathbf{C}_{chem}$ of the right Cauchy-Green deformation tensor gives:

$$\mathbf{C}_{chem}^3 - I_1\mathbf{C}_{chem}^2 + I_2\mathbf{C}_{chem} = J^2\mathbf{I} \tag{I.A1}$$

The Nanson relation $dv = J\,dV$, between volumes in the actual and initial configurations, dv and dV, respectively, may be written as:

$$J\mathbf{I}dv = J^2\mathbf{I}dV \tag{I.A2}$$

Substituting Eq. (I.A1) into Eq. (I.A2), we obtain:

$$J\mathbf{I}dv = \left(\mathbf{C}_{chem}^3 - I_1\mathbf{C}_{chem}^2 + I_2\mathbf{C}_{chem}\right)dV \tag{I.A3}$$

Multiplying the two sides of Eq. (I.A3) by the unit vector $\boldsymbol{a}_0$, we get:

$$\boldsymbol{a}_0 J\mathbf{I}\boldsymbol{a}_0 dv = \boldsymbol{a}_0\left(\mathbf{C}_{chem}^3 - I_1\mathbf{C}_{chem}^2 + I_2\mathbf{C}_{chem}\right)\boldsymbol{a}_0 dV \tag{I.A4}$$

which can be also written as:

$$J\,\overset{1}{\boldsymbol{a}_0}\mathbf{I}\boldsymbol{a}_0\,dv = \left(\overbrace{\boldsymbol{a}_0\mathbf{C}_{chem}^3\boldsymbol{a}_0}^{I_6} - I_1\overbrace{\boldsymbol{a}_0\mathbf{C}_{chem}^2\boldsymbol{a}_0}^{I_5} + I_2\overbrace{\boldsymbol{a}_0\mathbf{C}_{chem}\boldsymbol{a}_0}^{I_4}\right)dV \tag{I.A5}$$

The invariants in Eq. (I.11) of the main chapter body are used to re-write Eq. (I.A5) as follows:

$$\frac{dv}{dV} = \sqrt{I_6 - I_1I_5 + I_2I_4} \tag{I.A6}$$

The quantity $\boldsymbol{a}_0\mathbf{C}_{chem}^3\boldsymbol{a}_0$ is termed I_6 in the present study.

Eq. (I.A6) describes the volumetric change in the LM layers. In the ILM zones devoid of OCF, the volumetric change is simply given by:

$$\frac{dv}{dV} = \sqrt{I_3} \tag{I.A7}$$

An exponential form of the free energies of LM and ILM layers was proposed in Eq. (I.19) of the main chapter body using Eq. (I.A6) or Eq. (I.A7), respectively, for dv/dV:

$$W_{fluid} = \frac{1}{2}\frac{K_1}{K_2}\left(\exp\left(K_2\left(\frac{dv}{dV} - 1\right)^2\right) - 1\right) \tag{I.A8}$$

The behavior of the formulated free energy function (I.A8) has to be verified to get physically reasonable responses and convergence of solutions (Balzani et al., 2006; Ehret et al., 2011). In the case of a confined stretching $\mathbf{F} = \mathrm{diag}(\lambda,1,1)$, Figure I.A1 presents the free energy function and its derivative with respect to *J*, in the stretch-K_2 space and for different K_1 values. A global view at

these plots shows that the free energy presents a minimum whereas its derivative continuously increases. This behavior ensures the existence of a stable equilibrium state for any stretching condition in which the derivative is null whatever the values of the model parameters.

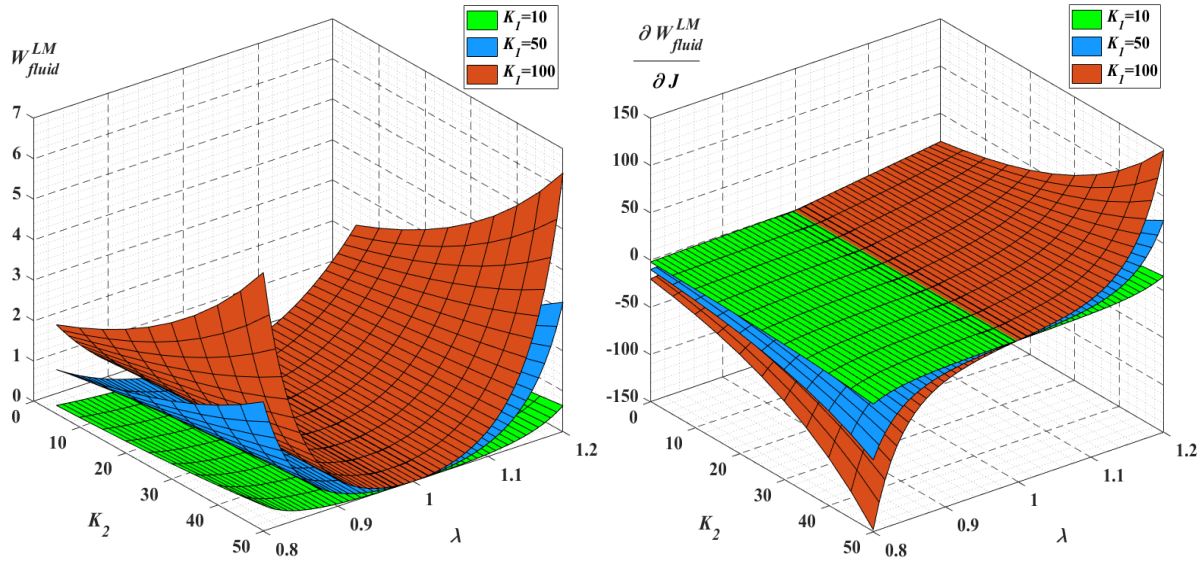

(a) (b)

Figure I.A1. Surface of (a) free energy and (b) free energy derivative in the stretch-K_2 space for different K_1 values.

Appendix I.B. Structural features

In order to account the gradual variation of the thickness of layers, which increases from the outer annulus towards the inner annulus (Cassidy et al., 1989; Marchand and Ahmed, 1990; Hsu and Setton, 1999; Holzapfel et al., 2005), a second-order polynomial function is introduced:

$$z_{layer}^{LM\_i} = ai^2 + bi + c \quad i = 1,3,...m \tag{I.B1}$$

in which m is the total number of layers and, a, b and c are parameters governing the graduation. Figure I.6 shows the dimensional graduation taken for this study.

According to Tavakoli et al. (2017), the thickness of the LM phase is eight times that of the ILM phase, and the ILM thickness is given by:

$$z_{layer}^{ILM\_i} = \frac{1}{8}\left(\frac{z_{layer}^{LM\_i-1} + z_{layer}^{LM\_i+1}}{2} \right) \quad i = 2,4,...m-1 \tag{I.B2}$$

The total thickness of the multi-layered annulus is then given by:

$$z_{tissue} = z_{layer}^{LM} + z_{layer}^{ILM} = \sum_{i=1,3,..}^{m} z_{layer}^{LM\_i} + \sum_{i=2,4,..}^{m-1} z_{layer}^{ILM\_i} \tag{I.B3}$$

I. References

Adam, C., Rouch, P., Skalli, W., 2015. Inter-lamellar shear resistance confers compressive stiffness in the intervertebral disc: an image-based modelling study on the bovine caudal disc. Journal of Biomechanics 48, 4303-4308.

Antoniou, J., Demers, C.N., Beaudoin, G., Goswami, T., Mwale, F., Aebi, M., Alini, M., 2004. Apparent diffusion coefficient of intervertebral discs related to matrix composition and integrity. Magnetic Resonance Imaging 22, 963-972.

Baldit, A., Ambard, D., Cherblanc, F., Royer, P., 2014. Experimental analysis of the transverse mechanical behaviour of annulus fibrosus tissue. Biomechanics and Modeling in Mechanobiology 13, 643-652.

Balzani, D., Neff, P., Schroder, J., Holzapfel, G.A., 2006. A polyconvex framework for soft biological tissues: adjustment to experimental data. International Journal of Solids and Structures 43, 6052-6070.

Buckwalter, J.A., 1995. Aging and degeneration of the human intervertebral disc. Spine 20,1307-1314.

Cassidy, J.J., Hiltner, A., Baer, E., 1989. Hierarchical structure of the intervertebral disc. Connective Tissue Research 23, 75-88.

Chen, H., Liu, Y., Zhao, X., Lanir, Y., Kassab, G.S., 2011. A micromechanics finite-strain constitutive model of fibrous tissue. Journal of the Mechanics and Physics of Solids 59, 1823-1837.

Crank, J., 1979. The mathematics of diffusion. Oxford University press.

Demers, C.N., Antoniou, J., Mwale, F., 2004. Value and limitations of using the bovine tail as a model for the human lumbar spine. Spine 29, 2793-2799.

Derrouiche, A., Zaouali, A., Zaïri, F., Ismail, J., Chaabane, M., Qu, Z., Zaïri, F., 2019a. Osmo-inelastic response of the intervertebral disc. Proceedings of the Institution of Mechanical Engineers. Part H: Journal of Engineering in Medicine 233, 332-341.

Derrouiche, A., Zaïri, F., Zaïri, F., 2019b. A chemo-mechanical model for osmo-inelastic effects in the annulus fibrosus. Biomechanics and Modeling in Mechanobiology 18, 1773-1790.

Derrouiche, A., Karoui, A., Zaïri, F., Ismail, J., Qu, Z., Chaabane, M., Zaïri, F., 2020a. The two Poisson's ratios in annulus fibrosus: relation with the osmo-inelastic features. Mechanics of Soft Materials 2, 1-12.

Derrouiche, A., Feki, F., Zaïri, F., Taktak, R., Moulart, M., Qu, Z., Ismail, J., Charfi, S., Haddar, N., Zaïri, F., 2020b. How pre-strain affects the chemo-torsional response of the intervertebral disc. Clinical Biomechanics 76, 105020.

Ehlers, W., Karajan, N., Markert, B., 2009. An extended biphasic model for charged hydrated tissues with application to the intervertebral disc. Biomechanics and Modeling in Mechanobiology 8, 233-251.

Ehret, A.E., Bol, M., Itskov, M., 2011. A continuum constitutive model for the active behaviour of skeletal muscle. Journal of the Mechanics and Physics of Solids 59, 625-636.

Emanuel, K.S., van der Veen, A.J., Rustenburg, C.M.E., Smit, T.H., Kingma, I., 2018. Osmosis and viscoelasticity both contribute to time-dependent behaviour of the intervertebral disc under compressive load: a caprine in vitro study. Journal of Biomechanics 70, 10-15.

Eyre, D.R., 1979. Biochemistry of the intervertebral disc. International Review of Connective Tissue Research 8, 227-291.

Ferguson, S.J., Ito, K., Nolte, L.P., 2004. Fluid flow and convective transport of solutes within the intervertebral disc. Journal of Biomechanics 37, 213-221.

Frijns, A.J.H., Huyghe, J.M., Janssen, J.D., 1997. A validation of the quadriphasic mixture theory for intervertebral disc tissue. International Journal of Engineering Science 35, 1419-1429.

Gu, W.Y., Yao, H., Vega, A.L., Flagler, D., 2004. Diffusivity of ions in agarose gels and intervertebral disc: effect of porosity. Annals of Biomedical Engineering 32, 1710-1717.

Guo, Z.Y., Peng, X.Q., Moran, B., 2006. A composites-based hyperelastic constitutive model for soft tissue with application to the human annulus fibrosus. Journal of the Mechanics and Physics of Solids 54, 1952-1971.

Holmes, M.H., Mow, V.C., 1990. The nonlinear characteristics of soft gels and hydrated connective tissues in ultrafiltration. Journal of Biomechanics 23, 1145-1156.

Holzapfel, G.A., Gasser, T.C., Ogden, R.W., 2000. A new constitutive framework for arterial wall mechanics and a comparative study of material models. Journal of Elasticity 61, 1-48.

Holzapfel, G.A., Schulze-Bauer, C.A.J., Feigl, G., Regitnig, P., 2005. Single lamellar mechanics of the human lumbar anulus fibrosus. Biomechanics and Modeling in Mechanobiology 3, 125-140.

Hsu, E.W., Setton, L.A., 1999. Diffusion tensor microscopy of the intervertebral disc anulus fibrosus. Magnetic Resonance in Medicine 41, 992-999.

Huyghe, J.M., Janssen, J.D., 1997. Quadriphasic mechanics of swelling incompressible porous media. International Journal of Engineering Science 35, 793-802.

Huyghe, J.M., Jongeneelen, C.J.M., 2012. 3D non-affine finite strains measured in isolated bovine annulus fibrosus tissue samples. Biomechanics and Modeling in Mechanobiology 11, 161-170.

Iatridis, J.C., Laible, J.P., Krag, M.H., 2003. Influence of fixed charge density magnitude and distribution on the intervertebral disc: applications of a poroelastic and chemical electric (PEACE) model. Journal of Biomechanical Engineering 125, 12-24.

Iatridis, J.C., Gwynn, A.I., 2004. Mechanisms for mechanical damage in the intervertebral disc annulus fibrosus. Journal of Biomechanics 37, 1165-1175.

Jackson, A.R., Yao, H., Brown, M.D., Gu, W.Y., 2006. Anisotropic ion diffusivity in intervertebral disc: an electrical conductivity approach. Spine 31, 2783-2789.

Jackson, A.R., Yuan, T.Y., Huang, C.Y., Travascio, F., Gu, W.Y., 2008. Effect of compression and anisotropy on the diffusion of glucose in annulus fibrosus. Spine 33, 1-7.

Jackson, A.R., Yuan, T.Y., Huang, C.Y., Gu, W.Y., 2009. A conductivity approach to measuring fixed charge density in intervertebral disc tissue. Annals of Biomedical Engineering 37, 2566-2573.

Jiang, Q., Zaïri, F., Frederix, C., Yan, Z., Derrouiche, A., Qu, Z., Liu, X., Zaïri F., 2019. Biomechanical response of a novel intervertebral disc prosthesis using functionally graded polymers: a finite element study. Journal of the Mechanical Behavior of Biomedical Materials 94, 288-297.

Kandil, K., Zaïri, F., Derrouiche, A., Messager, T., Zaïri F., 2019. Interlamellar-induced time-dependent response of intervertebral disc annulus: a microstructure-based chemo-viscoelastic model. Acta Biomaterialia 100, 75-91.

Kandil, K., Zaïri, F., Messager, T., Zaïri, F., 2020. Interlamellar matrix governs human annulus fibrosus multiaxial behavior. Scientific Reports 10, 1-14.

Kroon, M., Holzapfel, G.A., 2007. A model for saccular cerebral aneurysm growth by collagen fibre remodelling. Journal of Theoretical Biology 247, 775-787.

Labus, K.M., Han, S.K., Hsieh, A.H., Puttlitz, C.M., 2014. A computational model to describe the regional interlamellar shear of the annulus fibrosus. Journal of Biomechanical Engineering 136, 051009.

Lai, W.M., Hou, J.S., Mow, V.C., 1991. A triphasic theory for the swelling and deformation behaviors of articular cartilage. Journal of Biomechanical Engineering 113, 245-258.

Li, D., Robertson, A.M., 2009. A structural multi-mechanism constitutive equation for cerebral arterial tissue. International Journal of Solids and Structures 46, 2920-2928.

Marchand, F., Ahmed, A.M., 1990. Investigation of the laminate structure of lumbar disc anulus fibrosus. Spine 15, 402-410.

Maroudas, A., 1975. Biophysical chemistry of cartilaginous tissues with special reference to solute and fluid transport. Biorheology 12, 233-248.

McEvoy, E., Holzapfel, G.A., McGarry, P., 2018. Compressibility and anisotropy of the ventricular myocardium: experimental analysis and microstructural modeling. Journal of Biomechanical Engineering 140, 081004.

Mengoni, M., Luxmoore, B.J., Wijayathunga, V.N., Jones, A.C., Broom, N.D., Wilcox, R.K., 2015. Derivation of inter-lamellar behaviour of the intervertebral disc annulus. Journal of the Mechanical Behavior of Biomedical Materials 48, 164-172.

Michalek, A.J., Buckley, M.R., Bonassar, L.J., Cohen, I., Iatridis, J.C., 2009. Measurement of local strains in intervertebral disc anulus fibrosus tissue under dynamic shear: contributions of matrix fiber orientation and elastin content. Journal of Biomechanics 42, 2279-2285.

Mow, V.C., Kuei, S.C., Lai, W.M., Armstrong, C.G., 1980. Biphasic creep and stress relaxation of articular cartilage in compression: theory and experiments. Journal of Biomechanical Engineering 102, 73-84.

Nachemson, A., Morris, J.M., 1964. In vivo measurements of intradiscal pressure: discometry, a method for the determination of pressure in the lower lumbar discs. The Journal of Bone and Joint Surgery 46, 1077-1092.

Nerurkar, N.L., Baker, B.M., Sen, S., Wible, E.E., Elliott, D.M., Mauck, R.L., 2009. Nanofibrous biologic laminates replicate the form and function of the annulus fibrosus. Nature Materials 8, 986-992.

Nerurkar, N.L., Mauck, R.L., Elliott, D.M., 2011. Modeling interlamellar interactions in angle-ply biologic laminates for annulus fibrosus tissue engineering. Biomechanics and Modeling in Mechanobiology 10, 973-984.

Oldham, K.B., Spanier, J., 1970. The replacement of Fick's laws by a formulation involving semidifferentiation. Journal of Electroanalytical Chemistry and Interfacial Electochemistry 26, 331-341.

Oshima, H., Ishihara, H., Urban, J.P.G., Tsuji, H., 1993. The use of coccygeal discs to study intervertebral disc metabolism. Journal of Orthopaedic Research 11, 332-338.

Parsons, E., Boyce, M.C., Parks, D.M., 2004. An experimental investigation of the large-strain tensile behavior of neat and rubber-toughened polycarbonate. Polymer 45, 2665-2684.

Peng, X.Q., Guo, Z.Y., Moran, B., 2005. An anisotropic hyperelastic constitutive model with fiber-matrix shear interaction for the human annulus fibrosus. Journal of Applied Mechanics 73, 815-824.

Perie, D.S., Maclean, J.J., Owen, J.P., Iatridis, J.C., 2006. Correlating material properties with tissue composition in enzymatically digested bovine annulus fibrosus and nucleus pulposus tissue. Annals of Biomedical Engineering 34, 769-777.

Pezowicz, C.A., Robertson, P.A., Broom, N.D., 2006. The structural basis of interlamellar cohesion in the intervertebral disc wall. Journal of Anatomy 208, 317-330.

Pierce, D.M., Ricken, T., Holzapfel, G.A., 2013. A hyperelastic biphasic fibre-reinforced model of articular cartilage considering distributed collagen fibre orientations: continuum basis, computational aspects and applications. Computer Methods in Biomechanics and Biomedical Engineering 16, 1344-1361.

Pipes, R.B., Pagano, N.J., 1970. Interlaminar stresses in composite laminates under uniform axial extension. Journal of Composite Materials 4, 538-548.

Pyrz, M., Zaïri, F., 2007. Identification of viscoplastic parameters of phenomenological constitutive equations for polymers by deterministic and evolutionary approach. Modelling and Simulation in Materials Science and Engineering 15, 85-103.

Roberts, S., Menage, J., Urban, J.P., 1989. Biochemical and structural properties of the cartilage end-plate and its relation to the intervertebral disc. Spine 14, 166-174.

Roberts, S., Evans, H., Trivedi, J., Menage, J., 2006. Histology and pathology of the human intervertebral disc. Journal of Bone and Joint Surgery 88, 10-14.

Rodriguez, J.F., Cacho, F., Bea, J.A., Doblare, M., 2006. A stochastic-structurally based three dimensional finite-strain damage model for fibrous soft tissue. Journal of the Mechanics and Physics of Solids 54, 864-886.

Roux, D.C., Cooper-White, J.J., McKinley, G.H., Tirtaatmadja, V., 2003. Drop impact of newtonian and elastic fluids. Physics of Fluids 15, S12-S12.

Soukane, D.M., Shirazi-Adl, A., Urban, J.P.G., 2009. Investigation of solute concentrations in a 3D model of intervertebral disc. European Spine Journal 18, 254-262.

Spencer, A.J.M., 1984. Constitutive theory for strongly anisotropic solids. In Continuum Theory of the Mechanics of Fibre-Reinforced Composites, Springer, Vienna, pp. 1-32.

Stalhand, J., Klarbring, A., Holzapfel, G.A., 2011. A mechanochemical 3D continuum model for smooth muscle contraction under finite strains. Journal of Theoretical Biology 268, 120-130.

Stracuzzi, A., Mazza, E., Ehret, A.E., 2018. Chemomechanical models for soft tissues based on the reconciliation of porous media and swelling polymer theories. Zeitschrift für Angewandte Mathematik und Mechanik 98, 2135-2154.

Swedberg, A.M., Reese, S.P., Maas, S.A., Ellis, B.J., Weiss, J.A., 2014. Continuum description of the Poisson's ratio of ligament and tendon under finite deformation. Journal of Biomechanics 47,3201-3209.

Tavakoli, J., Elliott, D.M., Costi, J.J., 2016. Structure and mechanical function of the inter-lamellar matrix of the annulus fibrosus in the disc. Journal of Orthopaedic Research 34,1307-1315.

Tavakoli, J., Elliott, D.M., Costi, J.J., 2017. The ultra-structural organization of the elastic network in the intra-and inter-lamellar matrix of the intervertebral disc. Acta Biomaterialia 58,269-277.

Tavakoli, J., Costi, J.J., 2018. New insights into the viscoelastic and failure mechanical properties of the elastic fiber network of the inter-lamellar matrix in the annulus fibrosus of the disc. Acta Biomaterialia 77,292-300.

Tixier, R., Mobasher, B., 2003. Modeling of damage in cement-based materials subjected to external sulfate attack. I: Formulation. Journal of Materials in Civil Engineering 15,305-313.

Travascio, F., Gu, W.Y., 2007. Anisotropic diffusive transport in annulus fibrosus: experimental determination of the diffusion tensor by FRAP technique. Annals of Biomedical Engineering 35,1739-1748.

Urban, J.P., Holm, S., Maroudas, A., 1978. Diffusion of small solutes into the intervertebral disc: as in vivo study. Biorheology 15,203-221.

Urban, J.P., Maroudas, A., 1981. Swelling of the intervertebral disc in vitro. Connective Tissue Research 9,1-10.

van Dommelen, J.A.W., Parks, D.M., Boyce, M.C., Brekelmans, W.A.M., Baaijens, F.P.T., 2003. Micromechanical modeling of the elasto-viscoplastic behavior of semi-crystalline polymers. Journal of the Mechanics and Physics of Solids 51,519-541.

Vergari, C., Mansfield, J., Meakin, J.R., Winlove, P.C., 2016. Lamellar and fibre bundle mechanics of the annulus fibrosus in bovine intervertebral disc. Acta Biomaterialia 37,14-20.

Yao, H., Gu, W.Y., 2007. Three-dimensional inhomogeneous triphasic finite-element analysis of physical signals and solute transport in human intervertebral disc under axial compression. Journal of Biomechanics 40,2071-2077.

Chapter II

A multiscale and multiaxial model for anisotropic damage and failure of human annulus fibrosus

A multiscale and multiaxial model for anisotropic damage and failure of human annulus fibrosus[7]

Abstract

This article presents a multiscale model to predict deformation-induced damage and failure of human annulus fibrosus under multiaxial loading. In the modeling approach, formulated within the framework of nonlinear continuum mechanics, the hierarchical structure of the soft tissue is considered from the nano-sized collagen fibrils to the micro-sized oriented collagen fibers. At the macroscale, the multi-layered lamellar/inter-lamellar organization of the soft tissue is introduced by considering the effective interactions between adjacent layers. The stochastic process of progressive damage events operating at different scales of the solid phase is introduced for the extracellular matrix and the network of nano-sized fibrils/micro-sized fibers. The damage is made anisotropic due to lamellar oriented collagen fibers and special orientation distribution of the inter-fibrillar and inter-lamellar network of fibrils. The chemical-induced volumetric strain is also considered in our modeling approach to take into account the osmolarity effects along with the anisotropic time-dependent transversal deformations. The capacity of the model is discussed using a few available stretching datasets till failure along circumferential and radial directions. Model predictions under tilted stretching, biaxial stretching and shearing are also presented to illustrate further the efficiencies of our modeling approach. This work shows for the first time the directional effects on annulus mechanics and failure in relation to external loading mode, structure features, damage events and hydration.

Keywords: Multiscale; Osmolarity; Multiaxial; Damage; Failure.

[7] This chapter is based on the following paper: Tamoud, A., Zaïri, F., Mesbah, A., Zaïri, F., 2021. A multiscale and multiaxial model for anisotropic damage and failure of human annulus fibrosus. International Journal of Mechanical Sciences, 106558.

Nomenclature

F : Deformation gradient tensor
L : Velocity gradient tensor
C : Right Cauchy-green strain tensor
E : Green-Lagrange strain tensor
σ : Cauchy stress tensor
P : First Piola-Kirchhoff stress tensor
R : Rotational basis-change tensor
I : Identity tensor
$\boldsymbol{x}$, $\boldsymbol{y}$, $\boldsymbol{z}$: Cartesian coordinate vectors
$\boldsymbol{a}$: Unit vector of collagen fiber
$\boldsymbol{b}$: Unit vector of collagen fibril
$\boldsymbol{n}$: Unit vector at the inter-layer interfaces
θ : Fiber angle with respect to the ***xy***-plane
ψ : Fibril angle with respect to the ***az***-plane
γ : Load angle with respect to ***xz***-plane
q : Fibril quantity
η : Fibril bundle number
z : Layer thickness
m : Number of layers
ϕ : Volume fraction

W : Free energy function
p : Hydrostatic pressure
$\bar{I}$: Isochoric invariant
J : Volumetric change
λ : Stretch
λ^* : Transition stretch
κ : Shear strain

Operators

$H(\bullet)$ Heaviside
$\otimes$ Direct (outer) product
$(\bullet)^T$ Transpose
$\cdot$ Simple contraction

Abbreviations

LM: Lamellar
ILM: Inter-lamellar
ECM: Extracellular matrix
OCF: Oriented collagen fibers
NEF: Nano-sized elastic fibers

II.1. Introduction

The ineluctable deterioration of the intervertebral disc annulus fibrosus is a multiscale phenomenon due to the hierarchical structure of this soft tissue (Yu et al., 2002, 2015; Pezowicz et al., 2006a, 2006b; Melrose et al., 2008; Schollum et al., 2008; Han et al., 2012; Vergari et al., 2016; Han et al., 2016; Tavakoli at al., 2016, 2017, 2020a, 2020b). The irreversible degradation in annulus fibrosus operates from the nanoscale (Tang et al., 2009) to the macroscale (Werbner et al.,2019) and results in the development of multiple cracks and tears (Osti et al., 1992; Vernon-Roberts et al., 2007). There is a considerable qualitative understanding of the microstructure and chemical factors that govern the response of the soft tissue. However, the coupling between these factors and mechanics is yet far to be fully understood in annulus fibrosus.

The introduction of the tissue structure at different scales in a continuum-based modeling framework would allow to propose predictive tools for mechanical damage and failure in a physically consistent

way. Over the years, macroscopic continuum-based damage models were proposed using two main approaches. The first one considers reduction factors incorporated in the free energy function (Rodriguez et al., 2006; Calvo et al., 2007; Pena et al., 2010; Blanco et al., 2015; Shahraki et al., 2015; Li, 2016; Holzapfel and Fereidoonnezhad, 2017; Li and Holzapfel, 2019; Ghezelbash et al., 2020a). The second one introduces an energy limiter in the expression of the free energy function (Volokh, 2007, 2011). No model until now is able to predict the multiaxial behavior of annulus fibrosus till failure and such a development remains a challenging task. The main difficulty comes from the anisotropic mechanics of a tissue with a complex hierarchical solid phase starting from the nanoscale (Tavakoli et al., 2020a, 2020b). The degree of knowledge of the collagen network has considerably increased thanks to the technological advances in the imaging field (Yu et al., 2002, 2015; Pezowicz et al., 2006a, 2006b; Melrose et al., 2008; Schollum et al., 2008; Han et al., 2012; Vergari et al., 2016; Han et al., 2016; Tavakoli at al., 2016, 2017). For a physically consistent constitutive representation, an accurate structure of the solid phase must be taken into account (Ghezelbash et al., 2020b) in interaction with the surrounding environment. In this regard, the fluid phase transfer by osmotic effect through the tissue solid phase affects largely the biochemical volumetric behavior (Derrouiche et al., 2019a, 2020a; Yang and O'Connell, 2019; Feki et al., 2020). The coupling between deformation-induced stress and swelling due to internal fluid content variation by osmosis is mandatory to quantitatively analyze the annulus fibrosus multiaxial mechanics (Kandil et al., 2020) along with the failure (Werbner et al., 2019).

The deterioration of the annulus fibrosus is indeed a multi-physics phenomenon since it implies biochemical degradation processes interacting in a complex manner with the external loading mode and the induced mechanical damage. A loss of electrolytic properties of extracellular matrix (ECM) proteoglycan macromolecules occurs with the tissue degeneration, which results in a decrease of osmotic pressure (Kiani et al., 2002; Urban and Robert, 2003). In the meantime, high mechanical loads cause tissue degenerative changes resulting in the degradation of the proteoglycan

macromolecules associated with the enzymes of the ECM metalloproteinase activity (Iatridis et al., 2011). The induced metabolic phenomena in the ECM cause a degradation of the osmotic properties of the annulus fibrosus associated with a decrease in water content and structure changes (Iatridis at al., 2006). These changes may alter the resistance of the annulus fibrosus to the mechanical-induced crack propagation (Werbner et al., 2019; Vergari et al., 2017). Establishing annulus damage-structure-osmotic relationships is a fundamental task for a detailed understanding of the degeneration mechanisms, to reduce their effects and to potentially prevent dangerous degenerative cases from happening. For an accurate annulus behavior, the structure-chemo-mechanics relationship can only be seen by considering, in addition to the annulus stretching in the circumferential direction, representative of the disc compression mechanics, the multiaxiality of the external mechanical loading representative of the body movements (Kandil et al., 2020). The latter is the key point to better understand the origin of multi-directional micro-cracks and tears commonly observed in the annulus fibrosus (Boos et al., 2002).

In this chapter, a multiscale model for deformation-induced damage and failure of annulus fibrosus is proposed by considering the structure at different scales, the micromechanical deformation processes leading to the final failure, the anisotropic nonlinear mechanics and the coupling with the osmotic effects. The proposed model, fully three-dimensional, is used to examine the multiaxial mechanics of the tissue and the directional effects. Uniaxial stretching, biaxial stretching and shearing are all being considered. The multiaxial model results are correlated to the microstructure features, to their progressive deformation-induced changes, to the tissue volumetric behavior and to the final failure.

This chapter is organized as follows. In Section II.2, the annulus multiscale model is presented within the framework of nonlinear continuum mechanics. In Section II.3, the model is verified for different loading paths and is used to discuss important aspects of the annulus mechanics in relation

to volumetric effects and to damage accumulation in the tissue due to progressive local failure events. Section II.4 closes the chapter with some concluding remarks.

II.2. Model formulation

The following notation is used throughout the text. Tensors and vectors are respectively denoted by normal boldfaced letters and italicized boldfaced letters, while scalars and individual components of vectors and tensors are denoted by normal italicized letters. The superposed dot designates the time derivative.

II.2.1. Hierarchical organization of annulus fibrosus

Let us start by the presentation of the hierarchical organization of all discrete solid components. Figure II.1 presents a schematic representation of the soft tissue hierarchical structure based on earlier experimental observations starting from the intervertebral disc at the upper scale and ending to the organization of the collagen network at the microscale and at the nanoscale. The multiple-network medium is constantly immerged in a physiological solution of water and ions. At the scale of the annulus fibrosus, inter-lamellar (ILM) matrix connects fibers-reinforced lamellae (LM) such that a (concentric) multi-layered material element is formed with distinct radial and circumferential microstructure features (retaining inner gel-like disc portion, i.e. nucleus pulposus). The tangled ECM consists in very large randomly oriented proteoglycan macromolecules with glycosaminoglycan chains that have ionic imbalances and interact with the ionic components of the surrounding physiological fluid to maintain electroneutrality by osmotic effect.

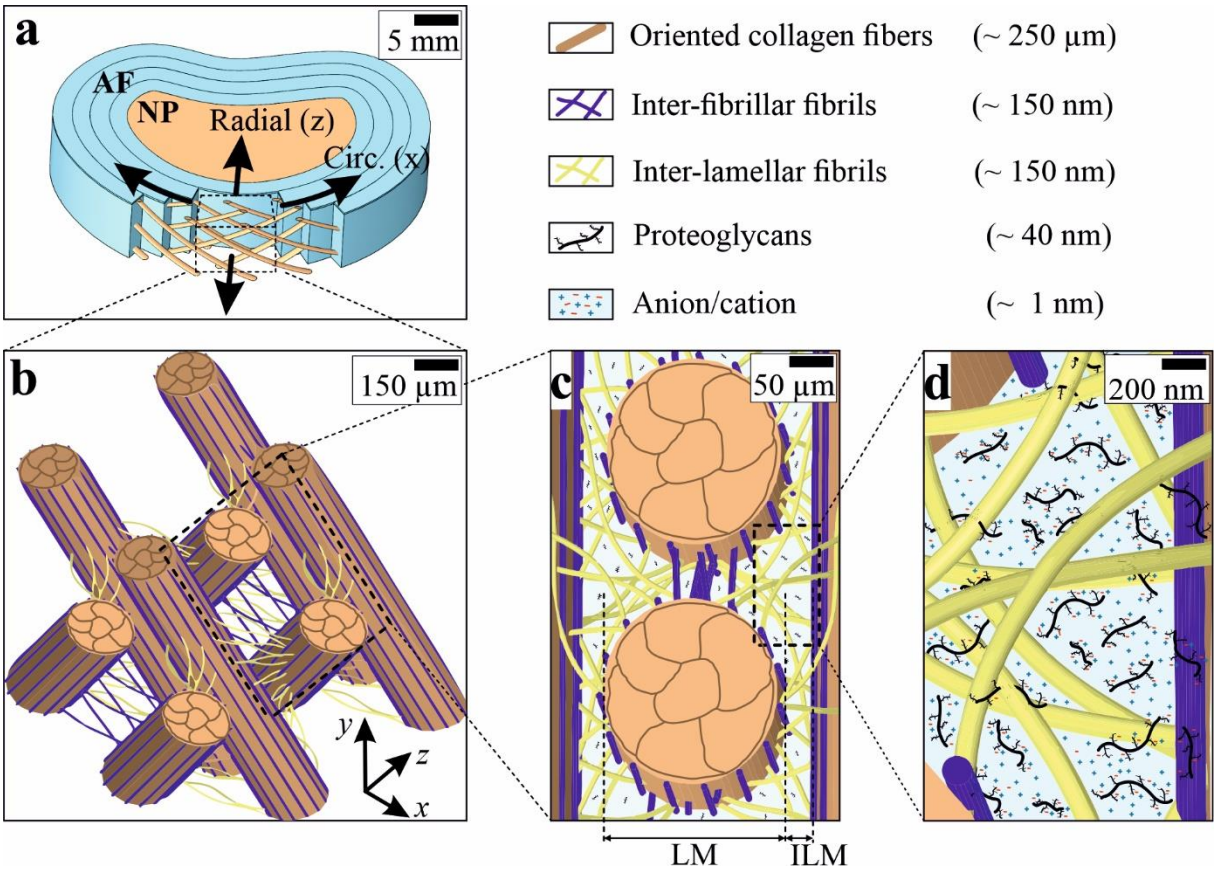

Figure II.1. Multiscale view of (a) the intervertebral disc annulus fibrosus (AF: annulus fibrosus, NP: nucleus pulposus) starting from (b) the multi-layered material element to the local organization of the collagen-network at the (c) microscale and the (d) nanoscale. The picture is adapted from the experimental analyzes in (Han et al., 2012; Yu et al., 2015; Tavakoli et al., 2017).

The micro-sized type-I oriented collagen fibers (OCF) represent up to 80% of the total volume of collagen network $\phi_{collagen}$ (Yu et al., 2002; Schollum et al., 2008; Sharabi et al., 2018). This family of fibers is described geometrically by a unit vector $\boldsymbol{a}$ in the initial configuration with respect to the global benchmark of the disc as illustrated in Figure II.2a. It is expressed in the Cartesian coordinates by:

$$\boldsymbol{a} = \cos\theta\,\boldsymbol{x} + |\sin\theta|\,\boldsymbol{y} \tag{II.1}$$

where θ is the fibers angle with respect to the circumferential direction.

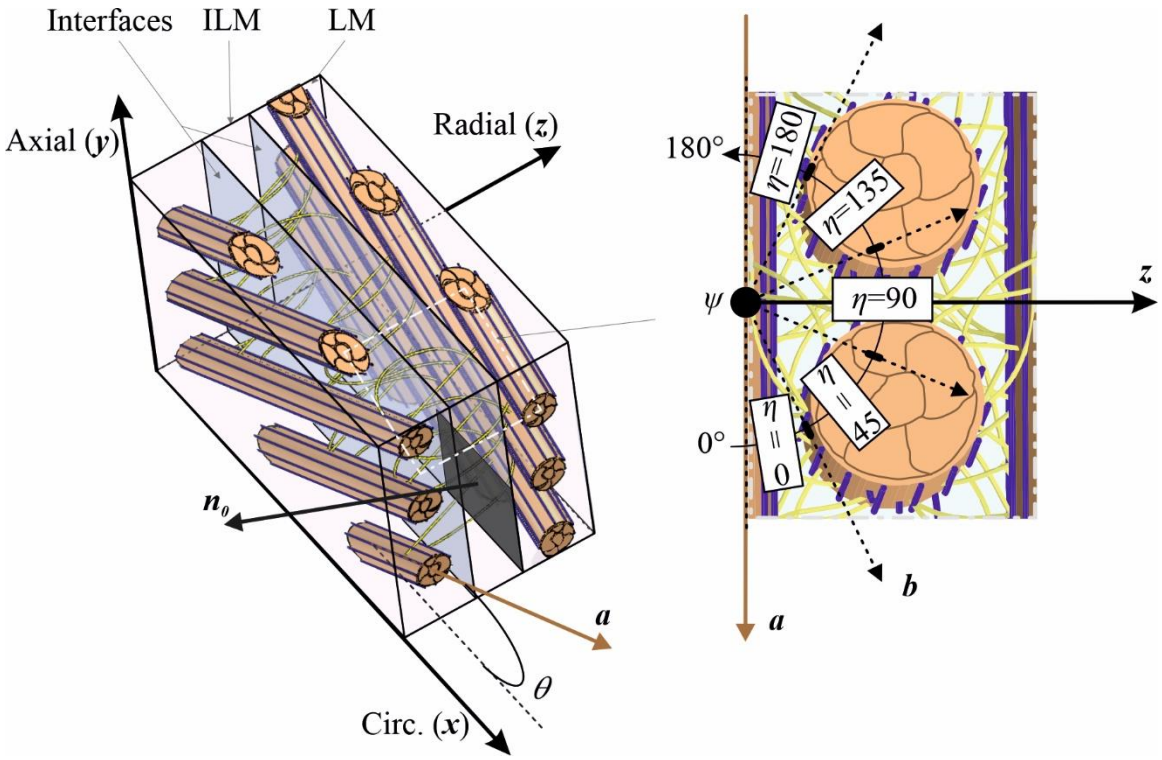

(a) (b)

Figure II.2. Coordinate systems of (a) the multi-layered material element ($\boldsymbol{n_0}$-axis is the unit vector at inter-layer interfaces and $\boldsymbol{a}$-axis is the unit vector along OCF that forms an angle θ with the $\boldsymbol{x}$-axis) and (b) of the five NEF bundles $\eta = \{0°, 45°, 90°, 135°, 180°\}$ ($\boldsymbol{b}$-axis is the unit vector along NEF that forms an angle ψ with the $\boldsymbol{a}$-axis).

The nano-sized elastic fibers (NEF) consist in a complex network of collagen fibrils, present both in the LM zone and in the ILM zone. In the LM zone, they act as inter-fibrillar connections of type-I collagen fibers (Figure II.1c). In the ILM zone, they act as inter-lamellar connections of two adjacent lamellae (Figure II.1d) (Yu et al., 2002, 2015; Melrose et al., 2008; Schollum et al., 2008; Han et al., 2012). For symmetry reasons, the distribution of NEF is described geometrically by an angle ψ ranged from 0° to 180° with respect to the radial direction in the parallel plane of the fibers as illustrated in Figure II.2b. The unit vector $\boldsymbol{b}$ of each fibril in the initial configuration is expressed with respect to the global benchmark of the disc in the Cartesian coordinates as follows:

$$\boldsymbol{b} = \left|\cos\theta\cos\psi\right| \boldsymbol{x} + \left|\sin\theta\cos\psi\right| \boldsymbol{y} + \sin\psi\, \boldsymbol{z} \tag{II.2}$$

The fruitful experimental quantifications of NEF performed by Tavakoli et al. (2017) are used as direct inputs of our modeling approach. Figure II.3 provides the number of NEF in the LM and ILM layers as a function of the orientation ψ. We use a Gaussian probability density function to describe these experimental trends:

$$q_\eta^{LM} = \chi_\eta^{LM} \exp\left(-\varsigma^{LM}\left(\psi-\eta\right)^2\right) \text{ and } q_\eta^{ILM} = \chi_\eta^{ILM} \exp\left(-\varsigma^{ILM}\left(\psi-\eta\right)^2\right) \quad \text{(II.3)}$$

where χ_η^{LM} and χ_η^{ILM} denote the respective peak values with η = {0°, 45°, 90°, 135°, 180°} and, ς^{LM} = 0.05 and ς^{ILM} = 0.11 are two factors.

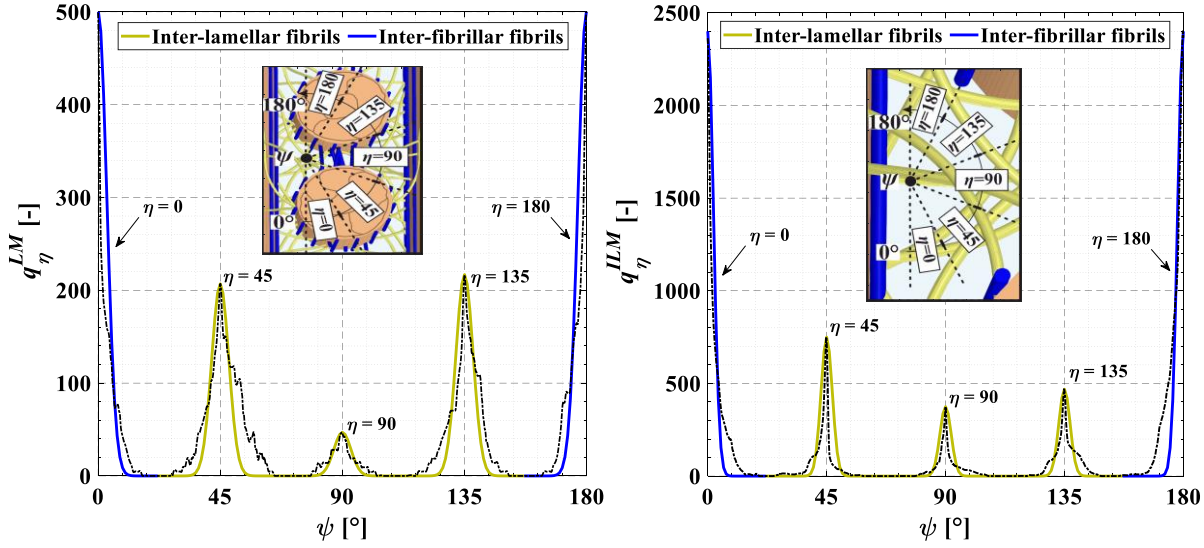

(a) (b)

Figure II.3. Quantity of NEF (a) in LM and (b) in ILM; continuous lines: Eq. (II.3), dashed lines: experimental data (Tavakoli et al., 2017).

The volume fraction of a fibril in each layer *i* is given by:

$$\phi_\eta^{LM\_i} = \begin{cases} \dfrac{q_\eta^{LM} + q_\eta^{ILM}}{q^{LM}} & \eta = 0°,180° \\ \dfrac{q_\eta^{LM}}{q^{LM}} & \eta = 45°,90°,135° \end{cases} \text{ and } \phi_\eta^{ILM\_i} = \begin{cases} 0 & \eta = 0°,180° \\ \dfrac{q_\eta^{ILM}}{q^{ILM}} & \eta = 45°,90°,135° \end{cases} \quad \text{(II.4)}$$

where q^{LM} and q^{ILM} are the respective total number of NEF in each layer *i*:

$$q^{LM} = \sum_{\eta}\sum_{\psi} q_{\eta}^{LM} + \sum_{\eta=0°,180°}\sum_{\psi} q_{\eta}^{ILM} \text{ and } q^{ILM} = \sum_{\eta=45°,90°,135°}\sum_{\psi} q_{\eta}^{ILM} \quad \text{(II.5)}$$

Due to the presence of inter-fibrillar connections of type-I collagen fibers in LM zone, a second term appears in the first equation.

In what follows, the features of the annulus mechanics are described along with a set of constitutive equations for the solid phase behavior using a physically realistic approach accounting for microstructure organization at different scales, damage and hydration.

II.2.2. Free energy of the fluid phase and swelling-related changes

Local ionic diffusion is responsible for dilatation effects and nonlinear time-dependent transversal stretch response of the multi-lamellar annulus (Sarkadi and Parker, 1991; Guizouarn and Motais, 1999; de los Heros et al., 2018; Derrouiche et al., 2020b). The derivation of the constitutive model must take into account this chemical coupling in the description of the finite-strain kinematics (Derrouiche et al., 2019b). In this framework, the basic quantity is the deformation gradient tensor mapping material tangent vectors in their reference configuration to their actual position in the deformed configuration. It is designated here as $\mathbf{F}^i$ for each layer *i* of the multi-layered material element. The introduction of an intermediate (virtual) configuration assumed stress-free allows to multiplicatively decompose the deformation gradient tensor $\mathbf{F}^i$ into a chemical-induced volumetric part $\mathbf{F}^i_{chem}$ and a mechanical part $\mathbf{F}^i_{mech}$ as follows:

$$\mathbf{F}^i = \mathbf{F}^i_{chem}.\mathbf{F}^i_{mech} \quad \text{(II.6)}$$

in which $\mathbf{F}^i_{chem}$ is the swelling expansion due to internal fluid content variation and $\mathbf{F}^i_{mech}$ is the mechanical (isochoric) stress-producing contribution. The sequence of configurations implies also an additive split of the gradient tensor $\mathbf{L}^i$ of the spatial velocity into a chemical-induced volumetric part $\mathbf{L}^i_{chem}$ and a mechanical part $\mathbf{L}^i_{mech}$ as:

$$\mathbf{L}^i = \underbrace{\dot{\mathbf{F}}^i_{chem}.\mathbf{F}^{i^{-1}}_{chem}}_{\mathbf{L}^i_{chem}} + \underbrace{\mathbf{F}^i_{chem}.\dot{\mathbf{F}}^i_{mech}.\mathbf{F}^{i^{-1}}_{mech}.\mathbf{F}^{i^{-1}}_{chem}}_{\mathbf{L}^i_{mech}} \tag{II.7}$$

The determinant (Jacobian) $J^i = \det\left(\mathbf{F}^i\right) > 0$ of the deformation gradient tensor $\mathbf{F}^i$ gives:

$$J^i = J^i_{chem} J^i_{mech},\ J^i_{mech} = \det\left(\mathbf{F}^i_{mech}\right) = 1 \text{ and } J^i_{chem} = \det\left(\mathbf{F}^i_{chem}\right) \tag{II.8}$$

where the term J^i_{chem} represents the tissue chemical-induced volumetric change. In view of the mechanical incompressibility of all solid components (ECM, OCF and NEF), the term J^i_{mech} is equal to one. We may define the total Green-Lagrange strain tensor $\mathbf{E}^i$, the mechanical (isochoric) Green-Lagrange strain tensor $\mathbf{E}^i_{mech}$ and the chemical-induced volumetric strain ε^i_{chem}:

$$\mathbf{E}^i = \frac{1}{2}\left(\mathbf{C}^i - \mathbf{I}\right),\ \mathbf{E}^i_{mech} = \frac{1}{2}\left(\mathbf{C}^i_{mech} - \mathbf{I}\right) \text{ and } \varepsilon^i_{chem} = J^i_{chem} - 1 \tag{II.9}$$

where $\mathbf{I}$ is the unit tensor, $\mathbf{C}^i = \mathbf{F}^{i^T}.\mathbf{F}^i$ is the total right Cauchy-Green strain tensor and $\mathbf{C}^i_{mech} = \mathbf{F}^{i^T}_{mech}.\mathbf{F}^i_{mech}$ is the mechanical (isochoric) right Cauchy-Green strain tensor.

For each layer, the respective volume fractions of the three solid components (ECM, OCF and NEF) may be expressed as:

$$\phi^i_{ECM} = \frac{\phi^i_{ECM\_0}}{J^i_{chem}},\ \phi^i_{OCF} = \frac{\phi^i_{OCF\_0}}{J^i_{chem}} \text{ and } \phi^i_{NEF} = \frac{\phi^i_{NEF\_0}}{J^i_{chem}} \tag{II.10}$$

where $\phi^i_{ECM\_0}$, $\phi^i_{OCF\_0}$ and $\phi^i_{NEF\_0}$ are the initial volume fractions in each layer *i*.

The volume fraction of the fluid phase ϕ^i_{fluid} in each layer *i* is then given by:

$$\phi^i_{fluid} = 1 - \frac{\phi^i_{ECM\_0} + \phi^i_{OCF\_0} + \phi^i_{NEF\_0}}{J^i_{chem}} \tag{II.11}$$

The Cauchy stress tensor $\boldsymbol{\sigma}^i$, defined in the deformed configuration, is additively split into a mechanical part $\boldsymbol{\sigma}^i_{mech}$ and a chemical-induced volumetric part $\boldsymbol{\sigma}^i_{chem}$. The latter tensor is given by:

$$\boldsymbol{\sigma}^i_{chem} = \frac{\partial W^i_{chem}}{\partial J^i_{chem}}\mathbf{I} \tag{II.12}$$

where W_{chem}^{i} is the chemical-induced volumetric free energy function, due to the internal fluid content variation, expressed in the following form:

$$W_{chem}^{i} = \phi_{fluid}^{i} \frac{1}{2} \frac{K_1}{K_2} \left(\exp\left(K_2 \left(J_{chem}^{i} - 1 \right)^2 \right) - 1 \right) \tag{II.13}$$

where K_1 and K_2 are material constants, K_1 and K_1/K_2 being respectively the initial and maximal volumetric stiffness values.

II.2.3. Free energies of the solid phase

Each individual component of the solid phase (ECM, OCF and NEF) is assumed as isotropic, homogeneous, incompressible and hyperelastic body. The mechanical Cauchy stress tensor $\boldsymbol{\sigma}_{mech}^{i}$ is obtained from the differentiation of the mechanical free energy function W_{mech}^{i} with respect to the corresponding deformation:

$$\boldsymbol{\sigma}_{mech}^{i} = 2\mathbf{F}_{mech}^{i} \cdot \frac{\partial W_{mech}^{i}}{\partial \mathbf{C}_{mech}^{i}} . \mathbf{F}_{mech}^{iT} - p^{i}\mathbf{I} \tag{II.14}$$

where p^{i} is determined from boundary conditions.

The mechanical free energy W_{mech}^{i} is given as a function of the free energies of the three solid components (ECM, OCF and NEF) using the volume fraction concept:

$$W_{mech}^{LM\_i} = \phi_{ECM}^{i} W_{ECM}^{i} + \phi_{OCF}^{i} W_{OCF}^{LM\_i} + \phi_{NEF}^{i} W_{NEF}^{LM\_i} \tag{II.15}$$

in LM layer and,

$$W_{mech}^{ILM\_i} = \phi_{ECM}^{i} W_{ECM}^{i} + \phi_{NEF}^{i} W_{NEF}^{ILM\_i} \tag{II.16}$$

in ILM layer.

The free energy functions of the solid components (ECM, OCF and NEF) are separately described below.

II.2.3.1. ECM free energy

The ECM proteoglycan macromolecular network is described as an isotropic deformable solid component with a free energy W_{ECM}^{i} expressed by a Neo-Hookean form:

$$W_{ECM}^{i} = \frac{1}{2} G_{ECM} \left(\bar{I}_1^{i} - 3 \right) \tag{II.17}$$

in which G_{ECM} is the ECM shear modulus and $\bar{I}_1^{i} = \text{trace}\left(\mathbf{C}_{mech}^{i} \right)$ is the first stretch invariant.

II.2.3.2. OCF free energy

The OCF network gives anisotropy, high stiffness and mechanical resistance to annulus. The sketch in Figure II.4 shows the different stretch stages of a stretched fiber in relation to its deformation behavior. In addition to fiber orientation and intrinsic properties, the description of the OCF nonlinear response requires two distinct relations below and above a stretch λ_{OCF}^{*} to consider the deformation-induced morphological evolution. The OCF free energy W_{OCF}^{i} is expressed as a function of the fourth stretch invariant $\bar{I}_{4\theta}^{i} = \boldsymbol{a}.\mathbf{C}_{mech}^{i}.\boldsymbol{a} = \lambda_{\theta}^{i\,2}$ by:

$$W_{OCF}^{i} = H\left(\bar{I}_{4\theta}^{i} - 1 \right) \left[\frac{1}{2} \frac{C_1}{C_2} \left(\exp\left(C_2 \left(\bar{I}_{4\theta}^{i} - 1 \right)^2 \right) - 1 \right) \right] \quad \lambda_{\theta}^{i} < \lambda_{OCF}^{*} \tag{II.18}$$

below λ_{OCF}^{*} and,

$$W_{OCF}^{i} = H\left(\bar{I}_{4\theta}^{i} - 1 \right) \left[\frac{C_3}{2} \left(\bar{I}_{4\theta}^{i} - \bar{I}_{4\theta}^{*} \right)^2 + \zeta \left(\bar{I}_{4\theta}^{i} - \nu \right) \right] \quad \lambda_{\theta}^{i} \geq \lambda_{OCF}^{*} \tag{II.19}$$

above λ_{OCF}^{*} .

The stretch λ_{OCF}^{*} defines the stretch transition between the ‘toe’ and ‘linear’ regions of the stress-stretch curve (Quapp and Weiss, 1998; Werbner et al., 2017; Li and Holzapfel, 2019). These two regions are related to the peculiar local behavior of a collagen fiber passing from the initially undulated configuration to the fully stretched state as illustrated in Figure II.4. The terms C_1, C_2 and C_3 are material constants of the OCF, $H(\bullet)$ is the Heaviside function that ensures only

stretching of the OCF, $\bar{I}_{4\theta}^{*}$ is the fourth stretch invariant for $\lambda_{\theta}^{i}=\lambda_{OCF}^{*}$ and, ζ and ν are functions that ensure continuity between 'toe' and 'linear' regions:

$$\zeta=C_1\left(\bar{I}_{4\theta}^{*}-1\right)\exp\left(C_2\left(\bar{I}_{4\theta}^{*}-1\right)^2\right) \text{ and } \nu=\bar{I}_{4\theta}^{*}-\frac{C_1}{2C_2\zeta}\left(\exp\left(C_2\left(\bar{I}_{4\theta}^{*}-1\right)^2\right)-1\right) \quad \text{(II.20)}$$

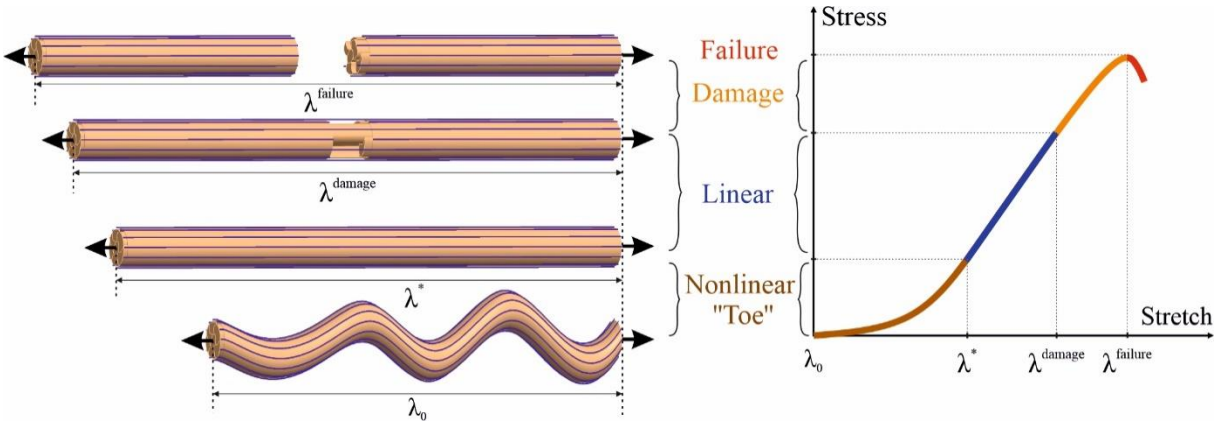

Figure II.4. Behavior of a single collagen fiber stretched until failure.

II.2.3.3. NEF free energy

The inter-fibrillar and inter-lamellar network of fibrils is described by the free energy W_{NEF}^{i} given by:

$$W_{NEF}^{LM\_i}=\sum_{\eta}\sum_{\psi}\phi_{\eta}^{LM\_i}W_{\psi}^{i} \text{ and } W_{NEF}^{ILM\_i}=\sum_{\eta=45,90,135}\sum_{\psi}\phi_{\eta}^{ILM\_i}W_{\psi}^{i} \quad \text{(II.21)}$$

For the same reasons invoked for OCF, the free energy of each fibril W_{ψ}^{i} is given by two distinct relations below and above a stretch λ_{NEF}^{*}:

$$W_{\psi}^{i}=H\left(\bar{I}_{4\psi}^{i}-1\right)\left[\frac{1}{2}\frac{C_4}{C_5}\left(\exp\left(C_5\left(\bar{I}_{4\psi}^{i}-1\right)^2\right)-1\right)\right] \quad \lambda_{\psi}^{i}<\lambda_{NEF}^{*} \quad \text{(II.22)}$$

below λ_{NEF}^{*} and,

$$W_{\psi}^{i}=H\left(\bar{I}_{4\psi}^{i}-1\right)\left[\frac{C_6}{2}\left(\bar{I}_{4\psi}^{i}-\bar{I}_{4\psi}^{*}\right)^2+\zeta_{\psi}\left(\bar{I}_{4\psi}^{i}-\nu_{\psi}\right)\right] \quad \lambda_{\psi}^{i}\geq\lambda_{NEF}^{*} \quad \text{(II.23)}$$

above λ_{NEF}^{*}.

The terms C_4, C_5 and C_6 are material constants of the NEF, $H(\bullet)$ is again the Heaviside function, $\bar{I}^i_{4\psi} = \boldsymbol{b}_\psi . \mathbf{C}^i_{mech} . \boldsymbol{b}_\psi = \lambda^{i\,2}_\psi$ is the fourth stretch invariant for the NEF, $\bar{I}^*_{4\psi}$ is the fourth stretch invariant for $\lambda^i_\psi = \lambda^*_{NEF}$ and, ζ_ψ and ν_ψ are two functions expressed as:

$$\zeta_\psi = C_4\left(\bar{I}^*_{4\psi} - 1\right)\exp\left(C_5\left(\bar{I}^*_{4\psi} - 1\right)^2\right) \text{ and } \nu_\psi = \bar{I}^*_{4\psi} - \frac{C_4}{2C_5\zeta_\psi}\left(\exp\left(C_5\left(\bar{I}^*_{4\psi} - 1\right)^2\right) - 1\right) \quad \text{(II.24)}$$

II.2.4. Damage

Under external mechanical loading, the nature of local failure is the scission of the ECM tangled proteoglycan macromolecules, the detachment of the internal bonds in the discrete (inter-fibrillar and inter-lamellar) fibrils and the breaking of the regularly-oriented fibers. When an individual solid component (ECM, OCF and NEF) is broken, it does no longer contribute to sustain the macro-stress. Damage induces thus a progressive evolution of the effective amount of the solid components:

$$\phi^i_{ECM\_d} = \phi^i_{ECM}\left(1 - d^i_{ECM}\right),\ \phi^i_{OCF\_d} = \phi^i_{OCF}\left(1 - d^i_{OCF}\right) \text{ and } \phi^i_{\eta\_d} = \phi^i_\eta\left(1 - d^i_\psi\right) \quad \text{(II.25)}$$

where d^i_{ECM}, d^i_{OCF} and d^i_ψ characterize the damage evolution occurring within the multi-layered material element microstructure. This damage representation is in line with the general damage mechanics framework for the hyperelasticity theory. The respective internal stress of each solid component is considered as the quantity controlling the progressive damage evolution from 0.0 for the virgin state to 1.0 for the fully damaged state. Two-parameter Weibull statistical distributions are used to introduce the stochastic nature of the damage process:

$$d^i_{ECM} = 1 - \exp\left(-\left(\frac{\left\|\mathbf{P}^i_{ECM}\right\|}{\beta_{ECM}}\right)^{\alpha_{ECM}}\right) \quad \text{(II.26)}$$

$$d^i_{OCF} = 1 - \exp\left(-\left(\frac{\left\|\mathbf{P}^i_{OCF}\right\|}{\beta_{OCF}}\right)^{\alpha_{OCF}}\right) \quad \text{(II.27)}$$

$$d_{\psi}^{i} = 1 - \exp\left(-\left(\frac{\left\| \mathbf{P}_{\psi}^{i} \right\|}{\beta_{NEF}} \right)^{\alpha_{NEF}} \right) \tag{II.28}$$

in which α and β are respectively the Weibull shape parameter and the Weibull scale parameter and, $\left\| \mathbf{P}_{ECM}^{i} \right\|$, $\left\| \mathbf{P}_{OCF}^{i} \right\|$ and $\left\| \mathbf{P}_{\psi}^{i} \right\|$ are the effective first Piola-Kirchhoff stresses given by the Frobenius norm:

$$\left\| \mathbf{P}_{ECM}^{i} \right\| = \sqrt{\mathrm{tr}\left(\mathbf{P}_{ECM}^{i} . \mathbf{P}_{ECM}^{iT} \right)}, \left\| \mathbf{P}_{OCF}^{i} \right\| = \sqrt{\mathrm{tr}\left(\mathbf{P}_{OCF}^{i} . \mathbf{P}_{OCF}^{iT} \right)} \text{ and } \left\| \mathbf{P}_{\psi}^{i} \right\| = \sqrt{\mathrm{tr}\left(\mathbf{P}_{\psi}^{i} . \mathbf{P}_{\psi}^{iT} \right)} \tag{II.29}$$

Taking into consideration the organization of the collagen network at different scales (as illustrated in Figure II.1) allows to propose a proper description of the progressive degradation considering both localization and anisotropy. The coupling between damage and osmotic effects is considered by introducing the following modification of the chemical-induced volumetric change:

$$\varepsilon_{chem\_d}^{i} = \varepsilon_{chem}^{i} \left(1 - d_{ECM}^{i} \right) \left(1 - d_{OCF}^{i} \right) \left(1 - d_{NEF}^{i} \right) \tag{II.30}$$

in which $d_{NEF}^{i} = 1/n \sum_{\psi}^{n} d_{\psi}^{i}$ is the damage of NEF and n is the number of fibrils.

II.2.5. Summary of the model

A new model for the microscopic description of the annulus mechanics is constructed by using the constitutive equations described above. To formulate the overall mechanical response of the multi-layered annulus under general three-dimensional loading conditions, the compatibility at inter-layer interfaces (Figure II.2a) must be respected while the above descriptions and definitions are used. In this regard, the continuity conditions in deformation and stress to be satisfied are:

$$\mathbf{F}^{LM\_i} . \boldsymbol{n}_{0}^{i} = \mathbf{F}^{ILM\_i+1} . \boldsymbol{n}_{0}^{i} \text{ and } \boldsymbol{\sigma}^{LM\_i} . \boldsymbol{n}^{i} = \boldsymbol{\sigma}^{ILM\_i+1} . \boldsymbol{n}^{i} \tag{II.31}$$

where $\boldsymbol{n}_{0}^{i}$ and $\boldsymbol{n}^{i}$ are the arbitrary unit vectors between two adjacent layers in the initial and current configurations, respectively.

The macro-deformation $\mathbf{F}$ and the macro-stress $\boldsymbol{\sigma}$ of the soft tissue are expressed as:

$$\mathbf{F} = \sum_{i=1,3...}^{m} \phi_{layer\_0}^{i} \mathbf{F}^{LM\_i} + \sum_{i=2,4...}^{m-1} \phi_{layer\_0}^{i} \mathbf{F}^{ILM\_i} \tag{II.32}$$

and

$$\boldsymbol{\sigma} = \sum_{i=1,3,..}^{m} \phi_{layer}^{i} \boldsymbol{\sigma}^{LM\_i} + \sum_{i=2,4,..}^{m-1} \phi_{layer}^{i} \boldsymbol{\sigma}^{ILM\_i} \tag{II.33}$$

where the deformation gradients and the Cauchy stresses in LM and ILM are given by their volumetric and mechanical parts:

$$\mathbf{F}^{LM\_i} = \mathbf{F}_{chem}^{LM\_i} . \mathbf{F}_{mech}^{LM\_i} \text{ and } \mathbf{F}^{ILM\_i} = \mathbf{F}_{chem}^{ILM\_i} . \mathbf{F}_{mech}^{ILM\_i} \tag{II.34}$$

and

$$\boldsymbol{\sigma}^{LM\_i} = \boldsymbol{\sigma}_{mech}^{LM\_i} + \boldsymbol{\sigma}_{chem}^{LM\_i} \text{ and } \boldsymbol{\sigma}^{ILM\_i} = \boldsymbol{\sigma}_{mech}^{ILM\_i} + \boldsymbol{\sigma}_{chem}^{ILM\_i} \tag{II.35}$$

The deformation gradients are detailed in Appendix II.A. The different parts of the Cauchy stress tensor are provided in Appendix II.B. The volume fractions in the initial and current configurations, $\phi_{layer\_0}^{i}$ and ϕ_{layer}^{i} are, respectively:

$$\phi_{layer\_0}^{i} = \frac{z_{layer\_0}^{i}}{z_{tissue}} \text{ and } \phi_{layer}^{i} = \frac{J_{chem}^{i} z_{layer\_0}^{i}}{\sum_{j=1}^{m} J_{chem}^{j} z_{layer\_0}^{j}} \tag{II.36}$$

in which $z_{layer\_0}^{i}$ is the initial thickness of the layer *i* and z_{tissue} is the tissue thickness:

$$z_{tissue} = z_{layer}^{LM} + z_{layer}^{ILM} = \sum_{i=1,3,..}^{m} z_{layer}^{LM\_i} + \sum_{i=2,4,..}^{m-1} z_{layer}^{ILM\_i} \tag{II.37}$$

with $z_{layer}^{LM\_i}$ $i = 1,3,...m$ and $z_{layer}^{ILM\_i}$ $i = 2,4,...m-1$ are the functions describing respectively the LM thickness and the ILM thickness:

$$z_{layer}^{LM\_i} = ai + b \text{ and } z_{layer}^{ILM\_i} = r_{ILM/LM} \left(z_{layer}^{LM\_i-1} / 2 + z_{layer}^{LM\_i+1} / 2 \right) \tag{II.38}$$

where $r_{ILM/LM}$ represents the thickness ratio of the two zones and, *a* and *b* are constants calculated according to the maximum and minimum thicknesses of the annulus layers z_{max} and z_{min}:

$$a = \frac{z_{max} - z_{min}}{m-1} \text{ and } b = z_{min} - a \tag{II.39}$$

where *m* is the number of layers.

The model makes it possible to estimate the deformation-induced damage and failure of annulus under three-dimensional loading conditions. The multi-layered material element will be subjected to the different mechanical paths illustrated in Figure II.5, namely, uniaxial (UA) stretching in different directions (circumferential, radial and tilted), biaxial stretching and shearing.

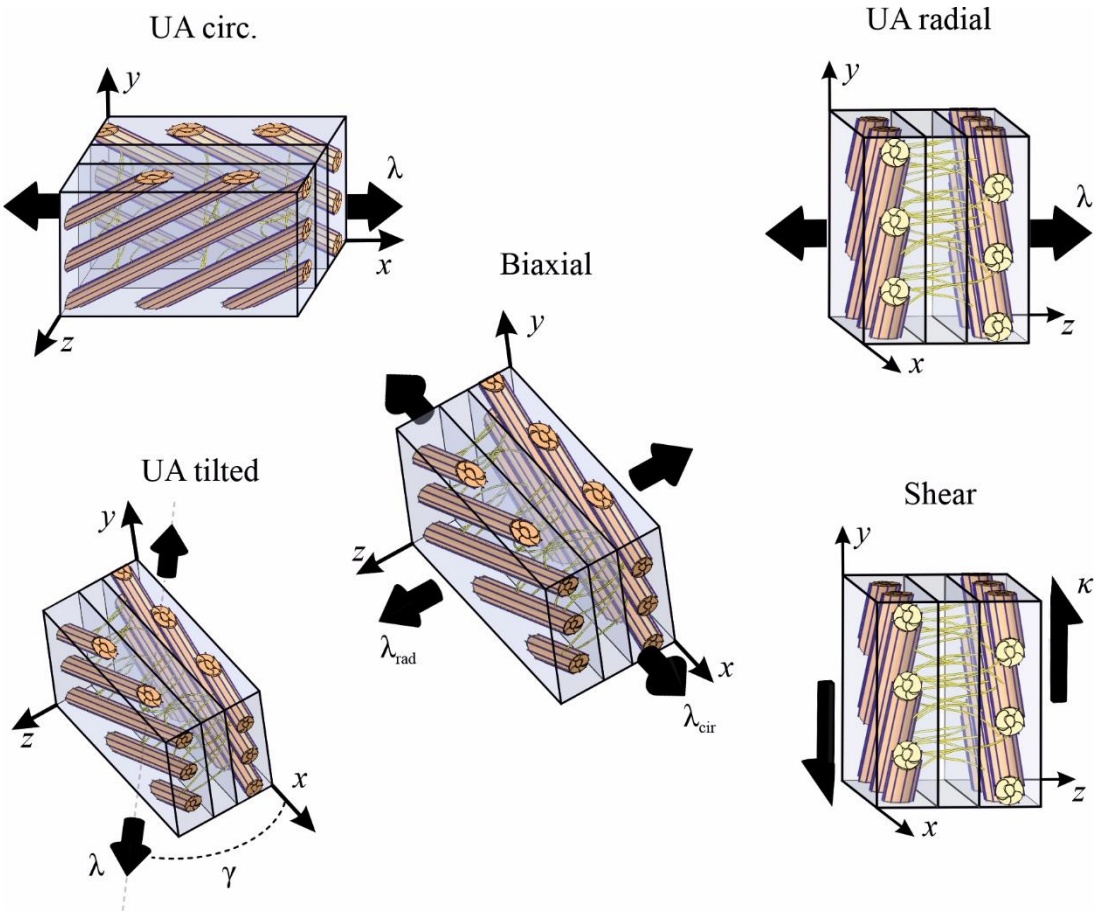

Figure II.5. Loading paths applied on the multi-layered material element.

II.3. Results and discussion

In addition to the hierarchical organization of the collagen network presented in Section II.2.1, some direct structure inputs required by the modeling (namely dimensions, collagen orientation/content and water content) are extracted from well-documented papers of the literature (Skaggs et al., 1994; Acaroglu et al., 1995; Holzapfelet al., 2005; Baldit, 2013; Tavakoli et al., 2017) and are listed in Table II.1.

Parameters	Values		References
z_{max}	0.76	$[\mathrm{mm}]$	Holzapfel et al. (2005)
z_{min}	0.69	$[\mathrm{mm}]$	Holzapfel et al. (2005)
$r_{ILM/LM}$	0.133	$[-]$	Tavakoli et al. (2017)
θ	30	$[\mathrm{deg}]$	Holzapfel et al. (2005), Baldit 2013
$\phi_{collagen}$	0.07	$[-]$	Skaggs et al. (1994)
ϕ_{fluid_0}	0.7	$[-]$	Acaroglu et al. (1995)

Table II.1. Structural parameters.

The in-vitro experiments used for model identification and verification do not generally precise the exact disc region whereas variations in water content and collagen content/orientation actually exist. Due to the lack of precise information, the selected structure features are representative of the annulus anterior area. Nine LM/ILM layers are considered resulting in a parallelepipedic material element of $10 \times 4 \times 4$ mm^3 for circumferential direction, and $2 \times 2 \times 4$ mm^3 for radial direction, in order to respect the sample size effect on the mechanical behavior of the annulus (Zhou et al., 2019; Kandil et al., 2020) The simulations were performed by using a constant strain rate of 0.001 s^{-1}.

Components	Parameters	Values

Swelling	Fluid	K_1	0.14	[MPa]
		K_2	0.075	[–]
Toe	ECM	G_{ECM}	0.01	[MPa]
	OCF	C_1	26	[MPa]
		C_2	12	[–]
	NEF	C_4	25	[MPa]
		C_5	0.2	[–]
Linear	OCF	C_3	70	[MPa]
		λ^*_{OCF}	1.09	[–]
	NEF	C_6	1.5	[MPa]
		λ^*_{NEF}	1.7	[–]
Damage	ECM	α_{ECM}	2	[–]
		β_{ECM}	5.5	[MPa]
	OCF	α_{OCF}	5	[–]
		β_{OCF}	43	[MPa]
	NEF	α_{NEF}	6	[–]
		β_{NEF}	850	[MPa]

Table II.2. Model parameters.

Table II.2. gives the identified values of the intrinsic mechanical parameters of the solid components (ECM, OCF and NEF) and the swelling response. Their identification was solved numerically as an optimization problem using MATLAB software considering the two following objective functions $F^{obj}_{swelling}$ and F^{obj}_{stress} to be minimized:

$$F^{obj}_{swelling} = \frac{1}{\rho}\sum_{h=1}^{\rho}\left(\left(\frac{\lambda_y^h - \tilde{\lambda}_y^h}{\tilde{\lambda}_y^h}\right)^2 + \left(\frac{\lambda_z^h - \tilde{\lambda}_z^h}{\tilde{\lambda}_z^h}\right)^2 + \left(\frac{\varepsilon_{chem}^h - \tilde{\varepsilon}_{chem}^h}{\tilde{\varepsilon}_{chem}^h}\right)^2\right) \tag{II.40}$$

$$F^{obj}_{stress} = \frac{1}{\rho}\sum_{h=1}^{\rho}\left(\left(\frac{P_{circ}^h - \tilde{P}_{circ}^h}{\tilde{P}_{circ}^h}\right)^2 + \left(\frac{P_{rad}^h - \tilde{P}_{rad}^h}{\tilde{P}_{rad}^h}\right)^2\right) \tag{II.41}$$

in which the letters with an overbar denote the experimental data with ρ the number of considered data points. The optimization of the model parameters was performed using a few well-known available datasets of the swelling response (transversal stretches and volumetric strain) and the UA

(circumferential and radial) stress responses till moderate stretching and ultimate failure. Before their final optimization using formulae (II.40) and (II.41), a first set of model parameters was estimated via a step-by-step approach to dissociate the different phenomena: osmotic effect, directional-dependent straightening of collagen networks and damage effect. The volumetric parameters, K_1 and K_2, were identified using the UA circumferential data of Baldit (2013) describing the time-dependent volumetric response upon stretching followed by relaxation. The collagen parameters, C_1, C_2, C_4 and C_5, were identified using the nonlinear part (toe zone) of the UA circumferential data of Acaroglu et al. (1995) and the radial data of Fujita et al. (1997). The stretches, λ^*_{OCF} and λ^*_{NEF}, as well as the remaining collagen parameters, C_3 and C_6, were determined using the transition between the UA nonlinear response and the UA linear response of the Acaroglu et al. (1995) and Fujita et al. (1997) data. The OCF damage parameters, α_{OCF} and β_{OCF}, were determined using the UA circumferential data of Acaroglu et al. (1995) whereas the ECM and NEF damage parameters, α_{ECM}, β_{ECM}, α_{NEF} and β_{NEF}, were determined using the UA radial data of Fujita et al. (1997).

Unless explicitly otherwise stated, the values in Table II.2. will be employed in all model results, especially to generate the multiaxial model predictions under other loading paths.

II.3.1. Chemical-induced swelling

The swelling response was identified using experimental data under free-swelling and UA circumferential stretching (Acaroglu et al., 1995; Baldit, 2013). For the latter, only moderate levels of stretching are available in the literature. The variation of fluid content by osmotic effect is firstly used to identify the free-swelling response. The identification result is provided in Figure II.6a until chemical equilibrium in a physiological NaCl solution (0.15 M). The volumetric tissue deformation induced by the internal fluid content variation under mechanical loading was then calibrated using

the experimental data of Baldit (2013) considering UA circumferential stretching and relaxation at constant circumferential stretch under a physiological surrounding environment. The temporal changes of transversal (radial and axial) stretches and the associated circumferential stress are given in Figure II.7. Our model considers the time-dependent chemo-mechanical coupling in the soft tissue to capture the unusual transversal strain history in relation to the actual structure and the chemical-induced internal fluid variation. The strong shrinking in the axial direction and the swelling in the radial direction upon UA circumferential stretching tend towards more usual transversal behavior upon relaxation due to chemo-mechanical equilibrium. The ILM zone is introduced as the key structural parameter governing inter-lamellae fluid exchanges under external mechanical loading and especially the auxetic behavior. This annulus feature was only appreciated through very recent contributions (Derrouiche et al., 2019b; Kandil et al., 2019; Tamoud et al., 2021) and was shown as determinant in the time-dependent multiaxial response (Kandil et al., 2020). The ILM anatomic function is also to confer a shearing resistance to the annulus and the inclusion of the network of inter-lamellar fibrils in the model allows a more realistic material representation. Note that the ECM reorganization may induce viscoelastic features in the annulus fibrosus (Tavakoli and Costi, 2018). Nonetheless, the quantitative estimation of the coupling between viscoelastic effects and chemical-induced volumetric effects showed that the volumetric features are first-order factors in the annulus mechanics compared to the deformation-induced viscoelastic stress in ECM (Derrouiche et al., 2019b; Kandil et al., 2019, 2020). Although the solid components are described by purely hyperelastic laws, the present constitutive representation considers the rate-dependency of the annulus mechanics implied by the deformation-induced damage mechanisms and the volumetric effects.

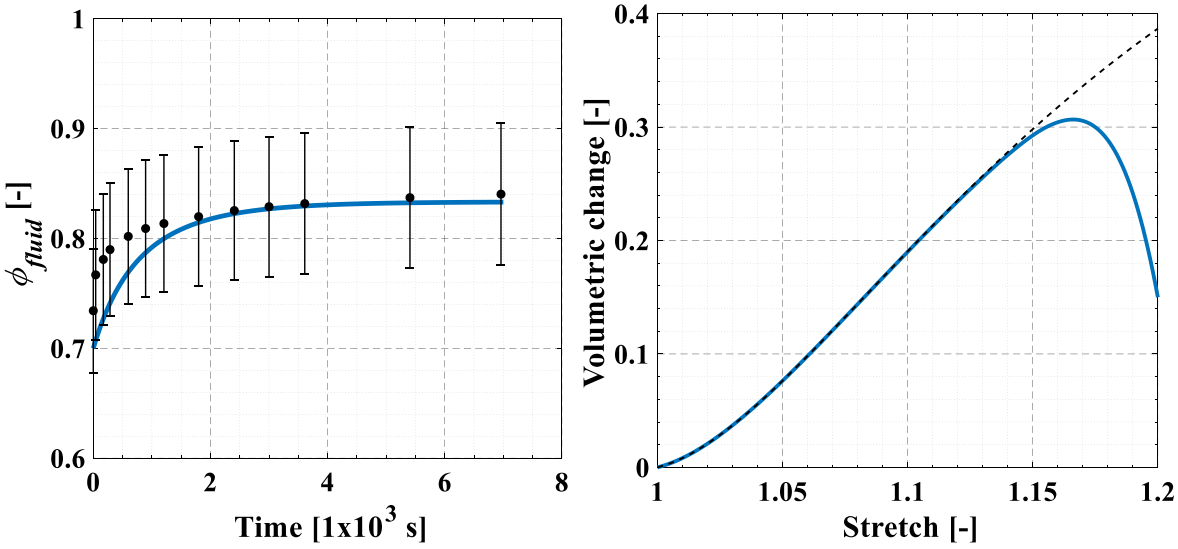

(a) (b)

Figure II.6. Volumetric response of the multi-layered material element: (a) under free swelling (line: model, symbol: experimental data of Acaroglu et al. (1995)), (b) under UA circumferential stretching (solid line: model, dashed line model without damage).

The results in Figure II.7 are presented for a moderate stretch range within which the soft tissue stays in a physiological level avoiding any damage effects. The question which arises is now how the tissue behaves under large strains till final failure by including as time-dependent physical process both volumetric effects and damage accumulation.

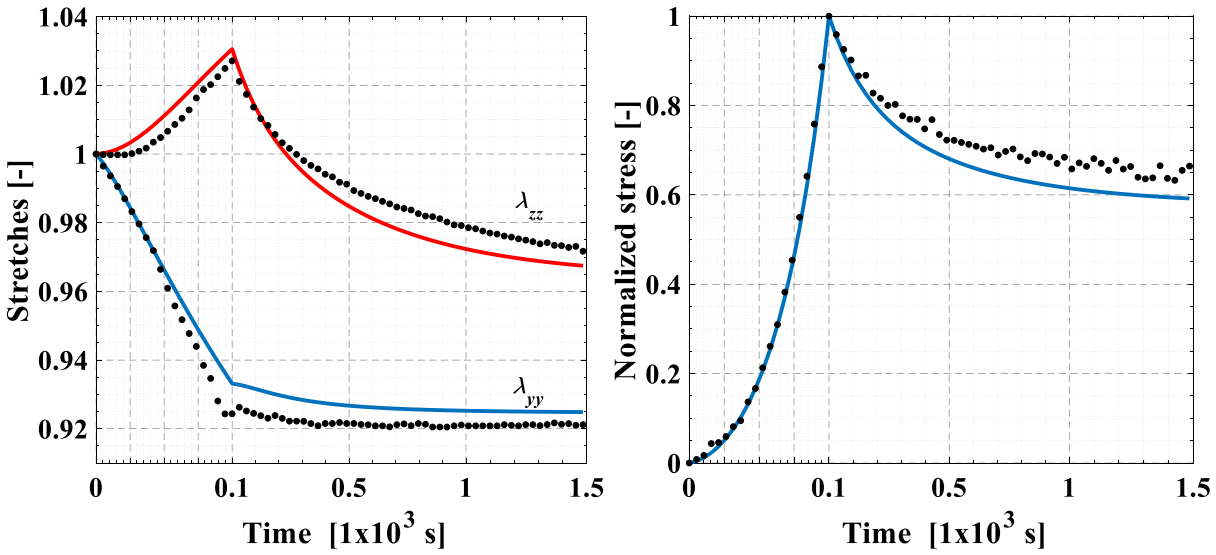

(a) (b)

Figure II.7. Temporal changes of (a) transversal stretches and (b) normalized stress of the multi-layered material element under a UA circumferential stretching until 1.1 followed by a relaxation (lines: model, symbols: experimental data of Baldit (2013)).

II.3.2.UA stretching path

The model efficiencies to capture the stress-stretch behavior of the annulus till failure under UA stretching is presented in Figures II.8 and II.9 for the two main directions in comparison with the experimental data extracted from the works of Acaroglu et al. (1995) and Tavakoli and Costi (2018). The numerical curves show an excellent agreement with the annulus circumferential experimental results of Acaroglu et al. (1995) in Figure II.8a including the nonlinear stress-stretch response and the failure stage displaying stress drop. Figure II.8c shows that both moduli and ultimate properties are in agreement with other data taken form the literature (Ebara et al., 1996). A direct relation between the annulus circumferential mechanics and the microstructure at the different scales can be pointed out. The straightening of the collagen network during stretching causes a (toe) nonlinear macro-response until the disappearance of the undulations of the collagen fibers at a strain of about 13%. Then, a nearly linear response appears up to reach the limiting extensibility of the collagen fibers that is seen at a strain of about 16%. A catastrophic stiffness decrease is then observed at a strain of about 18% due to damage accumulation that arises out of a wide fibril network degradation. The circumferential stretching creates ionic imbalance and chemical stress due to chemo-mechanical coupling. The predicted volumetric change is provided in Figure II.6b and is found moderately affected by the damage. Nonetheless, the chemical disorder induced by the fluid phase diffusion through the tissue plays an important role in absorbing the mechanical loads applied to the annulus. Figure II.8b shows the progressive damage events in ECM, OCF and NEF upon a circumferential UA stretching. The figure provides a clear picture of the sequence of damage operating in the different solid components. Before the incubation stretch, from which the damage initiates, the chemo-mechanical coupling is a reversible process dependent on hydration. The critical stretch is the lowest for ECM and the highest for OCF. The progressive breaking of NEF leads to the progressive loss of connectivity between neighboring OCF in a same LM layer, but also between OCF of two neighboring LM layers. The damage in NEF during circumferential stretching can be

explained by NEF stretching due to annulus chemical expansion (Figure II.6b). The latter has profound impact on the local damage events and thus on the overall annulus mechanics, especially along the circumferential direction. Without diffusion mechanism, the damage process is activated prematurely as evidenced in Figure II.8b. That results in stiffening, lower stretchability and a remarkably weakened stress peak as shown in Figure II.8a.

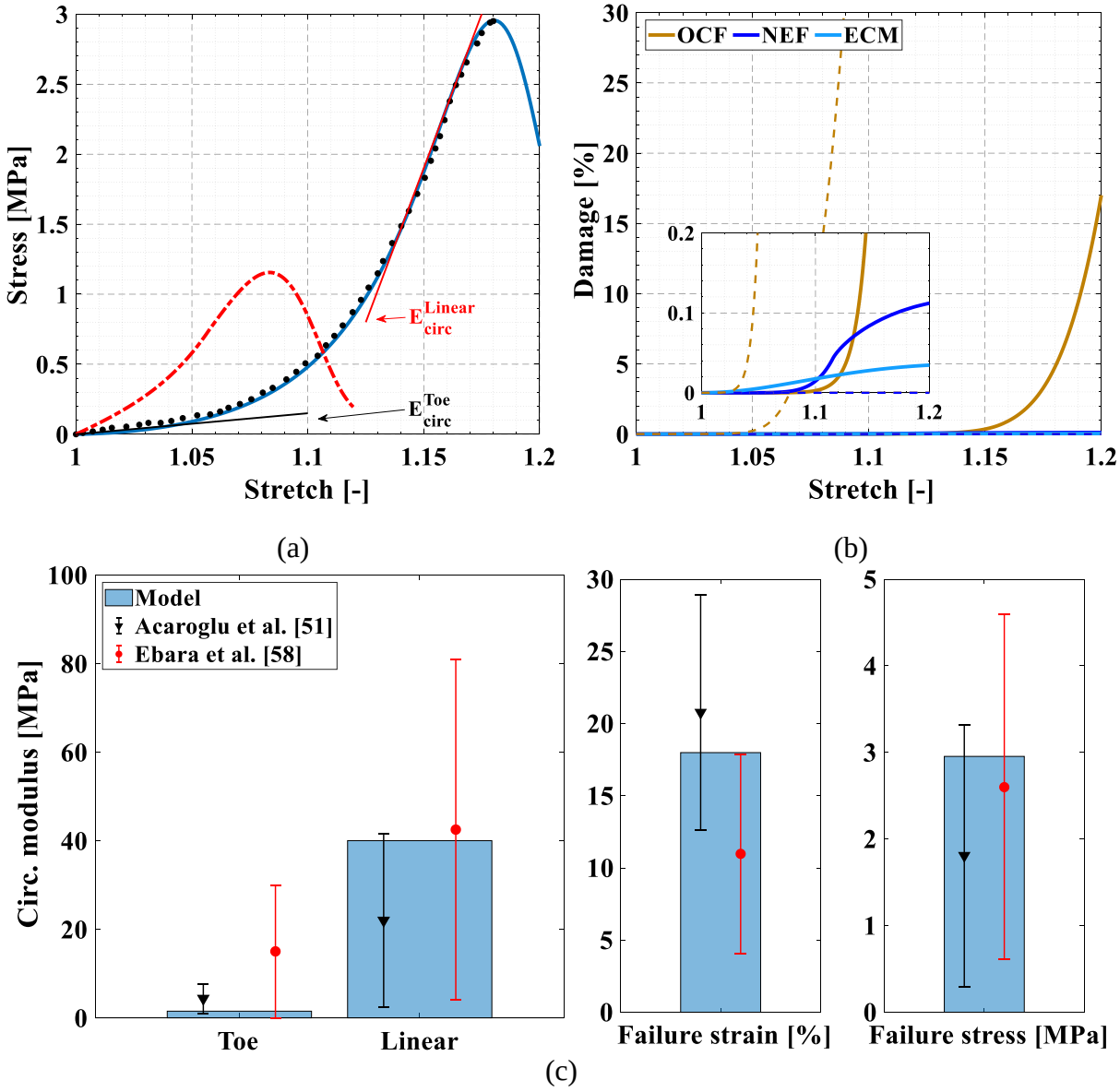

Figure II.8. UA circumferential stretching of the multi-layered material element: (a) stress-stretch response (solid line: model; dashed line: model without chemical effect, symbols: experimental data of Acaroglu et al. (1995)), (b) local damage events in the different solid constituents (solid line: model; dashed line: model without chemical effect), (c) toe and linear circumferential moduli, failure strain and failure stress.

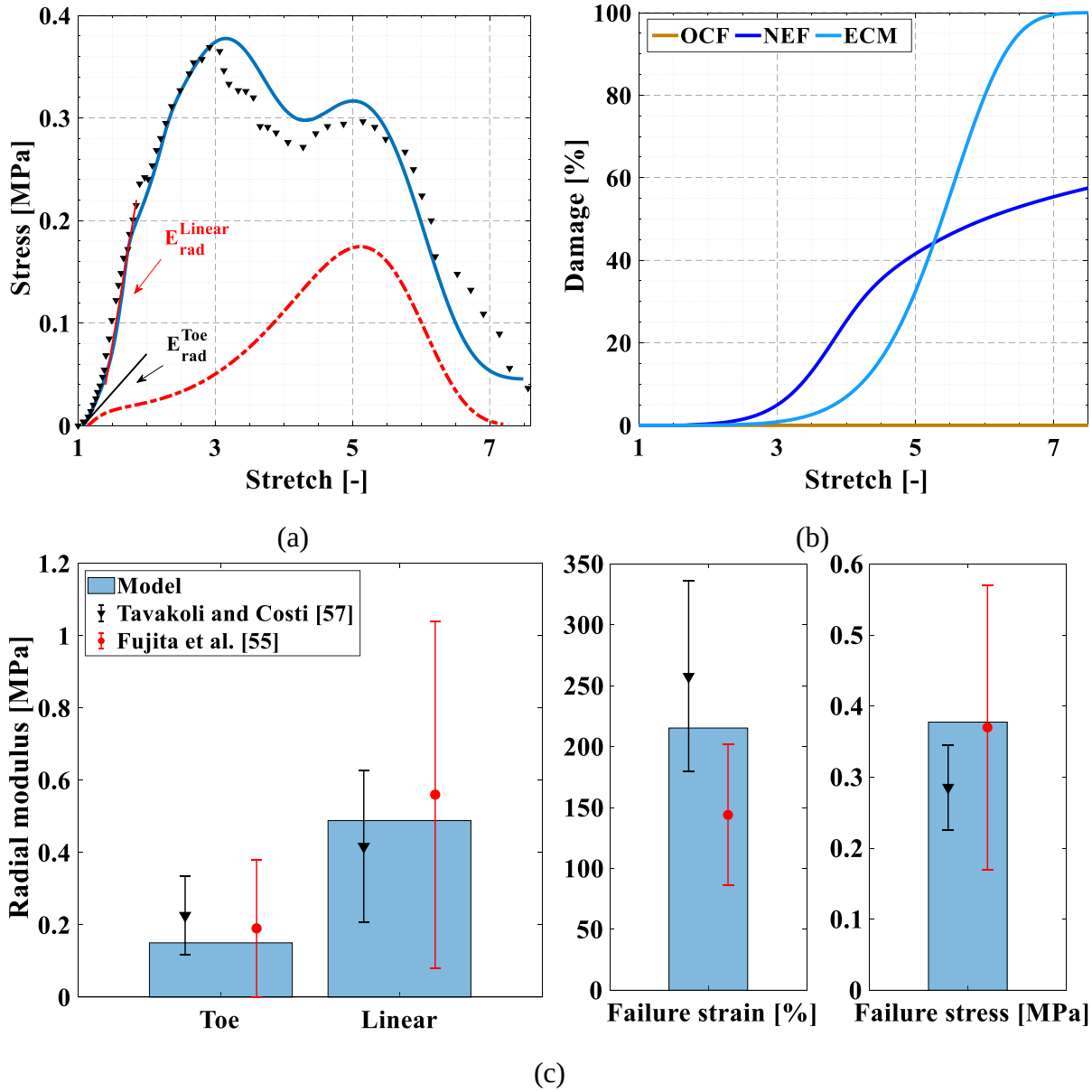

Figure II.9. UA radial stretching of the multi-layered material element: (a) stress-stretch response (solid line: model; dashed line: model without NEF activation, symbols: experimental data of Tavakoli and Costi (2018)), (b) local damage events in the different solid constituents, (c) toe and linear radial moduli, failure strain and failure stress.

Figure II.9a shows the UA macro-stress response in the radial direction. A fairly good agreement between the experimental data of Tavakoli and Costi (2018) and the model result is shown in Figure II.9a, and that, until complete loss of tissue integrity. Although the data of Tavakoli and Costi (2018) concern bovine annulus, Figure II.9c points out that both moduli and ultimate properties of human annulus, taken from the work of Fujita et al. (1997), are also well reproduced by the model using

the same set of parameters. Stretching in the radial direction shows a different behavior to that exhibited in the circumferential direction. This directional effect is observed both in the stress response and in the damage mechanisms. The radial stretchability of the annulus is considerably higher than the circumferential stretchability. The maximum stress is observed at a strain of approximately 200%. Because they are load-bearing elements in the radial direction, the onset of damage is earlier in NEF than in ECM as shown in Figure II.9b. In this direction, OCF experiences no damage. The increase in damage amount of NEF causes a decrease in stiffness until the observable peak stress at approximately 0.37 MPa. After the peak stress, both undamaged NEF and ECM continue to resist the applied stretching until the appearance of a second local peak stress at a strain of approximately 400%. Figure II.9c presents the moduli and the ultimate properties.

As shown in Figure II.10 the local stress response in fibrils differs according to the macroscopic stretching direction. In physics, the localization and concentration of the maximum stress in fibrils is highly dependent on the regional variation of the orientation of the bundles of fibrils, i.e. inter-fibrillar and inter-lamellar fibrils, respectively, in LM and ILM zones.

The model is also used to analyze the macroscopic failure behavior. The annulus is uniaxially stretched till failure along a loading direction successively tilted from the circumferential direction to the radial direction. The failure state is identified as the maximum stress corresponding to the first local failure detected. The computed ultimate points in terms of effective stress and maximum principal strain are reported in Figure II.11 such that failure envelops are formed. A global view at these plots shows a strong directional effect on the macroscopic ultimate properties due to the layered LM/ILM organization and to the anisotropic local response of the collagen network in the LM and ILM zones. The respective role of the collagen network and the chemical effect on the UA failure response is identified in Figure II.11.

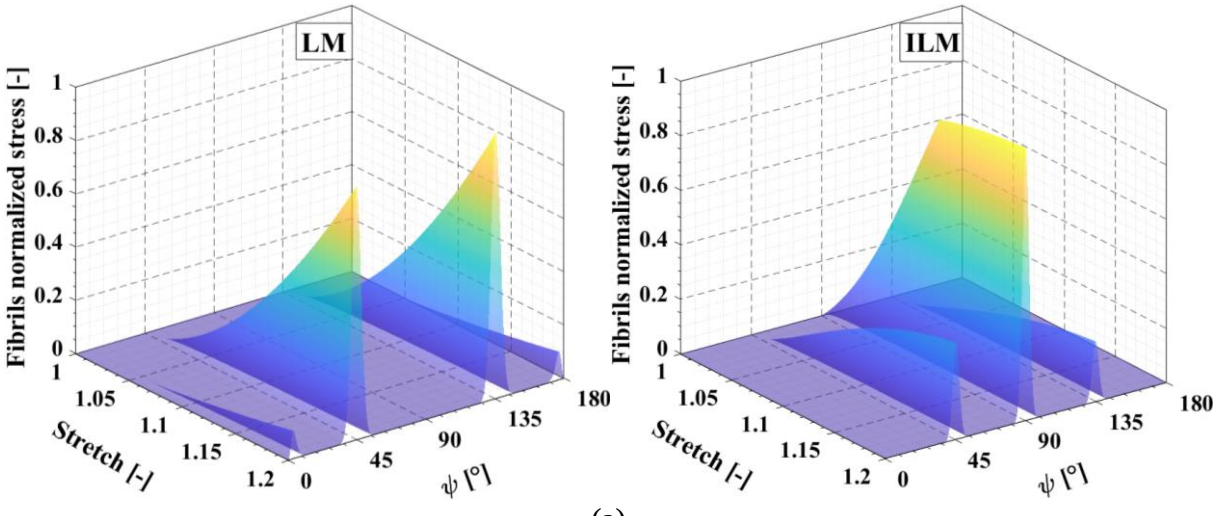

(a)

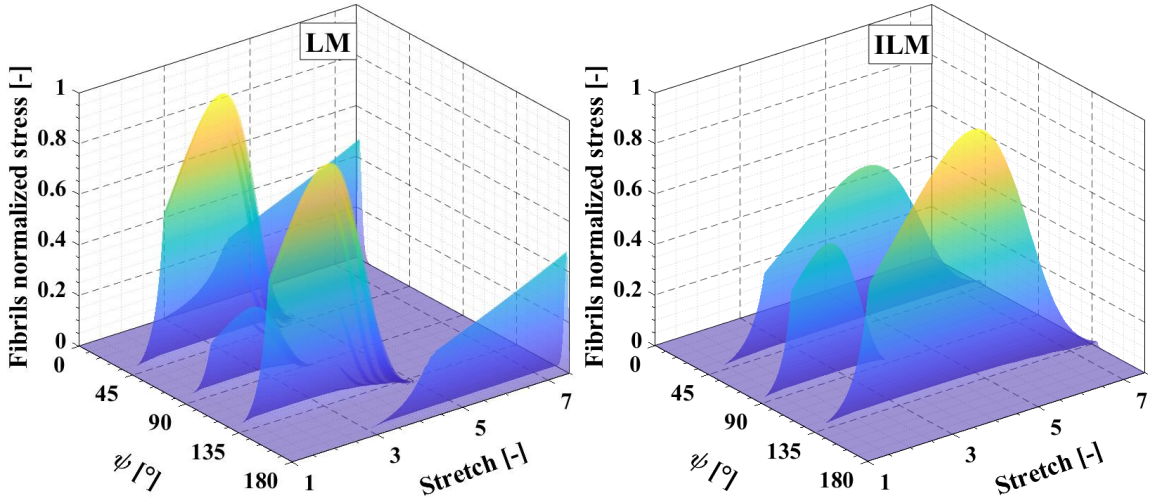

(b)

Figure II.10. Local NEF stress maps under (a) UA circumferential stretching and (b) UA radial stretching.

A deeper understanding of the annulus mechanics till final failure is brought by our modeling approach. The NEF supports the inter-layer connection and makes the annulus stiff especially in the radial direction. As illustrated in Figure II.9a when the NEF influence is neglected in the model a weak annulus resistance is obtained in the radial direction and a single peak stress is observed. By contrast, in the circumferential direction, no significant change is pointed out in the failure response as shown in Figure II.11. Nonetheless, as the stretching direction approaches radially, the annulus becomes much softer, with low failure stresses and high failure strains.

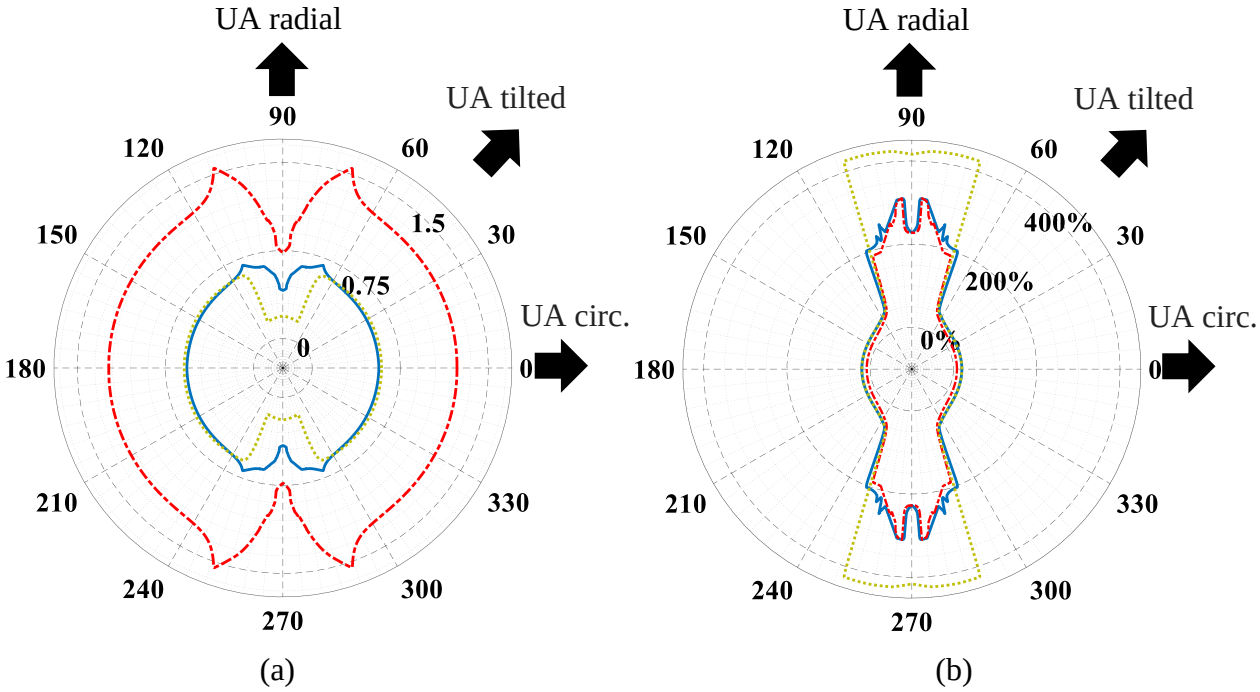

Figure II.11. UA failure envelopes: (a) effective stress [MPa] and (b) maximum principal strain [%] (continuous blue line: model, dashed yellow line: model without NEF, dashed red line: model without chemical effect).

II.3.3. Biaxial stretching path

The biaxiality effects on the annulus stress-stretch curves till failure are presented in Figure II.12 for different biaxial states. As far as we know, no experimental data are available in the literature when circumferential stretching and radial stretching are combined. These results are for predictive purpose only. The computed results are shown for different strain loading ratios (= circumferential strain : radial strain, {1:0, 0:1, 1:0.5, 1:1 and 1:2}). The stiffness and ultimate properties are strongly influenced by the biaxial stretch ratio with a larger effect on the radial behavior than on the circumferential one. The radial stretchability of the annulus is considerably decreased under a biaxial stretching state. The difference in circumferential and radial behaviors is connected to the difference in how local failure occurs due to the collagen orientation.

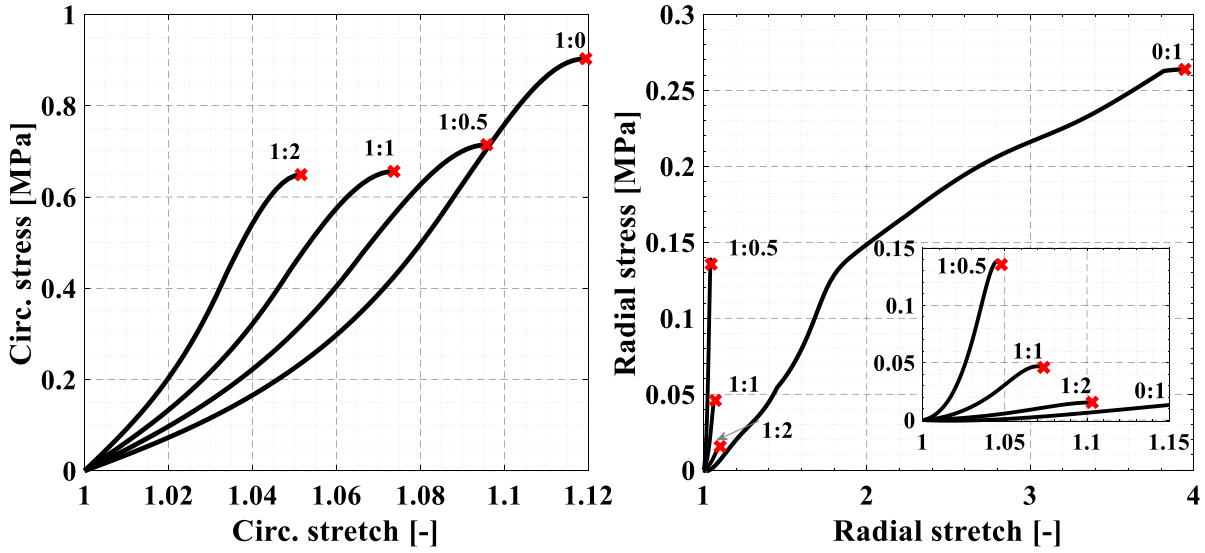

(a) (b)

Figure II.12. Biaxial stretching of the multi-layered material element for different biaxiality ratios: (a) circumferential stress-stretch response, (b) radial stress-stretch response.

The model takes into consideration the directional effects along with electro-chemical activity reproduced thought the volumetric effects. It can be employed to study how individual failure of the annulus components acts on the overall progressive failure under biaxial loading. The macro-stretches at failure are presented in Figure II.13 under a wide range of biaxial loading conditions such that a failure envelope is obtained. Again, the retained criterion is the nucleation of the local failure macroscopically identified by the maximum stress. The biaxial failure envelopes are normalized by their maximal stretch values. Different microstructure cases are considered and important insights are observed. When the collagen network is not considered, the failure is governed by the isotropic ECM and a symmetric failure envelope with respect to the main bisectrix is obtained. The symmetry is lost for the other cases. Both collagen network and LM/ILM organization significantly impact the ultimate properties by conferring a directional effect on the failure envelope.

Both tilted and biaxial stretching help us to better understand the chemo-mechanical-damage behavior of the annulus till failure in relation to the hierarchical organization of all discrete solid components.

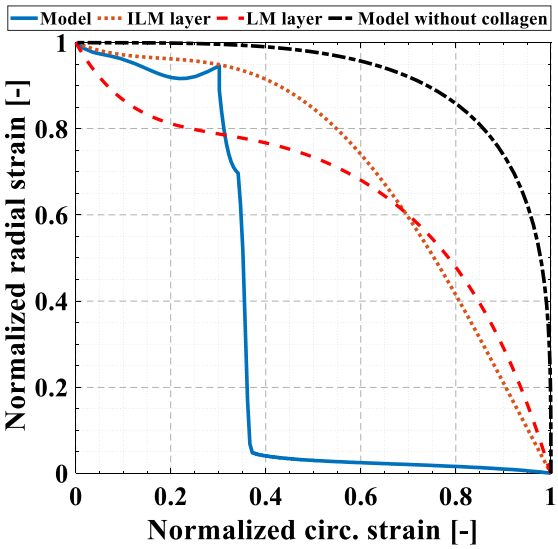

Figure II.13. Biaxial failure envelope.

II.3.4.Shearing path

To illustrate further the predictive capability of the model, the numerical results are compared to the annulus shearing data extracted from the literature in Figures II.14 and II.15. The predicted stress-strain curve is found in acceptable agreement with the typical experimental curve of Tavakoli and Costi (2018) in Figure II.14, highlighting the predictive capabilities of the model. Recall that this typical curve is taken from bovine annulus.

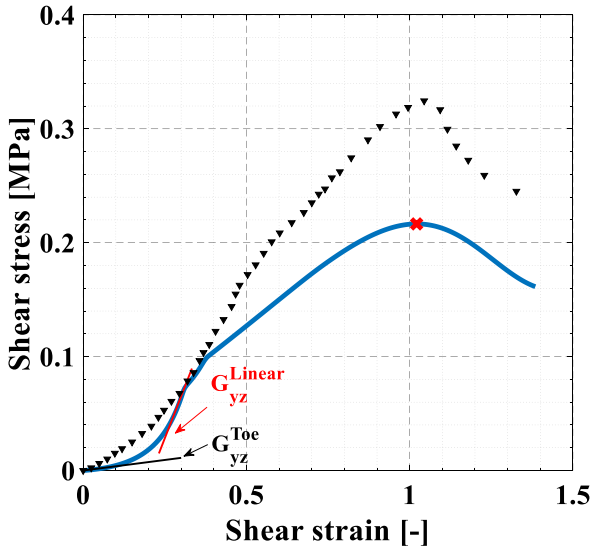

Figure II.14. Shearing of the multi-layered material element (continuous line: model, symbols: experimental data of Tavakoli and Costi (2018)).

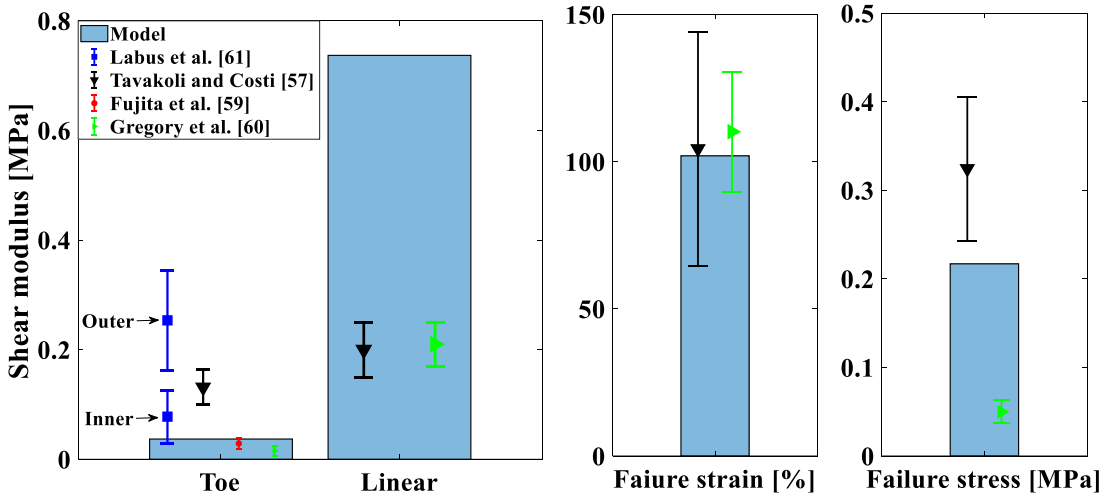

(a) (b) (c)

Figure II.15. Shearing of the multi-layered material element: (a) Toe and linear shear moduli, (b) failure strain and (c) failure stress.

The numerical shear modulus is calculated in the toe and linear regions and reported in Figure II.15a. It is compared to shear values reported in other papers considering different species: Fujita et al. (2000) for human, Gregory et al. (2011) for porcine and Labus et al. (2014) for bovine. Except Labus et al. (2014), the precise annulus position is not provided. The model prediction of the toe shear modulus is found in acceptable agreement with that of the inner annulus from (Labus et al., 2014); it is lower than the outer annulus since collagen content and layers dimensions are smaller. The Tavakoli and Costi (2018) toe shear data, that is between the inner and outer values of Labus et al. (2014), is underestimated by the model prediction. By contrast, the model is in good agreement with the value of Fujita et al. (2000). The model overestimates the values of Gregory et al. (2011) in the toe and linear regions. But for the shearing failure strain, it falls within the experimental standard deviation intervals of Gregory et al. (2011) as shown in Figure II.15b. However, the shearing failure stress of Gregory et al. (2011) is largely overestimated as shown in Figure II.15c. Although the predicted failure stress is found smaller than the Tavakoli and Costi (2018) shearing data, the predicted failure strain is in excellent agreement with the experiments. Like a loading in radial stretching, the important role of NEF to keep the integrity of the inter-layer connection is shown again.

II.4. Concluding remarks

In the present chapter, a novel human annulus multiscale model was proposed to constitutively relate the structure at different scales (tangled ECM, network of nano-sized fibrils/micro-sized fibers and multi-layered LM/ILM organization) and the multiaxial macroscopic response till failure in connection to volumetric effects and damage mechanisms. It was shown that the model captures quantitatively experimental observations including directional effects upon different loading histories. The model provides a useful tool for annulus failure estimate in relation to complex interactions between external loading mode, structure features, damage events and hydration.

For future works, the annulus regional microstructure will be implemented in an axisymmetric version of the present (multiscale and multiaxial) model in the main goal to predict anisotropic damage and failure in a complete intervertebral disc model including nucleus-annulus interaction.

Appendix II.A. Deformation gradients

II.A.1. Chemical-induced swelling

The hydration effect is considered in our modeling approach. Under a free-swelling, the deformation gradients of a layer *i* are:

$$\begin{aligned} \mathbf{F}_{mech}^{i} &= \mathbf{I} \\ \mathbf{F}_{chem}^{i} &= \mathrm{diag}\left(\lambda_{chem\_x}^{i}, \lambda_{chem\_y}^{i}, \lambda_{chem\_z}^{i}\right) \quad i = 1, 2, ...m \end{aligned} \tag{II.A1}$$

in which $\lambda_{chem\_x}^{i}$, $\lambda_{chem\_y}^{i}$ and $\lambda_{chem\_z}^{i}$ are the chemical stretches in the ***x***, ***y*** and ***z*** directions, respectively.

No fluid transfer occurs under shearing, i.e., $\mathbf{F}_{chem}^{i} = \mathbf{I}$. Under UA or biaxial stretching, the chemical deformation gradient is empirically expressed as follows:

$$\mathbf{F}_{chem}^{i} = \mathbf{I} + \mathrm{diag}\left(\xi_{x}^{i}\chi_{x}^{i}\cos\omega,\ \xi_{y}^{i}\chi_{y}^{i}\cos\omega,\ \xi_{z}^{i}\chi_{z}^{i}\right) \tag{II.A2}$$

Such that the chemical-induced volumetric strain ε_{chem}^{i} is given by:

$$\varepsilon_{chem}^{i} = \left(1+\xi_x^i \chi_x^i \cos\omega\right)\left(1+\xi_y^i \chi_y^i \cos\omega\right)\left(1+\xi_z^i \chi_z^i\right) - 1 \quad \text{(II.A3)}$$

where ω is a coefficient that changes according to the loading mode.

Guided by the experimental observations of Baldit (2013) and Derrouiche et al. (2020b) on circumferentially stretched annulus specimens, the chemical deformation gradient (II.A2) was initially proposed in the previous chapter. The term ω is introduced here to consider the loading angle effect on tilted stretching behavior and on biaxial stretching behavior.

For tilted stretching, the term ω is given by:

$$\omega = \gamma \quad \text{(II.A4)}$$

in which γ is the angle between the loading direction and the circumferential direction.

For biaxial stretching, the term ω is geometrically deduced from the biaxiality ratio:

$$\omega = \text{acrtan}\left(\left(\lambda_{rad}-1\right)/\left(\lambda_{circ}-1\right)\right) \quad \text{(II.A5)}$$

in which λ_{circ} and λ_{rad} are the applied stretches in the circumferential and radial directions, respectively.

The terms ξ_x^i, ξ_y^i and ξ_z^i are the chemical expansions at the equilibrium state and, χ_x^i , χ_y^i and χ_z^i are functions of time (chapter I):

$$\chi_x^i = 1-\exp\left(-t/\tau_x^i\right),\ \chi_y^i = 1-\exp\left(-t/\tau_y^i\right) \text{ and } \chi_z^i = 1-\exp\left(-t/\tau_z^i\right) \quad \text{(II.A6)}$$

where τ_x^i, τ_y^i and τ_z^i are the chemical expansion rates.

In what follows, the mechanical deformation gradients of each loading case, given in Figure II.5, are separately provided.

II.A.2. UA stretching path

The UA stretching of the multi-layered material element can be carried out along the circumferential direction, along the radial direction or along a direction tilted by an angle γ with respect to the

circumferential direction. The mechanical deformation gradients may be expressed as a function of the applied stretch λ and the stretch in the fiber direction λ_f:

$$\mathbf{F}_{mech}^{LM\_i} = \mathbf{R}_y^{\gamma}.\left[\mathbf{R}_z^{\theta\_i}.\mathrm{diag}\left(\lambda_f, \lambda_f^{-1/2}, \lambda_f^{-1/2}\right).\mathbf{R}_z^{\theta\_i{}^T}\right].\mathbf{R}_y^{\gamma\,T} \quad i = 1,3,...m \tag{II.A7}$$

in LM layer and,

$$\mathbf{F}_{mech}^{ILM\_i} = \mathbf{R}_y^{\gamma}.\mathrm{diag}\left(\frac{\lambda}{\lambda_{chem\_x}^i}, \left(\frac{\lambda}{\lambda_{chem\_x}^i}\right)^{-1/2}, \left(\frac{\lambda}{\lambda_{chem\_x}^i}\right)^{-1/2}\right).\mathbf{R}_y^{\gamma\,T} \quad i = 2,4,...m-1 \tag{II.A8}$$

in ILM layer.

The quantities $\mathbf{R}_z^{\theta\_i}$ and $\mathbf{R}_y^{\gamma}$ are the basis-change tensor in each layer, with a rotation θ^i around the ***z***-axis and stretch direction γ around the ***y***-axis, respectively:

$$\mathbf{R}_z^{\theta\_i} = \begin{bmatrix} \cos\theta^i & \sin\theta^i & 0 \\ -\sin\theta^i & \cos\theta^i & 0 \\ 0 & 0 & 1 \end{bmatrix} \text{ and } \mathbf{R}_y^{\gamma} = \begin{bmatrix} \cos\gamma & 0 & -\sin\gamma \\ 0 & 1 & 0 \\ \sin\gamma & 0 & \cos\gamma \end{bmatrix} \tag{II.A9}$$

After a series of lengthy but straightforward derivations, we get the mechanical deformation gradients under UA stretching path:

$$\mathbf{F}_{mech}^{LM\_i} = \begin{bmatrix} \dfrac{\lambda\cos^2\gamma}{\lambda_{chem\_x}^i} + \dfrac{\sin^2\gamma}{\sqrt{S_2^i}} & S_3^i\cos\gamma & \cos\gamma\sin\gamma\left(\dfrac{\lambda}{\lambda_{chem\_x}^i} - \dfrac{1}{\sqrt{S_2^i}}\right) \\ S_3^i\cos\gamma & \dfrac{\lambda_{chem\_x}^i}{\lambda}\left(\sqrt{S_2^i} + S_3^{i\,2}\right) & S_3^i\sin\gamma \\ \cos\gamma\sin\gamma\left(\dfrac{\lambda}{\lambda_{chem\_x}^i} - \dfrac{1}{\sqrt{S_2^i}}\right) & S_3^i\sin\gamma & \dfrac{\lambda\sin^2\gamma}{\lambda_{chem\_x}^i} + \dfrac{\cos^2\gamma}{\sqrt{S_2^i}} \end{bmatrix} \tag{II.A10}$$

in LM layer and,

$$\mathbf{F}_{mech}^{ILM\_i}=\begin{bmatrix} \dfrac{\lambda\cos^2\gamma}{\lambda_{chem\_x}^{i}}+\dfrac{\sin^2\gamma}{\sqrt{\dfrac{\lambda}{\lambda_{chem\_x}^{i}}}} & 0 & \cos\gamma\sin\gamma\left(\dfrac{\lambda}{\lambda_{chem\_x}^{i}}-\dfrac{1}{\sqrt{\dfrac{\lambda}{\lambda_{chem\_x}^{i}}}}\right) \\ 0 & \dfrac{1}{\sqrt{\dfrac{\lambda}{\lambda_{chem\_x}^{i}}}} & 0 \\ \cos\gamma\sin\gamma\left(\dfrac{\lambda}{\lambda_{chem\_x}^{i}}-\dfrac{1}{\sqrt{\dfrac{\lambda}{\lambda_{chem\_x}^{i}}}}\right) & 0 & \dfrac{\lambda\sin^2\gamma}{\lambda_{chem\_x}^{i}}+\dfrac{\cos^2\gamma}{\sqrt{\dfrac{\lambda}{\lambda_{chem\_x}^{i}}}} \end{bmatrix} \quad \text{(II.A11)}$$

in ILM layer.

The terms S_1^i, S_2^i and S_3^i are given by:

$$\begin{aligned} S_1^i &= \left(\sqrt{\frac{\tan^4\theta^i}{4}-\left(\frac{\lambda}{\lambda_{chem\_x}^{i}}\frac{1}{3\cos^2\theta^i}\right)^3}-\frac{\tan^2\theta^i}{2}\right)^{1/3} \\ S_2^i &= \left(S_1^i+\frac{\lambda}{\lambda_{chem\_x}^{i}}\frac{1}{3S_1^i\cos^2\theta^i}\right)^2 \\ S_3^i &= \cos\theta^i\sin\theta^i\left(S_2^i-\frac{1}{\sqrt{S_2^i}}\right) \end{aligned} \quad \text{(II.A12)}$$

II.A.3. Biaxial stretching path

The biaxial mechanical deformation gradients may be expressed as a function of the stretches in the fiber axes $\lambda_{f_{x_1}}$, $\lambda_{f_{x_2}}$ and $\lambda_{f_{x_3}}$:

$$\mathbf{F}_{mech}^{LM\_i}=\mathbf{R}_z^{\theta\_i}.\mathrm{diag}\left(\lambda_{f_{x_1}},\lambda_{f_{x_2}},\lambda_{f_{x_3}}\right).\mathbf{R}_z^{\theta\_i^T} \quad i=1,3,...m \quad \text{(II.A13)}$$

in LM layer and,

$$\mathbf{F}_{mech}^{ILM\_i}=\mathrm{diag}\left(\frac{\lambda_{circ}}{\lambda_{chem\_x}^{i}},\frac{\lambda_{chem\_x}^{i}\lambda_{chem\_z}^{i}}{\lambda_{circ}\lambda_{rad}},\frac{\lambda_{rad}}{\lambda_{chem\_z}^{i}}\right) \quad i=2,4,...m-1 \quad \text{(II.A14)}$$

in ILM layer.

The mechanical deformation gradient in LM layer is given by:

$$\mathbf{F}_{mech}^{LM\_i} = \begin{bmatrix} \dfrac{\lambda_{circ}}{\lambda_{chem\_x}^{i}} & S_6^i & 0 \\ S_6^i & S_5^i & 0 \\ 0 & 0 & \dfrac{\lambda_{rad}}{\lambda_{chem\_z}^{i}} \end{bmatrix} \tag{II.A15}$$

The terms S_4^i, S_5^i and S_6^i are given by:

$$\begin{aligned} S_4^i &= \frac{\lambda_{circ}}{\lambda_{chem\_x}^{i}} - \sqrt{\left(\frac{\lambda_{cir}}{\lambda_{chem\_x}^{i}}\right)^2 - \frac{\lambda_{chem\_z}^{i}\left(2\cos\theta^i \sin\theta^i\right)^2}{\lambda_{rad}}} \\ S_5^i &= \tan^2\theta^i \left(\frac{\lambda_{circ}}{\lambda_{chem\_x}^{i}} + \frac{S_4^i\left(\tan^{-4}\theta^i - 1\right)}{2}\right) \\ S_6^i &= \frac{\lambda_{circ}\tan\theta^i}{\lambda_{chem\_x}^{i}} - \frac{S_4^i}{2\cos\theta^i \sin\theta^i} \end{aligned} \tag{II.A16}$$

II.A.4. Shearing path

The annulus under shearing is subjected to the following mechanical deformation gradients:

$$\mathbf{F}_{mech}^{LM\_i} = \mathbf{F}_{mech}^{ILM\_i} = \begin{bmatrix} 1 & 0 & 0 \\ 0 & 1 & \kappa \\ 0 & \kappa & 1 \end{bmatrix} \tag{II.A17}$$

where κ is the shear stretch.

Appendix II.B. Multi-layered annulus behavior

The mechanical Cauchy stress tensor $\boldsymbol{\sigma}_{mech}^{i}$ is written as follows:

$$\boldsymbol{\sigma}_{mech}^{LM\_i} = \boldsymbol{\sigma}_{ECM}^{i} + \boldsymbol{\sigma}_{OCF}^{LM\_i} + \boldsymbol{\sigma}_{NEF}^{LM\_i} \tag{II.B1}$$

in LM layer and,

$$\boldsymbol{\sigma}_{mech}^{ILM\_i} = \boldsymbol{\sigma}_{ECM}^{i} + \boldsymbol{\sigma}_{NEF}^{ILM\_i} \tag{II.B2}$$

in ILM layer.

The NEF Cauchy stress tensor $\boldsymbol{\sigma}_{NEF}^{i}$ is given by the sum of the Cauchy stress tensor $\boldsymbol{\sigma}_{NEF_{\psi}^{\eta}}^{i}$ of all discrete fibrils as follows:

$$\boldsymbol{\sigma}_{NEF}^{LM\_i}=\sum_{\eta}\sum_{\psi}\boldsymbol{\sigma}_{NEF_{\psi}^{\eta}}^{LM\_i}\ \text{ and }\ \boldsymbol{\sigma}_{NEF}^{ILM\_i}=\sum_{\eta=45,90,135}\sum_{\psi}\boldsymbol{\sigma}_{NEF_{\psi}^{\eta}}^{ILM\_i} \tag{II.B3}$$

In Eq. (II.14), the derivation may be expressed as follows:

$$\frac{\partial W_{mech}^{i}}{\partial \mathbf{C}_{mech}^{i}}=\frac{\partial W_{mech}^{i}}{\partial \bar{I}_{1}^{i}}\frac{\partial \bar{I}_{1}^{i}}{\partial \mathbf{C}_{mech}^{i}}+\frac{\partial W_{mech}^{i}}{\partial \bar{I}_{4\theta}^{i}}\frac{\partial \bar{I}_{4\theta}^{i}}{\partial \mathbf{C}_{mech}^{i}}+\frac{\partial W_{mech}^{i}}{\partial \bar{I}_{4\psi}^{i}}\frac{\partial \bar{I}_{4\psi}^{i}}{\partial \mathbf{C}_{mech}^{i}} \tag{II.B4}$$

with

$$\frac{\partial \bar{I}_{1}^{i}}{\partial \mathbf{C}_{mech}^{i}}=\mathbf{I}\,,\ \frac{\partial \bar{I}_{4\theta}^{i}}{\partial \mathbf{C}_{mech}^{i}}=\boldsymbol{a}\otimes\boldsymbol{a}\ \text{ and }\ \frac{\partial \bar{I}_{4\psi}^{i}}{\partial \mathbf{C}_{mech}^{i}}=\boldsymbol{b}_{\psi}\otimes\boldsymbol{b}_{\psi} \tag{II.B5}$$

After a series of straightforward derivations, the different parts of the Cauchy stress tensor are given by:

$$\boldsymbol{\sigma}_{ECM}^{i}=\phi_{ECM\_d}^{i}G_{ECM}\mathbf{F}_{mech}^{i}.\mathbf{F}_{mech}^{i^{T}}-p^{i}\mathbf{I} \tag{II.B6}$$

$$\begin{aligned}\boldsymbol{\sigma}_{OCF}^{LM\_i}&=H\left(\bar{I}_{4\theta}^{i}-1\right)\left[2\phi_{OCF\_d}^{i}\left(C_1\left(\bar{I}_{4\theta}^{i}-1\right)\exp\left(C_2\left(\bar{I}_{4\theta}^{i}-1\right)^{2}\right)\right)\right]\mathbf{F}_{mech}^{i}.\left(\boldsymbol{a}\otimes\boldsymbol{a}\right).\mathbf{F}_{mech}^{i^{T}} && \lambda_{OCF}^{i}<\lambda_{OCF}^{*}\\ \boldsymbol{\sigma}_{OCF}^{LM\_i}&=H\left(\bar{I}_{4\theta}^{i}-1\right)\left[2\phi_{OCF\_d}^{i}\left(C_3\left(\bar{I}_{4\theta}^{i}-\bar{I}_{4\theta}^{*}\right)+\zeta\right)\right]\mathbf{F}_{mech}^{i}.\left(\boldsymbol{a}\otimes\boldsymbol{a}\right).\mathbf{F}_{mech}^{i^{T}} && \lambda_{OCF}^{i}\geq\lambda_{OCF}^{*}\end{aligned} \tag{II.B7}$$

$$\begin{aligned}\boldsymbol{\sigma}_{NEF_{\psi}^{\eta}}^{LM\_i}&=H\left(\bar{I}_{4\psi}^{i}-1\right)\left[2\phi_{NEF}^{i}\phi_{\eta\_d}^{LM\_i}\left(C_4\left(\bar{I}_{4\psi}^{i}-1\right)\exp\left(C_5\left(\bar{I}_{4\psi}^{i}-1\right)^{2}\right)\right)\right]\mathbf{F}_{mech}^{i}.\left(\boldsymbol{b}_{\psi}\otimes\boldsymbol{b}_{\psi}\right).\mathbf{F}_{mech}^{i^{T}} && \lambda_{\psi}^{i}<\lambda_{NEF}^{*}\\ \boldsymbol{\sigma}_{NEF_{\psi}^{\eta}}^{LM\_i}&=H\left(\bar{I}_{4\psi}^{i}-1\right)\left[2\phi_{NEF}^{i}\phi_{\eta\_d}^{LM\_i}\left(C_6\left(\bar{I}_{4\psi}^{i}-\bar{I}_{4\psi}^{*}\right)+\zeta_{\psi}\right)\right]\mathbf{F}_{mech}^{i}.\left(\boldsymbol{b}_{\psi}\otimes\boldsymbol{b}_{\psi}\right).\mathbf{F}_{mech}^{i^{T}} && \lambda_{\psi}^{i}\geq\lambda_{NEF}^{*}\end{aligned} \tag{II.B8}$$

$$\begin{aligned}\boldsymbol{\sigma}_{NEF_{\psi}^{\eta}}^{ILM\_i}&=H\left(\bar{I}_{4\psi}^{i}-1\right)\left[2\phi_{NEF}^{i}\phi_{\eta\_d}^{ILM\_i}\left(C_4\left(\bar{I}_{4\psi}^{i}-1\right)\exp\left(C_5\left(\bar{I}_{4\psi}^{i}-1\right)^{2}\right)\right)\right]\mathbf{F}_{mech}^{i}.\left(\boldsymbol{b}_{\psi}\otimes\boldsymbol{b}_{\psi}\right).\mathbf{F}_{mech}^{i^{T}} && \lambda_{\psi}^{i}<\lambda_{NEF}^{*}\\ \boldsymbol{\sigma}_{NEF_{\psi}^{\eta}}^{ILM\_i}&=H\left(\bar{I}_{4\psi}^{i}-1\right)\left[2\phi_{NEF}^{i}\phi_{\eta\_d}^{ILM\_i}\left(C_6\left(\bar{I}_{4\psi}^{i}-\bar{I}_{4\psi}^{*}\right)+\zeta_{\psi}\right)\right]\mathbf{F}_{mech}^{i}.\left(\boldsymbol{b}_{\psi}\otimes\boldsymbol{b}_{\psi}\right).\mathbf{F}_{mech}^{i^{T}} && \lambda_{\psi}^{i}\geq\lambda_{NEF}^{*}\end{aligned} \tag{II.B9}$$

$$\boldsymbol{\sigma}_{chem}^{i}=\phi_{fluid}^{i}K_1\varepsilon_{chem\_d}^{i}\exp\left(K_2\varepsilon_{chem\_d}^{i^{2}}\right)\mathbf{I} \tag{II.B10}$$

where p^{i} is written from boundary conditions in each loading case:

$$p^{LM\_i} = \phi^i_{ECM\_d} G_{ECM} \left[\left(\frac{\lambda^i_{chem\_x}}{\lambda} \left(\sqrt{S_2^i} + S_3^{i\,2} \right) \right)^2 + S_3^{i\,2} \right] \text{ and } p^{ILM\_i} = \phi^i_{ECM\_d} G_{ECM} \left(\frac{\lambda^i_{chem\_x}}{\lambda} \right)^2 \quad \text{(II.B11)}$$

for UA stretching path,

$$p^{LM\_i} = \phi^i_{ECM\_d} G_{ECM} \left(S_5^{i\,2} + S_6^{i\,2} \right) \text{ and } p^{ILM\_i} = \phi^i_{ECM\_d} G_{ECM} \left(\frac{\lambda^i_{chem\_x} \lambda^i_{chem\_z}}{\lambda_{circ} \lambda_{rad}} \right)^2 \quad \text{(II.B12)}$$

for biaxial stretching path and,

$$p^i = \phi^i_{ECM\_d} G_{ECM} \left(\kappa^2 + 1 \right) \quad \text{(II.B13)}$$

for shearing path.

II. References

Acaroglu, E.R., Iatridis, J.C., Setton, L.A., Foster, R.J., Mow, V.C., Weidenbaum, M., 1995. Degeneration and aging affect the tensile behavior of human lumbar anulus fibrosus. Spine 20, 2690-2701.

Baldit, A., 2013. Etude des interactions hydro-chimio-mécaniques dans les tissus biologiques: application à la nutrition du disque intervertébral. Phd Thesis, University of Montpellier.

Blanco, S., Polindara, C.A., Goicolea, J.M., 2015. A regularised continuum damage model based on the mesoscopic scale for soft tissue. International Journal of Solids and Structures 58, 20-33.

Boos, N., Weissbach, S., Rohrbach, H., Weiler, C., Spratt, K.F., Nerlich, A.G., 2002. Classification of age-related changes in lumbar intervertebral discs. Spine 27, 2631-2644.

Calvo, B., Pena, E., Martinez, M.A., Doblare, M., 2007. An uncoupled directional damage model for fibred biological soft tissues. Formulation and computational aspects. International Journal for Numerical Methods in Engineering 69, 2036-2057.

de los Heros, P., Pacheco-Alvarez, D., Gamba, G., 2018. Role of WNK kinases in the modulation of cell volume. In Current Topics in Membranes 81, 207-235.

Derrouiche, A., Zaouali, A., Zaïri, F., Ismail, J., Chaabane, M., Qu, Z., Zaïri, F., 2019a. Osmo-inelastic response of the intervertebral disc. Proceedings of the Institution of Mechanical Engineers. Part H: Journal of Engineering in Medicine 233, 332-341.

Derrouiche, A., Zaïri, F., Zaïri, F., 2019b. A chemo-mechanical model for osmo-inelastic effects in the annulus fibrosus. Biomechanics and Modeling in Mechanobiology 18, 1773-1790.

Derrouiche, A., Feki, F., Zaïri, F., Taktak, R., Moulart, M., Qu, Z., Ismail, J., Charfi, S., Haddar, N., Zaïri, F., 2020a. How pre-strain affects the chemo-torsional response of the intervertebral disc. Clinical Biomechanics 76, 105020.

Derrouiche, A., Karoui, A., Zaïri, F., Ismail, J., Qu, Z., Chaabane, M., Zaïri, F., 2020b. The two Poisson's ratios in annulus fibrosus: relation with the osmo-inelastic features. Mechanics of Soft Materials 2, 1.

Ebara, S., Iatridis, J.C., Setton, L.A., Foster, R.J., Mow, V.C., Weidenbaum, M., 1996. Tensile properties of nondegenerate human lumbar anulus fibrosus. Spine 21, 452-461.

Feki, F., Taktak, R., Kandil, K., Derrouiche, A., Moulart, M., Haddar, N., Zaïri, F., Zaïri, F., 2020. How osmoviscoelastic coupling affects recovery of cyclically compressed intervertebral disc. Spine 45, 160553.

Fujita, Y., Duncan, N.A., Lotz, J.C., 1997. Radial tensile properties of the lumbar annulus fibrosus are site and degeneration dependent. Journal of Orthopaedic Research 15, 814-819.

Fujita, Y., Wagner, D.R., Biviji, A.A., Duncan, N.A., Lotz, J.C., 2000. Anisotropic shear behavior of the annulus fibrosus: effect of harvest site and tissue prestrain. Medical Engineering and Physics 22, 349-357.

Ghezelbash, F., Shirazi-Adl, A., Baghani, M., Eskandari, A.H., 2020a. On the modeling of human intervertebral disc annulus fibrosus: elastic, permanent deformation and failure responses. Journal of Biomechanics 102, 109463.

Ghezelbash, F., Eskandari, A.H., Shirazi-Adl, A., Kazempour, M., Tavakoli, J., Baghani, M., Costi, J.J., 2020b. Modeling of human intervertebral disc annulus fibrosus with complex multi-fiber networks. Acta Biomaterialia 123, 208-221.

Gregory, D.E., Veldhuis, J.H., Horst, C., Brodland, G.W., Callaghan, J.P., 2011. Novel lap test determines the mechanics of delamination between annular lamellae of the intervertebral disc. Journal of Biomechanics 44, 97-102.

Guizouarn, H., Motais, R., 1999. Swelling activation of transport pathways in erythrocytes: effects of Cl−, ionic strength, and volume changes. American Journal of Physiology-Cell Physiology 276, 210-220.

Han, W.M., Nerurkar, N.L., Smith, L.J., Jacobs, N.T., Mauck, R.L., Elliott, D.M., 2012. Multi-scale structural and tensile mechanical response of annulus fibrosus to osmotic loading. Annals of Biomedical Engineering 40, 1610-1621.

Han, S.K., Chen, C.W., Labus, K.M., Puttlitz, C.M., Chen, Y., Hsieh, A.H., 2016. Optical coherence tomographic elastography reveals mesoscale shear strain inhomogeneities in the annulus fibrosus. Spine 41, 770-777.

Holzapfel, G.A., Schulze-Bauer, C.A.J., Feigl, G., Regitnig, P., 2005. Single lamellar mechanics of the human lumbar anulus fibrosus. Biomechanics and Modeling in Mechanobiology 3, 125-140.

Holzapfel, G.A., Fereidoonnezhad, B., 2017. Modeling of damage in soft biological tissues. In Biomechanics of Living Organs 5, 101-123.

Iatridis, J.C., MacLean, J.J., Roughley, P.J., Alini, M., 2006. Effects of mechanical loading on intervertebral disc metabolism in vivo. The Journal of Bone and Joint Surgery 88, 41-46.

Iatridis, J.C., Godburn, K., Wuertz, K., Alini, M., Roughley, P.J., 2011. Region-dependent aggrecan degradation patterns in the rat intervertebral disc are affected by mechanical loading in vivo. Spine 36, 203-209.

Kandil, K., Zaïri, F., Derrouiche, A., Messager, T., Zaïri, F., 2019. Interlamellar-induced time-dependent response of intervertebral disc annulus: a microstructure-based chemo-viscoelastic model. Acta Biomaterialia 200, 75-91.

Kandil, K., Zaïri, F., Messager, T., Zaïri, F., 2020. Interlamellar matrix governs human annulus fibrosus multiaxial behavior. Scientific Reports 10, 19292.

Kiani, C., Chen, L., Wu, Y.J., Yee, A.J., Yang, B.B., 2002. Structure and function of aggrecan. Cell Research 12, 19-32.

Labus, K.M., Han, S.K., Hsieh, A.H., Puttlitz, C. M., 2014. A computational model to describe the regional interlamellar shear of the annulus fibrosus. Journal of Biomechanical Engineering 136, 0510091.

Li, W., 2016. Damage models for soft tissues: a survey. Journal of Medical and Biological Engineering 36, 285-307.

Li, K., Holzapfel, G.A., 2019. Multiscale modeling of fiber recruitment and damage with a discrete fiber dispersion method. Journal of the Mechanics and Physics of Solids 126, 226-244.

Melrose, J., Smith, S.M., Appleyard, R.C., Little, C.B., 2008. Aggrecan, versican and type VI collagen are components of annular translamellar crossbridges in the intervertebral disc. European Spine Journal 17, 314-324.

Osti, O.L., Vernon-Roberts, B., Moore, R., Fraser, R.D., 1992. Annular tears and disc degeneration in the lumbar spine: a post-mortem study of 135 discs. The Journal of Bone and Joint Surgery 74, 678-682.

Pena, E., Alastrue, V., Laborda, A., Martínez, M.A., Doblare, M., 2010. A constitutive formulation of vascular tissue mechanics including viscoelasticity and softening behaviour. Journal of Biomechanics 43, 984-989.

Pezowicz, C.A., Robertson, P.A., Broom, N.D., 2006a. The structural basis of interlamellar cohesion in the intervertebral disc wall. Journal of Anatomy 208, 317-330.

Pezowicz, C.A., Schechtman, H., Robertson, P.A., Broom, N.D., 2006b. Mechanisms of anular failure resulting from excessive intradiscal pressure: a microstructural-micromechanical investigation. Spine 31, 2891-2903.

Quapp, K.M., Weiss, J.A., 1998. Material characterization of human medial collateral ligament. Journal of Biomechanical Engineering 120, 757-763.

Rodriguez, J.F., Cacho, F., Bea, J.A., Doblaré, M., 2006. A stochastic-structurally based three dimensional finite-strain damage model for fibrous soft tissue. Journal of the Mechanics and Physics of Solids 54, 864-886.

Sarkadi, B., Parker, J.C., 1991. Activation of ion transport pathways by changes in cell volume. Biochimica et Biophysica Acta-Reviews on Biomembranes 1071, 407-427.

Schollum, M.L., Robertson, P.A., Broom, N.D., 2008. ISSLS prize winner: microstructure and mechanical disruption of the lumbar disc annulus: part I: a microscopic investigation of the translamellar bridging network. Spine 33, 2702-2710.

Shahraki, N.M., Fatemi, A., Agarwal, A., 2015. Failure Criteria for Prediction of Clinically Relevant Damage of Annulus Fibrosus. Spine Research 1, 1-7.

Sharabi, M., Wade, K., Haj-Ali, R., 2018. The mechanical role of collagen fibers in the intervertebral disc. In Biomechanics of the Spine 7, 105-123.

Skaggs, D.L., Weidenbaum, M., Iatridis, J.C., Ratcliffe, A., Mow, V.C., 1994. Regional variation in tensile properties and biochemical composition of the human lumbar anulus fibrosus. Spine, 19, 1310-1319.

Tamoud, A., Zaïri, F., Mesbah, A., Zaïri, F., 2021. A microstructure-based model for time-dependent mechanics of multi-layered soft tissues and its application to intervertebral disc annulus. Meccanica 56, 585-606.

Tang, H., Buehler, M.J., Moran, B., 2009. A constitutive model of soft tissue: from nanoscale collagen to tissue continuum. Annals of Biomedical Engineering 37, 1117-1130.

Tavakoli, J., Elliott, D.M., Costi, J.J., 2016. Structure and mechanical function of the inter-lamellar matrix of the annulus fibrosus in the disc. Journal of Orthopaedic Research 34, 1307-1315.

Tavakoli, J., Elliott, D.M., Costi, J.J., 2017. The ultra-structural organization of the elastic network in the intra-and inter-lamellar matrix of the intervertebral disc. Acta Biomaterialia 58, 269-277.

Tavakoli, J., Costi, J.J., 2018. New findings confirm the viscoelastic behaviour of the inter-lamellar matrix of the disc annulus fibrosus in radial and circumferential directions of loading. Acta Biomaterialia 71, 411-419.

Tavakoli, J., Diwan, A.D., Tipper, J.L., 2020a. The ultrastructural organization of elastic fibers at the interface of the nucleus and annulus of the intervertebral disk. Acta Biomaterialia 114, 323-332.

Tavakoli, J., Diwan, A.D., Tipper, J.L., 2020b. Elastic fibers: the missing key to improve engineering concepts for reconstruction of the nucleus pulposus in the intervertebral disc. Acta Biomaterialia 113, 407-416.

Urban, J.P., Roberts, S., 2003. Degeneration of the intervertebral disc. Arthritis Research and Therapy 5, 120-130.

Vergari, C., Mansfield, J., Meakin, J.R., Winlove, P.C., 2016. Lamellar and fibre bundle mechanics of the annulus fibrosus in bovine intervertebral disc. Acta Biomaterialia 37, 14-20.

Vergari, C., Mansfield, J.C., Chan, D., Clarke, A., Meakin, J.R., Winlove, P.C., 2017. The effects of needle damage on annulus fibrosus micromechanics. Acta Biomaterialia 63, 274-282.

Vernon-Roberts, B., Moore, R.J., Fraser, R.D., 2007. The natural history of age-related disc degeneration: the pathology and sequelae of tears. Spine 32, 2797-2804.

Volokh, K.Y., 2007. Hyperelasticity with softening for modeling materials failure. Journal of the Mechanics and Physics of Solids 55, 2237-2264.

Volokh, K.Y., 2011. Modeling failure of soft anisotropic materials with application to arteries. Journal of the Mechanical Behavior of Biomedical Materials 4, 1582-1594.

Werbner, B., Zhou, M., O'Connell, G., 2017. A novel method for repeatable failure testing of annulus fibrosus. Journal of Biomechanical Engineering 139, 1-7.

Werbner, B., Spack, K., O'Connell, G.D., 2019. Bovine annulus fibrosus hydration affects rate-dependent failure mechanics in tension. Journal of Biomechanics 89, 34-39.

Yang, B., O'Connell, G.D., 2019. Intervertebral disc swelling maintains strain homeostasis throughout the annulus fibrosus: a finite element analysis of healthy and degenerated discs. Acta Biomaterialia, 100, 61-74.

Yu, J., Peter, C., Roberts, S., Urban, J.P., 2002. Elastic fibre organization in the intervertebral discs of the bovine tail. Journal of Anatomy 201, 465-475.

Yu, J., Schollum, M.L., Wade, K.R., Broom, N.D., Urban, J.P., 2015. A detailed examination of the elastic network leads to a new understanding of annulus fibrosus organization. Spine 40, 1149-1157.

Zhou, M., Bezci, S.E., O'Connell, G.D., 2019. Multiscale composite model of fiber-reinforced tissues with direct representation of sub-tissue properties. Biomechanics and Modeling in Mechanobiology 19, 745-759.

Chapter III

Modeling multiaxial damage regional variation in human annulus fibrosus

Modeling multiaxial damage regional variation in human annulus fibrosus[8]

Abstract

In the present article, a fully three-dimensional human annulus fibrosus model is developed by considering the regional variation of the complex structural organization of collagen network at different scales to predict the regional anisotropic multiaxial damage of the intervertebral disc. The model parameters are identified using experimental data considering as elementary structural unit, the single annulus lamellae stretched till failure along the micro-sized collagen fibers. The multi-layered lamellar/inter-lamellar annulus model is constructed by considering the effective interactions between adjacent layers and the chemical-induced volumetric strain. The regional dependent model predictions are analyzed under various loading modes and compared to experimental data when available. The stretching along the circumferential and radial directions till failure serves to check the predictive capacities of the annulus model. Model results under simple shear, biaxial stretching and plane-strain compression are further presented and discussed. Finally, a full disc model is constructed using the regional annulus fibrosus model and simulations are presented to assess the most likely failed areas under disc axial compression.

Keywords: Annulus fibrosus; Regional dependence; Multiscale structure; Multiaxial damage and failure.

[8] This chapter is based on the following paper: Tamoud, A., Zaïri, F., Mesbah, A., Zaïri, F., 2021. Modeling multiaxial damage regional variation in human annulus fibrosus. Acta Biomaterialia 136, 375-388.

III.1. Introduction

The annulus fibrosus of the intervertebral disc is probably one of the most extraordinary composites that the nature produces. The annulus soft tissues exhibit an organized structural arrangement of collagen network at different scales of hierarchical organization (Yu et al., 2002; Pezowicz et al., 2006a, 2006b; Melrose et al.,2008; Schollum et al., 2008). The detailed information was only appreciated very recently (Han et al., 2012; Yu et al., 2015; Vergari et al., 2016; Han et al., 2016; Tavakoli et al., 2016, 2017, 2020a, 2020b). The structural arrangement of collagen network varies throughout the disc which leads to a regional variation of its mechanics. In this regards, various damage and failure mechanisms operate in the different disc regions (Osti et al., 1992; Boos et al., 2002; Vernon-Roberts et al., 2007). In order to prevent all kinds of sudden disc injuries, it is necessary to understand the failure risks considering the regional variation under various static loading conditions. Fruitful experimental studies have been undertaken over the years allowing the assessment of the annulus intrinsic constitutive response in relation to disc region and mechanical loading (Acaroglu et al., 1995; Ebara et al., 1996; Fujita et al., 1997; O'Connell et al., 2012). Modeling multiaxial damage regional variation in annulus can provide a better understanding of the failure onset and location in the disc, beyond experimental observations. Modeling mechanics of the healthy annulus was developed in several papers considering different approaches as physically realistic as possible, to name a few recently published (Derrouiche et al., 2019b; Kandil et al., 2019; Ghezelbash et al., 2021; Kandil et al., 2020; Castro and Alves, 2020; Komeili et al., 2021; Tamoud et al., 2021a; Zhou et al., 2019, 2021). The quantitative prediction of the annulus damage is less reported. Damage criteria were proposed to predict annulus failure under different loading conditions (Qasim et al., 2012, 2014; Shahraki et al., 2015; Subramani et al., 2020). Nevertheless, the interest of this approach is questionable because it is intrinsically decoupled from the intrinsic properties and disconnected from the real microstructure and its evolution. The progressive loss of collagen network integrity implies a damage accumulation in annulus (Tamoud et al., 2021b).

Proper description of damage and failure requires to consider the latter that can be introduced in continuum-based models. Mengoni et al. (2016) developed a damage model for the non-fibrillar matrix restricted to the anterior annulus stretched in the radial direction. Later, Gao et al. (2017) and Ghezelbash et al. (2020) proposed a damage model considering only the collagen fibers failure as local damage event. Tamoud et al. (2021b) developed a damage model considering the multiscale failure due to network hierarchical organization. The chemical-induced volumetric effects on the structure-damage relation were also introduced to consider the hydration state effects. Nonetheless, our previous work in (Tamoud et al., 2021b) disregards the regional variation while it is the prerequisite condition to any disc prediction. The directional effects due to the structural arrangement along with the regional dependence make damage prediction a challenging task that still remains largely an open issue. To date, no constitutive model has been proposed to predict the multiaxial mechanics of the annulus fibrosus while the regional dependence of the relation between structure and damage is taken into consideration.

The main objective of this work is to formulate a fully three-dimensional constitutive representation of the annulus fibrosus to capture the regional dependence of the structure-damage relation. In order to reproduce the multiaxial loadings as close as to those undergone in-vivo by the annulus fibrosus, the material representation considers the complex collagen network arrangement of each disc region. To consider the progressive deformation-induced changes in the tissue, the model introduces the stretch-induced network re-orientation as well as the network damage leading to final failure. The model is identified at the scale of single annulus lamellae stretched along the fibers main direction. The regional dependent model predictions are then analyzed under various loading modes at the scale of multi-lamellae and compared to experimental data when available. The human annulus constitutive model is finally used to predict the heterogeneous mechanics of a full disc model.

The outline of the present chapter is as follows. The constitutive model is fully described in Section III.2. Section III.3 presents the constitutive model identification and predictions. Full disc model predictions are presented and discussed in Section III.4. Finally, remarks and conclusions are given in Section III.5.

The following notation is used throughout the text. Tensors and vectors are respectively denoted by normal boldfaced letters and italicized boldfaced letters, while scalars and individual components of vectors and tensors are denoted by normal italicized letters. The superposed dot designates the time derivative.

III.2. Model formulation

We propose here a two-step strategy consisting in single lamellae identification followed by multi-lamellae multiaxial predictions as illustrated in Figure III.1. The required model parameters are identified on axial tests performed along the micro-sized collagen fibers of single annulus lamellae extracted from the different disc regions (AO: Anterior-Outer, AI: Anterior-Inner, PI: Posterior-Inner, PO: Posterior-Outer). Beyond taking into account the regional effect, this identification strategy is a valuable difference with our previous work (Tamoud et al., 2021b) in which the model identification had been performed at the scale of multi-lamellae. In this chapter, after its identification at the scale of single lamellae, the model is then verified by comparing its prediction with the experimental data of multi-lamellae performed under multiaxial loading. Uniaxial (UA), simple shear (SS), biaxial (BA) and plane-strain compression (PSC) tests are all being considered.

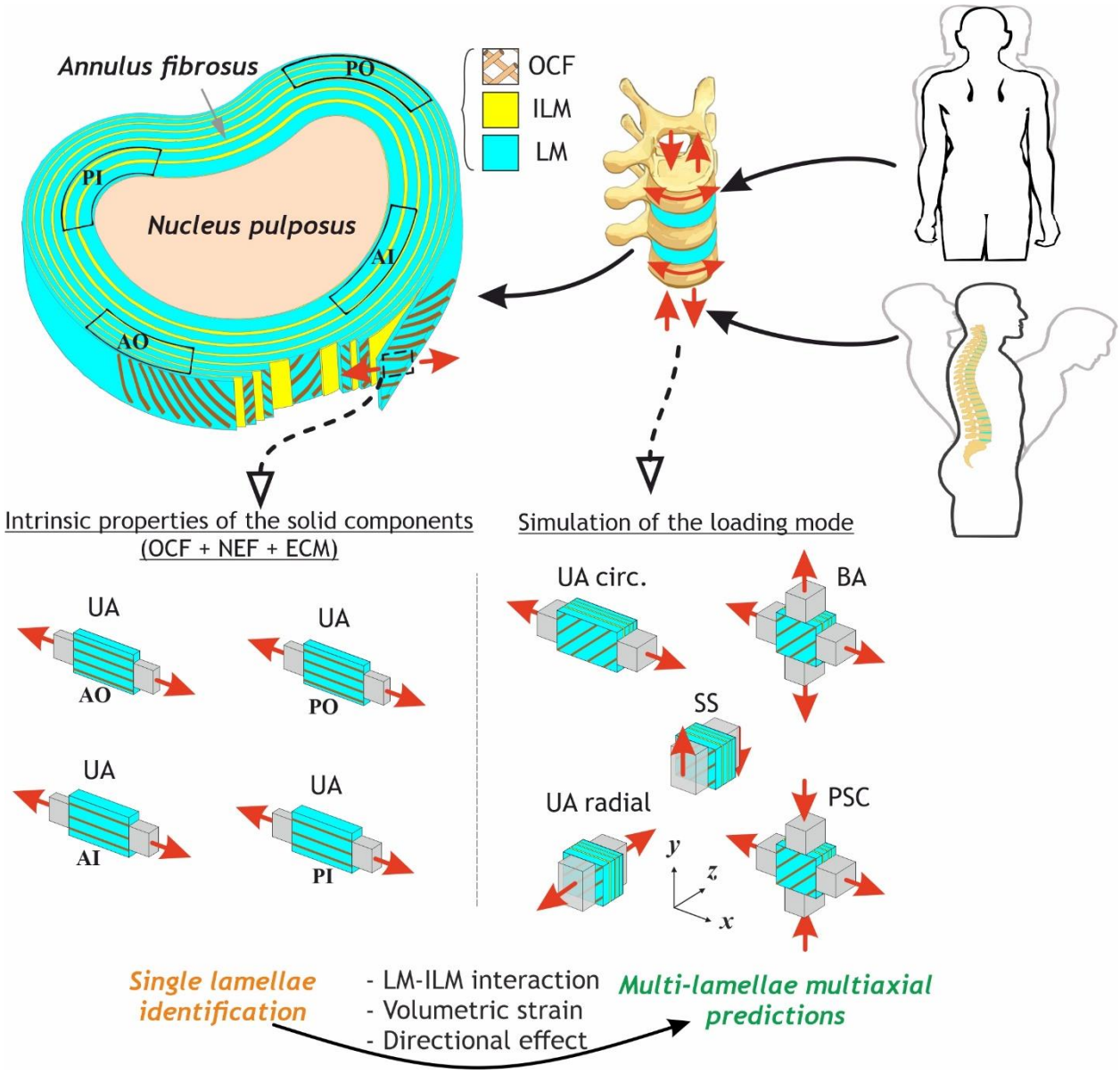

Figure III.1. Two-step strategy consisting in annulus model identification using single lamellae extracted from different disc regions followed by multi-lamellae annulus model predictions for multiaxial elementary loading modes representative of the spine movement.

III.2.1. Multiscale structure

The model considers the hierarchical organization of the solid phase starting from the nanoscale (Tavakoli et al., 2020a, 2020b) as well as its regional variation. As schematically represented in Figure III.2, the disc annulus is a multiple-network medium in which the organization in terms of orientation and distribution is regional dependent. The annulus consists in concentric lamellae (LM) reinforced by micro-sized type-I oriented collagen fibers (OCF). Two adjacent LM are connected

by an inter-lamellar (ILM) matrix. A network of nano-sized elastic fibers (NEF) connects both two OCF and two adjacent LM between them (Yu et al., 2002; Melrose et al., 2008). The network of OCF and NEF will be described geometrically with respect to the global benchmark of the disc, respectively, with the angle θ with respect to the circumferential direction and with the angle ψ with respect to the radial direction in the parallel plane of the fibers.

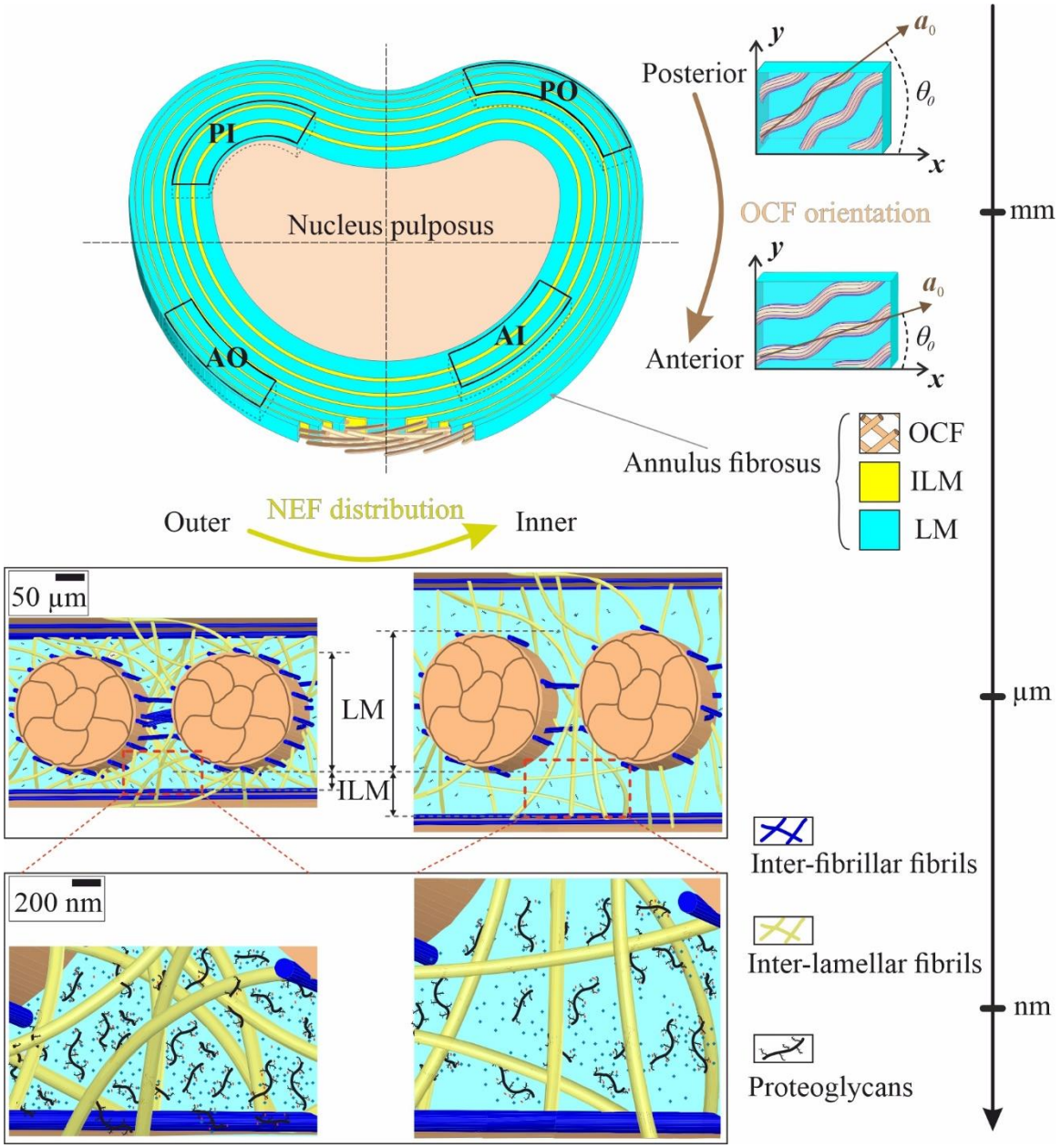

Figure III.2. Multiscale view of the intervertebral disc annulus. The organization, in terms of orientation and distribution, of this multiple-network medium is regional dependent.

Quantities and orientations of the constituents can be found in the Appendix III.A. The latter is based on well-documented papers for the four main disc regions (Skaggs et al., 1994; Acaroglu et al., 1995; Ebara et al., 1996; Holzapfel et al., 2005; Tavakoli et al., 2020a, 2020b).

III.2.2. Damaged free energy functions

The randomly oriented proteoglycan macromolecules of the extracellular matrix (ECM), the OCF and the (inter-fibrillar and inter-lamellar) NEF are all being considered to model the solid phase. Each individual component is assumed as isotropic, homogeneous, incompressible and hyperelastic body. During the mechanical loading, the initiation and propagation of damage occur through a continuous evolution over the entire loading history. A damage variable d is introduced to provide a mathematical description of the local damage events occurring within the collagen network. Their progressive evolution is given by an expression following a two-parameter Weibull statistical distribution governed by the internal stress:

$$d = 1 - \exp\left(-\left(\frac{\|\mathbf{P}\|}{\beta} \right)^{\alpha} \right) \tag{III.1}$$

in which α and β are two damage parameters and $\|\mathbf{P}\| = \sqrt{\mathrm{tr}\left(\mathbf{P}.\mathbf{P}^{T}\right)}$ is the Frobenius norm of the effective first Piola-Kirchhoff stress $\mathbf{P}$ of the individual solid component (ECM, OCF and NEF).

The damage variable d varies between 0 for the virgin state and can increase up to 1 in the case of fully damaged (cracking) state. It is taken as a monotonic increasing function of loading, i.e. the damage is considered as an irreversible phenomenon without possible recovery. Note that the anisotropy of the damage mechanisms developed in the annulus is due to the collagen network organization. The model is based on the general damage mechanics framework for the hyperelasticity theory that introduced hyperelastic laws derived from free energy functions (Lemaitre and Chaboche, 1994; Miehe, 1995). The mechanical free energy W_{mech} is expressed as a function of the ECM free energy W_{ECM} and the collagen networks free energies W_{θ} and W_{ψ} :

$$W_{mech} = \left(1-d_{ECM}\right)\phi_{ECM}W_{ECM} + \left(1-d_{\theta}\right)\phi_{OCF}W_{\theta} + \sum_{\psi}\left(1-d_{\psi}\right)\phi_{\psi}W_{\psi} \qquad \text{(III.2)}$$

where d_{ECM}, d_{θ} and d_{ψ} are the damage variables that degrade the internal stiffness of respective components, $\phi_{ECM} = \phi_{ECM\_0}/J_{chem}$ is the ECM volume fraction, $\phi_{OCF} = \phi_{OCF\_0}/J_{chem}$ is the OCF volume fraction, $\phi_{\psi} = \phi_{\eta}\phi_{NEF}$ is the fibrils volume fraction calculated using the NEF volume fraction $\phi_{NEF} = \phi_{NEF\_0}/J_{chem}$ in a layer and the volume fraction of fibril bundles ϕ_{η} in a layer dependent on η with $\sum_{\eta}\phi_{\eta} = 1$. The terms ϕ_{ECM_0}, ϕ_{OCF_0} and ϕ_{NEF_0} are the volume fractions at the chemical equilibrium state. The term J_{chem} is the chemical-induced volumetric change.

The set of free energies must be prescribed for each component of the solid phase. The simple Neo-Hookean formulation is employed for the ECM free energy W_{ECM}:

$$W_{ECM} = \frac{1}{2}G_{ECM}\left(\bar{I}_1 - 3\right) \qquad \text{(III.3)}$$

in which G_{ECM} is the ECM shear modulus and $\bar{I}_1 = \mathrm{tr}\left(\mathbf{C}_{mech}\right)$ is the first stretch invariant of the right Cauchy-Green deformation[9] $\mathbf{C}_{mech} = \mathbf{F}_{mech}^{T}.\mathbf{F}_{mech}$.

The collagen response exhibits 'toe' and 'linear' regions as described in Figure III.3. The 'toe' region is due to the collagen straightening during stretching that is followed by the "linear" region when the undulations disappear. The free energies W_{θ} and W_{ψ} are expressed by two distinct relations below and above $\lambda^{*}_{\theta,\psi}$ to describe the transition between 'toe' and 'linear' regions:

$$W_{\theta,\psi} = H\left(\bar{I}_{4\theta,\psi} - 1\right)\left[\frac{1}{2}\frac{C_1}{C_2}\left(\exp\left(C_2\left(\bar{I}_{4\theta,\psi} - 1\right)^2\right) - 1\right)\right] \quad \lambda_{\theta,\psi} < \lambda^{*}_{\theta,\psi} \qquad \text{(III.4)}$$

[9] The chemo-mechanical coupling is considered by the multiplicative decomposition of the total deformation gradient $\mathbf{F} = \mathbf{F}_{chem}.\mathbf{F}_{mech}$ into chemically-induced volumetric and mechanical parts $\mathbf{F}_{chem}$ and $\mathbf{F}_{mech}$.

$$W_{\theta,\psi} = H\left(\bar{I}_{4\theta,\psi} - 1\right)\left[\frac{C_3}{2}\left(\bar{I}_{4\theta,\psi} - \bar{I}^{*}_{4\theta,\psi}\right)^2 + \zeta_{\theta,\psi}\left(\bar{I}_{4\theta,\psi} - \nu_{\theta,\psi}\right)\right] \quad \lambda_{\theta,\psi} \geq \lambda^{*}_{\theta,\psi} \tag{III.5}$$

where C_1, C_2 and C_3 are material constants, $H(\bullet)$ is the Heaviside function, $\zeta_{\theta,\psi}$ and $\nu_{\theta,\psi}$ are functions that ensure continuity between 'toe' and 'linear' regions:

$$\zeta_{\theta,\psi} = C_1\left(\bar{I}^{*}_{4\theta,\psi} - 1\right)\exp\left(C_2\left(\bar{I}^{*}_{4\theta,\psi} - 1\right)^2\right) \tag{III.6}$$

$$\nu_{\theta,\psi} = \bar{I}^{*}_{4\theta,\psi} - \frac{C_1}{2C_2\zeta_{\theta,\psi}}\left(\exp\left(C_2\left(\bar{I}^{*}_{4\theta,\psi} - 1\right)^2\right) - 1\right) \tag{III.7}$$

The fourth stretch invariants $\bar{I}_{4\theta}$ and $\bar{I}_{4\psi}$ are given by:

$$\bar{I}_{4\theta} = \boldsymbol{a}.\mathbf{C}_{mech}.\boldsymbol{a} = \lambda_\theta^2 \text{ and } \bar{I}_{4\psi} = \boldsymbol{b}.\mathbf{C}_{mech}.\boldsymbol{b} = \lambda_\psi^2 \tag{III.8}$$

where $\boldsymbol{a}$ and $\boldsymbol{b}$ are the unit vectors expressed in the Cartesian coordinates by:

$$\boldsymbol{a} = \cos\theta\,\boldsymbol{x} + \left|\sin\theta\right|\boldsymbol{y} \text{ and } \boldsymbol{b} = \left|\cos\theta\cos\psi\right|\boldsymbol{x} + \left|\sin\theta\cos\psi\right|\boldsymbol{y} + \sin\psi\,\boldsymbol{z} \tag{III.9}$$

The term $\bar{I}^{*}_{4\theta,\psi}$ is the fourth stretch invariant for $\lambda_{\theta,\psi} = \lambda^{*}_{\theta,\psi}$. The two angles follow the following geometrical relations to consider stretch-induced re-orientation of the OCF and NEF networks:

$$\tan(\theta) = \tan(\theta_0)\frac{\lambda_y}{\lambda_x} \text{ and } \tan(\psi) = \begin{cases} \dfrac{\lambda_z}{\lambda_f}\tan(\psi_0) & \psi_0 \leq 90° \\ 180° + \dfrac{\lambda_z}{\lambda_f}\tan(\psi_0) & \psi_0 > 90° \end{cases} \tag{III.10}$$

where θ_0 and ψ_0 are the angles in the initial configuration, λ_x, λ_y and λ_z are the principal stretches, respectively, in the circumferential (***x***), axial (***y***) and radial (***z***) directions, and λ_f is the stretch in the OCF direction. The re-orientation allows to update the fourth invariant by considering the current fibers orientation in the deformed configuration (Karsaj et al., 2009; O'Connell et al., 2012; Ghezelbash et al., 2021).

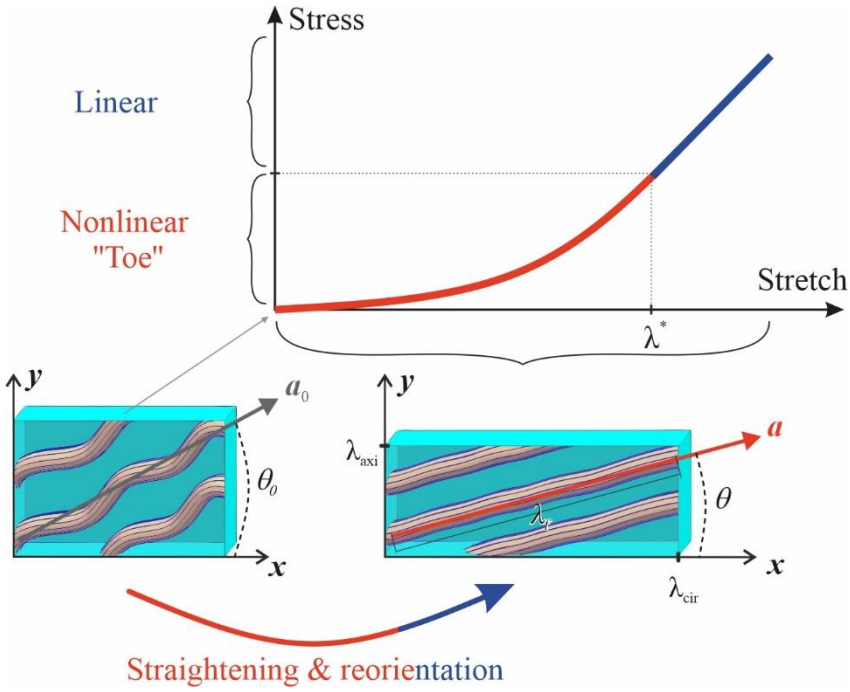

Figure III.3. Phenomenon of reorientation of collagen fibers.

The hydration state of the annulus soft tissues due to internal fluid content variation by osmosis has a considerable effect on the disc mechanics (Yang and O'Connell, 2019; Derrouiche et al., 2019a, 2020; Feki et al., 2020) and especially on the failure response (Werbner et al., 2019). The chemical free energy W_{chem} takes the following form (see chapter I):

$$W_{chem} = \phi_{fluid} \frac{1}{2} \frac{K_1}{K_2} \left(\exp\left(K_2 \varepsilon_{chem\_d}^2 \right) - 1 \right) \tag{III.11}$$

where $\phi_{fluid} = 1 - \phi_{ECM} - \phi_{OCF} - \phi_{FCN}$ is the volume fraction of the fluid phase, K_1 and K_2 are material constants, K_1 and K_1/K_2 being the initial and maximal volumetric stiffness values, respectively, and ε_{chem_d} is the damaged chemical-induced volumetric strain. The latter quantity must be connected to the damage accumulation due to progressive local failure events. The following relation is used (see chapter I):

$$\varepsilon_{chem\_d} = \varepsilon_{chem} \left(1 - d_{ECM} \right) \left(1 - d_{\theta} \right) \left(1 - \frac{1}{n} \sum_{\psi}^{n} d_{\psi} \right) \tag{III.12}$$

with $\varepsilon_{chem} = \det\left(\mathbf{F}_{chem}\right) - 1$.

In virtue of the chemo-mechanical coupling, the total free energy W can be additively split into a mechanical part W_{mech} and a chemical part W_{chem} : $W = W_{mech} + W_{chem}$. The multi-layered lamellar/inter-lamellar annulus model is constructed by considering the compatibility conditions to be respected between adjacent layers. Some details are provided in the Appendix III.B.

III.3. Simulation vs. experiments

In this section, after its identification using available experimental data, the predictability of the above-described model is discussed. The constitutive equations were coded in MATLAB software and reduced to different loading forms.

III.3.1. Single lamellae identification

The intrinsic constitutive response of the annulus under UA loading was experimentally determined by Skaggs et al. (1994) and Holzapfel et al. (2005) on single annulus lamellae stretched along the fibers main direction. Figure III.4 shows the computed results for the identification of the OCF properties for the different disc regions.

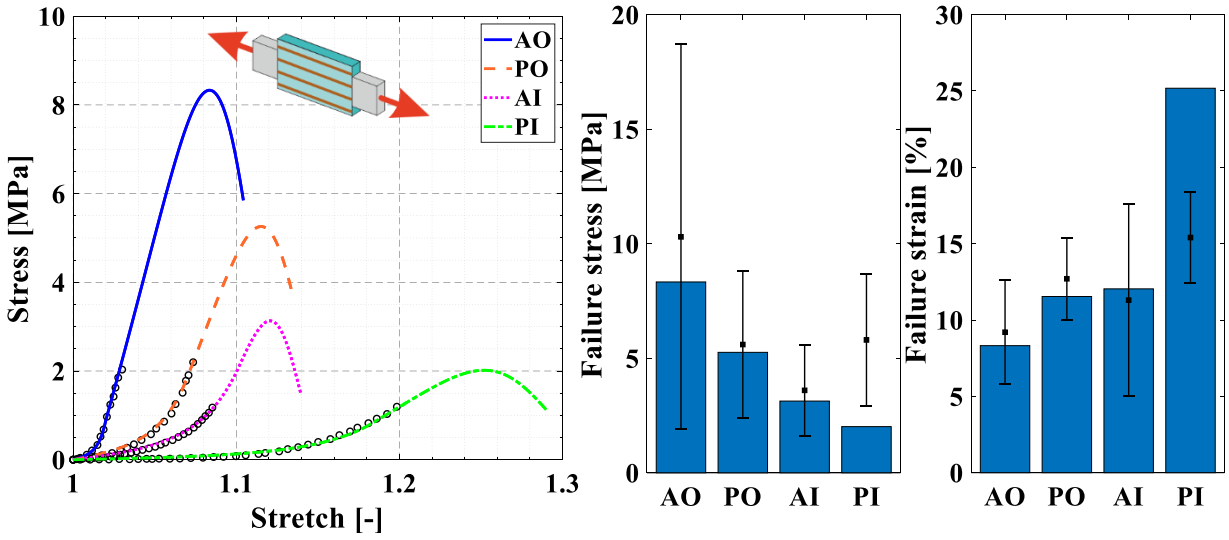

(a) (b)

Figure III.4. Single lamellae identification for the different disc regions: (a) stress-stretch responses (lines: model simulations, symbols: experimental data of Holzapfel et al. (2005)), (b) ultimate properties (bars: model simulations, symbols with standard deviation intervals: experimental data of Skaggs et al. (1994)).

The identification was performed numerically using the MATLAB software to minimize the following objective function:

$$F_{stress}^{obj} = \frac{1}{\rho}\sum_{h=1}^{\rho}\left(\frac{P_{mod}^{h} - \tilde{P}_{exp}^{h}}{\tilde{P}_{exp}^{h}}\right)^{2} \tag{III.13}$$

in which the letters with an overbar denote the experimental data with ρ the number of considered data points. Table III.1. provides the obtained values for the OCF properties. Note that the regional dependence of the single lamellae stiffness is explained by a difference in the initial undulated state and the OCF content (Skaggs et al., 1994; Holzapfel et al., 2005).

Parameters		Regions			
		AO	PO	AI	PI
C_1	[MPa]	40	26	26	3
C_2	[–]	880	58	30	11
C_3	[MPa]	500	300	400	80
λ_θ^*	[–]	1.02	1.07	1.1	1.14
α_{OCF}	[–]	5	5	5	5
β_{OCF}	[MPa]	215	125	120	70

Table III.1. OCF parameters.

This structural difference is reflected by distinct values. The other model parameters come from the previous chapter and are listed in Table III.2.

The simulated curves of the single lamellae are in good agreement with the experiments of Holzapfel et al. (2005). The results are shown until the complete loss of OCF load-bearing capability in order to compare the ultimate points with the experimental data of Skaggs et al. (1994). Except PI, it can be observed that the simulated stress and strain thresholds fall within the experimental standard deviation intervals.

Constituents	Parameters	Values	
ECM	G_{ECM}	0.01	[MPa]
	α_{ECM}	2	[−]
	β_{ECM}	5.5	[MPa]
NEF	C_1	12	[MPa]
	C_2	0.2	[−]
	C_3	1.5	[MPa]
	λ_ψ^*	1.7	[−]
	α_{NEF}	6	[−]
	β_{NEF}	400	[MPa]
Swelling	K_1	0.14	[MPa]
	K_2	0.0075	[−]

Table III.2. ECM, NEF and swelling parameters.

III.3.2.Multi-lamellae multiaxial predictions

Table III.3. presents the range of mechanical paths used to check the predictive capacities of the multi-lamellae model. It includes UA stretching in the circumferential direction, UA stretching in the radial direction, SS loading, BA stretching and PSC loading[10]. Except the latter loading (in which the sample is confined in the radial direction), the samples are loaded in specific directions while the others are free. All the samples are considered to be immersed in a physiological solution at a concentration of 0.15 M NaCl. When experimental data are available, a quantitative comparison with the model results is presented. The dimensions of the annulus specimens are given in Table III.3. for the different loading conditions and disc regions.

[10] These different loadings are representative of the disc mechanics. UA stretching along the circumferential direction and PSC are representative of the disc axial compression (Shah et al., 1978). UA stretching along the radial direction may be related to the disc shearing whereas SS may be related to the disc axial twist. BA stretching may be caused for example by a disc bending (i.e. flexion, extension and lateral flexion) (Costi et al., 2007).

Loading modes			Sample size $[mm^3]$ Anterior	Sample size $[mm^3]$ Posterior	Experimental data
Uniaxial (UA)	Circ.	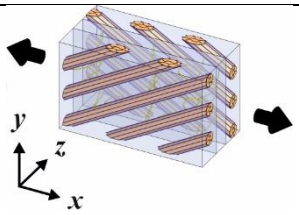	7×2×2	10×4×4	Acaroglu et al. (1995) and Ebara et al. (1996)
Uniaxial (UA)	Radial	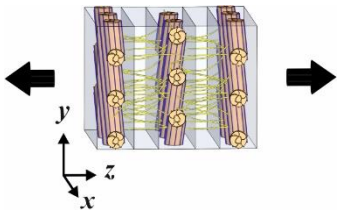	2×2×2	4×4×4	Fujita et al. (1997)
Simple shear (SS)		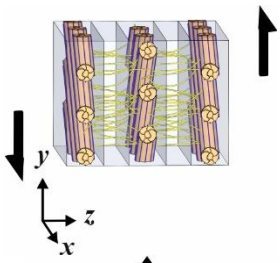	2×2×2	4×4×4	No available data
Biaxial (BA)	Axial-circ.	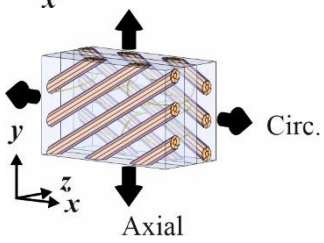	7×7×2	10×10×4	O'Connell et al. (2012)
Plane-strain compression (PSC)	Axial-circ.	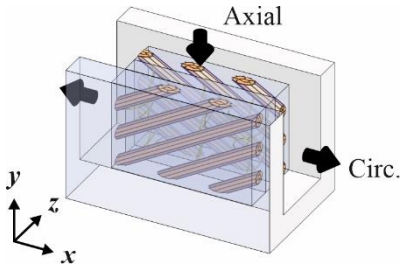	7×7×2	10×10×4	No available data

Table III.3. Loading modes for the multi-lamellae.

The multi-lamellae predictions are presented in Figures III.5 and III.6 for UA stretching along the circumferential direction. The simulated stress-stretch curves are compared with the typical experimental curves presented by Ebara et al. (1996) in Figure III.5a. Considering the important variability in the experimental annulus response and that these experimental data are typical results

(without statistical analysis), the model-experiments comparison can be considered as acceptable. In accordance with experiments, the outer regions have much higher stiffness than the inner regions, due mainly to regional variation in OCF angle. The simulations are conducted until stress drop corresponding to the failure stage. The simulated ultimate properties are reported in Figure III.5b and compared to the failure points with their standard deviation intervals extracted from the works of Acaroglu et al. (1995) and Ebara et al. (1996).

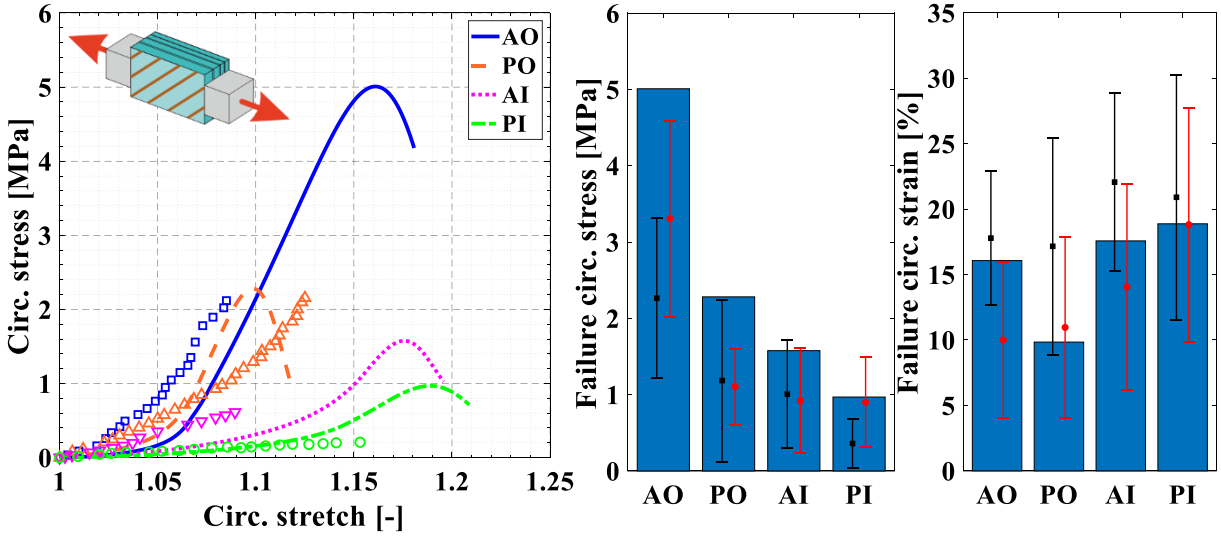

(a) (b)

Figure III.5. Multi-lamellae UA predictions along circumferential direction for the different disc regions: (a) stress-stretch responses (lines: model simulations, symbols: experimental data of Ebara et al. (1996)), (b) ultimate properties (bars: model simulations, square symbols with standard deviation intervals: experimental data of Ebara et al. (1996), circle symbols with standard deviation intervals: experimental data of Acaroglu et al. (1995)).

The failure strain predictions fail within the standard deviation intervals. Although the predicted failure stress can be found outside the experimental intervals, the predictive trends provide a regional difference in agreement with the experimental data. This important result confirms that the model provides a quite proper description of the regional effects on the relationship between the actual microstructure, the damage events and the macroscopic ultimate properties. Recall that the model connects macroscopic response and hydration (volumetric) effects. The capacity of the model to capture the regional variation of the transverse responses is shown in Figure III.6. The LM-ILM interaction highlights the crucial role that the OCF regional orientations play in the transverse

response (Kandil et al., 2020). In particular, regarding the possibility of an apparent auxeticity manifested by the positive transversal strains of the lamellae plane (Baldit, 2013).

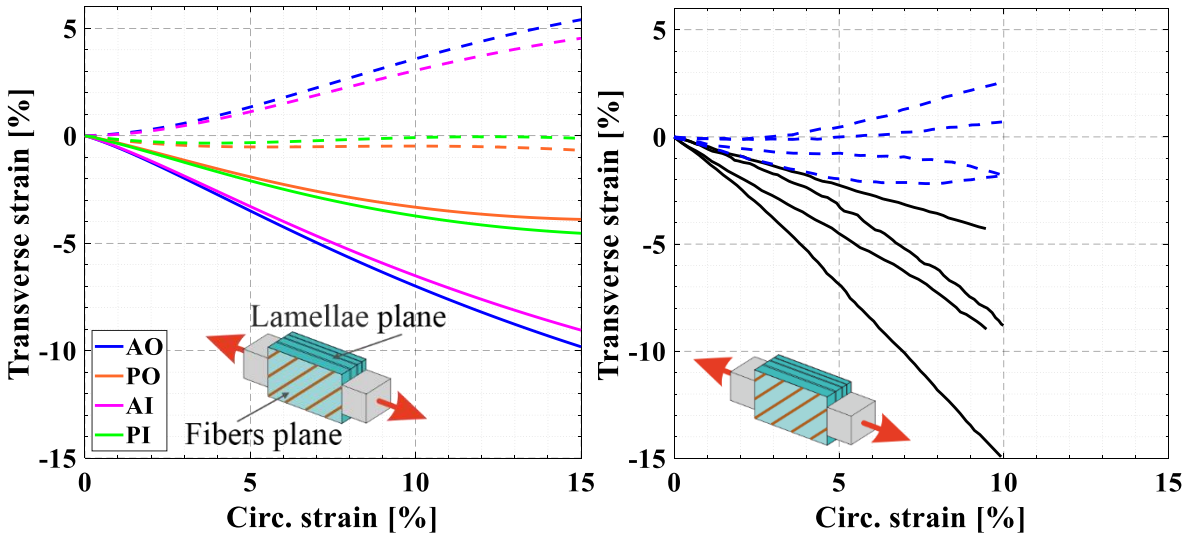

(a) (b)

Figure III.6. Multi-lamellae transverse responses under UA circumferential stretching for the different disc regions (solid lines: fibers plane, dashed lines: lamellae plane): (a) model results, (b) experimental data of Baldit (2013).

Thanks to the incorporation of the actual nanostructure materialized by the network of fibrils, the model can predict the regional behavior of the annulus in the radial direction. Figure III.7a shows the multi-lamellae stress-stretch responses under UA stretching along the radial direction. Again, the simulations are conducted until the appearance of the stress drop. The experimental data of Fujita et al. (1997) are reported in Figure III.8 to further verify the model predictive capacities. Both moduli and ultimate properties fall within the experimental standard deviation intervals of Fujita et al. (1997). By taking into account accurately the connections between layers, the model allows also to predict the shearing resistance. Figure III.7b shows such predictions for which it can be observed a strong regional dependence. In addition to amount, type and orientation of the collagen network, the regional variation of the NEF arrangement leads to different predicted stiffness and failure thresholds according to the disc region. The connection of collagen network between lamellae from nanoscale made it possible to represent precisely the damage processes in the LM and ILM connections in the different annulus regions. The model shows that the different regional thresholds

of radial and shear failures are caused by the regional arrangement of the NEF. These results are in agreement with the qualitative data analyzed in Fujita et al. (1997). Indeed, it was reported from image analysis that inter-layer connections such as NEF contribute to the annulus radial resistance (Pezowicz et al., 2006a; Tavakoli and Costi, 2018).

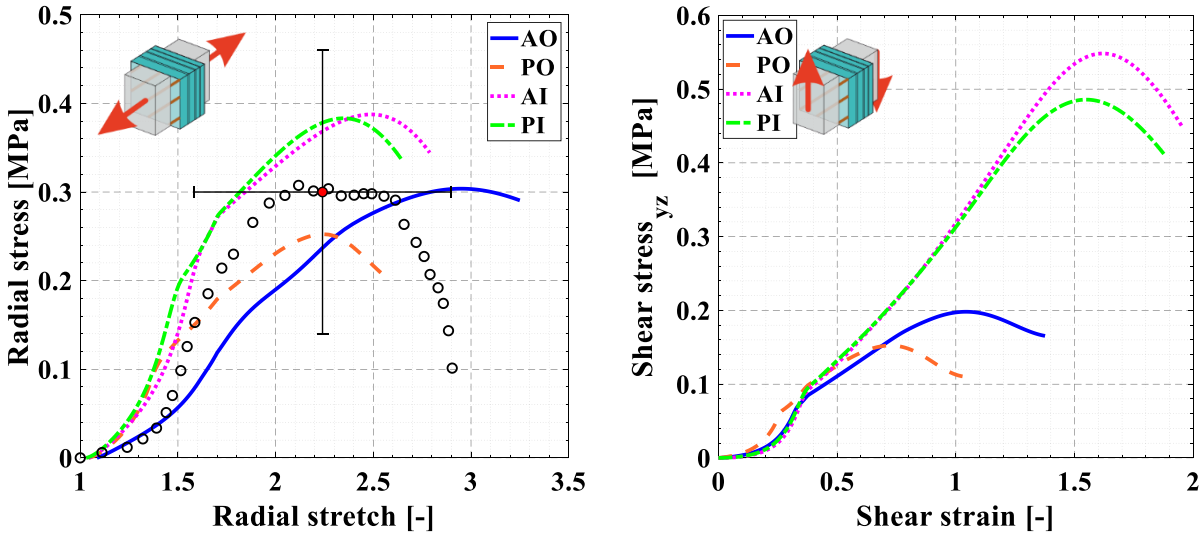

Figure III.7. Multi-lamellae stress-stretch responses under (a) UA radial stretching and (b) SS loading for the different disc regions (lines: model simulations, circle symbols: experimental data of Fujita et al. (1997).

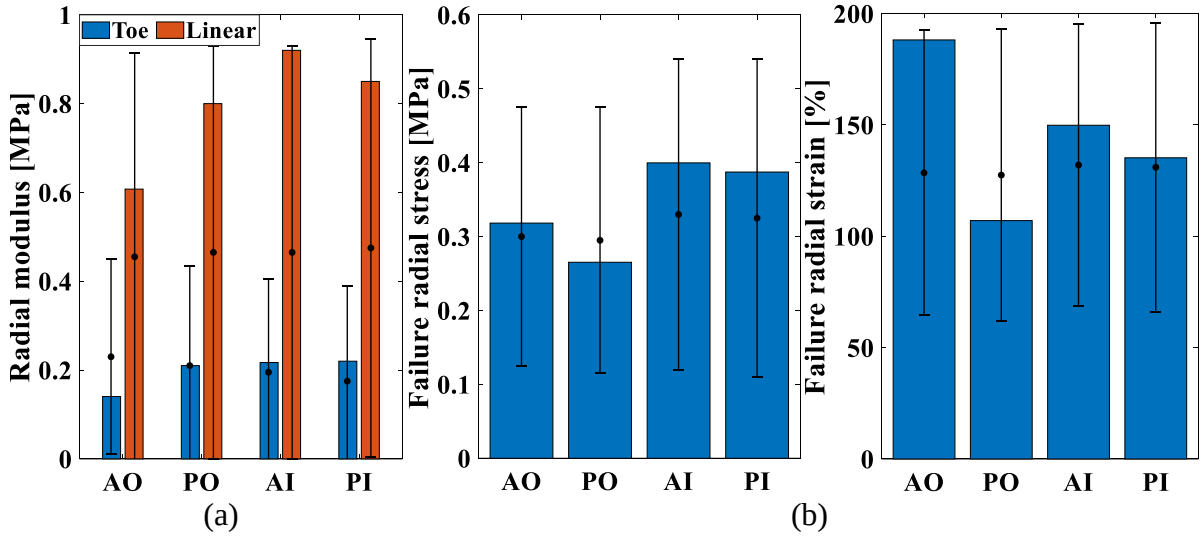

Figure III.8. Multi-lamellae UA predictions along radial direction for the different disc regions: (a) moduli, (b) ultimate properties (bars: model simulations, circle symbols with standard deviation intervals: experimental data of Fujita et al. (1997)).

The directional effects are quite well captured by the model, especially the much higher stretchability along the radial direction than along the circumferential direction. The BA stress-strain responses are presented in Figure III.9 for different strain ratios (= circumferential strain : axial strain, {1:1, 1:2 and 2:1}). In order to further evidence the directional effects, Figure III.10 presents the PSC stress-stretch responses for different strain ratios. The strain ratio has an important effect on the stiffness and the ultimate properties, with a stronger effect on the axial properties than the circumferential ones. The posterior zones show higher stiffness than the anterior zones. That can be justified by the fact that the OCF angles are close to 45°, and that the forces are well shared according to the two loading directions (circumferential and axial). Although the location was not indicated in the paper of O'Connell et al. (2012), it is satisfactory to observe that the BA predictions of the inner parts are in acceptable agreement with their typical experimental curves. The model indicates that the damage first initiates in the posterior zone. This result is actually found for all examined loading modes. PO has indeed a weak circumferential stretchability compared to other regions, as shown in UA stretching along the circumferential direction (see Figure III.5) and in BA stretching (see Figure III.7). That explains why PO exhibits a low ductility in PSC as observed in Figure III.10. Indeed, once PO reaches the circumferential failure, the axial failure occurs. As a consequence, PO shows a very low failure axial stress.

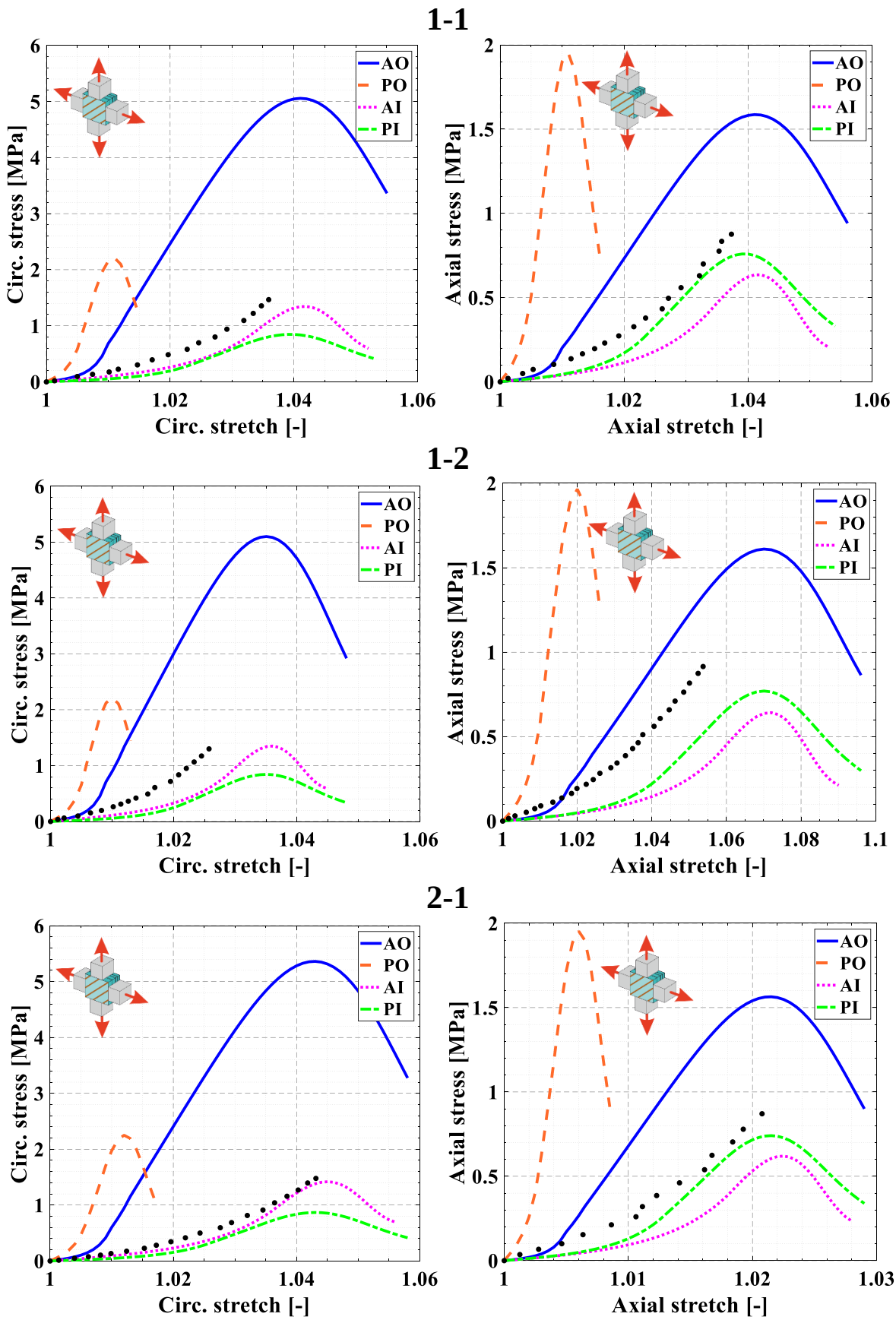

Figure III.9. Multi-lamellae stress-stretch responses under BA stretching with various strain ratios for the different disc regions (lines: model simulations, circle symbols: experimental data of O'Connell et al. (2012)).

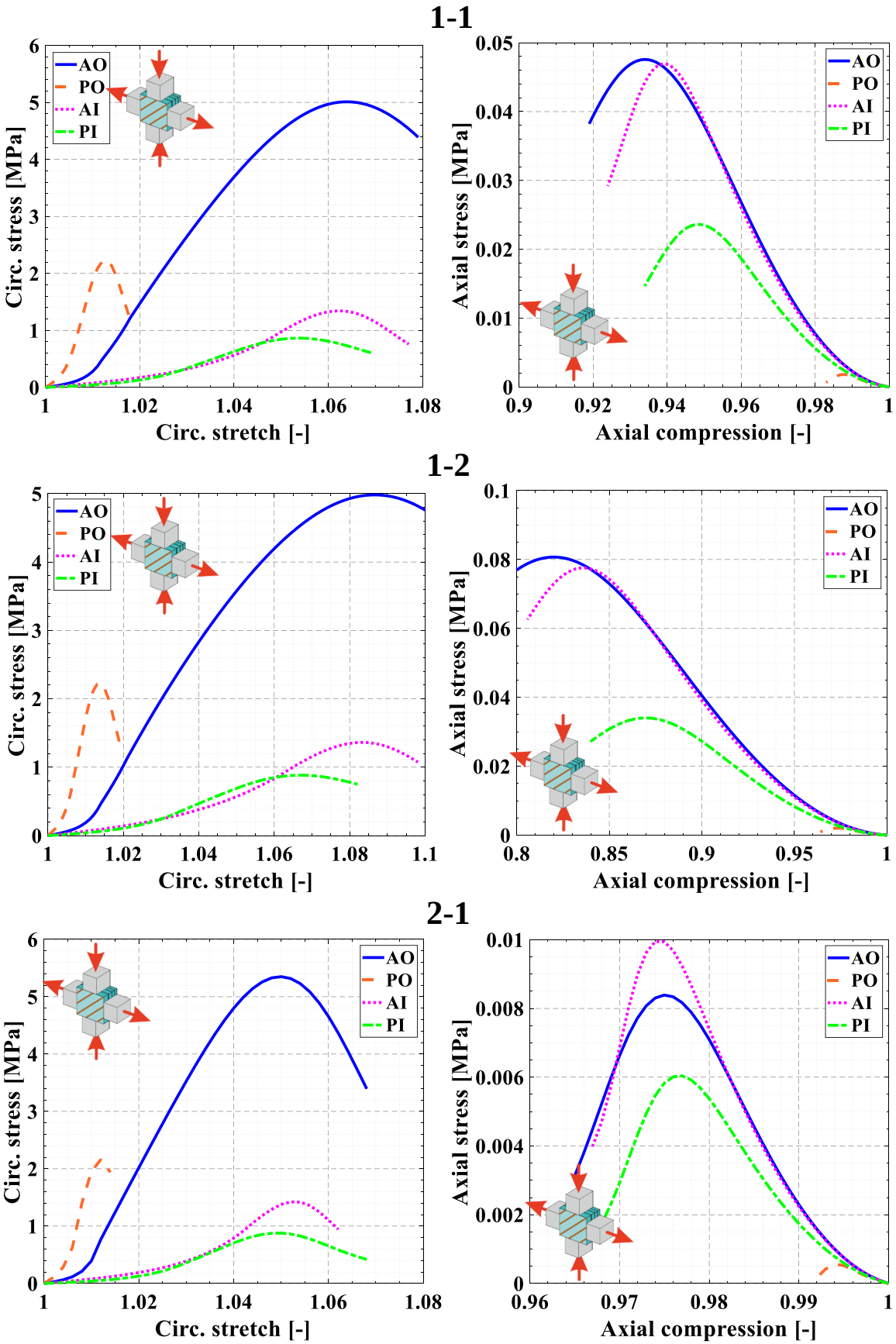

Figure III.10. Multi-lamellae stress-stretch responses under PSC loading with various strain ratios for the different disc regions.

III.4. Full disc model

In this section, predictions of a full disc model are presented using the regional dependent constitutive representation of multi-lamellae and local damage mechanisms are clarified in order to get a basic insight about the starting areas of failure modes.

III.4.1. Disc construction and boundary conditions

A lot of finite element disc models were developed in the literature (Qasim et al., 2012, 2014; Castro and Alves, 2020; Subramani et al., 2020; Komeil et al., 2021; Kandil et al., 2021). Beyond fundamental differences in the constitutive representation of the disc tissues, the time of model design and the time of calculation remain the main common weak points of all previous disc models. In the final objective to create time and cost-efficient patient-specific models of human discs, the present disc modeling strategy is purely analytical and again coded in MATLAB. The volume element of multi-lamellae, constitutively designed in the Cartesian space (x, y, z), was transferred to the Cylindrical space (r, θ, z) in order to consider the full disc geometry as illustrated in Figure III.11a. From the theoretical point of view, the constitutive equations were re-written within a finite-strain kinematic framework in Cylindrical coordinates. The reader is referred to the work of Holzapfel et al. (2000) for the general theory on tube-like solid mechanics. In the present chapter, we restrict the loading to a uniaxial compression at the disc external boundary. The disc is thus seen as a cylindrical solid loaded in compression on the superior surface and with a pressure in the cylindrical internal wall (Figure III.11b). The latter simulates the nucleus swelling applied to the internal wall of the disc annulus; the applied vertical axial displacement was translated to an internal pressure by considering the nucleus bulk modulus. The regional variation in structure and properties of the disc annulus was taken into account using the constitutive representation of each human annulus region. In order to ensure smooth transitions of the microstructural features (ECM, NEF, OCF and fluid) and properties from a disc annulus region to another, with a radial and circumferential variation, linear interpolations were considered.

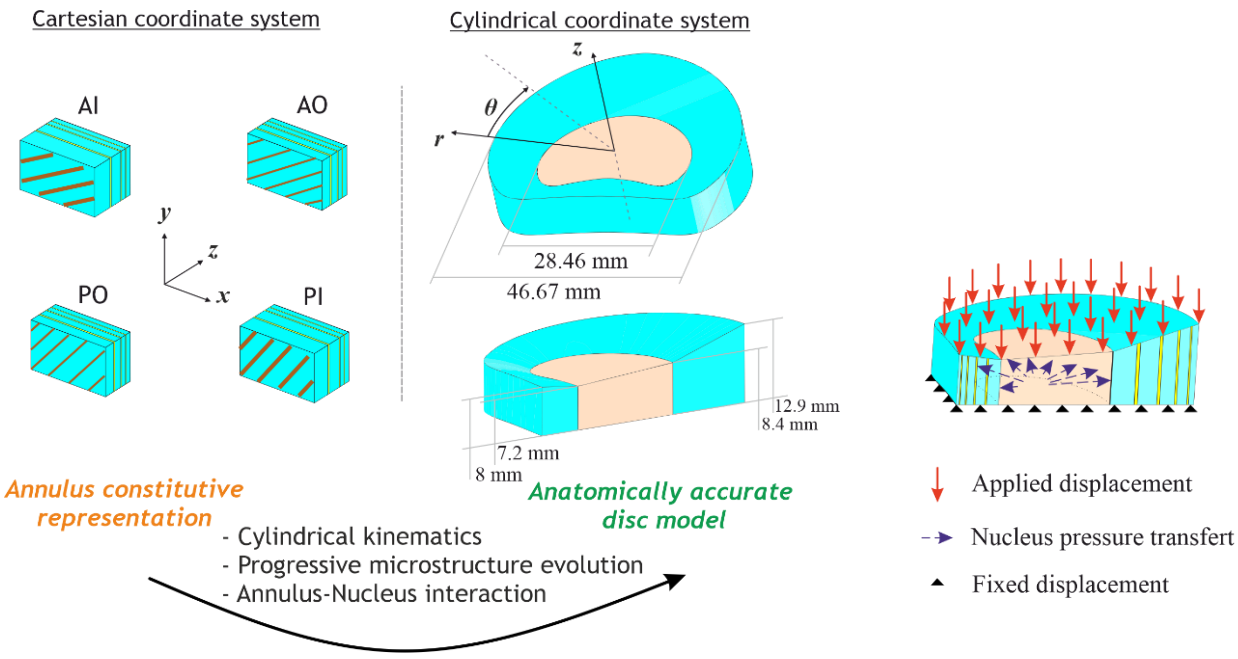

(a) (b)

Figure III.11. Full disc model: (a) Passage from annulus constitutive model to anatomically accurate disc model including volumetric strain, regional and directional effects (disc dimensions at the L1-L2 level), (b) boundary conditions of the uniaxially compressed disc.

An anatomically accurate three-dimensional model of a lumbar disc at the L1-L2 level was constructed using quantitative anatomical data taken from the work of Holzapfel et al. (2005). The L1-L2 disc geometric contours were approximated using special mathematical functions considering especially non-symmetric thicknesses and heights (Figure III.11a). Note that they may be adapted to consider the shape and size-changing with the spinal level and age (Amonoo-Kuofi, 1991). The annulus was subdivided into 15 different layers according to the L1-L2 disc dimensions provided by Holzapfel et al. (2005). The annulus size is considered to be approximately 50% of the disc volume (Violas et al., 2007). It is worth noticing that a notable difference exists between in-vivo and in-vitro responses regarding fluid exudation. In-vivo, the healthy disc completely recovers its height and intradiscal pressure after long diurnal loading. In-vitro, several studies reported losses in the disc height and intradiscal pressure (Feki et al., 2020). The chemical-induced volumetric strain was then affected by a multiplying factor. Several numerical simulations were performed with different values of the multiplying factor ranged from 0 to 100%, and a value of 50% was retained

in the present work. During the simulations, a vertical axial displacement was applied on the superior surface while the inferior surface was constrained (Figure III.11b). The simulations were performed at a displacement rate of 0.01 mm/s in order to maintain quasi-static loading conditions.

III.4.2. Damage fields

The damage process in the disc core simulated by the model is recorded in Figure III.12 by differentiating the damage of the different solid constituents (ECM, NEF and OCF). That permits a better understanding of the origin of the damage mechanisms affecting the disc and existing at different scales, nanoscale for ECM proteoglycan macromolecules and for NEF network and microscale for OCF. A global view at the contour plots shows that damage progressively increases in intensity and in extent as the applied compression increases, which is accompanied by a disc volumetric change and an annulus-nucleus non-symmetric interaction. The different damage mechanisms may co-exist at the same time and initiate at different locations. Remind that, in the present model, damage initiation and propagation are dependent on structure-property regional variation but also on the variation in displacement fields due to local differences in disc height. The highest damage zones in OCF are mainly observed in the anterior outer/lateral anterior ring. Excessive damage accumulation in these zones suggests the possibility of tear creation that may lead to an anterior herniation as experimentally reported in (Osti et al., 1992; Schollum et al., 2018; Sapiee et al., 2019). Besides, the ECM and NEF damage patterns are presented in the two layers in order to appreciate the specific role of the ILM matrix and compare it to the adjacent LM. For both ECM and NEF, two critical zones appear in the lamellae on either side of the annulus with very low intensities. With relatively higher intensities, critical damage spots in the ILM matrix (for both ECM and NEF) are firstly located in the anterior side of the annulus and are then progressively more likely located in the neighborhood of the anterior inner part of the annulus.

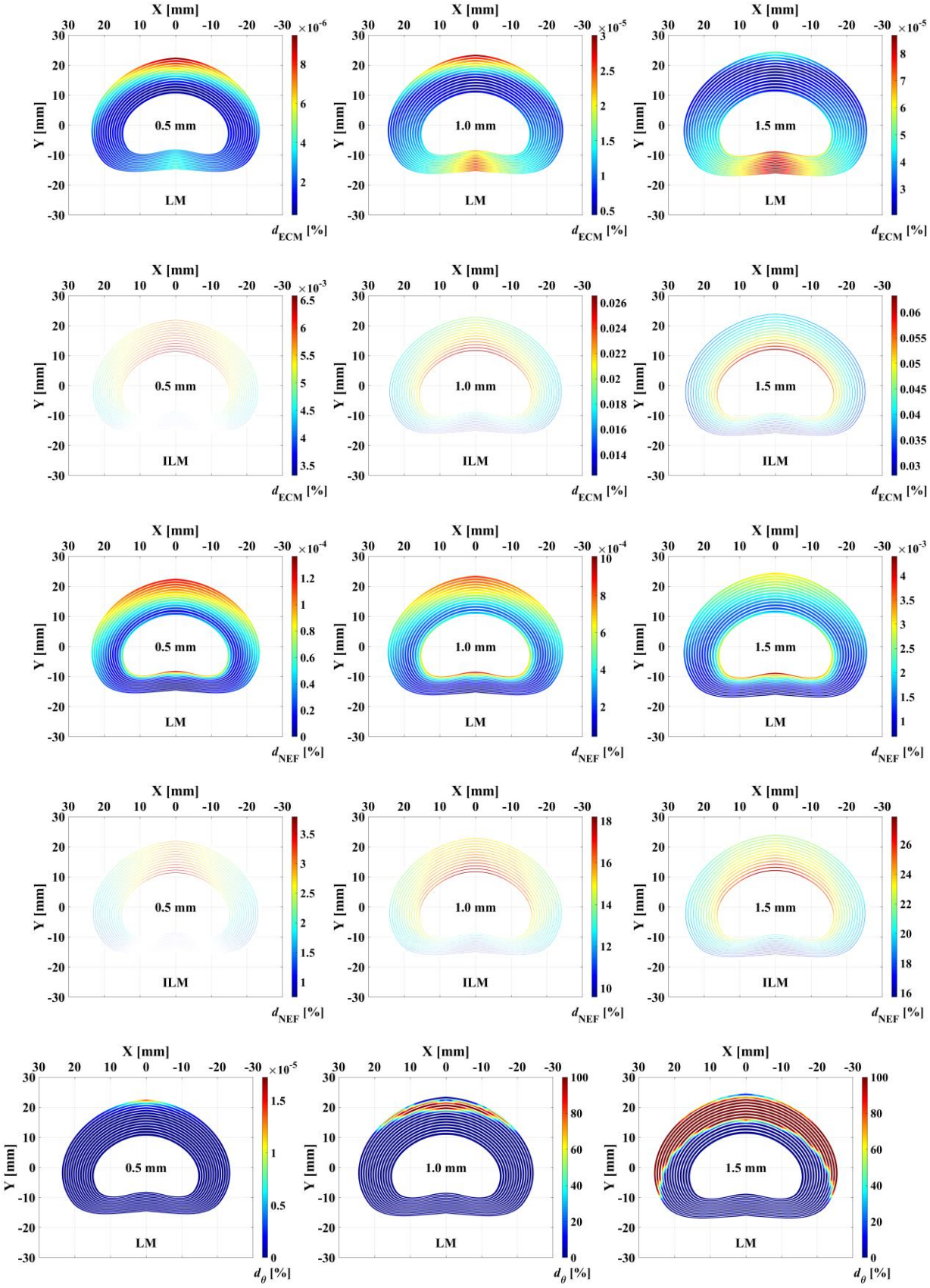

Figure III.12. Damage contour plots in the superior view of the uniaxially compressed disc for different applied displacement levels (0.5, 1.0 and 1.5 mm); ECM damage d_{ECM} in LM and in ILM, NEF damage d_{NEF} in LM and in ILM, OCF damage d_θ in LM.

Quite interestingly, a confined distribution of the ILM damage can be observed in the lateral anterior inner and posterior inner sides of the annulus. The latter is often judged as one of the most dangerous disc failure modes with the highest risk of disc delamination and failure propagation in the radial direction of the disc as experimentally reported in (Osti et al., 1992; Schollum et al., 2018; Sapiee et al., 2019). The distribution of the fibrils makes the damage anisotropic. To illustrative this model capacity, the damage of the fibrils is plotted in Figure III.13 for two zones taken in posterior and anterior sides of the inner annulus (close to the annulus-nucleus interface), respectively, in LM and in ILM. The contour plots are plotted in a dial (90° representing the radial direction) in such a way that the directional effects can be observed during continuous loading. Whereas the damage in LM is confined to small degrees around the radial direction, with an onset for relatively important applied displacements, the damage in ILM is developed earlier and is more diffused.

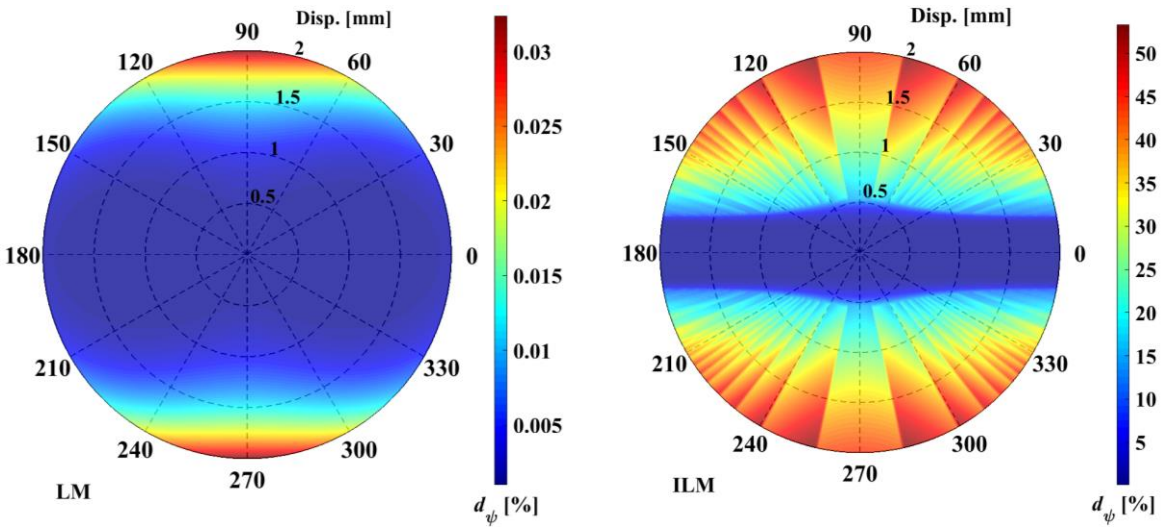

(a) (b)

Figure III.13. Damage of the fibrils in different directions (90° is the radial direction) at two zones of the uniaxially compressed disc: (a) posterior (in LM) and (b) anterior (in ILM) sides of the inner annulus for different applied displacement levels (from zero in the dial center to 2 mm in the dial boundary).

III.1. Discussion and concluding remarks

In the present chapter, a novel human annulus model was proposed to constitutively relate the regional variation in structural arrangement of collagen network at different scales and the multiaxial mechanics till failure. The model provides a useful tool to predict a variation of the annulus stiffness and ultimate properties with both disc region and loading mode. The different loading modes were simulated and chosen to better understand the regional behavior until the failure of the solid components in interaction with the chemical-induced volumetric response. The capabilities of the model were analyzed and an acceptable agreement between predicted values and experimental data was highlighted. A full disc model was constructed using the regional dependent constitutive representation of multi-lamellae and damage fields in the compressed disc were analyzed to assess the areas where the risk of failure is the highest.

The present model can be considered as the stepstone for the long-term prediction of the disc dysfunctions. During different complex loading scenarios of the spine, the disc dysfunctions may occur either by: i) mechanical damage due to a high level of loads (Acaroglu et al., 1995; Ebara et al., 1996) or relatively moderate loads repeated several times which cause damage accumulation (Green et al., 1993; Iatridis et al., 2005; Qasim et al., 2012; Subramani et al., 2020), ii) by an age-related biological degeneration (Thompson et al., 1990; Urban and Roberts, 2003; Cegoñino et al., 2014) or by the cellular disorders, including the cell death, the production of inflammatory mediators and a shift towards catabolism (Bruehlmann et al., 2004; Walter et al., 2011; Bloom et al., 2021). Nonetheless, it is difficult to identify or precisely model the disc failure taking into account the two causes of dysfunction at the same time. Since our study is based on the in-vitro annulus results, it cannot be directly extrapolated to the in-vivo disc response. Indeed, the understanding of the disc mechanobiology must be taken into account by the model considering especially nutrition and cellular activity along with degenerative aspects (Bruehlmann et al., 2004; Walter et al., 2011; Bloom et al., 2021). The model could be then a real help to provide solutions for remodeling and

self-healing response of the disc tissues (Likhitpanichkul et al., 2014; Borde et al., 2015; Wan et al., 2016; Peng et al., 2020). Moreover, the near-field direct local interactions within the collagen network and the ECM ought to be treated through either the incorporation of a supplementary energy term (Guerin and Elliott, 2007) or a mean-field approach (Saadedine et al., 2021).

Appendix III.A. Quantities and orientations

The total number of NEF is reported in Figure III.A1 as a function of the orientation ψ. The information is extracted from the two works of Tavakoli et al. (2017, 2020a); the observed Gaussian-type shape is mathematically represented by a special function proposed in the previous chapter. Due to the lack of information regarding the regional variation, we admitted similar NEF distributions in LM and ILM layers for outer and inner regions.

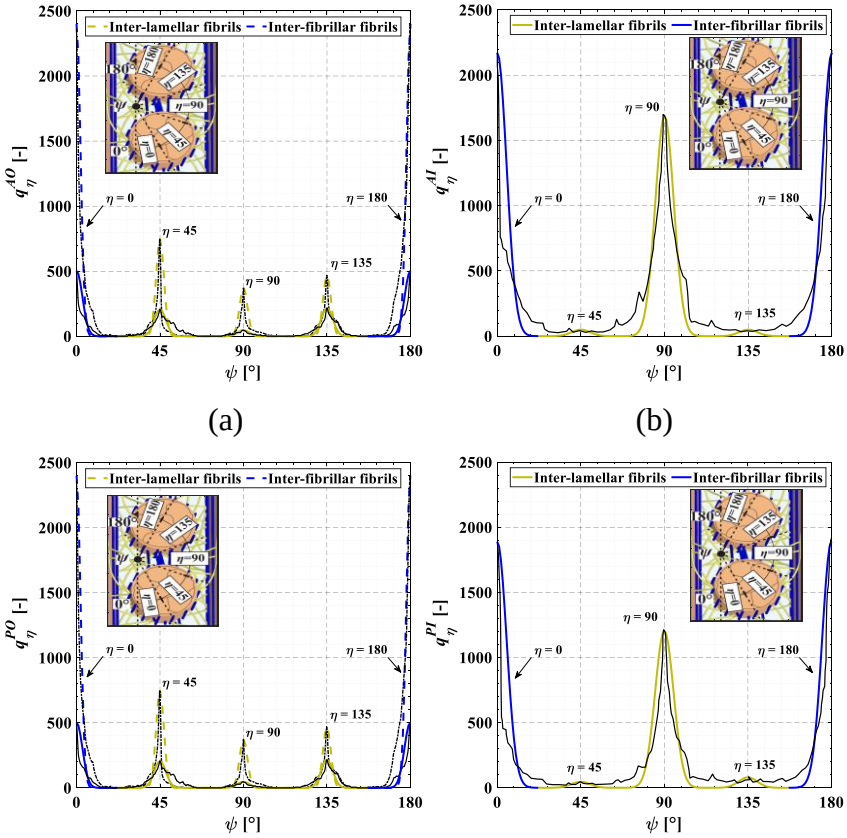

Figure III.A1. Quantity of NEF in the different disc regions: (a) AO, (b) AI, (c) PO and (d) PI (solid lines: inter-fibrillar fibrils in LM layers, dashed lines: inter-lamellar fibrils in ILM layers, black lines: experimental data from Tavakoli et al. (2017) for (a) and (c) and Tavakoli et al. (2020a) for (b) and (d)).

The volume fractions of fibril bundles $\boldsymbol{d}$ ϕ_η^i in the two layers are estimated as follows:

$$\phi_\eta^{LM} = \begin{cases} \dfrac{q_\eta^{LM} + q_\eta^{ILM}}{q^{LM}} & \eta = 0°,180° \\ \dfrac{q_\eta^{LM}}{q^{LM}} & \eta = 45°,90°,135° \end{cases} \quad \text{and} \quad \phi_\eta^{ILM} = \begin{cases} 0 & \eta = 0°,180° \\ \dfrac{q_\eta^{ILM}}{q^{ILM}} & \eta = 45°,90°,135° \end{cases} \tag{III.A1}$$

where q^{LM} and q^{ILM} are the respective total number of NEF in each layer *i*:

$$q^{LM} = \sum_\eta \sum_\psi q_\eta^{LM} + \sum_{\eta=0°,180°} \sum_\psi q_\eta^{ILM} \quad \text{and} \quad q^{ILM} = \sum_{\eta=45°,90°,135°} \sum_\psi q_\eta^{ILM} \tag{III.A2}$$

Quantities and orientations of the other constituents are extracted from well-documented papers for the four main disc regions (Acaroglu et al., 1995; Ebara et al., 1996; Skaggs et al., 1994; Holzapfel et al., 2005). Theses inputs required by the model are provided in Figure III.A2.

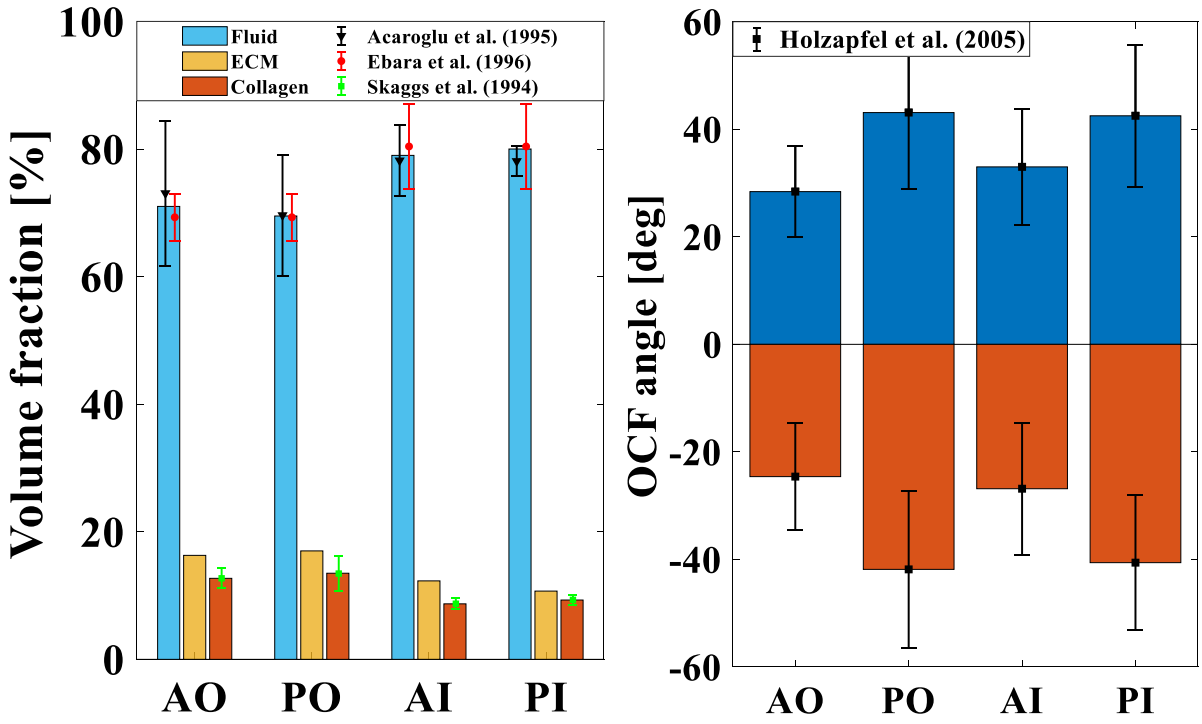

Figure III.A2. Model inputs in terms of (a) quantities and (b) orientations for the different disc regions (bars: model inputs, symbols with standard deviation intervals: experimental data).

Appendix III.B. Multi-lamellae mechanics

By separating chemical-induced volumetric and mechanical quantities, the macroscopic deformation gradient tensor $\mathbf{F}$ is given from chapter I:

$$\mathbf{F} = \sum_{i=1,3...}^{m} \phi_{layer\_0}^{i} \left(\mathbf{F}_{chem}^{LM\_i} . \mathbf{F}_{mech}^{LM\_i} \right) + \sum_{i=2,4...}^{m-1} \phi_{layer\_0}^{i} \left(\mathbf{F}_{chem}^{ILM\_i} . \mathbf{F}_{mech}^{ILM\_i} \right) \tag{III.B1}$$

in which $\phi_{layer\_0}^{i} = z_{layer\_0}^{i} / z_{tissue}$ is the initial volume fraction of a layer *i* with $z_{layer\_0}^{i}$ the initial thickness of the layer *i* and z_{tissue} the tissue thickness.

To consider the effective interactions between adjacent layers, the compatibility condition on the deformation gradients is introduced at the LM/ILM interfaces:

$$\mathbf{F}^{LM\_i} . \boldsymbol{n}_0^{i} = \mathbf{F}^{ILM\_i+1} . \boldsymbol{n}_0^{i} \tag{III.B2}$$

where $\boldsymbol{n}_0^{i}$ is the arbitrary unit vector between two adjacent layers in the initial configuration.

From the first chapter, the macroscopic Cauchy stress tensor $\boldsymbol{\sigma}$ is expressed as:

$$\boldsymbol{\sigma} = \sum_{i=1,3,..}^{m} \phi_{layer}^{i} \left(\boldsymbol{\sigma}_{mech}^{LM\_i} + \boldsymbol{\sigma}_{chem}^{LM\_i} \right) + \sum_{i=2,4,..}^{m-1} \phi_{layer}^{i} \left(\boldsymbol{\sigma}_{mech}^{ILM\_i} + \boldsymbol{\sigma}_{chem}^{ILM\_i} \right) \tag{III.B3}$$

in which ϕ_{layer}^{i} is the current volume fraction of a layer *i*:

$$\phi_{layer}^{i} = \frac{J_{chem}^{i} z_{layer\_0}^{i}}{\sum_{j=1}^{m} J_{chem}^{j} z_{layer\_0}^{j}} \tag{III.B4}$$

where $J_{chem}^{i} = \det\left(\mathbf{F}_{chem}^{i} \right)$ is the chemical-induced volumetric change.

The stress equilibrium condition at the LM/ILM interfaces is given by:

$$\boldsymbol{\sigma}^{LM\_i} . \boldsymbol{n}^{i} = \boldsymbol{\sigma}^{ILM\_i+1} . \boldsymbol{n}^{i} \tag{III.B5}$$

where $\boldsymbol{n}^{i}$ is the arbitrary unit vector between two adjacent layers in the current configuration.

The initial thickness $z_{layer\_0}^{i}$ of the layer *i* and the tissue thickness z_{tissue} are given by:

$$z_{tissue} = z_{layer}^{LM} + z_{layer}^{ILM} = \sum_{i=1,3,..}^{m} z_{layer}^{LM\_i} + \sum_{i=2,4,..}^{m-1} z_{layer}^{ILM\_i} \tag{III.B6}$$

with $z_{layer}^{LM\_i}$ $i=1,3,...m$ and $z_{layer}^{ILM\_i}$ $i=2,4,...m-1$ are the functions describing the LM thickness and the ILM thickness, respectively:

$$z_{layer}^{LM\_i} = ai + b \text{ and } z_{layer}^{ILM\_i} = r_{ILM/LM}\left(z_{layer}^{LM\_i-1}/2 + z_{layer}^{LM\_i+1}/2\right) \quad \text{(III.B7)}$$

where $r_{ILM/LM}$ represents the thickness ratio of the two zones and, *a* and *b* are constants calculated according to the maximum and minimum thicknesses of the annulus layers z_{max} and z_{min}:

$$a = \frac{z_{max} - z_{min}}{m-1} \text{ and } b = z_{min} - a \quad \text{(III.B8)}$$

where *m* is the number of layers.

For each disc region, structural parameters are extracted from well-documented papers (Tavakoli et al., 2017; Holzapfel et al., 2005) and are listed in Table III.B1.

Parameters		Regions				References
		AO	PO	AI	PI	
z_{max}	$[\text{mm}]$	0.76	0.42	0.86	0.46	Holzapfel et al. (2005)
z_{min}	$[\text{mm}]$	0.62	0.34	0.66	0.34	Holzapfel et al. (2005)
$r_{ILM/LM}$	$[-]$	0.133	0.133	0.133	0.133	Tavakoli et al. (2017)

Table III.B1. Structural parameters for the different disc regions.

III. References

Acaroglu, E.R., Iatridis, J.C., Setton, L.A., Foster, R.J., Mow, V.C., Weidenbaum, M., 1995. Degeneration and aging affect the tensile behavior of human lumbar anulus fibrosus. Spine 20, 2690-2701.

Amonoo-Kuofi, H.S., 1991. Morphometric changes in the heights and anteroposterior diameters of the lumbar intervertebral discs with age. Journal of Anatomy 175, 159-168.

Baldit, A., 2013. Etude des interactions hydro-chimio-mécaniques dans les tissus biologiques: application à la nutrition du disque intervertébral. Phd Thesis, University of Montpellier.

Bloom, E.T., Lee, A.H., Elliott, D.M., 2021. Tendon multiscale structure, mechanics, and damage are affected by osmolarity of bath solution. Annals of Biomedical Engineering 49, 1058-1068.

Boos, N., Weissbach, S., Rohrbach, H., Weiler, C., Spratt, K.F., Nerlich, A.G., 2002. Classification of age-related changes in lumbar intervertebral discs. Spine 27, 2631-2644.

Borde, B., Grunert, P., Härtl, R., Bonassar, L.J., 2015. Injectable, high-density collagen gels for annulus fibrosus repair: an in vitro rat tail model. Journal of Biomedical Materials Research Part A 103, 2571-2581.

Bruehlmann, S.B., Hulme, P.A., Duncan, N.A., 2004. In situ intercellular mechanics of the bovine outer annulus fibrosus subjected to biaxial strains. Journal of Biomechanics 37, 223-231.

Castro, A.P.G., Alves, J.L., 2020. Numerical implementation of an osmo-poro-visco-hyperelastic finite element solver: application to the intervertebral disc. Computer Methods in Biomechanics and Biomedical Engineering 5, 538-550.

Cegoñino, J., Moramarco, V., Calvo-Echenique, A., Pappalettere, C., Pérez del Palomar, A., 2014. A constitutive model for the annulus of human intervertebral disc: implications for developing a degeneration model and its influence on lumbar spine functioning. Journal of Applied Mathematics 2014, 1-15.

Costi, J.J., Stokes, I.A., Gardner-Morse, M., Laible, J.P., Scoffone, H.M., Iatridis, J.C., 2007. Direct measurement of intervertebral disc maximum shear strain in six degrees of freedom: motions that place disc tissue at risk of injury. Journal of Biomechanics 40, 2457-2466.

Derrouiche, A., Zaouali, A., Zaïri, F., Ismail, J., Chaabane, M., Qu, Z., Zaïri, F., 2019a. Osmo-inelastic response of the intervertebral disc. Proceedings of the Institution of Mechanical Engineers. Part H: Journal of Engineering in Medicine 233, 332-341.

Derrouiche, A., Zaïri, F., Zaïri, F., 2019b. A chemo-mechanical model for osmo-inelastic effects in the annulus fibrosus. Biomechanics and Modeling in Mechanobiology 18, 1773-1790.

Derrouiche, A., Feki, F., Zaïri, F., Taktak, R., Moulart, M., Qu, Z., Ismail, J., Charfi, S., Haddar, N., Zaïri, F., 2020. How pre-strain affects the chemo-torsional response of the intervertebral disc. Clinical Biomechanics 76, 105020.

Ebara, S., Iatridis, J.C., Setton, L.A., Foster, R.J., Mow, V.C., Weidenbaum, M., 1996. Tensile properties of nondegenerate human lumbar anulus fibrosus. Spine 21, 452-461.

Feki, F., Taktak, R., Kandil, K., Derrouiche, A., Moulart, M., Haddar, N., Zaïri, F., Zaïri, F., 2020. How osmoviscoelastic coupling affects recovery of cyclically compressed intervertebral disc. Spine 45, 160553.

Fujita, Y., Duncan, N.A., Lotz, J.C., 1997. Radial tensile properties of the lumbar annulus fibrosus are site and degeneration dependent. Journal of Orthopaedic Research 15, 814-819.

Gao, X., Zhu, Q., Gu, W., 2017. An anisotropic multiphysics damage model with application to annulus fibrosus. Journal of Biomechanics 61, 88-93.

Ghezelbash, F., Shirazi-Adl, A., Baghani, M., Eskandari, A.H., 2020. On the modeling of human intervertebral disc annulus fibrosus: Elastic, permanent deformation and failure responses. Journal of Biomechanics 102, 109463.

Ghezelbash, F., Eskandari, A.H., Shirazi-Adl, A., Kazempour, M., Tavakoli, J., Baghani, M., Costi, J.J., 2021. Modeling of human intervertebral disc annulus fibrosus with complex multi-fiber networks. Acta Biomaterialia 123, 208-221.

Green, T.P., Adams, M.A., Dolan, P., 1993. Tensile properties of the annulus fibrosus. European Spine Journal 2, 209-214.

Guerin, H.L., Elliott, D.M., 2007. Quantifying the contributions of structure to annulus fibrosus mechanical function using a nonlinear, anisotropic, hyperelastic model. Journal of Orthopaedic Research 25, 508-516.

Han, S.K., Chen, C.W., Labus, K.M., Puttlitz, C.M., Chen, Y., Hsieh, A.H., 2016. Optical coherence tomographic elastography reveals mesoscale shear strain inhomogeneities in the annulus fibrosus. Spine 41, 770-777.

Han, W.M., Nerurkar, N.L., Smith, L.J., Jacobs, N.T., Mauck, R.L., Elliott, D.M., 2012. Multi-scale structural and tensile mechanical response of annulus fibrosus to osmotic loading. Annals of Biomedical Engineering 40, 1610-1621.

Holzapfel, G.A., Gasser, T.C., Ogden, R.W., 2000. A new constitutive framework for arterial wall mechanics and a comparative study of material models. Journal of Elasticity and the Physical Science of Solids 61, 1-48.

Holzapfel, G.A., Schulze-Bauer, C.A.J., Feigl, G., Regitnig, P., 2005. Single lamellar mechanics of the human lumbar anulus fibrosus. Biomechanics and Modeling in Mechanobiology 3, 125-140.

Iatridis, J.C., MacLean, J.J., Ryan, D.A., 2005. Mechanical damage to the intervertebral disc annulus fibrosus subjected to tensile loading. Journal of Biomechanics 38, 557-565.

Kandil, K., Zaïri, F., Derrouiche, A., Messager, T., Zaïri, F., 2019. Interlamellar-induced time-dependent response of intervertebral disc annulus: a microstructure-based chemo-viscoelastic model. Acta Biomaterialia 200, 75-91.

Kandil, K., Zaïri, F., Messager, T., Zaïri, F., 2020. Interlamellar matrix governs human annulus fibrosus multiaxial behavior. Scientific Reports 10, 19292.

Kandil, K., Zaïri, F., Messager, T., Zaïri, F., 2021. A microstructure-based model for a full lamellar-interlamellar displacement and shear strain mapping inside human intervertebral disc core. Computers in Biology and Medicine 135, 104629.

Karsaj, I., Sansour, C., Soric, J., 2009. The modelling of fibre reorientation in soft tissue. Biomechanics and Modeling in Mechanobiology 8, 359-370.

Komeili, A., Rasoulian, A., Moghaddam, F., El-Rich, M., 2021. The importance of intervertebral disc material model on the prediction of mechanical function of the cervical spine. BMC Musculoskeletal Disorders 22, 1-12.

Lemaitre, J., Chaboche, J.L., 1994. Mechanics of Solid Materials. Cambridge University Press, Cambridge.

Likhitpanichkul, M., Dreischarf, M., Illien-Junger, S., Walter, B.A., Nukaga, T., Long, R. G., Sakai, D., Hecht, A.C., Iatridis, J.C., 2014. Fibrin-genipin adhesive hydrogel for annulus fibrosus repair: performance evaluation with large animal organ culture, in situ biomechanics, and in vivo degradation tests. European Cells & Materials, 28, 25-38.

Melrose, J., Smith, S.M., Appleyard, R.C., Little, C.B., 2008. Aggrecan, versican and type VI collagen are components of annular translamellar crossbridges in the intervertebral disc. European Spine Journal 17, 314-324.

Mengoni, M., Jones, A.C., Wilcox, R.K., 2016. Modelling the failure precursor mechanism of lamellar fibrous tissues, example of the annulus fibrosus. Journal of the Mechanical Behavior of Biomedical Materials 63, 265-272.

Miehe, C., 1995. Discontinuous and continuous damage evolution in Ogden-type large strain elastic materials. European Journal of Mechanics - A/Solids 14, 697-720.

O'Connell, G.D., Sen, S., Elliott, D.M., 2012. Human annulus fibrosus material properties from biaxial testing and constitutive modeling are altered with degeneration. Biomechanics and Modeling in Mechanobiology 11, 493-503.

Osti, O.L., Vernon-Roberts, B., Moore, R., Fraser, R.D., 1992. Annular tears and disc degeneration in the lumbar spine: a post-mortem study of 135 discs. The Journal of Bone and Joint Surgery 74, 678-682.

Peng, Y., Huang, D., Li, J., Liu, S., Qing, X., Shao, Z., 2020. Genipin-crosslinked decellularized annulus fibrosus hydrogels induces tissue-specific differentiation of bone mesenchymal stem cells and intervertebral disc regeneration. Journal of Tissue Engineering and Regenerative Medicine 14, 497-509.

Pezowicz, C.A., Robertson, P.A., Broom, N.D., 2006a. The structural basis of interlamellar cohesion in the intervertebral disc wall. Journal of Anatomy 208, 317-330.

Pezowicz, C.A., Schechtman, H., Robertson, P.A., Broom, N.D., 2006b. Mechanisms of anular failure resulting from excessive intradiscal pressure: a microstructural-micromechanical investigation. Spine 31, 2891-2903.

Qasim, M., Natarajan, R.N., An, H.S., Andersson, G.B.J., 2012. Initiation and progression of mechanical damage in the intervertebral disc under cyclic loading using continuum damage mechanics methodology: a finite element study. Journal of Biomechanics 45, 1934-1940.

Qasim, M., Natarajan, R.N., An, H.S., Andersson, G.B.J., 2014. Damage accumulation location under cyclic loading in the lumbar disc shifts from inner annulus lamellae to peripheral annulus with increasing disc degeneration. Journal of Biomechanics 47, 24-31.

Saadedine, M., Zaïri, F., Ouali, N., Tamoud, A., Mesbah, A., 2021. A micromechanics-based model for visco-super-elastic hydrogel-based nanocomposites. International Journal of Plasticity 144, 103042.

Sapiee, N.H., Thambyah, A., Robertson, P.A., Broom, N.D., 2019. Sagittal alignment with downward slope of the lower lumbar motion segment influences its modes of failure in direct compression: A mechanical and microstructural investigation. Spine 44, 1118-1128.

Schollum, M.L., Robertson, P.A., Broom, N.D., 2008. ISSLS prize winner: microstructure and mechanical disruption of the lumbar disc annulus: part I: a microscopic investigation of the translamellar bridging network. Spine 33, 2702-2710.

Schollum, M.L., Wade, K.R., Shan, Z., Robertson, P.A., Thambyah, A., Broom, N.D., 2018. The influence of concordant complex posture and loading rate on motion segment failure: a mechanical and microstructural investigation. Spine 43, E1116-E1126.

Shah, J.S., Hampson, W.G., Jayson, M.I., 1978. The distribution of surface strain in the cadaveric lumbar spine. Journal of Bone and Joint Surgery 60, 246-251.

Shahraki, N.M., Fatemi, A., Agarwal, A., Goel, V.K., 2015. Failure criteria for prediction of clinically relevant damage of annulus fibrosus. Spine Research 1, 7.

Skaggs, D.L., Weidenbaum, M., Iatridis, J.C., Ratcliffe, A., Mow, V.C., 1994. Regional variation in tensile properties and biochemical composition of the human lumbar anulus fibrosus. Spine, 19, 1310-1319.

Subramani, A.V., Whitley, P.E., Garimella, H.T., Kraft, R.H., 2020. Fatigue damage prediction in the annulus of cervical spine intervertebral discs using finite element analysis. Computer Methods in Biomechanics and Biomedical Engineering 23, 773-784.

Tamoud, A., Zaïri, F., Mesbah, A., Zaïri, F., 2021a. A microstructure-based model for time-dependent mechanics of multi-layered soft tissues and its application to intervertebral disc annulus. Meccanica 56, 585-606.

Tamoud, A., Zaïri, F., Mesbah, A., Zaïri, F., 2021b. A multiscale and multiaxial model for anisotropic damage and failure of human annulus fibrosus. International Journal of Mechanical Sciences 205, 106558.

Tavakoli, J., Elliott, D.M., Costi, J.J., 2016. Structure and mechanical function of the inter-lamellar matrix of the annulus fibrosus in the disc. Journal of Orthopaedic Research 34, 1307-1315.

Tavakoli, J., Elliott, D.M., Costi, J.J., 2017. The ultra-structural organization of the elastic network in the intra-and inter-lamellar matrix of the intervertebral disc. Acta Biomaterialia 58, 269-277.

Tavakoli, J., Costi, J.J., 2018. New findings confirm the viscoelastic behaviour of the inter-lamellar matrix of the disc annulus fibrosus in radial and circumferential directions of loading. Acta Biomaterialia 71, 411-419.

Tavakoli, J., Diwan, A.D., Tipper, J.L., 2020a. The ultrastructural organization of elastic fibers at the interface of the nucleus and annulus of the intervertebral disk. Acta Biomaterialia 114, 323-332.

Tavakoli, J., Diwan, A.D., Tipper, J.L., 2020b. Elastic fibers: the missing key to improve engineering concepts for reconstruction of the nucleus pulposus in the intervertebral disc. Acta Biomaterialia 113, 407-416.

Thompson, J.P., Pearce, R.H., Schechter, M.T., Adams, M.E., Tsang, I.K., Bishop, P.B., 1990. Preliminary evaluation of a scheme for grading the gross morphology of the human intervertebral disc. Spine 15, 411-415.

Urban, J.P., Roberts, S., 2003. Degeneration of the intervertebral disc. Arthritis Research & Therapy 5,120-130.

Vergari, C., Mansfield, J., Meakin, J.R., Winlove, P.C., 2016. Lamellar and fibre bundle mechanics of the annulus fibrosus in bovine intervertebral disc. Acta Biomaterialia 37, 14-20.

Vernon-Roberts, B., Moore, R.J., Fraser, R.D., 2007. The natural history of age-related disc degeneration: the pathology and sequelae of tears. Spine 32, 2797-2804.

Violas, P., Estivalezes, E., Briot, J., Sales de Gauzy, J., Swider P., 2007. Objective quantification of intervertebral disc volume properties using MRI in idiopathic scoliosis surgery. Magnetic Resonance Imaging 25, 386-391.

Walter, B.A., Korecki, C.L., Purmessur, D., Roughley, P.J., Michalek, A.J., Iatridis, J.C., 2011. Complex loading affects intervertebral disc mechanics and biology. Osteoarthritis and Cartilage 19, 1011-1018.

Wan, S., Borland, S., Richardson, S.M., Merry, C.L., Saiani, A., Gough, J.E., 2016. Self-assembling peptide hydrogel for intervertebral disc tissue engineering. Acta Biomaterialia, 46, 29-40.

Werbner, B., Spack, K., O'Connell, G.D., 2019. Bovine annulus fibrosus hydration affects rate-dependent failure mechanics in tension. Journal of Biomechanics 89, 34-39.

Yang, B., O'Connell, G.D., 2019. Intervertebral disc swelling maintains strain homeostasis throughout the annulus fibrosus: a finite element analysis of healthy and degenerated discs. Acta Biomaterialia, 100, 61-74.

Yu, J., Peter, C., Roberts, S., Urban, J.P., 2002. Elastic fibre organization in the intervertebral discs of the bovine tail. Journal of Anatomy 201, 465-475.

Yu, J., Schollum, M.L., Wade, K.R., Broom, N.D., Urban, J.P., 2015. A detailed examination of the elastic network leads to a new understanding of annulus fibrosus organization. Spine 40, 1149-1157.

Zhou, M., Bezci, S.E., O'Connell, G.D., 2019. Multiscale composite model of fiber-reinforced tissues with direct representation of sub-tissue properties. Biomechanics and Modeling in Mechanobiology 19, 745-759.

Zhou, M., Werbner, B., O'Connell, G.D., 2021. Fiber engagement accounts for geometry-dependent annulus fibrosus mechanics: a multiscale, structure-based finite element study. Journal of the Mechanical Behavior of Biomedical Materials 115, 104292.

Chapter IV

A fully three-dimensional model of interpenetrating collagen fibrillar networks for intervertebral disc mechanics

A fully three-dimensional model of interpenetrating collagen fibrillar networks for intervertebral disc mechanics [11]

Abstract

In this work, a fully three-dimensional model of the human intervertebral disc is proposed within a purely analytical framework in the final goal to create time and cost-efficient patient-specific models. Special functions are introduced to generate versatile disc geometries and anatomically accurate model taking into morphology regional variation. The complex interpenetrating collagen fibrillar networks are explicitly introduced in the three-dimensional model considering the regional variation throughout the disc. A quantitative evaluation of the predictive capabilities of the model shows a good agreement with compression experiments from the literature both for the overall disc stiffness and for the direct MRI kinematic fields. Model predictions are then performed and critically discussed on axially/torsionally loaded human lumbar discs.

Keywords: Full disc model; Multiscale structure; Regional variation; Nucleus-annulus interaction.

[11] This chapter is based on the following paper: Tamoud, A., Zaïri, F., Mesbah, A., Zaïri, F., 2021. A fully three-dimensional model of interpenetrating collagen fibrillar networks for intervertebral disc mechanics. Submitted.

IV.1. Introduction

The complex structural organization of interpenetrating collagen fibrillar networks in the intervertebral disc has been only revealed and appreciated recently (Tavakoli et al., 2020a, 2020b). The disc presents a hierarchical lamellar structure in which nano-sized elastic fibers (NEF) connect both two micro-sized type-I oriented collagen fibers (OCF) of the concentric lamellae (LM) and two adjacent LM between them by crossing the inter-lamellar (ILM) ground matrix. Besides, the regional variation in organization of collagen fibrillar networks throughout the disc leads to a heterogeneous mechanics of the disc (Tamoud et al., 2021a). In the literature, a lot of disc models were proposed (Qasim et al., 2012, 2014; Shahraki et al., 2015; Castro et al., 2020; Subramani et al., 2020; Kandil et al., 2021; Komeili et al., 2021). A short overview shows that the disc is most naturally modeled using the finite element method. While the OCF network is commonly introduced in the current finite element models, the interpenetrating NEF network is still largely unappreciated and neglected. The consideration of the collagen fibrillar networks in disc modeling strategies is essential for an accurate prediction of the local and overall disc responses. To reflect the real disc mechanics, any model should also consider changes of the disc shape and size with the spinal level and age (Amonoo-Kuofi, 1991; Kim et al., 2013), the disc hydration state (Urban and Maroudas, 1981; Derrouiche et al., 2019) and the disc health state. The latter aspects are very attractive in the aim to create patient-specific models taking into account realistic structure/macrostructure features of each patient and disc changes under applied loadings at different levels including disc geometry and local degradation events.

The main objective of this work is to formulate a fully three-dimensional model of a complete human intervertebral disc while taking into account the most recent discoveries about the interpenetrating collagen fibrillar networks and the structure-mechanics relationships of the annulus. The disc model is developed within a purely analytical framework in the final goal to

create time and cost-efficient patient-specific models. The predictions are used to predict the heterogeneous mechanics in the intervertebral disc under axial/torsion loading modes.

The outline of the present chapter is as follows. Section IV.2 describes the theory considering general assessments of the tube-like solid mechanics along with specifities regarding disc structure and macrostructure. Predictions are presented and discussed in Section IV.3. Section IV.4 closes this chapter with concluding remarks.

The following notation is used throughout the text. Tensors and vectors are respectively denoted by normal boldfaced letters and italicized boldfaced letters, while scalars and individual components of vectors and tensors are denoted by normal italicized letters. The superposed dot designates the time derivative.

IV.2. Model

IV.2.1. Tube-like kinematics

This section provides the kinematics framework of the tube-like solid mechanics. The general theory is detailed by Ogden (1997) and Holzapfel et al. (2000) for arterial applications in which some adaptations to discs are here brought especially considering regional variations in morphology and in structure-property relationships. Combined axial/torsion loadings at the external boundary of the disc will be considered in the present theoretical developments as illustrated in Figure IV.1. An internal pressure simulating the nucleus swelling may be activated when the compression is considered (Shah et al., 1978; Derrouiche et al., 2020). The nucleus is referred as the central portion $i = 0$ and the annulus is seen as a multi-layered tube divided into n rings $i = 1, \ldots n$. The half-disc topology is provided in Figure IV.2 in superior and sagittal views.

In the initial configuration, the solid is referenced in cylindrical polar coordinates (R, Θ, Z):

$$R^i \in \left[R^i_{inner}, R^i_{outer} \right], \ \Theta \in [0, 2\pi] \ \text{and} \ Z^i \in \left[0, H^i \right] \tag{IV.1}$$

where R^i_{inner} and R^i_{outer} denote the initial inner and outer radii of each ring, respectively, and H^i is the initial height. These anatomical features vary from a region to another according to the circumferential axe $\boldsymbol{\Theta}$.

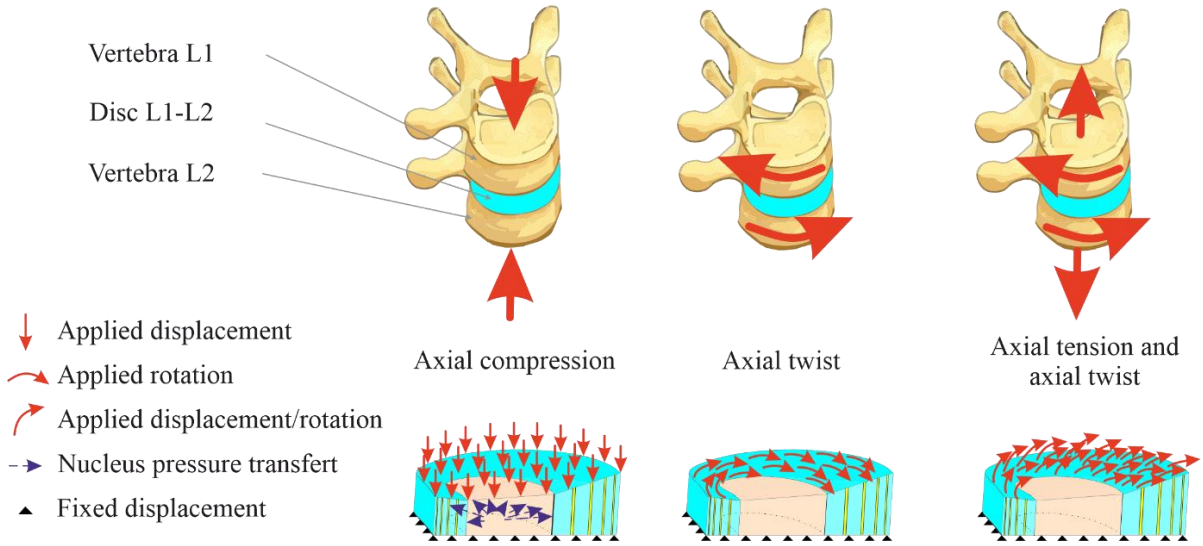

Figure IV.1. Axially/torsionally loaded functional spine unit (i.e. an intervertebral disc and two adjacent vertebrae) and related boundary conditions on the disc.

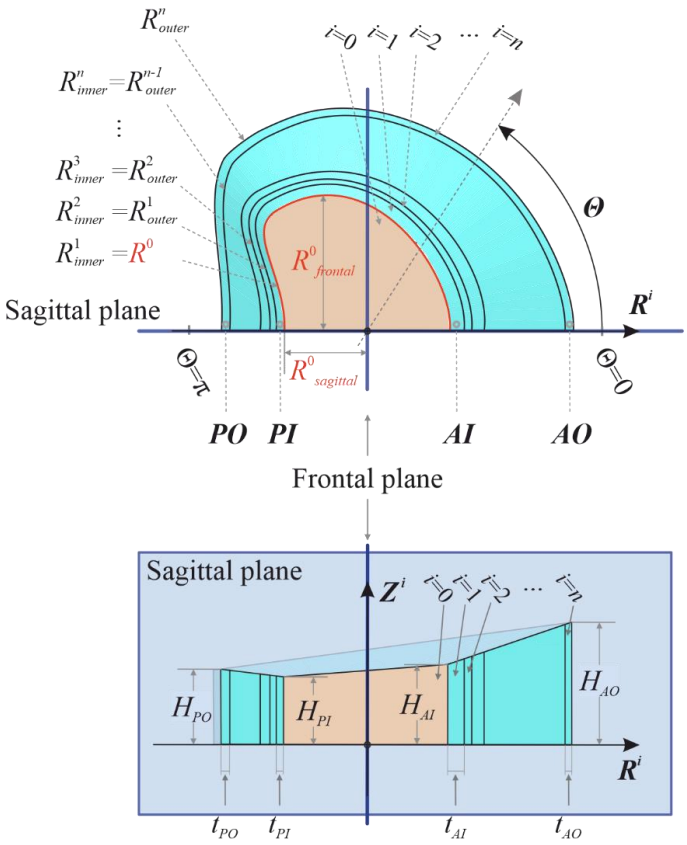

Figure IV.2. Disc macrostructure in the polar coordinates.

The kinematics of an axially/torsionally loaded tube-like solid is given as follows (Ogden, 1997):

$$r^i = f^i\left(R^i, r^{i-1}\right),\ \theta = \Theta + \frac{\varphi}{H^i} Z^i \quad \text{and} \quad z^i = \lambda_z^i Z^i \tag{IV.2}$$

with

$$r^i \in \left[r_{inner}^i, r_{outer}^i\right],\ \theta \in [0, 2\pi] \text{ and } z^i \in \left[0, h^i\right] \tag{IV.3}$$

In the present work, r_{inner}^i and r_{outer}^i denote the current inner and outer radii of each ring, respectively, and h^i is the current height. The term φ is the twist angle of the disc arising from the torsion and λ_z^i is the axial stretch applied in the ***z***-axis. The quantity f^i is a function dependent on the initial radius R^i of the ring *i* and the current radius r^{i-1} of the adjacent ring $i-1$.

The deformation gradient tensor $\mathbf{F}^i$ of each ring may be thus written as (Ogden, 1997):

$$\mathbf{F}^i = \frac{\partial r^i}{\partial R^i} \boldsymbol{e}_r \otimes \boldsymbol{E}_r + \frac{r^i}{R^i}\frac{\partial \theta}{\partial \Theta} \boldsymbol{e}_\theta \otimes \boldsymbol{E}_\theta + r^i \frac{\partial z^i}{\partial Z^i}\frac{\partial \theta}{\partial z^i} \boldsymbol{e}_\theta \otimes \boldsymbol{E}_z + \frac{\partial z^i}{\partial Z^i} \boldsymbol{e}_z \otimes \boldsymbol{E}_z \tag{IV.4}$$

where $\{\boldsymbol{E}_r, \boldsymbol{E}_\theta, \boldsymbol{E}_z\}$ and $\{\boldsymbol{e}_r, \boldsymbol{e}_\theta, \boldsymbol{e}_z\}$ are the unit vectors in the initial and current configurations, respectively.

The chemical-induced volumetric effects are also introduced via a chemo-mechanical coupling considering the multiplicative decomposition concept and the introduction of an intermediate configuration. The total deformation $\mathbf{F}^i = \mathbf{F}_{chem}^i \cdot \mathbf{F}_{mech}^i$ is decomposed into chemical-induced volumetric and mechanical parts $\mathbf{F}_{chem}^i$ and $\mathbf{F}_{mech}^i$.

The chemical deformation gradient tensor $\mathbf{F}_{chem}^i$ is expressed in each ring as follows:

$$\mathbf{F}_{chem}^i = \lambda_{chem\_r}^i \boldsymbol{e}_r \otimes \boldsymbol{E}_r + \lambda_{chem\_\theta}^i \boldsymbol{e}_\theta \otimes \boldsymbol{E}_\theta + \lambda_{chem\_z}^i \boldsymbol{e}_z \otimes \boldsymbol{E}_z \tag{IV.5}$$

where $\lambda_{chem\_r}^i$, $\lambda_{chem\_\theta}^i$ and $\lambda_{chem\_z}^i$ are the chemical stretches along the three polar directions ***r***, $\boldsymbol{\theta}$ and ***z***, respectively.

Using Eqs. (IV.4) to (IV.5), the mechanical deformation gradient tensor $\mathbf{F}_{mech}^{i}$ may be expressed as:

$$\mathbf{F}_{mech}^{i}=\frac{\partial r^{i}}{\partial R^{i}}\frac{1}{\lambda_{chem\_r}^{i}}\boldsymbol{e}_{r}\otimes\boldsymbol{E}_{r}+\frac{r^{i}}{R^{i}}\frac{1}{\lambda_{chem\_\theta}^{i}}\boldsymbol{e}_{\theta}\otimes\boldsymbol{E}_{\theta}+\frac{r^{i}\varphi}{H}\frac{1}{\lambda_{chem\_\theta}^{i}}\boldsymbol{e}_{\theta}\otimes\boldsymbol{E}_{z}+\frac{\lambda_{z}}{\lambda_{chem\_z}^{i}}\boldsymbol{e}_{z}\otimes\boldsymbol{E}_{z} \quad \text{(IV.6)}$$

The overall deformation gradient tensor $\mathbf{F}_{annulus}$ in the annulus may be calculated using a volume-weighted average of the LM deformations $\mathbf{F}^{LM\_i}=\mathbf{F}_{chem}^{LM\_i}.\mathbf{F}_{mech}^{LM\_i}$ and the ILM deformations $\mathbf{F}^{ILM\_i}=\mathbf{F}_{chem}^{ILM\_i}.\mathbf{F}_{mech}^{ILM\_i}$:

$$\mathbf{F}_{annulus}=\sum_{i=1,3...}^{n}\phi_{ring\_0}^{i}\mathbf{F}^{LM\_i}+\sum_{i=2,4...}^{n-1}\phi_{ring\_0}^{i}\mathbf{F}^{ILM\_i} \quad \text{(IV.7)}$$

in which $\phi_{ring\_0}^{i}$ is the initial volume fraction of a ring i.

IV.2.2. Annulus-nucleus interaction

IV.2.2.1. Nucleus swelling

When the disc is subjected to a compression, the nucleus swells (Figure IV.1). The latter may be introduced thanks to the chemical deformation gradient $\mathbf{F}_{chem}^{0}$ in the nucleus:

$$\mathbf{F}_{chem}^{0}=\left(1+\xi\chi\right)\mathbf{I} \quad \text{(IV.8)}$$

where ξ is the chemical expansion at the equilibrium state and χ is a function of time $\chi=1-\exp\left(-t/\tau\right)$ in which τ is the chemical expansion rate.

After a series of straightforward derivations, the nucleus actual radius r^{0} is given by:

$$r^{0}=\sqrt{\left(R^{0}\right)^{2}\frac{\varepsilon_{chem}^{0}+1}{\lambda_{z}^{0}}} \quad \text{(IV.9)}$$

in which $\varepsilon_{chem}^{0}=\det\left(\mathbf{F}_{chem}^{0}\right)-1$ is the chemical-induced volumetric strain in the nucleus with $\det\left(\mathbf{F}_{chem}^{0}\right)>0$ the Jacobian of the deformation gradient tensor $\mathbf{F}_{chem}^{0}$.

IV.2.2.2. Annulus swelling

The annulus volumetric change due to the internal fluid variation is expressed by the chemical deformation gradient $\mathbf{F}_{chem}^{i}$. Considering fluid diffusivity anisotropy in annulus, the latter is expressed in chapter II as:

$$\mathbf{F}_{chem}^{i} = \mathbf{I} + \frac{2}{\sqrt{3}} \cos\alpha^{i} \operatorname{diag}\left(\xi_r^i \chi_r^i,\ \xi_\theta^i \chi_\theta^i,\ \xi_z^i \chi_z^i\right) \tag{IV.10}$$

where ξ_r^i, ξ_θ^i and ξ_z^i are again chemical expansions at the equilibrium state and, χ_r^i, χ_θ^i and χ_z^i are again functions of time $\chi_{r,\theta,z}^i = 1 - \exp\left(-t/\tau_{r,\theta,z}^i\right)$ in which τ_r^i, τ_θ^i and τ_z^i are the chemical expansion rates. The term α^i denotes the OCF angle with respect to the circumferential direction of the disc.

After a series of straightforward derivations, the following expression is obtained for the function f^i using the continuity condition between the adjacent rings ($r_{inner}^i = r_{outer}^{i-1}$) and the mechanical incompressibility:

$$f^i = \sqrt{\left(\left(R_{inner,\,outer}^i\right)^2 - \left(R_{inner}^i\right)^2\right)\frac{\varepsilon_{chem}^i + 1}{\lambda_z^i} + \left(r_{outer}^{i-1}\right)^2} \tag{IV.11}$$

where $\varepsilon_{chem}^i = \det\left(\mathbf{F}_{chem}^i\right) - 1$ is the chemical-induced volumetric strain in the ring i.

The annulus is assembled by considering the effective interactions between adjacent layers via the compatibility conditions on the deformations $\mathbf{F}^i$ and on the Cauchy stresses $\boldsymbol{\sigma}^i$:

$$\mathbf{F}^{LM\_i}.\boldsymbol{n}_0^i = \mathbf{F}^{ILM\_i+1}.\boldsymbol{n}_0^i \text{ and } \boldsymbol{\sigma}^{LM\_i}.\boldsymbol{n}^i = \boldsymbol{\sigma}^{ILM\_i+1}.\boldsymbol{n}^i \tag{IV.12}$$

where $\boldsymbol{n}_0^i$ and $\boldsymbol{n}^i$ are arbitrary unit vectors at the LM/ILM interfaces in the initial and current configurations, respectively.

In the absence of body loads, the equilibrium equations write as the spatial divergence of the overall Cauchy stress tensor $\boldsymbol{\sigma}$:

$$\mathrm{div}(\boldsymbol{\sigma}) = 0 \tag{IV.13}$$

Considering the symmetry of the stress tensor $\boldsymbol{\sigma} = \boldsymbol{\sigma}^T$, Eq. (IV.13) can be re-written using the stress components in the cylindrical coordinate system as follows:

$$\frac{\partial \sigma_{rr}}{\partial r} + \frac{1}{r}\frac{\partial \sigma_{r\theta}}{\partial \theta} + \frac{\partial \sigma_{rz}}{\partial z} + \frac{\sigma_{rr} - \sigma_{\theta\theta}}{r} \equiv \frac{\mathrm{d}\sigma_{rr}}{\mathrm{d}r} + \frac{\sigma_{rr} - \sigma_{\theta\theta}}{r} = 0 \tag{IV.14}$$

From this equation and the boundary condition of the radial Cauchy stress $\sigma_{rr}^i \Big|_{r^i = r_{outer}^n} = 0$ on the outer wall of the last ring of the annulus, the internal pressure of the nucleus $\sigma_{nucleus} = -\sigma_{rr}^i \Big|_{r^i = r_{inner}^1}$ on the inner wall of the first ring of the annulus can be expressed dependent on θ direction in the form (Holzapfel et al., 2000):

$$\sigma_{nucleus} = 2\int_0^{\pi} \int_{r_{inner}^1}^{r_{outer}^n} \frac{\sigma_{\theta\theta}^i - \sigma_{rr}^i}{r^i} \mathrm{d}r^i \mathrm{d}\theta \tag{IV.15}$$

IV.2.3. Disc macrostructure

IV.2.3.1. Disc geometry

As shown in the half-disc topology provided in Figure IV.2, we consider radial and circumferential variations of the geometry in order to propose anatomically accurate patient-specific models. For reasons of symmetry with respect to the sagittal plane of the disc, the nucleus initial radius R^0 was defined by the following special mathematical function by an angle Θ between the anterior region $(\Theta = 0)$ and the posterior region $(\Theta = \pi)$ following the direction $\boldsymbol{\Theta}$ as illustrated in Figure IV.2:

$$R^0 = R_{frontal}^0 \left[\left(1 + f_R - f_R f_\Theta\right)\left(1 - H_\Theta\right) + \left(f_R \left(\frac{f_\Theta^4 - 1}{f_\Theta(\pi) - 1} \right) + 1 \right) H_\Theta \right] \tag{IV.16}$$

in which H_Θ is the Heaviside function:

$$H_\Theta = 1 \quad \Theta > \frac{2\pi}{3} \text{ and } H_\Theta = 0 \quad \Theta \le \frac{2\pi}{3} \tag{IV.17}$$

The function f_Θ is expressed as:

$$f_\Theta = \exp\left(-\left(\Theta - \frac{2\pi}{3}\right)^2\right) \tag{IV.18}$$

The term f_R is a shape factor of the nucleus given by the ratio between the sagittal and frontal initial radii $R^0_{sagittal}$ and $R^0_{frontal}$:

$$f_R = \frac{R^0_{sagittal}}{R^0_{frontal}} - 1 \tag{IV.19}$$

In the limit case $R^0_{sagittal} = R^0_{frontal}$, Eq. (IV.16) becomes $R^0 = R^0_{frontal}$ and the disc has a circular basis.

The initial radius R^i in each ring is calculated as follows:

$$R^i_{outer} = R^0 + \sum_{k=1}^{i} \frac{t_k}{2} \tag{IV.20}$$

in which t_k is the ring thickness. The continuity condition between the adjacent rings writtes $R^i_{inner} = R^{i-1}_{outer}$ (see Figure IV.2).

IV.2.3.2. Thickness regional variation

The thicknesses of the LM and ILM layers are given by the following linear equations:

$$t_i^{LM} = a_t i + b_t \quad \text{for} \quad i = 1,3,5...n \tag{IV.21}$$

$$t_i^{ILM} = r_{ILM/LM} t_i^{LM} \quad \text{for} \quad i = 2,4,6...n-1 \tag{IV.22}$$

where $r_{ILM/LM}$ represents the thickness ratio of the ILM and LM zones and, a_t and b_t are functions expressed as:

$$a_t = \frac{\left(t_{PO} - t_{PI} + t_{AI} - t_{AO}\right)\Theta + \left(t_{AO} - t_{AI}\right)\pi}{\left(n-1\right)\pi} \tag{IV.23}$$

$$b_t = \frac{\left(t_{PI} - t_{AI}\right)\Theta + t_{AI}\pi}{\pi} - a \tag{IV.24}$$

in which t_{PO}, t_{PI}, t_{AO} and t_{AI} are the regional ring thicknesses. The terms t_{AO} and t_{PO} denote the thicknesses for the outer side of the ring $i=n$, respectively, in the anterior region $(\Theta=0)$ and the posterior region $(\Theta=\pi)$ whereas the terms t_{AI} and t_{PI} are their counterparts for the inner side of the ring $i=1$. The linear interpolation is performed with an angular increment $\delta\theta$ of 1°. The same increment is fixed for all the other spatial discretizations in the circumferential direction. Note that the radial disctretization is fixed by the total number of layers *n*.

IV.2.3.3. Height regional variation

The regional variation of the disc height is taken into account using the following linear equation:

$$H^i = a_H i + b_H \tag{IV.25}$$

with

$$a_H = \frac{\left(H_{PO} + H_{AI} - H_{AO} - H_{PI}\right)\Theta + \left(H_{AO} - H_{AI}\right)\pi}{\left(n-1\right)\pi} \tag{IV.26}$$

$$b_H = \frac{\left(H_{PI} - H_{AI}\right)\Theta + H_{AI}\pi}{\pi} - a_H \tag{IV.27}$$

in which H_{PO}, H_{PI}, H_{AO} and H_{AI} are the regional disc heights.

The final model takes into account the non-symmetry both in thickness and in height in order to propose anatomically accurate representations.

IV.2.4. Disc structure

IV.2.4.1. Constituents

As illustrated in Figure IV.3, the disc collagen fibrillar networks are decomposed into OCF and (inter-fibrillar and inter-lamellar) NEF both superimposed into the extracellular matrix (ECM). The volume fractions of these different solid constituents are calculated as follows:

$$\phi_{ECM} = \frac{\phi_{ECM\_0}}{\varepsilon_{chem}+1},\ \phi_{OCF} = \frac{\phi_{OCF\_0}}{\varepsilon_{chem}+1} \text{ and } \phi_{NEF} = \frac{\phi_{NEF\_0}}{\varepsilon_{chem}+1} \tag{IV.28}$$

in which ϕ_{ECM_0}, ϕ_{OCF_0} and ϕ_{NEF_0} are the volume fractions at the chemical equilibrium state and, $\varepsilon_{chem} = \det\left(\mathbf{F}_{chem}\right) - 1$ is the chemical-induced volumetric strain. The volume fraction of the fluid phase ϕ_{fluid} corresponds to $\phi_{fluid} = 1 - \phi_{ECM} - \phi_{OCF} - \phi_{FCN}$.

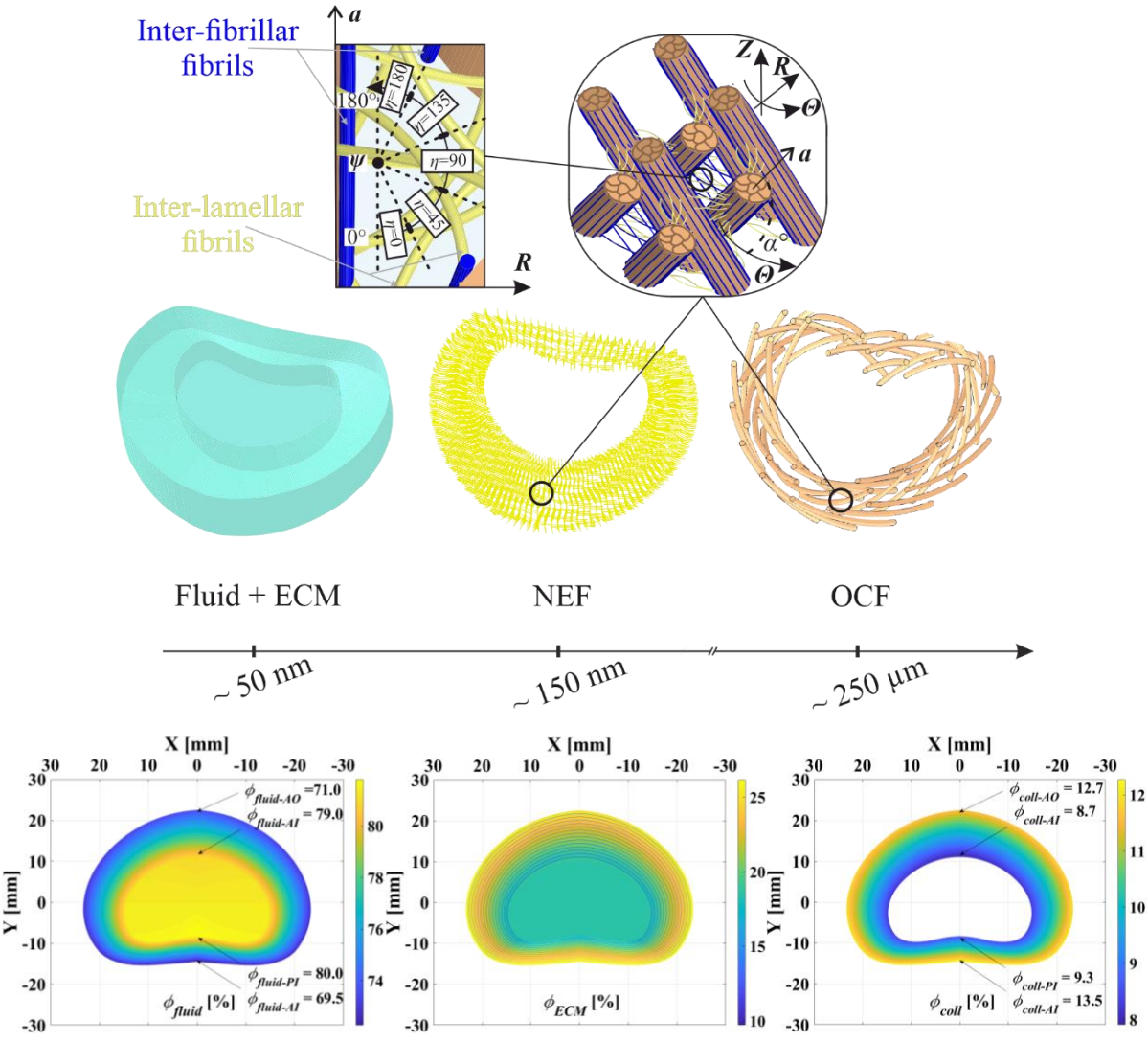

Figure IV.3. Disc structure decomposition into ECM (along with fluid) and interpenetrating collagen fibrillar networks at the nanoscale (NEF) and at the microscale (OCF). Contour plots in the superior view of the disc show the regional dependent quantities in terms of fluid phase fraction ϕ_{fluid}, collagen fraction $\phi_{coll} = \phi_{NEF} + \phi_{OCF}$ and ECM fraction $\phi_{ECM} = 1 - \phi_{fluid} - \phi_{coll}$.

The regional variation in quantities was taken into account using linear interpolations similar to those introduced above for the macrostructure features. Figure IV.3 provides the regional dependent quantities in the form of contour plots in the superior view of the disc.

IV.2.4.2. Hierarchical fibrillar structure

The interpenetrating collagen fibrillar networks are spatially disposed in the model using two representative angles with respect to the global benchmark of the disc. The angles α^i are introduced to dispose the micro-sized OCF with respect to the circumferential direction of the disc with alternate orientations between successive lamellae. The angles ψ^i is introduced to dispose the nano-sized NEF network with respect to the radial direction in the OCF parallel plane.

The OCF in each LM ring is described geometrically by the unit vector $\boldsymbol{a}^i$ expressed, in the current configuration, with respect to the global benchmark of the disc:

$$\boldsymbol{a}^i = \cos\alpha^i\,\boldsymbol{\theta} + \sin\alpha^i\,\boldsymbol{z} \tag{IV.29}$$

In order to introduce the change in the OCF angle induced by the circumferential stretch λ_θ, a measure of the reorientation may be considered geometrically using the following relation:

$$\alpha^i = \arctan\left(\frac{\lambda_\theta^i}{\lambda_z^i}\tan\alpha_0^i\right) \tag{IV.30}$$

in which α_0^i is the OCF angle with respect to the circumferential direction of the disc in the initial configuration (see Figure IV.4a) and λ_z^i is the axial stretch.

The unit vector $\boldsymbol{b}^i$ of each fibril is expressed, in the current configuration, with respect to the global benchmark of the disc as follows:

$$\boldsymbol{b}^i = \sin\psi^i\,\boldsymbol{r} + \cos\alpha\cos\psi^i\,\boldsymbol{\theta} + \sin\alpha^i\cos\psi^i\,\boldsymbol{z} \tag{IV.31}$$

Again, the stretch-induced reorientation of the fibrils array is geometrically considered in each ring using the following expression:

$$\psi^i = \arctan\left(\left(1-H\left(\psi_0^i-90°\right)\right)\frac{\lambda_r^i}{\lambda_f^i}\tan\psi_0^i + H\left(\psi_0^i-90°\right)\left(180° + \frac{\lambda_r^i}{\lambda_f^i}\tan\psi_0^i\right)\right) \tag{IV.32}$$

in which ψ_0^i is the fibrils angle in the initial configuration, λ_r^i is the radial stretch and λ_f^i is the stretch in the OCF direction. The term $H(\bullet)$ is the Heaviside function.

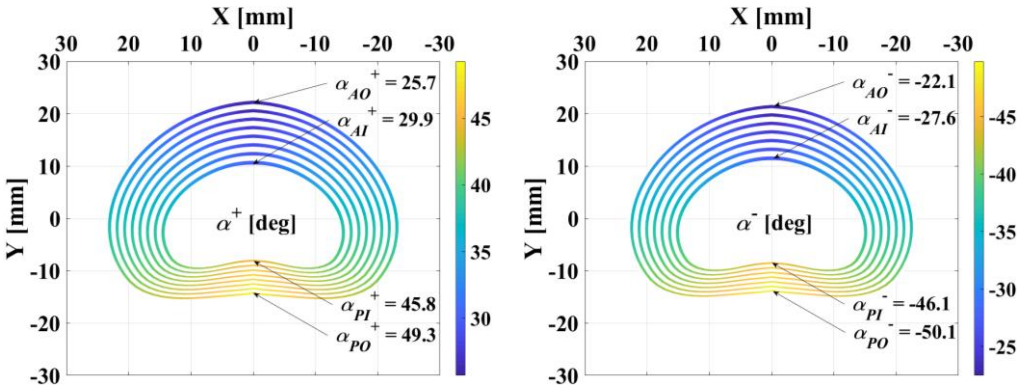

(a)

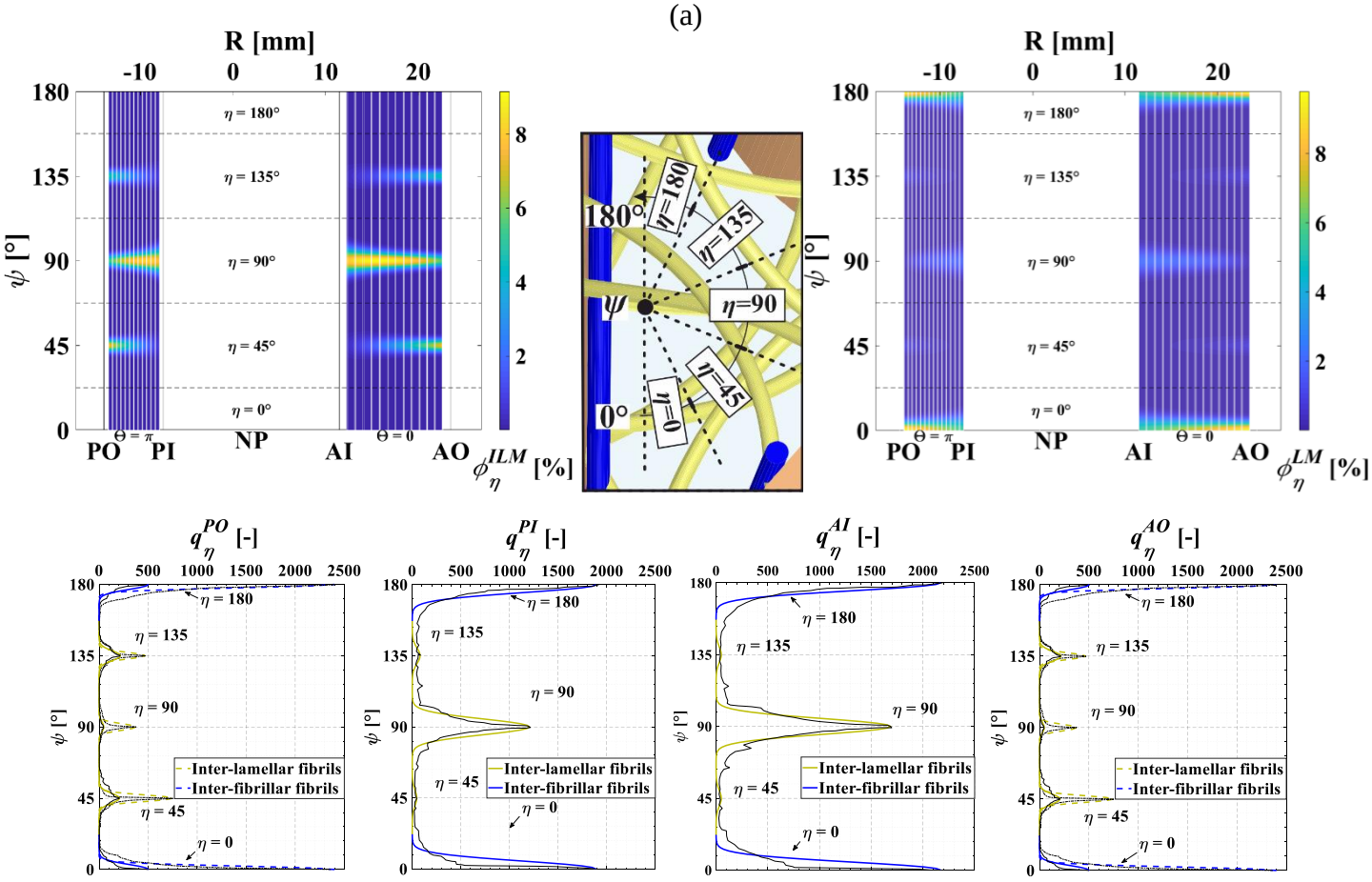

(b)

Figure IV.4. Organization of the interpenetrating collagen fibrillar networks: (a) OCF angle in the form of contour plots in the superior view of the disc, (b) fibrils angle in the form of contour plots in the sagittal view of the disc. The fibrils spatial distribution is obtained by the linear interpolation of approximated Gaussian-type distributions in the outer and inner boundaries of PO (Posterior-Outer), AO (Anterior-Outer), PI (Posterior-Inner) and AI (Anterior-Inner) regions. The dashed lines in the Gaussian-type distributions are extracted from the work of Tavakoli et al. (2017, 2020).

The regional variation in network orientation was considered using linear interpolations with radial and circumferential variations as detailed in Appendix IV.A. The collagen fibrillar organization is provided in Figure IV.4 in the form of contour plots in the superior view of the disc for the OCF network and in the form of contour plots in the sagittal view of the disc for the NEF network.

IV.2.5. Constitutive equations

The local structure-mechanics relations are described using a recently developed fully three-dimensional constitutive model (Tamoud et al., 2021a). The model efficiencies to reproduce regional dependent multiaxial mechanics till failure of the human lumbar disc annulus were shown. In what follows, we present a summary of the constitutive equations of both healthy and damaged components.

IV.2.5.1. Healthy components

In virtue of the chemo-mechanical coupling, the total free energy W is additively split into a mechanical part W_{mech} and a chemical part W_{chem}:

$$W = W_{mech} + W_{chem} \tag{IV.33}$$

The mechanical free energy W_{mech} is obtained using as ensemble-volume averaged homogenization procedure a volume-weighted average of the different solid components:

$$W_{mech} = \phi_{OCF} W_{\alpha} + \sum_{\psi} \phi_{\psi} W_{\psi} + \phi_{ECM} W_{ECM} \tag{IV.34}$$

in which W_{α} is the OCF free energy, W_{ψ} is the fibrils network free energy and W_{ECM} is the ECM free energy. The quantity $\phi_{\psi} = \phi_{\eta}\phi_{NEF}$ is the fibrils volume fraction calculated using the NEF volume fraction ϕ_{NEF} in a layer and the volume fraction of fibril bundles ϕ_{η} in a layer dependent on η with $\sum_{\eta} \phi_{\eta} = 1$.

The different free energies in Eq. (IV.27) are expressed by considering both collagen fibrillar networks and ECM as hyperelastic bodies with isotropic, homogeneous and incompressible features. The free energies W_α and W_ψ may be expressed as a function of the fourth stretch invariants $\bar{I}_{4\alpha} = \boldsymbol{a}.\mathbf{C}_{mech}.\boldsymbol{a} = \lambda_\alpha^2$ and $\bar{I}_{4\psi} = \boldsymbol{b}.\mathbf{C}_{mech}.\boldsymbol{b} = \lambda_\psi^2$ of the right Cauchy-Green deformation $\mathbf{C}_{mech} = \mathbf{F}_{mech}^T.\mathbf{F}_{mech}$. To describe the 'toe'-to-'linear' transition of the collagen response, two distinct relations are retained below and above $\lambda_{\alpha,\psi}^*$:

$$W_{\alpha,\psi} = H\left(\bar{I}_{4\alpha,\psi} - 1\right)\left[\frac{1}{2}\frac{C_1}{C_2}\left(\exp\left(C_2\left(\bar{I}_{4\alpha,\psi} - 1\right)^2\right) - 1\right)\right] \quad \lambda_{\alpha,\psi} < \lambda_{\alpha,\psi}^* \tag{IV.35}$$

below $\lambda_{\alpha,\psi}^*$ and,

$$W_{\alpha,\psi} = H\left(\bar{I}_{4\alpha,\psi} - 1\right)\left[\frac{C_3}{2}\left(\bar{I}_{4\alpha,\psi} - \bar{I}_{4\alpha,\psi}^*\right)^2 + \zeta_{\alpha,\psi}\left(\bar{I}_{4\alpha,\psi} - \nu_{\alpha,\psi}\right)\right] \quad \lambda_{\alpha,\psi} \geq \lambda_{\alpha,\psi}^* \tag{IV.36}$$

above $\lambda_{\alpha,\psi}^*$.

The terms C_1, C_2 and C_3 are material constants, $\bar{I}_{4\alpha,\psi}^*$ is the fourth stretch invariant for $\lambda_{\alpha,\psi} = \lambda_{\alpha,\psi}^*$, $H(\bullet)$ is the Heaviside function that ensures only stretching of the collagen and, $\zeta_{\alpha,\psi}$ and $\nu_{\alpha,\psi}$ are functions that ensure continuity between 'toe' and 'linear' regions:

$$\zeta_{\alpha,\psi} = C_1\left(\bar{I}_{4\alpha,\psi}^* - 1\right)\exp\left(C_2\left(\bar{I}_{4\alpha,\psi}^* - 1\right)^2\right) \tag{IV.37}$$

$$\nu_{\alpha,\psi} = \bar{I}_{4\alpha,\psi}^* - \frac{C_1}{2C_2\zeta_{\alpha,\psi}}\left(\exp\left(C_2\left(\bar{I}_{4\alpha,\psi}^* - 1\right)^2\right) - 1\right) \tag{IV.38}$$

The ECM free energy W_{ECM} is given by as a function of the first stretch invariant $\bar{I}_1 = \mathrm{tr}\left(\mathbf{C}_{mech}\right)$ of the right Cauchy-Green deformation $\mathbf{C}_{mech} = \mathbf{F}_{mech}^T.\mathbf{F}_{mech}$:

$$W_{ECM} = \frac{1}{2}G_{ECM}\left(\bar{I}_1 - 3\right) \tag{IV.39}$$

in which G_{ECM} is the ECM shear modulus.

The chemical free energy W_{chem} is expressed as follows:

$$W_{chem} = \phi_{fluid} \frac{1}{2} \frac{K_1}{K_2} \left(\exp\left(K_2 \varepsilon_{chem}^2 \right) - 1 \right) \tag{IV.40}$$

where K_1 and K_2 are material constants, K_1 and K_1/K_2 being the initial and maximal volumetric stiffness values.

The overall Cauchy stress tensor $\boldsymbol{\sigma}_{annulus}$ in the annulus may be calculated as:

$$\boldsymbol{\sigma}_{annulus} = \sum_{i=1,3,..}^{n} \phi_{ring}^{i} \left(\boldsymbol{\sigma}_{mech}^{LM\_i} + \boldsymbol{\sigma}_{chem}^{LM\_i} \right) + \sum_{i=2,4,..}^{n-1} \phi_{ring}^{i} \left(\boldsymbol{\sigma}_{mech}^{ILM\_i} + \boldsymbol{\sigma}_{chem}^{ILM\_i} \right) \tag{IV.41}$$

in which ϕ_{ring}^{i} is the current volume fraction of a ring *i*:

$$\phi_{ring}^{i} = \frac{\left(\varepsilon_{chem}^{i} + 1 \right) t_i}{\sum_{j=1}^{n} \left(\varepsilon_{chem}^{j} + 1 \right) t_j} \tag{IV.42}$$

The stress in the nucleus is given by Eq. (IV.15).

IV.2.5.2. Damaged components

The above free energies may be modified to consider the internal stiffness degradation due to the development of mechanical-induced damage (see chapter II):

$$W_{mech} = \left(1 - d_\alpha \right) \phi_{OCF} W_\alpha + \sum_{\psi} \left(1 - d_\psi \right) \phi_\psi W_\psi + \left(1 - d_{ECM} \right) \phi_{ECM} W_{ECM} \tag{IV.43}$$

in which d_α and d_ψ are variables representing the damage events occurring within the interpenetrating collagen fibrillar networks and d_{ECM} is the variable representing the ECM damage.

A continuous damage evolution is assumed over the entire loading history without healing possibilities. The progressive damage of each individual solid component (OCF, NEF and ECM) follows a two-parameter Weibull statistical distribution governed by their respective internal stress:

$$d_\alpha = 1 - \exp\left(-\left(\frac{\left\| \mathbf{P}_{OCF} \right\|}{\beta_{OCF}} \right)^{\gamma_{OCF}} \right) \quad 0 \le d_\alpha \le 1 \tag{IV.44}$$

$$d_\psi = 1 - \exp\left(-\left(\frac{\left\| \mathbf{P}_{\psi} \right\|}{\beta_{NEF}} \right)^{\gamma_{NEF}} \right) \quad 0 \le d_\psi \le 1 \tag{IV.45}$$

$$d_{ECM} = 1 - \exp\left(-\left(\frac{\left\| \mathbf{P}_{ECM} \right\|}{\beta_{ECM}} \right)^{\gamma_{ECM}} \right) \quad 0 \le d_{ECM} \le 1 \tag{IV.46}$$

in which γ_{OCF}, β_{OCF}, γ_{NEF}, β_{NEF}, γ_{ECM} and β_{ECM} are damage parameters. The term $\left\| \mathbf{P} \right\| = \sqrt{\mathrm{tr}\left(\mathbf{P}.\mathbf{P}^T \right)}$ denotes the Frobenius norm of the effective first Piola-Kirchhoff stress $\mathbf{P}$.

A strong coupling exists between hydration and mechanical-induced damage (Werbner et al., 2019). In ordert to consider the latter coupling, the chemical-induced volumetric strain ε_{chem} in the free energy (IV.40) is affected by the local damage events using the following expression (see chapter II):

$$\varepsilon_{chem} = \left(\det\left(\mathbf{F}_{chem} \right) - 1 \right) \left(1 - d_\alpha \right) \left(1 - \frac{1}{n} \sum_{\psi}^{n} d_\psi \right) \left(1 - d_{ECM} \right) \tag{IV.47}$$

IV.2.6. Overall disc response

For a known deformation state, the torsional couple M_t of the whole disc may be expressed as the additional contribution of the annulus and the nucleus $M_t = M_{t\_annulus} + M_{t\_nucleus}$:

$$M_{t\_annulus} = 2\int_0^{\pi} \int_{r_{inner}^1}^{r_{outer}^n} \sigma_{\theta z}^i \left(r^i \right)^2 \mathrm{d}r^i \mathrm{d}\theta \text{ and } M_{t\_nucleus} = 2\int_0^{\pi} \int_0^{r^0} \sigma_{\theta z}^0 \left(r^0 \right)^2 \mathrm{d}r^0 \mathrm{d}\theta \tag{IV.48}$$

in which $\sigma_{\theta z}^i$ is the local shear stress component.

For a known deformation state, the axial load $F_{annulus}$ of the annulus may be expressed by:

$$F_{annulus} = 2\int_0^{\pi} \int_{r_{inner}^1}^{r_{outer}^n} \sigma_{zz}^i r^i \, \mathrm{d}r^i \mathrm{d}\theta \tag{IV.49}$$

The axial load *F* of the disc is obtained from the following formula:

$$F = 2\int_{0}^{\pi}\int_{r_{inner}^{1}}^{r_{outer}^{n}} \left(2\sigma_{zz}^{i} - \sigma_{\theta\theta}^{i} - \sigma_{rr}^{i}\right) r^{i}\, \mathrm{d}r^{i}\mathrm{d}\theta \qquad \text{(IV.50)}$$

in which σ_{zz}^{i}, $\sigma_{\theta\theta}^{i}$ and σ_{rr}^{i} are the axial, circumferential and radial stress components.

IV.3. Results and discussion

The model was entirely coded in MATLAB software. At this step of the model development, predictions on axially/torsionally loaded discs can be analyzed. The simulations were performed at a displacement rate of 0.01 mm/s and a twist rate of 0.1 °/s in order to maintain quasi-static loading conditions. The maximum ranges are changed according to the observed local fields in the disc core.

IV.3.1. Model inputs

Table IV.1 provides the anatomical data used as direct inputs for a lumbar disc model geometry taken from cadaver disc images at the L1-L2 level of the Holzapfel et al. (2005) work. The annulus size is considered to be approximately 50% of the disc volume (Violas et al., 2007) and is subdivided into 15 different lamellae that are intercalated with 14 ILM. The base radius R^0 is calibrated from the cadaver disc images of Holzapfel et al. (2005) resulting in a ratio between the sagittal and frontal radii of $R^0_{sagittal} / R^0_{frontal}$ = 0.68 with a frontal radius of $R^0_{frontal}$ = 15 mm. The values of the OCF orientation (with alternating signs between successive lamellae), the collagen volume fraction and the fluid volume fraction are extracted from previous documented experimental findings (Skaggs et al., 1994; Acaroglu et al., 1995; Ebara et al., 1996) and are listed in Table IV.1.

	Regions				References
	AO	AI	PO	PI	
Layer thickness [mm]	t_{AO}	t_{AI}	t_{PO}	t_{PI}	Holzapfel et al. (2005)
	0.69	0.76	0.38	0.40	
Disc height [mm]	H_{AO}	H_{AI}	H_{PO}	H_{PI}	Holzapfel et al. (2005)
	12.8	8.40	8.00	7.20	
OCF orientation [deg]	$\alpha_{AO}^{+/-}$	$\alpha_{AI}^{+/-}$	$\alpha_{PO}^{+/-}$	$\alpha_{PI}^{+/-}$	Holzapfel et al. (2005)
	+25.7/-	+29.9/-	+49.3/-	+45.8/-	
	22.1	27.6	50.1	46.1	
Collagen volume fraction [-]	ϕ_{coll_AO}	ϕ_{coll_AI}	ϕ_{coll_PO}	ϕ_{coll_PI}	Skaggs et al. (1994)
	0.127	0.087	0.135	0.093	
Fluid volume fraction [-]	ϕ_{fluid_AO}	ϕ_{fluid_AI}	ϕ_{fluid_PO}	ϕ_{fluid_PI}	Acaroglu et al. (1995) and Ebara et al. (1996)
	0.710	0.790	0.695	0.800	

Table IV.1. Disc macrostructure and structure features.

The intrinsic material parameters, identified in the previous chapters, are listed in Tables IV.2 and IV.3. A linear interpolation is here achieved for the regional dependent fibers parameters using the formulation provided in Appendix IV.B.

Constituents	Parameters	Values	
ECM	G_{ECM}	0.01	$[\mathrm{MPa}]$
	γ_{ECM}	2	$[-]$
	β_{ECM}	5.5	$[\mathrm{MPa}]$
NEF	C_1	12	$[\mathrm{MPa}]$
	C_2	0.2	$[-]$
	C_3	1.5	$[\mathrm{MPa}]$
	λ_{ψ}^{*}	1.7	$[-]$
	γ_{NEF}	6	$[-]$
	β_{NEF}	400	$[\mathrm{MPa}]$
Swelling	K_1	0.14	$[\mathrm{MPa}]$
	K_2	0.0075	$[-]$

Table IV.2. ECM, NEF and swelling parameters.

Parameters		Regions			
		AO	PO	AI	PI
C_1	$[\mathbf{MPa}]$	40	26	26	3
C_2	$[-]$	880	58	30	11
C_3	$[\mathbf{MPa}]$	500	300	400	80
λ_θ^*	$[-]$	1.02	1.07	1.1	1.14
γ_{OCF}	$[-]$	5	5	5	5
β_{OCF}	$[\mathbf{MPa}]$	215	125	120	70

Table IV.3. OCF parameters.

IV.3.2. Overall disc response

The simulated load curve obtained on a healthy disc upon compression are compared in Figure IV.5a with available experimental observations taken from the literature (Virgin, 1951; Markolf et al., 1974; Adams et al., 1993). As far as we know, these papers are the only one that provide data on lumbar discs loaded till failure upon a displacement-controlled compression. Note that the exact level in the lumbar spine is not specified in these experimental works and important variabilities may exist regarding the disc health state of donor (age, degeneration…) and the testing protocol (loading conditions, environment…). In this regard, the predicted curve may be considered as acceptable since it falls through the experimental points. Nonetheless, when the damage process is introduced in the model prediction, the result underestimates the experimental points as observed in Figure IV.5b. When the OCF damage is excluded from the analysis, the overall disc response first follows the damaged disc response path and then converges progressively towards the healthy disc response path at higher applied displacements. Recall that the constitutive model has been identified at the scale of a unit lamella (stretched along the OCF direction) for the four main disc regions (PO, PI, AO and AI) (Tamoud et al., 2021a). It is clear that the passage from the structural unit to the whole macrostructure needs some adjustement to consider effective interactions between the different lamellae and even between the different networks by adjusting the damage severity to correct its effect on the overall disc stiffness. The latter statement holds true for the

interpenetrating network of fibrils for which identification has been carried out at the scale of multi-layered annulus stretched along the radial direction (Tamoud et al., 2021c). Whereas the fibrils in LM (inter-fibrillar fibrils) seems to play a minor role on the disc resistance, Figure IV.5a emphasizes the influential and decisive role of the NEF network in ILM (inter-lamellar fibrils) on the disc stiffness especially at low applied displacements. As shown in Figure IV.5b, when the NEF network damage in ILM is not taken into consideration, the overall response is first that of a healthy disc and then it diverges more and more as the applied displacement increases. It can be also observed that the ECM damage has a minor effect on the overall disc resistance.

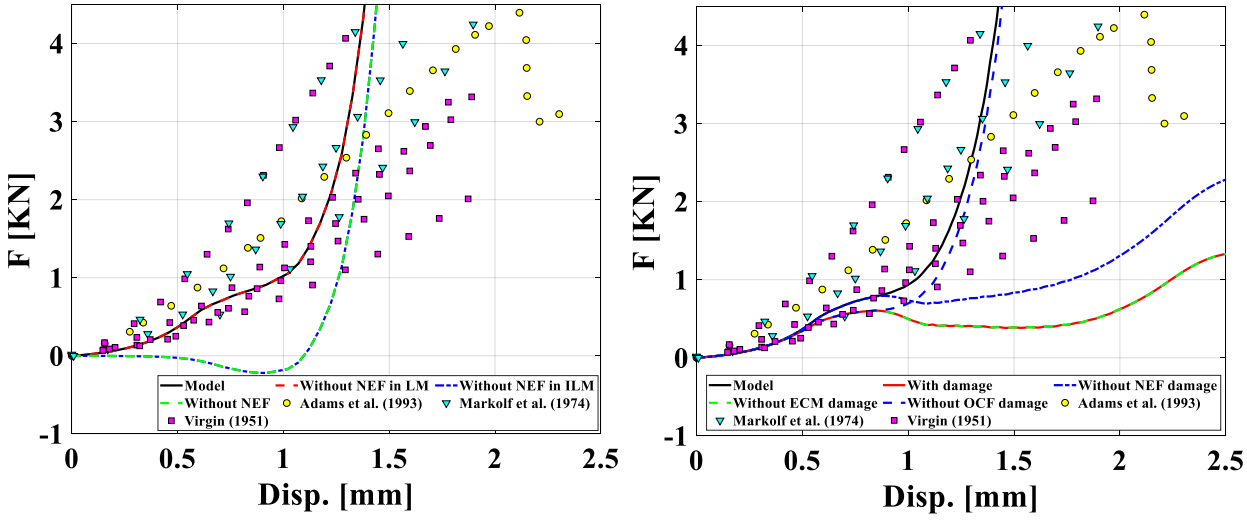

(a) (b)

Figure IV.5. Predicted load curves of the axially compressed disc in comparison to experiments (lines: model; symbols: experiments): (a) influence of the LM/ILM collagen networks, (b) influence of the damage events.

IV.3.3. Strain fields

The predicted radial strains in the core of a compressed healthy disc are compared in Figure IV.6 with the stereo-radiographic experimental data of Costi et al. (2007). The model results were averaged in different zones and then normalized by the applied displacement. Note that the Costi et al. (2007) data are typical results averaged for the asymmetric values in the right and left sides

of the sagittal plane. A weak regional variation is predicted but, except posterior and nucleus zones, the model provides acceptable predictions of the other disc regions.

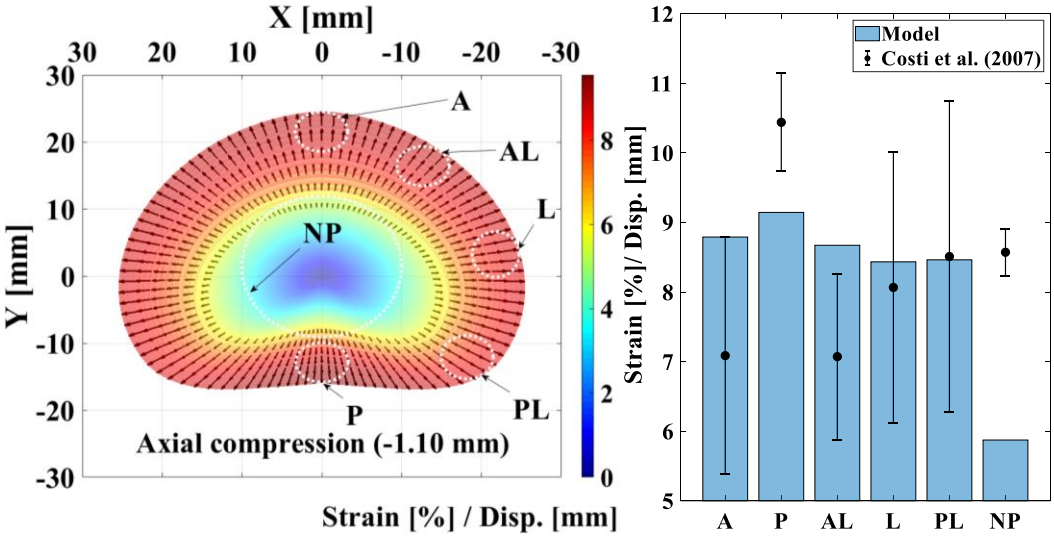

Figure IV.6. Predicted normalized radial strains (%/mm) in a disc compressed at 1.1 mm. The comparison to Costi et al. (2007) data is performed for different regions in which the local strains are averaged (A: Anterior, P: Posterior, AL: Anterior-Lateral, L: Lateral, PL: Posterior-Lateral, NP: nucleus pulposus).

For different loading cases of combined axial/torsion loadings, the local strain components can be analyzed in Figures IV.7 and IV.8. Figure IV.7 shows the low strain components that appeared under torsion are extremely amplified when the nucleus is activated by the combined effect of a compression.

Figure IV.8 highlights the very-low radial strains upon pure torsion and important values when the compression is applied. In the latter case, the ILM is found to severly swell whereas the LM shrinks. This phenomenon leads to an auxetic behavior in the radial direction (Tamoud et al., 2021b). This volumetric feature of the lamellar structure is fundamental for the disc functionality for maintaining nucleus swelling and absorbing applied loads. Interestingly, the auxetic response is also influenced by the disc morphology as evidenced in Figure IV.9 in which the contour plots of a simplified disc version are presented. Actually, the heterogeneity of the strain fields is determined by the local structure-mechanics relations but also by the morphology.

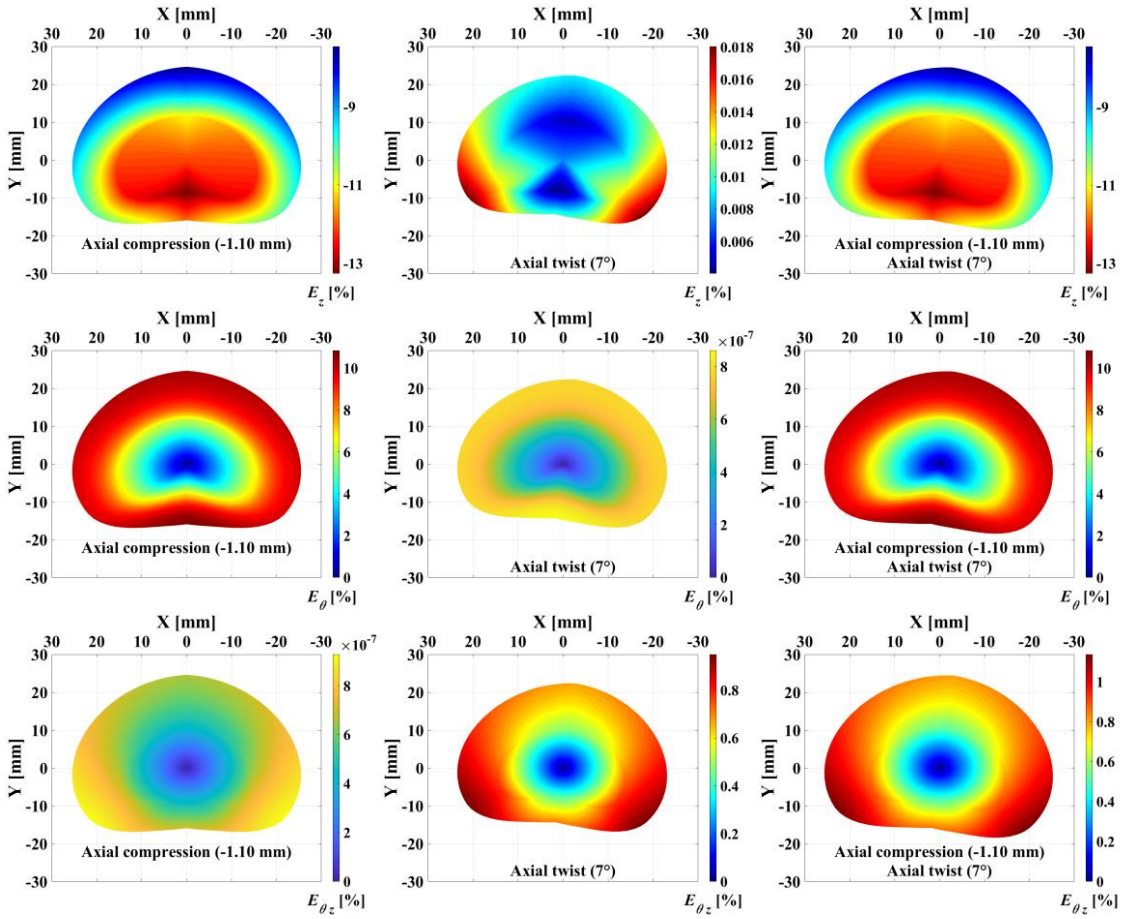

Figure IV.7. Contour plots of the local axial, circumferential and shear strains E_z, E_θ and $E_{\theta z}$ in axially/torsionally loaded discs.

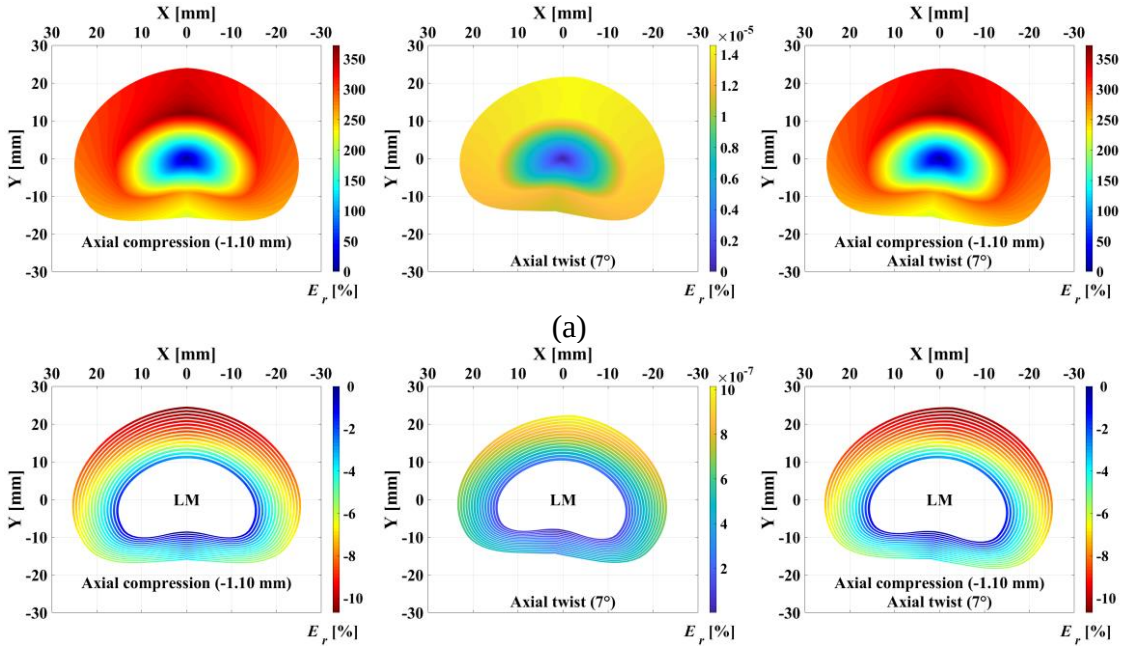

(a)

(b)

Figure IV.8. Contour plots of the local radial strain E_r in axially/torsionally loaded discs: (a) in ILM, (b) in LM.

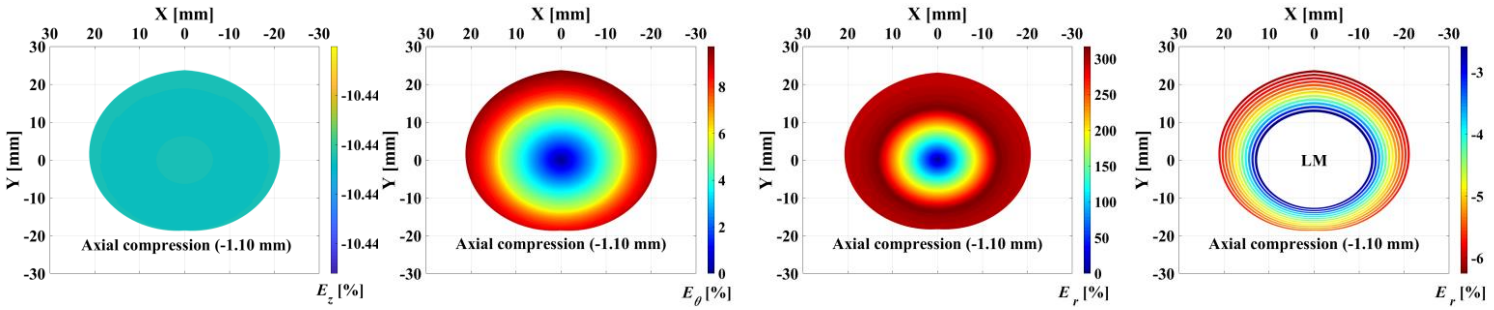

(a)

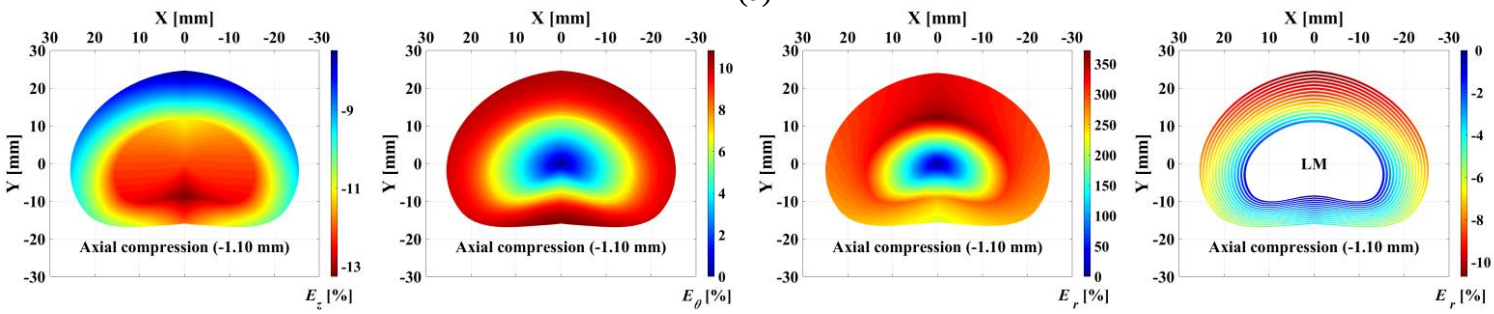

(b)

Figure IV.9. Morphology influence on the local strains local axial, circumferential and radial strains E_z, E_θ and E_r (in ILM and in LM) in axially compressed discs: (a) simplified disc morphology in circular basis with $R^0_{sagittal} = R^0_{frontal}$ (all initial heights and OCF orientations in Table IV.1 are averaged), (b) actual disc morphology.

IV.3.4. Damage fields

In this subsection, the damage fields for the different solid components (ECM, NEF and OCF) are analyzed in order to identify their respective role in the starting areas of failure modes under combined axial/torsion loadings.

The ECM and NEF damage are presented both in LM and in ILM in Figures IV.10 and IV.11, respectively. The ECM and the network of inter-lamellar fibrils (in LM) of the anterior side are more likely damaged when the disc is compressed. The latter can be the sign of the starting areas of the annulus delamination failure mode. The nucleus-annulus interface is also the site of a damage zone (Figures IV.10b and IV.11b) due to the pressure difference between the two portions. When the disc is stretched, the highest damage zones are shifted from the anterior side to the posterior side. Compared to the NEF network in ILM, the damage of inter-fibrillar fibrils (in LM) exhibits a very low intensity with an important effect of the loading mode both for the intensity

and the extent. Whatever the loading mode, the highest ECM damage zones in LM are located in the posterior side.

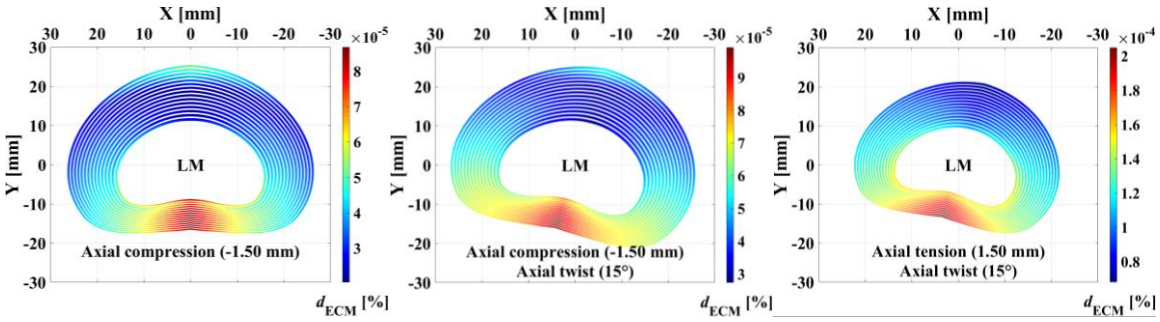

(a)

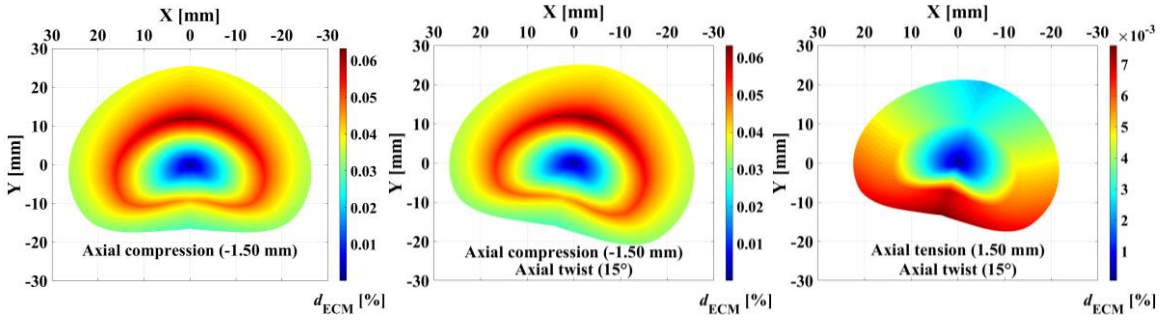

(b)

Figure IV.10. Contour plots of the ECM damage d_{ECM} in axially/torsionally loaded discs: (a) in LM, (b) in ILM.

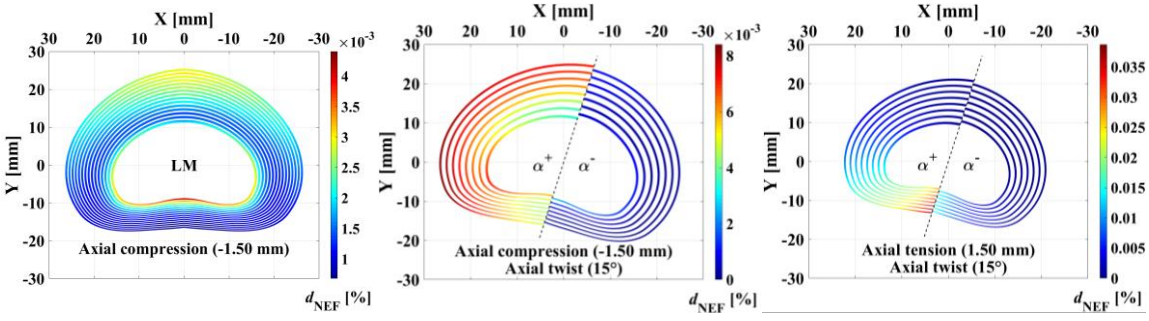

(a)

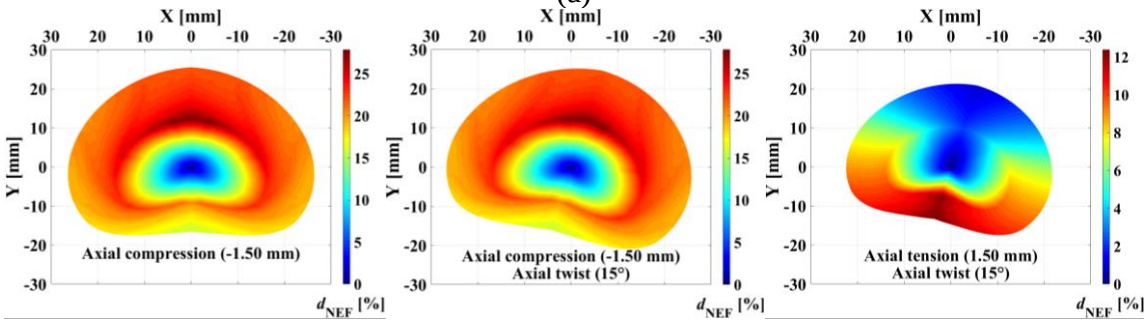

(b)

Figure IV.11. Contour plots of the NEF damage d_{NEF} in axially/torsionally loaded discs: (a) in LM, (b) in ILM.

Figure IV.12 shows the loading mode has a profound effect on the OCF damage. When the disc is compressed the highest OCF damage zones are mainly observed in mid-anterior/lateral anterior ring. The latter can be the sign of the starting areas of annulus circumferential tears. Combined to a compression, the twisted disc presents the highest OCF damage zones for the fibers oriented in twist direction with a progression from the AO side to the PO side. The alternate fibers are only damaged in a small area of the AO side. When the twisted disc is combined to a tension, the damage progression is reversed from the posterior side to the anterior side and, the damage of the alternate fibers is located in the PO region. The NEF network in ILM follows the same reverse compression/tension effect as shown in Figure IV.11. The latter may be due to the nucleus swelling effect but also to the regional difference in disc height.

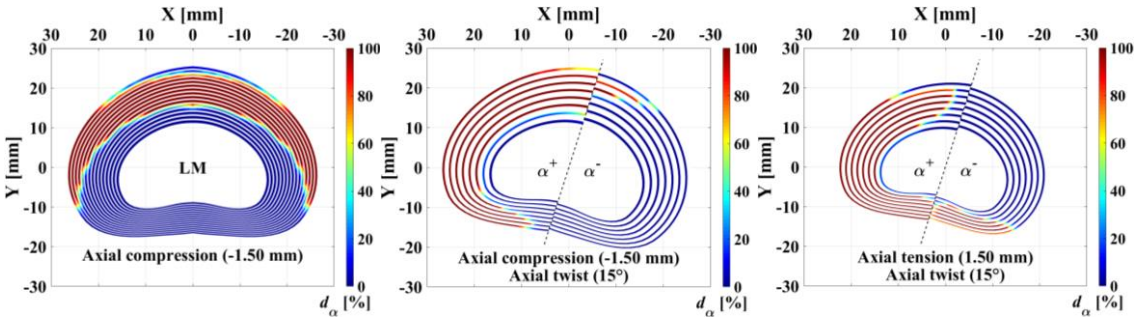

Figure IV.12. Contour plots of the OCF damage d_α (in LM) in axially/torsionally loaded discs.

IV.4. Conclusion

In this work, we have presented a new and direct analytical method for the creation of intervertebral discs considering accurate morphology, multiscale structure (ECM proteoglycan macromolecules, interpenetrating collagen fibrillar networks and LM/ILM/nucleus interaction) and hydration-damage effects. A first quantitative evaluation of the disc model was presented using available experimental observations. The model was used to assess the local fields under

combined axial/torsion loadings and especially the damage areas where the risk of failure is the highest.

The model can be improved by acting on the constitutive representation to take into consideration the age effects by biological coupling in order to assess the interaction with damage events. Other physiological movements could be introduced in further developments of the disc kinematics in order to propose quantitive predictions under more complex loading modes.

Appendix IV.A. Structure regional variation

IV.A.1. OCF regional variation

The regional variation in OCF angle is taken into account using the following linear equation:

$$\alpha_0^i = a^- i + b^- \text{ for } i = 3,7,11...n \tag{IV.A1}$$

$$\alpha_0^i = a^+ i + b^+ \text{ for } i = 1,5,9...n-2 \tag{IV.A2}$$

with

$$a^{+/-} = \frac{\left(\alpha_{PO}^{+/-} + \alpha_{AI}^{+/-} - \alpha_{AO}^{+/-} - \alpha_{PI}^{+/-}\right)\Theta + \left(\alpha_{AO}^{+/-} - \alpha_{AI}^{+/-}\right)\pi}{(n-1)\pi} \tag{IV.A3}$$

$$b^{+/-} = \frac{\left(\alpha_{PI}^{+/-} - \alpha_{AI}^{+/-}\right)\Theta + \alpha_{AI}^{+/-}\pi}{\pi} - a^{+/-} \tag{IV.A4}$$

in which $\alpha_{PO}^{+/-}$, $\alpha_{PI}^{+/-}$, $\alpha_{AO}^{+/-}$ and $\alpha_{AI}^{+/-}$ are the regional OCF angles.

IV.A.2. NEF regional variation

The volume fraction of a fibril in each ring *i* is given by:

$$\phi_\eta^{LM\_i} = \begin{cases} \dfrac{q_\eta^{LM\_i} + q_\eta^{ILM\_i}}{q^{LM\_i}} & \eta = 0°,180° \\ \dfrac{q_\eta^{LM\_i}}{q^{LM\_i}} & \eta = 45°,90°,135° \end{cases} \text{ and } \phi_\eta^{ILM\_i} = \begin{cases} 0 & \eta = 0°,180° \\ \dfrac{q_\eta^{ILM\_i}}{q^{ILM\_i}} & \eta = 45°,90°,135° \end{cases} \tag{IV.A5}$$

where q^{LM_i} and q^{ILM_i} are the respective total number of NEF in each ring *i*:

$$q^{LM\_i} = \sum_{\eta}\sum_{\psi} q_{\eta}^{LM\_i} + \sum_{\eta=0°,180°}\sum_{\psi} q_{\eta}^{ILM\_i} \text{ and } q^{ILM\_i} = \sum_{\eta=45°,90°,135°}\sum_{\psi} q_{\eta}^{ILM\_i} \quad \text{(IV.A6)}$$

The quantities $q_{\eta}^{LM\_i}$ and $q_{\eta}^{ILM\_i}$ are descibed using Gaussian probability density functions:

$$q_{\eta}^{LM\_i} = \chi_{\eta}^{LM\_i} \exp\left(-\varsigma_{\eta}^{LM\_i}\left(\psi-\eta\right)^2\right) \text{ and } q_{\eta}^{ILM\_i} = \chi_{\eta}^{ILM\_i} \exp\left(-\varsigma_{\eta}^{ILM\_i}\left(\psi-\eta\right)^2\right) \quad \text{(IV.A7)}$$

where $\chi_{\eta}^{LM\_i}$ and $\chi_{\eta}^{ILM\_i}$ denote the respective peak values of each fibrils bundle η = {0°, 45°, 90°, 135°, 180°} (Figure IV.4):

$$\chi_{\eta}^{LM\_i} = a_{\chi\_\eta}^{LM} i + b_{\chi\_\eta}^{LM} \text{ and } \chi_{\eta}^{ILM\_i} = a_{\chi\_\eta}^{ILM} i + b_{\chi\_\eta}^{ILM} \quad \text{(IV.A8)}$$

and, $\varsigma_{\eta}^{LM\_i}$ and $\varsigma_{\eta}^{ILM\_i}$ are unitless scale factors:

$$\varsigma_{\eta}^{LM\_i} = a_{\varsigma\_\eta}^{LM} i + b_{\varsigma\_\eta}^{LM} \text{ and } \varsigma_{\eta}^{ILM\_i} = a_{\varsigma\_\eta}^{ILM} i + b_{\varsigma\_\eta}^{ILM} \quad \text{(IV.A9)}$$

The terms $a_{\chi\_\eta}^{LM,ILM}$ and $b_{\chi\_\eta}^{LM,ILM}$ are expressed as a function of the posterior peak values $\chi_{\eta\_PO}^{LM,ILM}$ and $\chi_{\eta\_PI}^{LM,ILM}$ ($\Theta = \pi$) of the outer ring $i = n$ and the anterior peak values $\chi_{\eta\_AO}^{LM,ILM}$ and $\chi_{\eta\_AI}^{LM,ILM}$ ($\Theta = 0$) of the inner ring $i = 1$:

$$a_{\chi\_\eta}^{LM,ILM} = \frac{\left(\chi_{\eta\_PO}^{LM,ILM} + \chi_{\eta\_AI}^{LM,ILM} - \chi_{\eta\_AO}^{LM,ILM} - \chi_{\eta\_PI}^{LM,ILM}\right)\Theta + \left(\chi_{\eta\_AO}^{LM,ILM} - \chi_{\eta\_AI}^{LM,ILM}\right)\pi}{\left(n-1\right)\pi} \quad \text{(IV.A10)}$$

$$b_{\chi\_\eta}^{LM,ILM} = \frac{\left(\chi_{\eta\_PI}^{LM,ILM} - \chi_{\eta\_AI}^{LM,ILM}\right)\Theta + \chi_{\eta\_AI}^{LM,ILM}\pi}{\pi} - a_{\chi\_\eta}^{LM,ILM} \quad \text{(IV.A11)}$$

The terms $a_{\varsigma\_\eta}^{LM,ILM}$ and $b_{\varsigma\_\eta}^{LM,ILM}$ are expressed as a function of the posterior and anterior scale factors $\varsigma_{\eta\_PO}^{LM,ILM}$, $\varsigma_{\eta\_PI}^{LM,ILM}$, $\varsigma_{\eta\_AO}^{LM,ILM}$ and $\varsigma_{\eta\_AI}^{LM,ILM}$:

$$a_{\varsigma\_\eta}^{LM,ILM} = \frac{\left(\varsigma_{\eta\_PO}^{LM,ILM} + \varsigma_{\eta\_AI}^{LM,ILM} - \varsigma_{\eta\_AO}^{LM,ILM} - \varsigma_{\eta\_PI}^{LM,ILM}\right)\Theta + \left(\varsigma_{\eta\_AO}^{LM,ILM} - \varsigma_{\eta\_AI}^{LM,ILM}\right)\pi}{\left(n-1\right)\pi} \quad \text{(IV.A12)}$$

$$b_{\varsigma\_\eta}^{LM,ILM} = \frac{\left(\varsigma_{\eta\_PI}^{LM,ILM} - \varsigma_{\eta\_AI}^{LM,ILM}\right)\Theta + \varsigma_{\eta\_AI}^{LM,ILM}\pi}{\pi} - a_{\varsigma\_\eta}^{LM,ILM} \quad \text{(IV.A13)}$$

Appendix IV.B. Material properties regional variation

The regional variation of the (regional dependent) material properties is taken into account using the following linear equation:

$$C^i = a_C i + b_C \tag{IV.B1}$$

with

$$a_C = \frac{\left(C_{PO} + C_{AI} - C_{AO} - C_{PI}\right)\Theta + \left(C_{AO} - C_{AI}\right)\pi}{\left(n-1\right)\pi} \tag{IV.B2}$$

$$b_C = \frac{\left(C_{PI} - C_{AI}\right)\Theta + C_{AI}\pi}{\pi} - a_C \tag{IV.B3}$$

in which C_{PO}, C_{PI}, C_{AO} and C_{AI} are the regional material properties.

IV. References

Acaroglu, E.R., Iatridis, J.C., Setton, L.A., Foster, R.J., Mow, V.C., Weidenbaum, M., 1995. Degeneration and aging affect the tensile behavior of human lumbar anulus fibrosus. Spine 20, 2690-2701.

Adams, M.A., McNally, D.S., Wagstaff, J., Goodship, A.E., 1993. Abnormal stress concentrations in lumbar intervertebral discs following damage to the vertebral bodies: a cause of disc failure? European Spine Journal 1, 214-221.

Ambard, D., Cherblanc, F., 2009. Mechanical behavior of annulus fibrosus: a microstructural model of fibers reorientation. Annals of Biomedical Engineering 37, 2256-2265.

Amonoo-Kuofi, H.S., 1991. Morphometric changes in the heights and anteroposterior diameters of the lumbar intervertebral discs with age. Journal of Anatomy 175, 159-168.

Cassidy, J.J., Hiltner, A., Baer, E., 1989. Hierarchical structure of the intervertebral disc. Connective Tissue Research, 23, 75-88.

Castro, A.P.G., Alves, J.L., 2020. Numerical implementation of an osmo-poro-visco-hyperelastic finite element solver: application to the intervertebral disc. Computer Methods in Biomechanics and Biomedical Engineering 5, 538-550.

Costi, J.J., Stokes, I.A., Gardner-Morse, M., Laible, J.P., Scoffone, H.M., Iatridis, J.C., 2007. Direct measurement of intervertebral disc maximum shear strain in six degrees of freedom: motions that place disc tissue at risk of injury. Journal of Biomechanics 40, 2457-2466.

Derrouiche, A., Zaouali, A., Zaïri, F., Ismail, J., Chaabane, M., Qu, Z., Zaïri, F., 2019. Osmo-inelastic response of the intervertebral disc. Proceedings of the Institution of Mechanical Engineers. Part H: Journal of Engineering in Medicine 233, 332-341.

Derrouiche, A., Feki, F., Zaïri, F., Taktak, R., Moulart, M., Qu, Z., Ismail, J., Charfi, S., Haddar, N., Zaïri, F., 2020. How pre-strain affects the chemo-torsional response of the intervertebral disc. Clinical Biomechanics 76, 105020.

Ebara, S., Iatridis, J.C., Setton, L.A., Foster, R.J., Mow, V.C., Weidenbaum, M., 1996. Tensile properties of nondegenerate human lumbar anulus fibrosus. Spine 21, 452-461.

Guerin, H.A.L., Elliott, D.M., 2006. Degeneration affects the fiber reorientation of human annulus fibrosus under tensile load. Journal of Biomechanics 39, 1410-1418.

Holzapfel, G.A., Gasser, T.C., Ogden, R.W., 2000. A new constitutive framework for arterial wall mechanics and a comparative study of material models. Journal of Elasticity and the Physical Science of Solids 61, 1-48.

Holzapfel, G.A., Schulze-Bauer, C.A., Feigl, G., Regitnig, P., 2005. Single lamellar mechanics of the human lumbar anulus fibrosus. Biomechanics and Modeling in Mechanobiology 3, 125-140.

Kandil, K., Zaïri, F., Messager, T., Zaïri, F., 2021. A microstructure-based model for a full lamellar-interlamellar displacement and shear strain mapping inside human intervertebral disc core. Computers in Biology and Medicine 135, 104629.

Kim, K.H., Park, J.Y., Kuh, S.U., Chin, D.K., Kim, K.S., Cho, Y.E., 2013. Changes in spinal canal diameter and vertebral body height with age. Yonsei Medical Journal 54, 1498-1504.

Komeili, A., Rasoulian, A., Moghaddam, F., El-Rich, M., 2021. The importance of intervertebral disc material model on the prediction of mechanical function of the cervical spine. BMC Musculoskeletal Disorders 22, 1-12.

Marchand, F., Ahmed, A.M., 1990. Investigation of the laminate structure of lumbar disc anulus fibrosus. Spine 15, 402-410.

Markolf, K.L., Morris, J.M., 1974. The structural components of the intervertebral disc: a study of their contributions to the ability of the disc to withstand compressive forces. The Journal of Bone and Joint Surgery 56, 675-687.

Ogden, R.W., 1997. Non-linear elastic deformations. Dover Publication, New York.

Qasim, M., Natarajan, R.N., An, H.S., Andersson, G.B.J., 2012. Initiation and progression of mechanical damage in the intervertebral disc under cyclic loading using continuum damage mechanics methodology: a finite element study. Journal of Biomechanics 45, 1934-1940.

Qasim, M., Natarajan, R.N., An, H.S., Andersson, G.B.J., 2014. Damage accumulation location under cyclic loading in the lumbar disc shifts from inner annulus lamellae to peripheral annulus with increasing disc degeneration. Journal of Biomechanics 47, 24-31.

Shah, J.S., Hampson, W.G., Jayson, M.I., 1978. The distribution of surface strain in the cadaveric lumbar spine. Journal of Bone and Joint Surgery 60, 246-251.

Shahraki, N.M., Fatemi, A., Agarwal, A., Goel, V.K., 2015. Failure criteria for prediction of clinically relevant damage of annulus fibrosus. Spine Research 1, 7.

Skaggs, D.L., Weidenbaum, M., Iatridis, J.C., Ratcliffe, A., Mow, V.C., 1994. Regional variation in tensile properties and biochemical composition of the human lumbar anulus fibrosus. Spine, 19, 1310-1319.

Subramani, A.V., Whitley, P.E., Garimella, H.T., Kraft, R.H., 2020. Fatigue damage prediction in the annulus of cervical spine intervertebral discs using finite element analysis. Computer Methods in Biomechanics and Biomedical Engineering 23, 773-784.

Tamoud, A., Zaïri, F., Mesbah, A., Zaïri, F., 2021a. Modeling multiaxial damage regional variation in human annulus fibrosus. Acta Biomaterialia

Tamoud, A., Zaïri, F., Mesbah, A., Zaïri, F., 2021b. A microstructure-based model for time-dependent mechanics of multi-layered soft tissues and its application to intervertebral disc annulus. Meccanica 56, 585-606.

Tamoud, A., Zaïri, F., Mesbah, A., Zaïri, F., 2021c. A multiscale and multiaxial model for anisotropic damage and failure of human annulus fibrosus. International Journal of Mechanical Sciences 205, 106558.

Tavakoli, J., Elliott, D.M., Costi, J.J., 2017. The ultra-structural organization of the elastic network in the intra-and inter-lamellar matrix of the intervertebral disc. Acta Biomaterialia 58, 269-277.

Tavakoli, J., Diwan, A.D., Tipper, J.L., 2020a. The ultrastructural organization of elastic fibers at the interface of the nucleus and annulus of the intervertebral disk. Acta Biomaterialia 114, 323-332.

Tavakoli, J., Diwan, A.D., Tipper, J.L., 2020b. Elastic fibers: the missing key to improve engineering concepts for reconstruction of the nucleus pulposus in the intervertebral disc. Acta Biomaterialia 113, 407-416.

Urban, J.P., Maroudas, A., 1981. Swelling of the intervertebral disc in vitro. Connective Tissue Research 9, 1-10.

Virgin, W.J., 1951. Experimental investigations into the physical properties of the intervertebral disc. The Journal of Bone and Joint Surgery 33, 607-611.

Violas, P., Estivalezes, E., Briot, J., Sales de Gauzy, J., Swider P., 2007. Objective quantification of intervertebral disc volume properties using MRI in idiopathic scoliosis surgery. Magnetic Resonance Imaging 25, 386-391.

Werbner, B., Spack, K., O'Connell, G.D., 2019. Bovine annulus fibrosus hydration affects rate-dependent failure mechanics in tension. Journal of Biomechanics 89, 34-39.

General conclusions and perspectives

In this thesis, we have presented a physically-based model including realistic structural features in the material representation of the disc annulus. We have introduced features such as collagen orientation/content, interlamellar thickness and dimensional graduation along with the electro-chemical activity of the soft tissue. The model successfully reproduced a series of experimental data on bovine tissues under free swelling, quasi-static stretching and relaxation. It was demonstrated that for the evaluation of the overall time-dependent response, it is fundamental to consider simultaneously the structural features and diffusion-mechanics effects on volumetric change, Poisson's ratios and stress. The model was shown to be a powerful tool to better understand the annulus mechanics in relation to loading conditions, electro-chemical environment, intrinsic properties / proportion / orientation (if any) of constituents (ECM, fibers, fluid) and structural features.

The model was further enriched to constitutively relate the structure at different scales and the multiaxial macroscopic response till failure in connection to volumetric effects and damage mechanisms. It was shown that the model captures quantitatively experimental observations including directional effects upon different loading histories. The model provides a useful tool for annulus failure estimate in relation to complex interactions between external loading mode, structure features, damage events and hydration. It was also used to predict the variation of the annulus stiffness and ultimate properties with both disc region and loading mode. The different loading modes were simulated and chosen to better understand the regional behavior until the failure of the solid components in interaction with the chemical-induced volumetric response. The capabilities of the model were analyzed and an acceptable agreement between predicted values and experimental data was highlighted.

A full disc model was finally constructed. The model represents a new and direct analytical method for the creation of intervertebral discs considering accurate morphology, multiscale structure (ECM, interpenetrating collagen fibrillar networks and LM/ILM/nucleus interaction) and hydration-damage effects. A first quantitative evaluation of the disc model was presented using available experimental observations. The model was used to assess the local fields under combined axial/torsion loadings and especially the damage areas where the risk of failure is the highest.

Other physiological movements could be introduced in further developments of the disc kinematics in order to propose quantitive predictions under more complex loading modes. The model could be improved by acting on the constitutive representation to take into consideration the age effects by biological coupling in order to assess the interaction with damage events. The model could be indeed used to better understand the tissue response changes during aging and degeneration in response to changes in the tissue composition. The present model can be thus considered as the stepstone for the long-term prediction of the disc dysfunctions. During different complex loading scenarios of the spine, the disc dysfunctions may occur either by: i) mechanical damage due to a high level of loads or relatively moderate loads repeated several times which cause damage accumulation, ii) by an age-related biological degeneration or by the cellular disorders, including the cell death, the production of inflammatory mediators and a shift towards catabolism. Nonetheless, it is difficult to identify or precisely model the disc failure taking into account the two causes of dysfunction at the same time. Since our study is based on the in-vitro annulus results, it cannot be directly extrapolated to the in-vivo disc response. Indeed, the understanding of the disc mechanobiology must be taken into account by the model considering especially nutrition and cellular activity along with degenerative aspects. The model could be then a real help to provide solutions for remodeling and self-healing response of the disc tissues. Moreover, the near-field direct local interactions within the collagen network and the ECM ought to be treated through either the incorporation of a supplementary energy term or a mean-field approach.

Abstract

The damage in annulus soft tissues is a complex multiscale phenomenon due to a complex structural arrangement of collagen network at different scales of hierarchical organization. A constitutive representation that considers the structural complexity to estimate annulus multiaxial mechanics till failure has not yet been developed. In the present PhD dissertation, a model, formulated within the framework of nonlinear continuum mechanics, is developed to predict deformation-induced damage and failure of annulus under multiaxial loading histories. After model identification using an elementary lamellar unit, the model predictability is verified for various multiaxial loading modes representative of the spine movement. The heterogeneous mechanics of a full human disc model is finally presented.

Keywords: Multi-layered soft tissues; Intervertebral disc; Regional dependence; Multiscale structure; Multiaxial damage and failure; Constitutive modeling.

Résumé

L’endommagement dans les tissus souples de l'annulus fibrosus est un phénomène multi-échelle complexe dû à un arrangement structural complexe du réseau de collagène à différentes échelles d'organisation hiérarchique. Une représentation constitutive, considérant la complexité structurale, n'a pas encore été développée, pour estimer la mécanique multiaxiale de l'annulus jusqu'à la rupture. Dans la présente thèse de doctorat, un modèle, formulé dans le cadre de la mécanique non linéaire des milieux continues, est développé pour prédire l’endommagement et la rupture de l'annulus induits par la déformation sous des histoires de chargements multiaxiaux. Après identification du modèle sur une unité lamellaire élémentaire, le caractère prédictif du modèle est vérifié pour divers modes de chargement multiaxiaux représentatifs du mouvement de la colonne vertébrale. La mécanique hétérogène d’un disque humain complet est finalement présentée.

Mots-clés : Tissus souple multicouches ; Disque intervertébral ; Dépendance régionale ; Structure multi-échelles ; Endommagement multiaxial et rupture ; Modélisation constitutive.